Optical properties and electron/nuclear dynamics of nanoparticles

by

Pratima Pandeya

B.S., Tri-Chandra Multiple Campus, 2013
M.S., Tribhuvan University, 2016

AN ABSTRACT OF A DISSERTATION

submitted in partial fulfillment of the requirements for the degree

DOCTOR OF PHILOSOPHY

Department of Chemistry
College of Arts and Sciences

KANSAS STATE UNIVERSITY
Manhattan, Kansas

2021

Abstract

Studies of the excited state properties of nanoparticles are extremely important to find a good candidate for applications in the fields of catalysis, solar energy, biomedicine and so on. After absorption of light and excitation of electrons to excited states, the excited electrons can relax to the ground state through radiative and/or non-radiative pathways. We need to understand both the radiative and non-radiative relaxation times and mechanisms to choose the right candidate for different applications. For example, for a nanoparticle to be used as a photosensitizer, electrons should remain in excited states for a long time. In this dissertation, we first study the radiative and non-radiative relaxation mechanisms of excited electrons in thiolate-protected nanoclusters. We also investigate the effect of interparticle separations in tuning the optical properties of plasmonic nanowire assemblies. Finally, we examine the possibility of dinitrogen dissociation upon excitation of plasmonic resonances of single nanoparticles and nanoparticle assemblies.

We studied the non-radiative relaxation of excited electrons in $[Au_{25-n}Ag_n(SH)_{18}]^{-1}$ (n = 1, 12, 25) and $Au_{20}(SCH_3)_{16}$ using the fewest switches surface hopping approach. In all of the clusters, the electron relaxation from the first excited state (HOMO → LUMO) is found to have the longest decay time compared to the relaxation from higher excited states. This is because of the large gap (HOMO-LUMO gap) compared to the gap present between higher excited states. In the higher excited states, the orbitals are close in energy. So, the excited state population can immediately relax to the nearby orbitals and hence causes the fast relaxation of the excited state population. Among the silver doped Au_{25} clusters, $[Au_{13}Ag_{12}(SH)_{18}]^{-1}$ has the fastest decay times and the slowest ground state growth times (i.e. times for the population in an excited state to relax to the ground state) because of the closer lying orbitals in this nanocluster than in other

nanoclusters. This suggest that $[Au_{13}Ag_{12}(SH)_{18}]^{-1}$ is the best candidate to be used as a solar cell photosensitizer compared to other studied clusters.

Study of radiative relaxation of excited electrons in $Au_{20}(SCH_3)_{16}$ shows that luminescence can potentially occur from the S_1, S_2, and S_6 states. Dual luminescence is observed from S_1 at 0.41 eV and 0.68 eV. Without considering the underestimation due to the use of GGA functionals in our calculations, the experimentally observed luminescence at 1.51 eV matches with the S_6 luminescence at 1.50 eV. However, on considering the underestimation, this emission energy is higher than the experimental emission. On adding the underestimation, the S_2 emission at 1.44 eV is also close to the experimental emission at 1.51 eV. The cluster structure (mainly the ring and the trimeric staple motif) become the most distorted in the first excited state with luminescence at 0.41 eV whereas the cluster structure does not distort significantly in the S_2 and S_6 states.

We also studied the evolution of absorption spectra of plasmonic nanowire dimers and trimers at interparticle separations of 0.4-2.0 nm. We observed the appearance of an extra peak between the longitudinal and transverse peak when the interparticle separation is 0.6 nm and less. The extra peak was found to have charge transfer character where there is tunneling of electrons from one monomer to another.

Finally, we used real-time time dependent density functional methods to investigate the plasmon-mediated dinitrogen dissociation upon activation of plasmon resonances of the icosahedral $Al_{13}N_2^{-1}$ nanocluster and silver nanowire dimers. Because the occupation of nitrogen antibonding orbitals can lead to dinitrogen dissociation, we examined the occupation of virtual orbitals in $Al_{13}N_2^{-1}$. We observed the highest possibility of occupation of nitrogen antibonding orbitals by using off-resonant 0.01 au electric fields rather than by using 0.001 au resonant fields. For the parallel, end-to-end and hotspot oriented silver nanowire dimers, we analyzed the N-N

distance during the simulation using the Ehrenfest approach. The highest possibility of dinitrogen dissociation was observed using end-to-end oriented nanowires. The dissociation is more likely at small interparticle separation between the monomers compared to larger separation.

Optical properties and electron/nuclear dynamics of nanoparticles

by

Pratima Pandeya

B.S., Tri-Chandra Multiple Campus, 2013
M.S., Tribhuvan University, 2016

A DISSERTATION

submitted in partial fulfillment of the requirements for the degree

DOCTOR OF PHILOSOPHY

Department of Chemistry
College of Arts and Sciences

KANSAS STATE UNIVERSITY
Manhattan, Kansas

2021

Approved by:

Major Professor
Christine M. Aikens

Copyright

Abstract

Studies of the excited state properties of nanoparticles are extremely important to find a good candidate for applications in the fields of catalysis, solar energy, biomedicine and so on. After absorption of light and excitation of electrons to excited states, the excited electrons can relax to the ground state through radiative and/or non-radiative pathways. We need to understand both the radiative and non-radiative relaxation times and mechanisms to choose the right candidate for different applications. For example, for a nanoparticle to be used as a photosensitizer, electrons should remain in excited states for a long time. In this dissertation, we first study the radiative and non-radiative relaxation mechanisms of excited electrons in thiolate-protected nanoclusters. We also investigate the effect of interparticle separations in tuning the optical properties of plasmonic nanowire assemblies. Finally, we examine the possibility of dinitrogen dissociation upon excitation of plasmonic resonances of single nanoparticles and nanoparticle assemblies.

We studied the non-radiative relaxation of excited electrons in [Au25-nAgn(SH)18]-1 (n = 1, 12, 25) and Au20(SCH3)16 using the fewest switches surface hopping approach. In all of the clusters, the electron relaxation from the first excited state (HOMO □ LUMO) is found to have the longest decay time compared to the relaxation from higher excited states. This is because of the large gap (HOMO-LUMO gap) compared to the gap present between higher excited states. In the higher excited states, the orbitals are close in energy. So, the excited state population can immediately relax to the nearby orbitals and hence causes the fast relaxation of the excited state population. Among the silver doped Au25 clusters, [Au13Ag12(SH)18]-1 has the fastest decay times and the slowest ground state growth times (i.e. times for the population in an excited state to relax to the ground state) because of the closer lying orbitals in this nanocluster than in other

nanoclusters. This suggest that $[Au_{13}Ag_{12}(SH)_{18}]^{-1}$ is the best candidate to be used as a solar cell photosensitizer compared to other studied clusters.

Study of radiative relaxation of excited electrons in $Au_{20}(SCH_3)_{16}$ shows that luminescence can potentially occur from the S_1, S_2, and S_6 states. Dual luminescence is observed from S_1 at 0.41 eV and 0.68 eV. Without considering the underestimation due to the use of GGA functionals in our calculations, the experimentally observed luminescence at 1.51 eV matches with the S_6 luminescence at 1.50 eV. However, on considering the underestimation, this emission energy is higher than the experimental emission. On adding the underestimation, the S_2 emission at 1.44 eV is also close to the experimental emission at 1.51 eV. The cluster structure (mainly the ring and the trimeric staple motif) become the most distorted in the first excited state with luminescence at 0.41 eV whereas the cluster structure does not distort significantly in the S_2 and S_6 states.

We also studied the evolution of absorption spectra of plasmonic nanowire dimers and trimers at interparticle separations of 0.4-2.0 nm. We observed the appearance of an extra peak between the longitudinal and transverse peak when the interparticle separation is 0.6 nm and less. The extra peak was found to have charge transfer character where there is tunneling of electrons from one monomer to another.

Finally, we used real-time time dependent density functional methods to investigate the plasmon-mediated dinitrogen dissociation upon activation of plasmon resonances of the icosahedral $Al_{13}N_2^{-1}$ nanocluster and silver nanowire dimers. Because the occupation of nitrogen antibonding orbitals can lead to dinitrogen dissociation, we examined the occupation of virtual orbitals in $Al_{13}N_2^{-1}$. We observed the highest possibility of occupation of nitrogen antibonding orbitals by using off-resonant 0.01 au electric fields rather than by using 0.001 au resonant fields. For the parallel, end-to-end and hotspot oriented silver nanowire dimers, we analyzed the N-N

distance during the simulation using the Ehrenfest approach. The highest possibility of dinitrogen dissociation was observed using end-to-end oriented nanowires. The dissociation is more likely at small interparticle separation between the monomers compared to larger separation.

Table of Contents

List of Figures

List of Tables

Acknowledgements

My sincere and deepest gratitude to Professor Christine Aikens for giving me the opportunity of graduate studies in her group. I am very thankful to the guidance, support and patience she provided to me throughout these years.

I would also like to acknowledge my supervisory committee members Prof. Paul Smith, Prof. Peter Sues, Prof. Bin Liu, and Prof. Daniel Rolles for their support and time. I am also thankful to Prof. Emily McLaurin for supporting me by being on my supervisory committee for two years.

I am very grateful to the past and present Aikens and Liu group members for always making the lab environment and group meetings vibrant and for sharing their knowledge with me.

I am truly thankful to Dr. Dave Turner and all Beocat staff for helping me with technical issues with Beocat.

My sincere gratitude to Kansas State University, Department of Chemistry for giving me the opportunity of graduate studies.

I am thankful to all the teachers I met for inspiring me to be a good person.

My special thanks to my parents, sisters and husband for their endless love, care and support.

Dedication

To my family

Chapter 1 - Introduction

Nanoparticles are nanometer sized particles that have unique properties compared to their bulk counterparts.[1-3] Their properties vary with changes in their shapes and sizes. Metal nanoparticles can be composed of noble or non-noble metals. Noble metals (e.g. gold, silver nanoparticles) have full shells of d-orbitals and are resistant to chemical attack whereas the non-noble metals (e.g. aluminum) can easily undergo chemical attack. This is one reason that noble metal nanoparticles have found various applications.[4] However, because the noble metals are scarce and costly, the non-noble nanoparticles are also getting attention. Non-noble nanoparticles have also found various applications including hydrogenation, photocatalytic water splitting, and oxygen reduction.[5-7] Nanoparticles can also have ligands protecting their core or no ligands at all. In this dissertation, we study the geometrical and optical properties of the ligand protected and (non-ligated) bare nanoparticles.

1.1 Types of nanoparticles

1.1.1 Thiolate protected nanoparticles

The core of these nanoparticles are protected with thiolate (SH) ligands. The ligand protected nanoparticles with core diameters of less than 2 nm are known as nanoclusters.[8] The nanoclusters show molecular like properties, e.g. a discrete HOMO-LUMO transition and enhanced photoluminescence, due to their small size.

The stability of the thiolate protected nanoparticles can be predicted according to 'superatom electronic theory' that is analogous to atomic theory.[9] For the delocalized superatomic orbitals, the aufbau rule is $1S^2|\ 1P^6|\ 1D^{10}|\ 2S^2\ 1F^{14}|\ 2P^6\ 1G^{18}|\ 2D^{10}\ 3S^2\ 1H^{22}|$ …., where S, P, D, F, G, H refer to the angular momentum quantum numbers.[10] So, the nanoparticles have extra stability

if the number of valence electrons corresponds to a shell closure of superatomic orbitals. For the ligand protected nanoclusters with configuration $(A_NX_ML_S)^z$, the valence electrons can be counted according to

$$n = N - M - z \quad (1.1)$$

where A refers to atoms comprising the nanocluster core, N is the number of valence electrons from the metal atoms in the core (assuming that each atom A contributes exactly 1 electron), X refers to an electron withdrawing ligand, L refers to a dative ligand, and z is the charge of the cluster.[10]

The thiolate protected nanoparticles have found application in various areas including catalysis, solar energy and sensing.[3, 11-12] It is very important to understand the structure and electronic properties of these nanoclusters to tune them for the desired applications. Below, we will introduce the nanoclusters we have studied in this dissertation, along with their geometrical shapes and optical properties.

1.1.1.1 $[Au_{25}(SR)_{18}]^{-1}$

$[Au_{25}(SR)_{18}]^{-1}$ is one of the most stable noble metal nanoparticles.[13] The crystal structure of this cluster has an icosahedral Au_{13} core capped by an exterior shell of the remaining 12 Au atoms. These 12 Au atoms are arranged alternating with S atoms forming six −SR−Au−SR−Au−SR− staple motifs (Figure 1-1).[14] It has three prominent peaks at 1.8, 2.75, and 3.1 eV in its experimental absorption spectrum (Figure 1-2).[14]

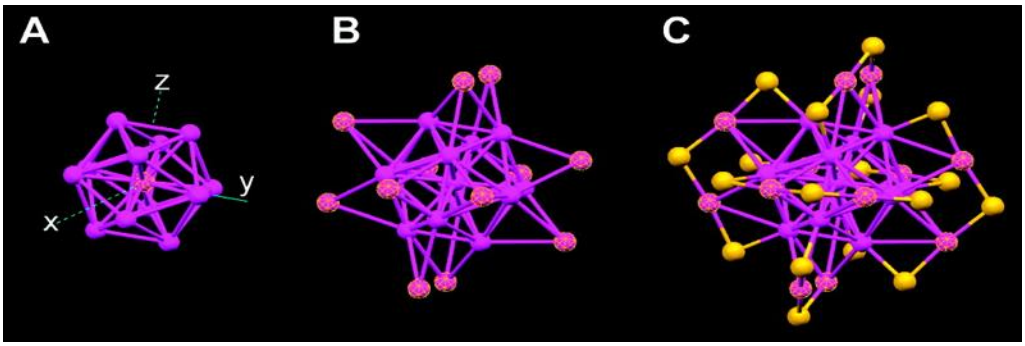

Figure 1-1 Crystal structure of $[Au_{25}(SR)_{18}]^{-1}$ (A) the icosahedral Au_{13} core (B) Au_{13} core plus the exterior 12 Au atoms (C) the whole Au_{25} cluster protected by 18 thiolate ligands (only S is shown for clarity, magenta−Au; yellow−S) (Reprinted with permission from *J. Am. Chem. Soc.* 2008, *130,* 5883-5885. Copyright 2008 American Chemical Society).

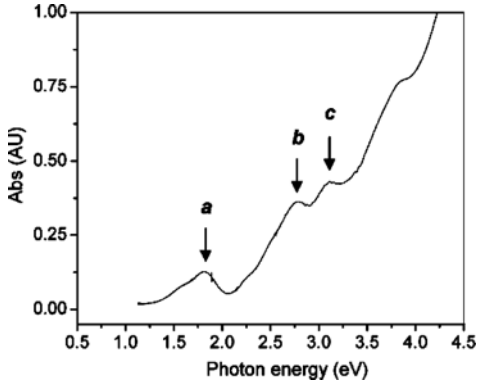

Figure 1-2 UV-Vis spectrum of Au_{25} single clusters re-dissolved in toluene (Reprinted with permission from *J. Am. Chem. Soc.* 2008, *130,* 5883-5885. Copyright 2008 American Chemical Society).

The cluster has a triply degenerate HOMO and doubly degenerate LUMO. The HOMO and the lowest three LUMO orbitals constitute the sp-band since they have their main contribution from the 6sp atomic orbitals of gold. The HOMO-1 to HOMO-5 are sometimes called the d-band orbitals since they are mainly composed from $5d^{10}$ atomic orbitals as well as 3p orbitals from sulfur (Figure 1-3).

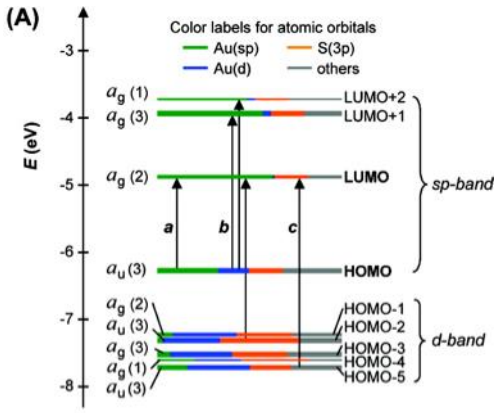

Figure 1-3 Kohn-Sham energy level diagram of $[Au_{25}(SR)_{18}]^{-1}$ (Reprinted with permission from *J. Am. Chem. Soc.* 2008, *130,* 5883-5885. Copyright 2008 American Chemical Society).

Doping of nanoparticles

Doping helps to tune the electronic and optical properties of nanoparticles to get desirable properties.[15-18] The first experimentally observed doped cluster was $Au_{24}Pd(SR)_{18}$.[19] Since then, different studies have been performed to dope single or multiple metal atoms in the nanoclusters.[20-24]

Various proportions of silver atoms can be doped in gold clusters since they have similar lattice constants.[25] Doping of silver in gold nanoclusters does not change the shape of nanoclusters but the optical properties get changed.[25] Theoretical studies on the doping of Ag atoms on $[Au_{25}(SR)_{18}]^{-1}$ nanocluster shows that the most favorable place to dope a single or many silver atoms is on the surface of the core.[20, 25] On doping more than a single atom, the structures in which the silver atoms are in close proximity are found to be less favorable.[25] On increasing the number of dopant Ag atoms, the peak of $[Au_{25}(SR)_{18}]^{-1}$ at ~1.8 eV blue shifts while the intensity increases for the higher energy peak at 2.75 eV. Additionally, the doped clusters have broader spectra due to the symmetry breaking. Researchers have been able to dope about 24 silver atoms into the $[Au_{25}(SR)_{18}]^{-1}$ cluster so far, as analyzed by mass spectrometry method.[26] In this dissertation, we

study the optical properties of single and twelve silver atoms doped $[Au_{25}(SR)_{18}]^{-1}$ nanocluster. This will help to understand the effect of a few dopants or a larger number of dopants on the electronic structure of the nanocluster.

1.1.1.2 $[Ag_{25}(SR)_{18}]^{-1}$

Bakr and co-workers first synthesized $[Ag_{25}(SR)_{18}]^{-1}$ that is an exact analog of $[Au_{25}(SR)_{18}]^{-1}$ in terms of size, superatom electronic configuration, charge, composition and crystal structure.[27] Similar to the $[Au_{25}(SR)_{18}]^{-1}$ nanocluster, it has an icosahedral Ag_{13} core and six −SR−Au−SR−Au−SR− staple motifs. It is found to be slightly less stable than $[Au_{25}(SR)_{18}]^{-1}$ at ambient conditions whereas both of the clusters are stable for weeks at 4 °C. UV−vis spectroscopy shows the absorption onset at ~850 nm (Figure 1-4). A theoretical study from Weerawardene et al. showed the luminescence in $[Ag_{25}(SR)_{18}]^{-1}$ to arise from HOMO-LUMO transition as observed for Au_{25} nanoclusters.[28] It is interesting to understand the optical properties of $[Ag_{25}(SR)_{18}]^{-1}$ which has properties similar to $[Au_{25}(SR)_{18}]^{-1}$. This helps to understand how the excited state electron dynamics gets effected from $[Au_{25}(SR)_{18}]^{-1}$ to $[Ag_{25}(SR)_{18}]^{-1}$.

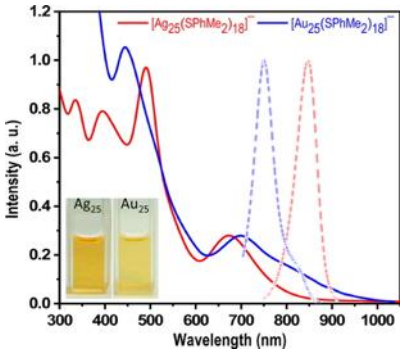

Figure 1-4 Absorption (solid-lines) and normalized emission (dotted-lines) spectra of $[Ag_{25}(SPhMe_2)_{18}]^-$ and $[Au_{25}(SPhMe_2)_{18}]^-$ in DCM. Inset: photographs showing actual color of the synthesized clusters (Reprinted with permission from *J. Am. Chem. Soc.* 2015, *137*, 11578-11581. Copyright 2015 American Chemical Society).

1.1.1.3 $Au_{20}(SCH_3)_{16}$

Jin and co-workers first synthesized $Au_{20}(SCH_2CH_2Ph)_{16}$ in 2009.[29] They observed the cluster to have a large HOMO-LUMO gap of 2.15 eV and to be extraordinarily robust against excess thiol etching. The cluster is found to have the most prominent absorption peak at 2.56 eV and two additional spectral features at 2.95 eV and 3.50 eV. The dimer of this cluster connected by diglyme ligands, i.e. ($Au_{20}(SC_2H_4Ph)_{15}$-diglyme-$Au_{20}(SC_2H_4Ph)_{15}$), shows strong visible photoluminescence which is absent in the monomer.[30-31] In this dissertation, we have studied the Au_{20} monomer that will provide a foundation for the future study on dimer-diglyme system.

After the synthesis of $Au_{20}(SCH_2CH_2Ph)_{16}$, many studies have been undertaken to understand the structure of this nanocluster.[32-36] These studies have proposed different structures for the cluster. X-ray crystallographic analysis of $Au_{20}(TBBT)_{16}$ (TBBT = SPh-^{t}Bu) by Jin and co-workers shows the cluster to have two monomeric and one trimeric staple motifs, one $Au_8(SR)_8$ ring structure and Au_7 core.[34] A theoretical study by Weerawardene et al.[35] supported that the lowest energy structure of Au_{20} is as predicted by the Jin group.[34] Another recent study from Pei and co-workers suggests the cluster to have two dimeric and one trimeric staple motifs, $Au_6(SR)_6$ ring structure and Au_7 core.[36] So, in this dissertation we compare the stability of these two structures to find the most stable structure and then we study its optical properties.

1.1.2 Bare nanoparticles

Bare nanoparticles have found interest in catalysis because their catalytic activity solely depend on the surface of nanoparticles and is not changed by the presence of the ligands.[37] They also provide larger surface area than the extended flat surfaces.[38-39] Since the surface atoms of these clusters are not fully coordinated, they are favorable for the binding of molecules during

catalysis. We have studied the optical properties of two types of bare nanoparticles: silver nanowires and an aluminum cluster.

1.1.2.1 Nanowires

Nanowires are cylindrical nanoparticles that have found significant interest because their optical properties are sensitive to their aspect ratio.[40-41] Aspect ratio is defined as the length of the major axis defined by the width of the minor axis.[42] So, one can tune the absorption peak of these nanoparticles just by changing the length and width of these nanoparticles.

Cylindrical nanoparticles like nanowires have two prominent plasmonic peaks in their absorption spectra: the longitudinal peak and the transverse peak.[40] The longitudinal peak appears due to the plasmon oscillation along the long axis of the nanowires while the transverse peak appears due the plasmon oscillation along the short axis of the nanowires. The longitudinal peak position is more sensitive to the aspect ratio of the nanowires than the transverse peak position. The longitudinal plasmon peak can red-shift to IR-region on increasing the aspect ratio.[43-44] Uppercase Greek letters Σ, Π, Δ, Φ, … are used to explain the angular momentum of the nanowire orbitals due to their cylindrical symmetry.[45]

Silver nanowires are plasmonic nanoparticles that show strong plasmon peaks in their absorption spectra.[46] When metal nanoparticles interact with light, the free electrons in metal oscillate collectively with the frequency of incident light relative to the positive ions. This process of oscillation of the free electrons is called the localized surface plasmon resonance. A strong electric field is generated during this process which enhances the optical properties.[47] These optical properties can be explained according to the Maxwell equations.[48-49] The plasmonic properties of nanoparticles are dependent on various parameters, e.g. shape, size, structure, of the nanoparticles.[50]

In this dissertation, we have studied the absorption spectra of the linear Ag_4, Ag_6 and Ag_{10} nanowire dimers and trimers. The optical properties of the assemblies get tuned on changing the interparticle separation. Although these small linear nanowires are not local minimum structures and are not in a linear shape under experimental conditions, these model systems help to understand the optical properties of larger nanoparticles. Because the plasmonic properties of the plasmonic nanowires/nanoparticles can be changed by making their assemblies, it is important to understand the tuning of the spectra in the nanowire assemblies.[51] So, we have studied the tuning of the spectra of the nanowire assemblies at the interparticle separation of 0.4-2.0 nm. We have used the plasmon hybridization model to explain the optical properties of nanoparticle assemblies. We have also studied plasmon enhanced photocatalytic dissociation of the nitrogen molecule upon excitation of plasmon resonances of Ag_4 nanowire dimers (Section 1.2.3).

Plasmon hybridization model

This model describes how plasmon hybridization arises due to coupling of plasmon modes of neighboring nanoparticles, which is analogous to the bonding and antibonding interactions of molecular orbital theory.[52] This interaction leads to two additional modes of the plasmon: a symmetrically coupled bonding mode with lower energy and an anti-symmetrically coupled antibonding mode with higher energy (Figure 1-5). If the mode has a net dipole moment, it can couple with electromagnetic radiation. So, this mode is also called the bright mode. If the mode does not have a net dipole moment, it cannot couple with the electromagnetic radiation and hence is also known as the dark mode. This model has been able to describe the plasmonic properties of several nanoparticles including nanoshells, nanoeggs, and nanorice.[53]

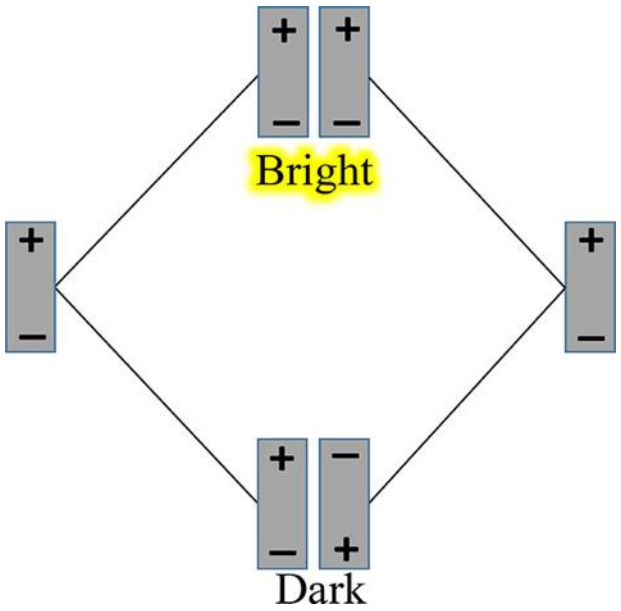

Figure 1-5 Plasmon hybridization model showing longitudinal plasmon interaction in nanoparticles (Reprinted with permission from *J. Phys. Chem. C* 2020, *124*, 13495-13507. Copyright 2020 American Chemical Society).

1.1.2.2 Aluminum nanoparticles

Aluminum nanoparticles (i.e. non-noble nanoparticles) are getting significant attention because they are cheaper than the noble metal nanoparticles and are also plasmonic in nature.[54-56] Although the plasmon peak of the noble metal nanoparticles can be tuned from visible to infrared region, reaching up to the UV region is challenging.[56] For gold nanoparticles, there are dissipative channels at wavelength shorter than 550 nm. The silver nanoparticles undergo rapid oxidation that suppresses their plasmonic activity.[56] The plasmons in the UV region are important for the detection of certain organic molecules that require high photon energies to match with their electronic transitions.[57] Aluminum is interesting to researchers because it has its plasmon peak in the UV region.[58]

Plasmonic aluminum nanoparticles have been used in different fields including catalysis and spectroscopy.[59-60] For example, Halas et al. showed the plasmon mediated dissociation of the

hydrogen molecule upon illuminating plasmonic aluminum nanocrystals at room temperature and atmospheric pressure.[60] They reported that the hot electron transfer from the aluminum nanocrystals to the hydrogen antibonding orbitals causes the dissociation. In another study, researchers have reported adenine detection upon using deep-UV surface-enhanced resonance Raman scattering on aluminum nanostructures.[59]

In this dissertation, we have studied plasmon enhanced photocatalytic dissociation of the nitrogen molecule upon excitation of plasmon resonances of the Al_{13}^{-1} nanocluster. The Al_{13}^{-1} plasmonic nanoparticle is a very stable cluster with an icosahedral shape.[61]

1.2 Excited state properties of nanoparticles

On absorption of a photon, electrons can become promoted into an excited state. The excited electrons cannot remain in the excited state forever; they have to eventually dissipate the energy they gained. So, they relax back to the lower excited states and finally to the ground state. There are two mechanisms of relaxation of the excited electrons: radiative and non-radiative mechanisms. Vibrational relaxation and internal conversion are non-radiative pathways whereas fluorescence and phosphorescence are the radiative pathways. All of the mechanisms of the relaxation of excited electron can be summarized in a Jablonski diagram (Figure 1-6).[62]

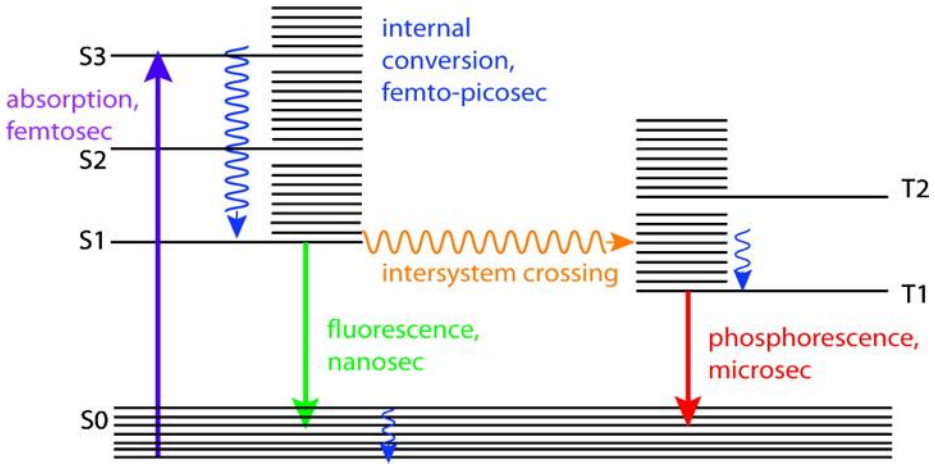

Figure 1-6 Jablonski diagram along with the time scale of photophysical processes (Reprinted with permission from *Chem. Rev.* 2010, *110*, 2641-2684. Copyright 2010 American Chemical Society).

1.2.1 Radiative relaxation of excited electrons

This mechanism is also known as photoluminescence; it is a process of emission of electromagnetic radiation resulting after the irradiation of a substance with light. It is an important process for biomedical applications because it provides easy detection, easy sample preparation, and high sensitivity.[63-64] However, the practical application of nanoparticles in bioimaging is hampered due to the low quantum yield.[65-66] So, researchers are interested to understand the origin of photoluminescence in nanoparticles in order to enhance their photoluminescence properties.

Charge transfer states, ligand based states, and intraband/interband transitions are thought to be responsible for emission in the nanoparticles.[67-69] Photoluminescence is also found to depend on the type of ligand, overall charge of the cluster, size of the cluster, solvent type, aggregation of the cluster, and temperature.[68, 70] A work on the $[Au_{25}(SR)_{18}]$ nanocluster showed that fluorescence is enhanced when using ligands with electron-rich atoms (e.g., N, O) or groups (e.g.,-COOH, NH_2).[68] This work suggested that the fluorescence can be increased by increasing the electron donation capacity of the ligands and by increasing the electropositivity of the metal core.

Radiative lifetimes τ_i of the excited states i are obtained with the equation:[71]

$$\frac{1}{\tau_i} = \frac{4}{3t_0}\alpha_0^3(\Delta E_i)^3 \sum_{\alpha\in(x,y,z)} |M_\alpha^i|^2 \qquad (1.2)$$

where α_0 is the fine structure constant, ΔE_i is the excitation energy, and M_α^i is the transition dipole moment in $\alpha = x, y, z$ direction. $t_0 = (4\pi\epsilon_0)^2\hbar^3/m_e e^4$, where ϵ_0 is the vacuum dielectric constant, $\hbar$ is the Planck constant divided by 2π, m_e is the mass of electron, and e is the charge of electron. In this dissertation, we have studied the geometrical and electronic structures of the excited states of the $Au_{20}(SCH_3)_{16}$ nanocluster. We also investigate the radiative relaxation mechanism of the electrons excited to various excited states and their lifetimes.

1.2.2 Nonradiative relaxation dynamics

In this mechanism, the absorbed energy is dissipated in the form of heat; no photon is generated. Researchers are interested to investigate this mechanism so that nonradiative processes can be decreased in order to get the nanoparticles with highly luminescent properties. Many experimental and theoretical studies have been done to understand the nonradiative relaxation mechanism of the $[Au_{25}(SR)_{18}]^{-1}$ nanocluster.[72-74] Knappenberger and co-workers observed a nonradiative core-to-ligand energy transfer process, following the internal conversion on a few picosecond time scale, as the main relaxation mechanism in anionic and neutral $Au_{25}L_{18}$ nanoclusters.[73] Recently, a theoretical study on the nonradiative dynamics of the $[Au_{25}(SR)_{18}]^{-1}$ nanocluster from Aikens and co-workers showed that the experimentally observed time constants[72] arise from core-to-core transitions rather than from a core-to-staple motif transition.[74] They have also investigated the effect of ligands (CH_3, C_2H_5, C_3H_7, MPA, PET) [MPA = mercaptopropanoic acid, PET = phenylethylthiol]) on the excited state dynamics of the nanocluster.[75] Non-radiative

electron relaxation has also been studied experimentally for Pd, Pt, and Hg doped $[Au_{25}(SR)_{18}]^{-1}$ nanoclusters and is found to be affected by doping.[76-78] However, there are no studies that investigate the non-radiative relaxation of excited electrons in the silver doped $[Au_{25}(SR)_{18}]^{-1}$ cluster. Herein, we have investigated the electron relaxation mechanism in $[Au_{25}(SR)_{18}]^{-1}$ nanoclusters doped with one or twelve silver atoms, i.e., $[Au_{24}Ag(SR)_{18}]^{-1}$ and $[Au_{13}Ag_{12}(SR)_{18}]^{-1}$. This study provides information on the relaxation mechanism of excited electrons on doped nanoclusters as well as the effect of doping on decay time constants. In addition, we have studied the electron relaxation dynamics in $[Ag_{25}(SR)_{18}]^{-1}$ which can be considered as a fully doped $[Au_{25}(SR)_{18}]^{-1}$. To the best of our knowledge, we are not aware of any experimental studies on the nonradiative relaxation in $[Ag_{25}(SR)_{18}]^{-1}$.

Electron relaxation mechanism studies are also important to understand the structure-property relationships of nanoparticles. We have also studied the non-radiative electron relaxation mechanism in $Au_{20}(SR)_{16}$. Zhou et al. have performed a femtosecond transient absorption study on $Au_{20}(SR)_{16}$.[79] A femtosecond transient absorption study of $Au_{20}(CH_2CH_2Ph)_{16}$ in toluene and tetrahydrofuran reported the intramolecular charge transfer from the outside shell to the inside core of the nanocluster. The electron relaxation is found to be faster using the more polar solvent tetrahydrofuran than on using the less polar solvent toluene. $Au_{20}(SR)_{16}$ is a one of the stable nanoclusters with a high HOMO-LUMO gap of 2.15 eV,[29] and thus nonradiative relaxation studies on this cluster might be important to determine its applicability for applications such as in photosensitizers.

1.2.3 Plasmon enhanced photocatalysis

In this process, solar radiation interacts with plasmonic nanoparticles to enable their use as a catalyst for different purposes. Upon solar light irradiation, hot carriers are generated in the plasmonic materials which then excite the electronic and vibrational states of the molecules adsorbed to the plasmonic materials.[80] There have been several studies on the use of plasmonic nanoparticles as photocatalyst for different purposes like CO_2 reduction and water splitting.[81-83] For example, Moon et al. studied the photocatalytic oxygen evolution reaction using TiO_2 nanotube arrays having plasmonic gold nanoparticles with a size of 5–30 nm.[81] The oxygen evolution reaction was observed due to the hot electron flux generated from the decay of the localized surface plasmon resonance. In their study, higher oxygen evolution was observed on the smaller nanoparticles.

Because dinitrogen dissociation is the most difficult step in the Haber Bosch process, which normally requires high temperature and pressure, we have investigated the possibility of dinitrogen dissociation at mild conditions upon excitation of plasmonic resonances of the Al_{13}^{-1} nanocluster and Ag_4 nanowire dimers. Because aluminum nanoclusters are cheaper than the noble metal nanoclusters and are also known to have strong absorption at UV region, it is important to understand the possibility of photocatalysis upon excitation of plasmon resonances of aluminum nanoclusters. There are very limited works done on the plasmon enhanced dissociation of nitrogen molecule in the literature.[84-89] Martirez et al.[84] investigated alloys of plasmonic gold nanoparticles for ammonia synthesis. They found that the nitrogen dissociation on the Au(111) can be improved on using Fe and Mo dopants respectively. So, it is essential to investigate the possibility of dinitrogen dissociation using various other plasmonic materials under ambient conditions.

1.3 Objectives of the dissertation

It is important to understand the excited state properties of nanoparticles for their use in solar cells, biomedicine and others. Researchers have studied the radiative and nonradiative relaxation of excited electrons to understand the mechanism and time of the relaxation. The excited electron relaxation mechanisms and time scales have been found to depend on the type and size of ligand and nanoparticles. Doping of nanoparticles is a method to tune the optical properties of nanoparticles to get desired properties. So, it is very important to understand the electron relaxation dynamics in doped nanoparticles as well. The main objective of this dissertation is to understand the electron relaxation mechanism in doped and other thiolate-protected nanoclusters. The secondary goal of this dissertation is to understand how the absorption spectra of nanoparticle assemblies get tuned on changing the interparticle separation. The final goal is to understand the plasmon mediated dissociation of the dinitrogen molecule.

Chapter 2 describes the computational details used in the dissertation. Chapter 3 explores the nonradiative relaxation dynamics in $[Au_{25-n}Ag_n(SH)_{18}]^{-1}$ (n = 1, 12, 25) thiolate-protected nanoclusters. Chapter 4 provides a theoretical study of radiative and nonradiative relaxation of excited electrons in $Au_{20}(SCH_3)_{16}$. Chapter 5 gives a theoretical analysis of optical absorption spectra of parallel nanowire dimers and dolmen trimers at large and small interparticle separations. Chapter 6 explains the real-time time dependent density functional theory examination of nanowire arrays for the plasmonic enhanced dissociation of dinitrogen. Chapter 7 provides a real-time electron dynamics study of plasmon-mediated photocatalysis on an icosahedral Al_{13}^{-1} nanocluster. Finally, Chapter 8 summarizes the main findings of this dissertation.

1.4 References

1. Murthy, S. K., Nanoparticles in Modern Medicine: State of the Art and Future Challenges. *Int. J. Nanomedicine* **2007,** *2* (2), 129-141.

2. Valden, M.; Lai, X.; Goodman, D. W., Onset of Catalytic Activity of Gold Clusters on Titania with the Appearance of Nonmetallic Properties. *Science* **1998,** *281* (5383), 1647-1650.

3. Zhu, Y.; Qian, H.; Drake, B. A.; Jin, R., Atomically Precise $Au_{25}(SR)_{18}$ Nanoparticles as Catalysts for the Selective Hydrogenation of α,β-Unsaturated Ketones and Aldehydes. *Angew. Chem. Int. Ed.* **2010,** *49* (7), 1295-1298.

4. Sau, T. K.; Rogach, A. L.; Jäckel, F.; Klar, T. A.; Feldmann, J., Properties and Applications of Colloidal Nonspherical Noble Metal Nanoparticles. *Adv. Mater.* **2010,** *22* (16), 1805-1825.

5. Liu, L.; Concepción, P.; Corma, A., Non-Noble Metal Catalysts for Hydrogenation: A Facile Method for Preparing Co Nanoparticles Covered with Thin Layered Carbon. *J. Catal.* **2016,** *340*, 1-9.

6. Byon, H. R.; Suntivich, J.; Shao-Horn, Y., Graphene-Based Non-Noble-Metal Catalysts for Oxygen Reduction Reaction in Acid. *Chem. Mater.* **2011,** *23* (15), 3421-3428.

7. Ran, J.; Zhang, J.; Yu, J.; Jaroniec, M.; Qiao, S. Z., Earth-Abundant Cocatalysts for Semiconductor-Based Photocatalytic Water Splitting. *Chem. Soc. Rev.* **2014,** *43* (22), 7787-7812.

8. Jin, R., Quantum Sized, Thiolate-Protected Gold Nanoclusters. *Nanoscale* **2010,** *2* (3), 343-362.

9. Khanna, S. N.; Jena, P., Assembling Crystals from Clusters. *Phys. Rev. Lett.* **1992,** *69* (11), 1664-1667.

10. Walter, M.; Akola, J.; Lopez-Acevedo, O.; Jadzinsky, P. D.; Calero, G.; Ackerson, C. J.; Whetten, R. L.; Grönbeck, H.; Häkkinen, H., A Unified View of Ligand-protected Gold Clusters as Superatom Complexes. *Proc. Natl. Acad. Sci. U.S.A.* **2008,** *105* (27), 9157.

11. Ramakrishna, G.; Varnavski, O.; Kim, J.; Lee, D.; Goodson, T., Quantum-Sized Gold Clusters as Efficient Two-Photon Absorbers. *J. Am. Chem. Soc.* **2008,** *130* (15), 5032-5033.

12. Kumar, S. S.; Kwak, K.; Lee, D., Electrochemical Sensing Using Quantum-Sized Gold Nanoparticles. *Anal. Chem.* **2011,** *83* (9), 3244-3247.

13. Kang, X.; Chong, H.; Zhu, M., $Au_{25}(SR)_{18}$: The Captain of the Great Nanocluster Ship. *Nanoscale* **2018,** *10* (23), 10758-10834.

14. Zhu, M.; Aikens, C. M.; Hollander, F. J.; Schatz, G. C.; Jin, R., Correlating the Crystal Structure of a Thiol-protected Au_{25} Cluster and Optical Properties. *J. Am. Chem. Soc.* **2008,** *130* (18), 5883-5885.

15. Negishi, Y.; Munakata, K.; Ohgake, W.; Nobusada, K., Effect of Copper Doping on Electronic Structure, Geometric Structure, and Stability of Thiolate-Protected Au_{25} Nanoclusters. *J. Phys. Chem. Lett.* **2012,** *3* (16), 2209-2214.

16. Yamazoe, S.; Kurashige, W.; Nobusada, K.; Negishi, Y.; Tsukuda, T., Preferential Location of Coinage Metal Dopants (M = Ag or Cu) in $[Au_{25-x}M_x(SC_2H_4Ph)_{18}]^-$ (x ~ 1) As Determined by Extended X-ray Absorption Fine Structure and Density Functional Theory Calculations. *J. Phys. Chem. C* **2014,** *118* (43), 25284-25290.

17. Jin, R.; Nobusada, K., Doping and Alloying in Atomically Precise Gold Nanoparticles. *Nano Res.* **2014,** *7* (3), 285-300.

18. Sharma, S.; Yamazoe, S.; Ono, T.; Kurashige, W.; Niihori, Y.; Nobusada, K.; Tsukuda, T.; Negishi, Y., Tuning the Electronic Structure of Thiolate-Protected 25-atom Clusters by Co-substitution with Metals Having Different Preferential Sites. *Dalton Trans.* **2016,** *45* (45), 18064-18068.

19. Fields-Zinna, C. A.; Crowe, M. C.; Dass, A.; Weaver, J. E. F.; Murray, R. W., Mass Spectrometry of Small Bimetal Monolayer-Protected Clusters. *Langmuir* **2009,** *25* (13), 7704-7710.

20. Alkan, F.; Pandeya, P.; Aikens, C. M., Understanding the Effect of Doping on Energetics and Electronic Structure for Au_{25}, Ag_{25}, and Au_{38} Clusters. *J. Phys. Chem. C* **2019,** *123* (14), 9516-9527.

21. Yao, C.; Lin, Y.-j.; Yuan, J.; Liao, L.; Zhu, M.; Weng, L.-h.; Yang, J.; Wu, Z., Mono-Cadmium vs Mono-Mercury Doping of Au_{25} Nanoclusters. *J. Am. Chem. Soc.* **2015,** *137* (49), 15350-15353.

22. Yan, N.; Liao, L.; Yuan, J.; Lin, Y.-j.; Weng, L.-h.; Yang, J.; Wu, Z., Bimetal Doping in Nanoclusters: Synergistic or Counteractive? *Chem. Mater.* **2016,** *28* (22), 8240-8247.

23. Kumara, C.; Aikens, C. M.; Dass, A., X-ray Crystal Structure and Theoretical Analysis of $Au_{25-x}Ag_x(SCH_2CH_2Ph)_{18}^-$ Alloy. *J. Phys. Chem. Lett.* **2014,** *5* (3), 461-466.

24. Fei, W.; Antonello, S.; Dainese, T.; Dolmella, A.; Lahtinen, M.; Rissanen, K.; Venzo, A.; Maran, F., Metal Doping of $Au_{25}(SR)_{18}^-$ Clusters: Insights and Hindsights. *J. Am. Chem. Soc.* **2019,** *141* (40), 16033-16045.

25. Guidez, E. B.; Mäkinen, V.; Häkkinen, H.; Aikens, C. M., Effects of Silver Doping on the Geometric and Electronic Structure and Optical Absorption Spectra of the $Au_{25-n}Ag_n(SH)_{18}^-$

(n = 1, 2, 4, 6, 8, 10, 12) Bimetallic Nanoclusters. *J. Phys. Chem. C* **2012,** *116* (38), 20617-20624.

26. Jin, R.; Zhao, S.; Liu, C.; Zhou, M.; Panapitiya, G.; Xing, Y.; Rosi, N. L.; Lewis, J. P.; Jin, R., Controlling Ag-doping in $[Ag_xAu_{25-x}(SC_6H_{11})_{18}]^-$ Nanoclusters: Cryogenic Optical, Electronic and Electrocatalytic Properties. *Nanoscale* **2017,** *9* (48), 19183-19190.

27. Joshi, C. P.; Bootharaju, M. S.; Alhilaly, M. J.; Bakr, O. M., $[Ag_{25}(SR)_{18}]^-$: The "golden" Silver Nanoparticle. *J. Am. Chem. Soc.* **2015,** *137* (36), 11578-11581.

28. Weerawardene, K. L. D. M.; Aikens, C. M., Origin of Photoluminescence of $Ag_{25}(SR)_{18}^-$ Nanoparticles: Ligand and Doping Effect. *J. Phys. Chem. C* **2018,** *122* (4), 2440-2447.

29. Zhu, M.; Qian, H.; Jin, R., Thiolate-Protected Au_{20} Clusters with a Large Energy Gap of 2.1 eV. *J. Am. Chem. Soc.* **2009,** *131* (21), 7220-7221.

30. Herbert, P. J.; Yi, C.; Compel, W. S.; Ackerson, C. J.; Knappenberger, K. L., Relaxation Dynamics of Electronically Coupled $Au_{20}(SC_8H_9)_{15}$-n-glyme-$Au_{20}(SC_8H_9)_{15}$ Monolayer-Protected Cluster Dimers. *J. Phys. Chem. C* **2018,** *122* (33), 19251-19258.

31. Compel, W. S.; Wong, O. A.; Chen, X.; Yi, C.; Geiss, R.; Häkkinen, H.; Knappenberger, K. L.; Ackerson, C. J., Dynamic Diglyme-Mediated Self-Assembly of Gold Nanoclusters. *ACS Nano* **2015,** *9* (12), 11690-11698.

32. Jiang, D.-e.; Chen, W.; Whetten, R. L.; Chen, Z., What Protects the Core When the Thiolated Au Cluster is Extremely Small? *J. Phys. Chem. C* **2009,** *113* (39), 16983-16987.

33. Pei, Y.; Gao, Y.; Shao, N.; Zeng, X. C., Thiolate-Protected $Au_{20}(SR)_{16}$ Cluster: Prolate Au_8 Core with New $[Au_3(SR)_4]$ Staple Motif. *J. Am. Chem. Soc.* **2009,** *131* (38), 13619-13621.

34. Zeng, C.; Liu, C.; Chen, Y.; Rosi, N. L.; Jin, R., Gold–Thiolate Ring as a Protecting Motif in the $Au_{20}(SR)_{16}$ Nanocluster and Implications. *J. Am. Chem. Soc.* **2014,** *136* (34), 11922-11925.

35. Weerawardene, K. L. D. M.; Aikens, C. M., Effect of Aliphatic Versus Aromatic Ligands on the Structure and Optical Absorption of $Au_{20}(SR)_{16}$. *J. Phys. Chem. C* **2016,** *120* (15), 8354-8363.

36. Wang, P.; Sun, X.; Liu, X.; Xiong, L.; Ma, Z.; Wang, Y.; Pei, Y., A Revisit to the Structure of $Au_{20}(SCH_2CH_2Ph)_{16}$: a Cubic Nanocrystal-Like Gold Kernel. *Nanoscale* **2018,** *10* (22), 10357-10364.

37. Hudson, R.; Feng, Y.; Varma, R. S.; Moores, A., Bare Magnetic Nanoparticles: Sustainable Synthesis and Applications in Catalytic Organic Transformations. *Green Chem.* **2014,** *16* (10), 4493-4505.

38. Li, Y.; Somorjai, G. A., Nanoscale Advances in Catalysis and Energy Applications. *Nano Lett.* **2010,** *10* (7), 2289-2295.

39. Johnson, G. E.; Colby, R.; Laskin, J., Soft Landing of Bare Nanoparticles with Controlled Size, Composition, and Morphology. *Nanoscale* **2015,** *7* (8), 3491-3503.

40. Pandeya, P.; Aikens, C. M., Theoretical Analysis of Optical Absorption Spectra of Parallel Nanowire Dimers and Dolmen Trimers. *J. Phys. Chem. C* **2020,** *124* (24), 13495-13507.

41. Guidez, E. B.; Aikens, C. M., Theoretical Analysis of the Optical Excitation Spectra of Silver and Gold Nanowires. *Nanoscale* **2012,** *4* (14), 4190-4198.

42. Murphy, C. J.; Jana, N. R., Controlling the Aspect Ratio of Inorganic Nanorods and Nanowires. *Adv. Mater.* **2002,** *14* (1), 80-82.

43. El-Sayed, M. A., Some Interesting Properties of Metals Confined in Time and Nanometer Space of Different Shapes. *Acc. Chem. Res.* **2001,** *34* (4), 257-264.

44. Jana, N. R.; Gearheart, L.; Murphy, C. J., Wet Chemical Synthesis of High Aspect Ratio Cylindrical Gold Nanorods. *J. Phys. Chem. B* **2001,** *105* (19), 4065-4067.

45. Ding, F.; Guidez, E. B.; Aikens, C. M.; Li, X., Quantum Coherent Plasmon in Silver Nanowires: A Real-time TDDFT Study. *J. Chem. Phys.* **2014,** *140* (24), 244705.

46. Yu, H.; Peng, Y.; Yang, Y.; Li, Z.-Y., Plasmon-Enhanced Light–Matter Interactions and Applications. *Npj Comput. Mater.* **2019,** *5* (1), 45.

47. Qian, X. M.; Nie, S. M., Single-Molecule and Single-Nanoparticle SERS: from Fundamental Mechanisms to Biomedical Applications. *Chem. Soc. Rev.* **2008,** *37* (5), 912-920.

48. Zakharian, A. R.; Moloney, J. V.; Mansuripur, M., Surface Plasmon Polaritons on Metallic Surfaces. *Opt. Express* **2007,** *15* (1), 183-197.

49. Ammari, H.; Deng, Y.; Millien, P., Surface Plasmon Resonance of Nanoparticles and Applications in Imaging. *Arch. Ration. Mech. Anal.* **2016,** *220* (1), 109-153.

50. Amendola, V.; Bakr, O. M.; Stellacci, F., A Study of the Surface Plasmon Resonance of Silver Nanoparticles by the Discrete Dipole Approximation Method: Effect of Shape, Size, Structure, and Assembly. *Plasmonics* **2010,** *5* (1), 85-97.

51. Song, J.-H.; Raza, S.; van de Groep, J.; Kang, J.-H.; Li, Q.; Kik, P. G.; Brongersma, M. L., Nanoelectromechanical Modulation of a Strongly-Coupled Plasmonic Dimer. *Nat. Commun.* **2021,** *12* (1), 48.

52. Prodan, E.; Radloff, C.; Halas, N. J.; Nordlander, P., A Hybridization Model for the Plasmon Response of Complex Nanostructures. *Science* **2003,** *302* (5644), 419-22.

53. Wang, H.; Brandl, D. W.; Nordlander, P.; Halas, N. J., Plasmonic Nanostructures: Artificial Molecules. *Acc. Chem. Res.* **2007,** *40* (1), 53-62.

54. Villesen, T. F.; Uhrenfeldt, C.; Johansen, B.; Nylandsted Larsen, A., Self-Assembled Al Nanoparticles on Si and Fused Silica, and their Application for Si Solar Cells. *Nanotechnology* **2013,** *24* (27), 275606.

55. Kochergin, V.; Neely, L.; Jao, C.-Y.; Robinson, H. D., Aluminum Plasmonic Nanostructures for Improved Absorption in Organic Photovoltaic Devices. *Appl. Phys. Lett.* **2011,** *98* (13), 133305.

56. Knight, M. W.; King, N. S.; Liu, L.; Everitt, H. O.; Nordlander, P.; Halas, N. J., Aluminum for Plasmonics. *ACS Nano* **2014,** *8* (1), 834-840.

57. Taguchi, A.; Saito, Y.; Watanabe, K.; Yijian, S.; Kawata, S., Tailoring Plasmon Resonances in the Deep-Ultraviolet by Size-Tunable Fabrication of Aluminum Nanostructures. *Appl. Phys. Lett.* **2012,** *101* (8), 081110.

58. Knight, M. W.; Liu, L.; Wang, Y.; Brown, L.; Mukherjee, S.; King, N. S.; Everitt, H. O.; Nordlander, P.; Halas, N. J., Aluminum Plasmonic Nanoantennas. *Nano Lett.* **2012,** *12* (11), 6000-6004.

59. Jha, S. K.; Ahmed, Z.; Agio, M.; Ekinci, Y.; Löffler, J. F., Deep-UV Surface-Enhanced Resonance Raman Scattering of Adenine on Aluminum Nanoparticle Arrays. *J. Am. Chem. Soc.* **2012,** *134* (4), 1966-1969.

60. Zhou, L.; Zhang, C.; McClain, M. J.; Manjavacas, A.; Krauter, C. M.; Tian, S.; Berg, F.; Everitt, H. O.; Carter, E. A.; Nordlander, P.; Halas, N. J., Aluminum Nanocrystals as a Plasmonic Photocatalyst for Hydrogen Dissociation. *Nano Lett.* **2016,** *16* (2), 1478-1484.

61. Li, X.; Wu, H.; Wang, X.-B.; Wang, L.-S., S - P Hybridization and Electron Shell Structures in Aluminum Clusters: A Photoelectron Spectroscopy Study. *Phys. Rev. Lett.* **1998,** *81* (9), 1909-1912.

62. Zimmermann, J.; Zeug, A.; Röder, B., A Generalization of the Jablonski Diagram to Account for Polarization and Anisotropy Effects in Time-Resolved Experiments. *Phys. Chem. Chem. Phys.* **2003,** *5* (14), 2964-2969.

63. Yang, X.; Yang, M.; Pang, B.; Vara, M.; Xia, Y., Gold Nanomaterials at Work in Biomedicine. *Chem. Rev.* **2015,** *115* (19), 10410-10488.

64. Jin, R.; Zeng, C.; Zhou, M.; Chen, Y., Atomically Precise Colloidal Metal Nanoclusters and Nanoparticles: Fundamentals and Opportunities. *Chem. Rev.* **2016,** *116* (18), 10346-10413.

65. Antaris, A. L.; Chen, H.; Diao, S.; Ma, Z.; Zhang, Z.; Zhu, S.; Wang, J.; Lozano, A. X.; Fan, Q.; Chew, L.; Zhu, M.; Cheng, K.; Hong, X.; Dai, H.; Cheng, Z., A High Quantum Yield Molecule-protein Complex Fluorophore for Near-infrared II Imaging. *Nat. Commun.* **2017,** *8* (1), 15269.

66. Wu, W.; Yang, Y.; Yang, Y.; Yang, Y.; Zhang, K.; Guo, L.; Ge, H.; Chen, X.; Liu, J.; Feng, H., Molecular Engineering of an Organic NIR-II Fluorophore with Aggregation-Induced Emission Characteristics for In Vivo Imaging. *Small* **2019,** *15* (20), 1805549.

67. Devadas, M. S.; Thanthirige, V. D.; Bairu, S.; Sinn, E.; Ramakrishna, G., Temperature-Dependent Absorption and Ultrafast Luminescence Dynamics of Bi-Icosahedral Au_{25} Clusters. *J. Phys. Chem. C* **2013,** *117* (44), 23155-23161.

68. Wu, Z.; Jin, R., On the Ligand's Role in the Fluorescence of Gold Nanoclusters. *Nano Lett.* **2010,** *10* (7), 2568-2573.

69. Green, T. D.; Yi, C.; Zeng, C.; Jin, R.; McGill, S.; Knappenberger, K. L., Temperature-Dependent Photoluminescence of Structurally-Precise Quantum-Confined $Au_{25}(SC_8H_9)_{18}$ and $Au_{38}(SC_{12}H_{25})_{24}$ Metal Nanoparticles. *J. Phys. Chem. A* **2014,** *118* (45), 10611-10621.

70. Zheng, J.; Zhou, C.; Yu, M.; Liu, J., Different Sized Luminescent Gold Nanoparticles. *Nanoscale* **2012,** *4* (14), 4073-4083.

71. Mori, K.; Goumans, T. P. M.; van Lenthe, E.; Wang, F., Predicting Phosphorescent Lifetimes and Zero-Field Splitting of Organometallic Complexes with Time-Dependent Density Functional Theory Including Spin–Orbit Coupling. *Phys. Chem. Chem. Phys.* **2014,** *16* (28), 14523-14530.

72. Miller, S. A.; Womick, J. M.; Parker, J. F.; Murray, R. W.; Moran, A. M., Femtosecond Relaxation Dynamics of $Au_{25}L_{18}^{-}$ Monolayer-protected Clusters. *J. Phys. Chem. C* **2009,** *113* (22), 9440-9444.

73. Green, T. D.; Knappenberger, K. L., Relaxation Dynamics of $Au_{25}L_{18}$ Nanoclusters Studied by Femtosecond Time-resolved Near Infrared Transient Absorption Spectroscopy. *Nanoscale* **2012,** *4* (14), 4111-4118.

74. Senanayake, R. D.; Akimov, A. V.; Aikens, C. M., Theoretical Investigation of Electron and Nuclear Dynamics in the $[Au_{25}(SH)_{18}]^{-1}$ Thiolate-Protected Gold Nanocluster. *J. Phys. Chem. C* **2016,** *121* (20), 10653-10662.

75. Senanayake, R. D.; Akimov, A. V.; Aikens, C. M., Theoretical Investigation of Electron and Nuclear Dynamics in the $[Au_{25}(SH)_{18}]^{-1}$ Thiolate-Protected Gold Nanocluster. *J. Phys. Chem. C* **2016,** *121* (20), 10653-10662.

76. Thanthirige, V. D.; Kim, M.; Choi, W.; Kwak, K.; Lee, D.; Ramakrishna, G., Temperature-Dependent Absorption and Ultrafast Exciton Relaxation Dynamics in $MAu_{24}(SR)_{18}$

Clusters (M = Pt, Hg): Role of the Central Metal Atom. *J. Phys. Chem. C* **2016,** *120* (40), 23180-23188.

77. Zhou, M.; Qian, H.; Sfeir, M. Y.; Nobusada, K.; Jin, R., Effects of Single Atom Doping on the Ultrafast Electron Dynamics of $M_1Au_{24}(SR)_{18}$ (M = Pd, Pt) Nanoclusters. *Nanoscale* **2016,** *8* (13), 7163-7171.

78. Miller, S. A.; Fields-Zinna, C. A.; Murray, R. W.; Moran, A. M., Nonlinear Optical Signatures of Core and Ligand Electronic States in $Au_{24}PdL_{18}$. *J. Phys. Chem. Lett.* **2010,** *1* (9), 1383-1387.

79. Zhou, M.; Vdović, S.; Long, S.; Zhu, M.; Yan, L.; Wang, Y.; Niu, Y.; Wang, X.; Guo, Q.; Jin, R.; Xia, A., Intramolecular Charge Transfer and Solvation Dynamics of Thiolate-Protected $Au_{20}(SR)_{16}$ Clusters Studied by Ultrafast Measurement. *J. Phys. Chem. A* **2013,** *117* (40), 10294-10303.

80. Baffou, G.; Quidant, R., Thermo-Plasmonics: Using Metallic Nanostructures as Nano-Sources of Heat. *Laser Photonics Rev.* **2013,** *7* (2), 171-187.

81. Moon, S. Y.; Song, H. C.; Gwag, E. H.; Nedrygailov, I. I.; Lee, C.; Kim, J. J.; Doh, W. H.; Park, J. Y., Plasmonic Hot Carrier-Driven Oxygen Evolution Reaction on Au Nanoparticles/TiO_2 Nanotube Arrays. *Nanoscale* **2018,** *10* (47), 22180-22188.

82. Ran, J.; Jaroniec, M.; Qiao, S.-Z., Cocatalysts in Semiconductor-Based Photocatalytic CO_2 Reduction: Achievements, Challenges, and Opportunities. *Adv. Mater.* **2018,** *30* (7), 1704649.

83. Zhou, X.; Liu, G.; Yu, J.; Fan, W., Surface Plasmon Resonance-Mediated Photocatalysis by Noble Metal-Based Composites Under Visible Light. *J. Mater. Chem.* **2012,** *22* (40), 21337-21354.

84. Martirez, J. M. P.; Carter, E. A., Thermodynamic Constraints in Using AuM (M = Fe, Co, Ni, and Mo) Alloys as N_2 Dissociation Catalysts: Functionalizing a Plasmon-Active Metal. *ACS Nano* **2016,** *10* (2), 2940-2949.

85. Martirez, J. M. P.; Carter, E. A., Excited-State N_2 Dissociation Pathway on Fe-Functionalized Au. *J. Am. Chem. Soc.* **2017,** *139* (12), 4390-4398.

86. Martirez, J. M. P.; Carter, E. A., Prediction of a Low-Temperature N_2 Dissociation Catalyst Exploiting Near-IR–To–Visible Light Nanoplasmonics. *Sci. Adv.* **2017,** *3* (12), eaao4710.

87. Yang, J.; Guo, Y.; Jiang, R.; Qin, F.; Zhang, H.; Lu, W.; Wang, J.; Yu, J. C., High-Efficiency "Working-in-Tandem" Nitrogen Photofixation Achieved by Assembling Plasmonic Gold Nanocrystals on Ultrathin Titania Nanosheets. *J. Am. Chem. Soc.* **2018,** *140* (27), 8497-8508.

88. Jia, H.; Du, A.; Zhang, H.; Yang, J.; Jiang, R.; Wang, J.; Zhang, C.-y., Site-Selective Growth of Crystalline Ceria with Oxygen Vacancies on Gold Nanocrystals for Near-Infrared Nitrogen Photofixation. *J. Am. Chem. Soc.* **2019,** *141* (13), 5083-5086.

89. Hu, C.; Chen, X.; Jin, J.; Han, Y.; Chen, S.; Ju, H.; Cai, J.; Qiu, Y.; Gao, C.; Wang, C.; Qi, Z.; Long, R.; Song, L.; Liu, Z.; Xiong, Y., Surface Plasmon Enabling Nitrogen Fixation in Pure Water through a Dissociative Mechanism under Mild Conditions. *J. Am. Chem. Soc.* **2019,** *141* (19), 7807-7814.

Chapter 2 - Computational methods

In this chapter, we describe the theoretical methods used for the calculations discussed in this dissertation.

2.1 The Schrödinger equation

In quantum mechanics, the properties of microscopic systems can be explained at the subatomic level; the electron behavior in molecules gives information about the properties like dipole moment, absorption spectra, and so on. The Schrödinger equation is used in order to obtain all of the possible information about a system. The time-dependent Schrödinger equation in three dimensions is expressed as:

$$i\hbar \frac{\partial}{\partial t}\Psi(\vec{r},t) = \left[-\frac{\hbar^2}{2m}\nabla^2 + V(\vec{r},t)\right]\Psi(\vec{r},t) \qquad (2.1)$$

In equation (2.1), i=$\sqrt{-1}$; t is time; Ψ is the wavefunction of the system; r refers to the three spatial coordinates x, y, and z; $\hbar$ is $h/2\pi$ where h is the Planck constant; and m is the mass of the system. The wavefunction Ψ depends on both the position (r) of the system and time (t). It is also called the state function because it describes the state of the system, which changes with time. The wavefunction contains all of the available information about the system. $V(\vec{r})$ in equation (2.1) is the potential of the system that depends on the position and time. ∇^2 is known as the Laplacian operator which is expressed as:

$$\nabla^2 = \frac{\partial^2}{\partial x^2} + \frac{\partial^2}{\partial y^2} + \frac{\partial^2}{\partial z^2} \qquad (2.2)$$

The term inside the brackets in equation (2.1) is called the Hamiltonian ($\widehat{H}$). It is the sum of kinetic and potential energy of the system. So, equation (2.1) can be written as:

$$i\hbar\frac{\partial}{\partial t}\Psi(\vec{r},t) = \widehat{H}\Psi(\vec{r},t) \tag{2.3}$$

The time-independent Schrödinger equation can also be used in order to describe systems that do not experience any time-dependent external forces. It is represented as:

$$\widehat{H}\Psi(\vec{r}) = E\Psi(\vec{r}) \tag{2.4}$$

So, the Schrödinger equation is an eigenvalue equation where the eigenvalues are the total energies of the system. An exact solution of the Schrödinger equation can be obtained only for the particle in a box and hydrogen atom (a single electron system). So, other approximate solutions are needed to study many-electron systems.

2.2 Density functional theory (DFT)

DFT uses the electronic density with fewer variables (3 spatial variables x, y, and z) instead of using the wavefunction with 4n variables (3n spatial and n spin coordinates for an n-electron system). So DFT is a computationally efficient method to study many-electron systems. In DFT, the ground state electron density is used to get the energy, dipole moment, and geometric and electronic properties of the system.[1]

The Hohenberg-Kohn theorems are the basis of DFT. The Hohenberg-Kohn existence theorem establishes a one-to-one correspondence between the non-degenerate ground state

electron density and the external potential $\hat{V}_{ext}$.[2] For the electronic systems, the Hamiltonian is expressed as:

$$\hat{H} = \hat{T} + \hat{V} + \hat{V}_{ext} \tag{2.5}$$

$\hat{V}_{ext}$ includes the Coulomb potential of the nuclei plus the external electric field. Since the $\hat{V}_{ext}$ has one-to-one correspondence with the electron density, the total energy is also a unique functional of electron density according to equation (2.5). So, according to the Hohenberg-Kohn existence theorem, the wavefunction and energy of the system can be uniquely determined by the ground state electron density. $\hat{T}$ and $\hat{V}$ in equation (2.5) are the kinetic energy and potential energy operators respectively.

According to the Hohenberg-Kohn variational theorem, the true ground state density minimizes the energy functional. However, this theorem does not give any prescription to choose the trial densities rationally. So, the Kohn-Sham method suggests a practical method to get the ground state trial density.

In the Kohn-Sham method, a Kohn-Sham system is defined which is a fictitious reference system of non-interacting particles (electrons) that have a same density as the interacting particles.[3] The non-interacting electrons move under the potential of the atomic nuclei (external potential). Since every electron of the fictitious system behaves individually, the Kohn-Sham Hamiltonian is the sum of one electron operators. Within the Kohn-Sham formalism, the ground state electronic energy of the system can be written as:

$$E = T + V_{ne} + V_{ee} + V_{xc} \tag{2.6}$$

In equation (2.6), T is the kinetic energy of the non-interacting electrons. It can be obtained by taking the sum of all one electron kinetic energies associated with the orbitals. V_{ne} is the electron-nuclear attraction energy, V_{ee} is the electron-electron repulsion energy and V_{xc} is the exchange-correlation term.

In wave function theory, Coulomb interactions are included only for two-particle interactions. So, an electron does not interact with itself. But in DFT, the energy is expressed as a functional of the single-particle electron density which in turn is treated as classical charge distribution. Hence two-body Coulomb interactions cannot be distinguished from self-interaction (inter-electronic repulsion of electron density with itself). So, the interaction of each electron with the entire electron density (including its own density) is included as a Coulomb energy in DFT.[4] It gives an error to DFT called the 'self-interaction error' because an electron cannot interact with itself. V_{xc} accounts for the errors in DFT obtained from self-interaction. It also accounts for the error obtained by considering the non-interacting system. The self-interaction error causes the energies of virtual orbitals to be too low, which leads to underestimated orbital energy gaps on using DFT.

Within an orbital φ_i expression for the density, equation (2.6) is expressed as shown in equation (2.7).[1] The first term gives the kinetic energy component, the second term gives the electron-nuclear attraction component, the third term gives the electron-electron interaction component and the last term gives the exchange-correlation.

$$E[\rho(r)] = \sum_{i}^{N}\left(\langle\varphi_i\left|-\frac{1}{2}\nabla_i^2\right|\varphi_i\rangle - \langle\varphi_i\left|\sum_{k}^{nuclei}\frac{Z_k}{|r_i - r_k|}\right|\varphi_i\rangle\right) + \sum_{i}^{N}\langle\varphi_i\left|\frac{1}{2}\int\frac{\rho(r')}{|r_i - r'|}dr'\right|\varphi_i\rangle + E_{xc}[\rho(r)] \tag{2.7}$$

In this equation, N is the number of electrons. The density at any position in space $\rho(r)$ is the sum of the square modulus of the occupied orbitals at that position (equation (2.8)).

$$\rho(r) = \sum_{i=1}^{N} \langle \varphi_i | \varphi_i \rangle \tag{2.8}$$

So, we need the information about the orbitals to get the density in the third term. Every time we get new orbitals, the density needs to be solved (i.e., the third term need to be solved self-consistently).

If we find the orbitals χ that minimize E in equation (2.7), the orbitals satisfy the pseudo eigenvalue equation

$$h_i^{KS} \chi_i = \varepsilon_i \varphi_i \tag{2.9}$$

where h_i^{KS} is the Kohn-Sham one-electron operator and is defined as:

$$h_i^{KS} = -\frac{1}{2}\nabla_i^2 - \sum_{k}^{nuclei} \frac{Z_k}{|r_i - r_k|} + \int \frac{\rho(r')}{|r_i - r'|} dr' + V_{xc} \tag{2.10}$$

and the functional derivative V_{xc} is:

$$V_{xc} = \frac{\partial E_{xc}}{\partial \rho} \tag{2.11}$$

E_{xc} is dependent on electron density via:

$$E_{xc}[\rho(r)] = \int \rho(r)\, \varepsilon_{xc}[\rho(r)] dr \tag{2.12}$$

where ε_{xc} is the energy density. It is treated as the sum of individual exchange and correlation contribution and is dependent on the electron density. In equation (2.12), the energy density is the per particle density whereas the electron density is the per unit volume density.

Because the accuracy of DFT depends on the accuracy of the last term in equation (2.7) (i.e. the exchange correlation functional), different approximations have been developed to get it. Some methods construct a function which incorporates the kinetic energy difference between the interacting and non-interacting systems. In some methods, some empirical parameters are used that introduce some kinetic energy correction based on the experiments. So, the functional can be validated with the help of benchmark calculations.

The different kinds of exchange correlation functionals can be summarized in the Jacob's ladder (Figure 2-1).[5] The lowest rung of the Jacob's ladder is the local density approximation (LDA).[6] In LDA, the exchange–correlation energy density depends only on the density at a given point. It means that the ε_{xc} at a certain position r is obtained from the value of ρ at that position. This approximation works well for the metals where the electron density varies slowly with position. The second rung is the generalized gradient approximation (GGA), which uses both the electron density and its gradient (first derivatives with respect to its position) at each point.[7] Meta-GGA includes either one or both of the second derivative of electron density ($\nabla^2\rho$) and the kinetic energy density (KED) at each point.[8] KED is defined as:[1]

$$KED = \sum_{i}^{occupied} \frac{1}{2}|\nabla\varphi_i(r)|^2 \tag{2.13}$$

where φ_i are the self-consistently obtained Kohn-Sham orbitals. It is more common to use KED instead of ($\nabla^2\rho$) in a meta-GGA functional. LDA, GGA and meta-GGA are pure density functionals and we can also have hybrid functionals. A hybrid functional adds exact Hartree-Fock

exchange on top of LDA or GGA or meta-GGA.[9] These functionals work well for the organic molecules.[10-11] The accuracy of the DFT increases on climbing up the ladder.

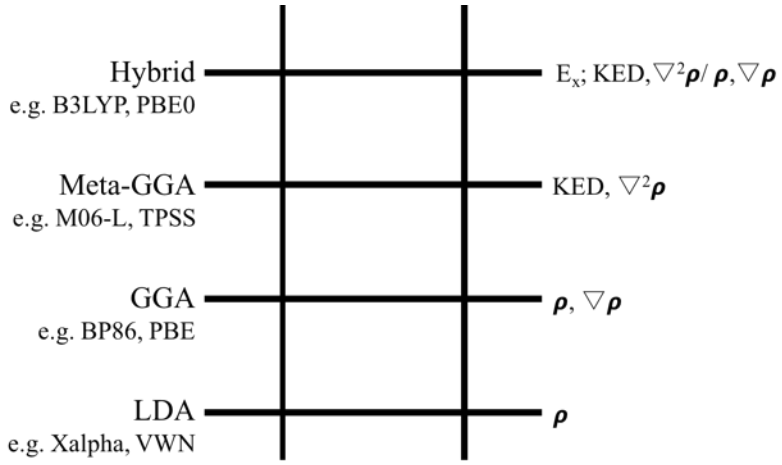

Figure 2-1 Jacobs ladder

2.3 Time-dependent density functional theory (TDDFT)

Because DFT is a static method that only approximates the time-independent Schrödinger equation, time-dependent DFT (TDDFT) is required to get an approximate solution of the time-dependent Schrödinger equation. TDDFT helps to understand time-dependent phenomena like excited state dynamics of the systems under study in the presence of the electric or magnetic fields. The Runge-Gross theorem (a time-dependent analogue of the Hohenberg-Kohn existence theorem) sets the foundation for TDDFT.[12-13] It provides the one-to-one mapping between the time-dependent external potential in which the system evolves and the time-dependent electron density of the system. Since the external potential can be expressed as a functional of the time-dependent electron density and the density can be obtained by summing over all occupied orbitals at that particular time, all the time-dependent properties can be obtained.

Similar to the time-independent Kohn-Sham formalism for ground state DFT, time-dependent Kohn-Sham (TDKS) formalisms are obtained for TDDFT.[14] TDKS formalism states that the time-dependent density of the non-interacting fictitious system with external potential $\hat{V}_{ext}$ has the same density as the interacting system. The time-dependent single particle Kohn-Sham equation can be expressed as:

$$i\frac{\partial}{\partial t}\varphi_i(r,t) = \left(-\frac{1}{2}\nabla_i^2 + v_{ext}[\rho](r,t) + \int d^3r_1 \frac{\rho(r_2,t)}{r_{12}} + \frac{\partial A_{xc}[\rho]}{\partial \rho(r,t)}\right)\varphi_i(r,t) \quad (2.14)$$

In this equation, the first term gives the kinetic energy of an electron in a Kohn-Sham orbital. The second term gives the single particle external potential which includes the Coulombic attractive potential of nuclei and the external time-dependent perturbation. The next two terms are the Coulombic repulsion between the electrons and the time-dependent exchange-correlation potential respectively. This exchange correlation term depends on the electronic density at all previous times (memory dependence) which makes its calculation rigorous. However, in the case of slowly varying densities, the adiabatic approximation can be used. In this approximation, all the history of density as well as the initial state dependence is ignored and the instantaneous electron density is used which makes the calculation easier.

Kohn-Sham molecular orbitals are expressed as a linear combination of atomic orbitals/basis functions χ_μ

$$\varphi_i(t) = \sum_\mu c_{\mu,j}(t)\,\chi_\mu \quad (2.15)$$

Then, the time-dependent coefficients give the Kohn-Sham density matrix elements (*P*)

$$P_{\mu\nu}(t) = \sum_j c^*_{\mu,j}(t) c_{\nu,j}(t) \quad (2.16)$$

In an orthonormal basis, the TDDFT equation for the density matrix can be expressed as:

$$i\hbar\frac{dP(t)}{dt} = [H(t), P(t)] \tag{2.17}$$

This equation is known as the quantum Liouville equation of motion.[15] One can use this equation to apply a small perturbation and retain only the linear response (LR) of the density to derive the LR matrix formulation of LR-TDDFT. One can also propagate the electron density in time via numerical integration for the real-time TDDFT (RT-TDDFT) method. H in this equation refers to the Hamiltonian in matrix form with matrix elements given by:

$$H_{\mu\nu}(t) = \langle\chi_\mu|\hat{H}(t)|\chi_\nu\rangle \tag{2.18}$$

LR-TDDFT and RT-TDDFT methods are used to get excitation energies and oscillator strengths.

2.3.1 Linear response TDDFT (LR-TDDFT)

This method is used when the applied field or perturbation is weak (i.e. the interaction between the molecule and the field is weaker than the intramolecular interactions). So, the excitation energies and spectrum are computed using first-order (linear) response of the density to a small perturbation. The excitation energies and optical spectra are obtained according to the Casida equations which consider the solutions to a non-Hermitian eigenvalue equation, derived from retaining only the first-order response of the density to a perturbation.[16]

$$\begin{bmatrix} A & B \\ B & A \end{bmatrix}\begin{bmatrix} X \\ Y \end{bmatrix} = \varepsilon\begin{bmatrix} 1 & 0 \\ 0 & -1 \end{bmatrix}\begin{bmatrix} X \\ Y \end{bmatrix} \tag{2.19}$$

The matrix elements A and B are defined as:

$$A_{ia\sigma,jb\tau} = \delta_{ij}\delta_{ab}\delta_{\sigma\tau}(\in_{a\sigma} - \in_{i\sigma}) + \Lambda_{ia\sigma,jb\tau} \quad (2.20)$$

$$B_{ia\sigma,jb\tau} = \Lambda_{ia\sigma,jb\tau} \quad (2.21)$$

A and B are excitation and de-excitation matrices respectively. In equations (2.20) and (2.21), i and j are the occupied orbitals; a and b are the virtual orbitals; σ and τ are the electron spin; $\in$ is the eigenvalue; and Λ is the interaction kernel (exchange-correlation matrix). So, one can obtain the transition energies (ε) and oscillator strengths from the Casida equation. The oscillator strengths of the absorption peaks can be obtained from the eigenvectors of the Casida equation.[17] Since this method requires the building and diagonalizing a large matrix, it is computationally expensive.[17]

2.3.2 Real-time TDDFT (RT-TDDFT)

This method is used with both strong (beyond linear response) and weak field regimes. RT-TDDFT gives the full time- and space-resolved solution to the Kohn-Sham equations instead of the solution in the frequency domain as given by LR-TDDFT.[18] In this method, the electronic density is propagated according to equation (2.17) using various methods of propagation.[19] In our calculation, the modified midpoint and unitary transformation (MMUT) algorithm is used to integrate this equation.[20] This propagator propagates the electron density using a unitary time evolution operator $U(t_n)$:[21]

$$U(t_{n+1}) = U(t_n).P(t_{n-1}).U^{\dagger}(t_n) \quad (2.22)$$

Spectral information can be obtained from RT-TDDFT via Fourier transform of time-dependent expectation values such as the dipole moment. We can obtain the time-dependent

properties (e.g. the time-dependent dipole moment, $\mu(t)$) of the system at each time step on applying an external perturbation as:

$$\mu(t) = Tr[DP(t)] \tag{2.23}$$

D in equation (2.23) is the dipole matrix in the orthonormal basis. Then, the dipole strength function $S(\omega)$ can be obtained from equation (2.24) when the dipole response in real time is known.[21]

$$S(\omega) = \frac{4\pi\omega}{3c} Tr[Im\alpha(\omega)] \tag{2.24}$$

In this equation, $\alpha(\omega)$ is the polarizability in the frequency domain. It is obtained by taking the Fourier transform of the dipole moment and step field:

$$\mu_i(\omega) = \alpha_{ii}(\omega) E_i(\omega) \tag{2.25}$$

where i refers to x, y, z Cartesian coordinates.

2.4 The Born-Oppenheimer (BO) approximation

The full non–relativistic time-independent Hamiltonian ($\widehat{H}$) can be expressed as:

$$\widehat{H} = \frac{\hbar^2}{2}\sum_{\alpha}\frac{1}{m_\alpha}\nabla_\alpha^2 - \frac{\hbar^2}{2m_e}\sum_i \nabla_i^2 + \sum_\alpha \sum_{\beta>\alpha} \frac{Z_\alpha Z_\beta}{R_{\alpha\beta}} - \sum_\alpha \sum_i \frac{Z_\alpha}{r_{ia}} + \sum_i \sum_{i>j} \frac{1}{r_{ij}} \tag{2.26}$$

where α and β refer to nuclei, i and j refer to electrons, Z_α and Z_β refer to the atomic numbers of the nuclei, $R_{\alpha\beta}$ refers to the distance between two nuclei α and β, r_{ia} refers to the distance between the electron and nucleus, and r_{ij} is the inter-electronic distance. The first and second terms refer to the kinetic energy operators for nuclei and electrons respectively. The third and fifth terms refer

to the inter-nuclear and inter-electronic repulsive potential energy. The fourth term refers to the potential energy of attraction between the electrons and nuclei.

It is impossible to solve the Schrödinger equation for many-particle systems without any approximations because the Hamiltonian contains the correlated motions of the particles (e.g. attraction and repulsion terms). The Born-Oppenheimer approximation provides a way to simplify the Hamiltonian in the Schrödinger equation.

Since the nuclei are much heavier than the electrons, electronic motion is much faster than the nuclear motion. So, the nuclear motion is considered to be fixed compared to the electronic motion in the BO approximation. Due to this approximation, the first term (i.e. the kinetic energy operator of the nuclei) can be omitted from equation (2.26). Because the third term is independent of the electronic coordinates and is constant for a given nuclear configuration, this constant term can also be omitted from equation (2.26) to get the purely electronic Hamiltonian, $\widehat{H}_{el}$:

$$\widehat{H}_{el} = -\frac{\hbar^2}{2m_e}\sum_i \nabla_i^2 + -\sum_\alpha \sum_i \frac{Z_\alpha}{r_{ia}} + \sum_i \sum_{i>j} \frac{1}{r_{ij}} \qquad (2.27)$$

On using this approximation, the pure electronic energy of the system depends parametrically on the nuclear coordinates. So, one needs to add the internuclear repulsion energy to the electronic (only) energy to get the total energy of the system. This approximation is very important because it also provides the concept of the potential energy surface. The potential energy surface is the surface that is obtained from the purely electronic energy values over all possible nuclear coordinates. The BO approximation is used in all of the methods we have discussed above.

2.5 Nonadiabatic dynamics

BO only treats the adiabatic processes, where the nuclear and electronic motions are not coupled. But when two electronic states are degenerate, the BO approximation cannot be applied and nonadiabatic methods are needed. So, the nonadiabatic methods are very important to describe processes where the nuclear and electronic motions are strongly coupled, e.g. radiationless decay of excited states. There are various methods to perform the nonadiabatic calculations, e.g. the Ehrenfest method, the surface hopping method, multiple spawning, and so on.[22]

2.5.1 Ehrenfest method

This method is also known as a mean field method[23-24] since the fast particles (electrons) move in the average field of the slow particles (nuclei), and vice versa.[25] Average feedback is incorporated between the fast and slow degrees of freedom in both directions.

The conventional molecular dynamics simulation has two approximations: the dynamics of the atomic motion is limited to the single potential energy surface and the atomic motion is treated classically. As mentioned above, a single potential energy surface is invalid for processes like electron transfer and a classical description of atomic motions is not valid when examining tunneling through reaction barriers and similar processes. So, mixed quantum classical dynamics methods like Ehrenfest and surface hopping (to be discussed in the next part) were developed in which most of the atoms are treated classically and form a multi-dimensional potential energy surface whereas a few important degrees of freedom are treated quantum mechanically. In mixed quantum classical dynamics methods, the quantum mechanical degrees of freedom evolve under the influence of the classical movement of atoms. Ideally, the classical degrees of freedom should also respond to the quantum transitions. In the Ehrenfest method, the classical potential evolves

subject to a single effective potential corresponding to an average over quantum states. So, this method neglects the quantum classical correlation.

In order to solve equation (2.17), the integration time step for the Ehrenfest method should be on the time scale of electronic motion.[26] In our calculations, the MMUT algorithm is used as the propagator, which is the same algorithm used for the real-time TDDFT methods used in this work.[26-27] In this algorithm, the nuclei are propagated using velocity Verlet with nuclear time steps Δt_N and the electronic time step is Δt_e (Figure 2-2). Because the change in the electronic wave function is much faster than the change in the nuclear coordinates, nuclei are assumed to be stationary for several electronic steps before updating the nuclear coordinates, which is denoted as time step Δt_{Ne}.

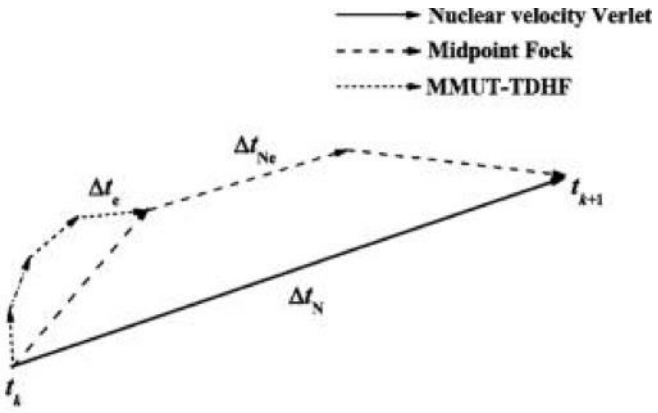

Figure 2-2 "Three-time-scale integration scheme for Ehrenfest dynamics". (Reprinted from *J. Chem. Phys.* 2005, *123 (8), 084106* with the permission of AIP Publishing).

2.5.2 Surface hopping method

In this method, the quantum classical correlation is included.[25] The given trajectory is divided into different branches each representing a quantum state and weighted by the amplitude of the state.[28] So, this method gives an accurate description in situations where multiple trajectories

are required (e.g. radiationless processes, charge transfer). It is computationally more expensive than the Ehrenfest method.

There are various hopping algorithms employed for the surface hopping method.[28-32] One of these is the fewest switches surface hopping (FSSH) algorithm.[33] It maintains the correct populations of each state $|c_i(t)|$ at all the times with the minimum number of hops. In this algorithm, the probability of a hop from state 1 to state 2 ($P_{1\to2}$) at time step Δt is given by:

$$P_{1\to2} = -d[\log|c_1(t)|^2]/dt \tag{2.28}$$

If the probability of the hop is positive, the hop happens with a change in the velocity component in the direction of nonadiabatic coupling vector to conserve the total energy of the system. The hop is restricted if the probability of the hop is negative. FSSH is a popular method that can capture the detailed balance (i.e., the thermal equilibrium population of excited states).[34-36]

FSSH for DFT with a Kohn-Sham representation of the electron density (FSSH-TDKS) has been developed.[37] This approach is useful for the real-time modelling of electron dynamics. Since this method incorporates the electron-nuclear correlation and detailed balance, it gives a more accurate description of the chemical properties than the Ehrenfest-TDKS method. In the Kohn-Sham representation, the electron density is given as:

$$\rho(x,t) = \sum_{p=1}^{N_e} |\varphi_p(x,t)|^2 \tag{2.29}$$

where N_e is the number of electrons, and $\varphi_p(x,t)$ are the single electron Kohn-Sham orbitals. The time-dependent variational principle can be used to determine the evolution of $\varphi_p(x,t)$ where H depends on the KS orbitals:

$$i\hbar \frac{\partial \varphi_p(x,t)}{\partial t} = H\big(\varphi(x,t)\big)\varphi_p(x,t);\ p = 1, \dots, N_e \tag{2.30}$$

The time-dependent $\varphi_p(x,t)$ can be expanded in the adiabatic KS orbitals $\tilde{\varphi}_k(x;R\rangle$:

$$\rho_p(x,t) = \sum_k^{N_e} c_{pk}(t)|\tilde{\varphi}_k(x;R\rangle)\,; R = nuclear\ trajectory \tag{2.31}$$

where N_e is the number of electrons. The TDKS equation (2.30) transforms to an equation in the coefficients c_{pk} as:

$$i\hbar \frac{\partial}{\partial t} c_{pk}(t) = \sum_m^{N_e} c_{pm}(t)(\in_m \delta_{km} + d_{km}.\dot{R}) \tag{2.32}$$

Then the nonadiabatic coupling is:

$$d_{km}.\dot{R} = -i\hbar\langle\tilde{\varphi}_k(x;R)|\nabla_R|\tilde{\varphi}_m(x;R)\rangle.\dot{R} = -i\hbar\left\langle\tilde{\varphi}_k\middle|\frac{\partial}{\partial t}\middle|\tilde{\varphi}_m\right\rangle \tag{2.33}$$

where ∇_R is gradient operator and the nonadiabatic coupling arises from the dependence of the adiabatic KS orbitals on the nuclear trajectory.

Since the standard FSSH method produces different nuclear trajectories and calculates the nonadiabatic coupling on-the-fly, this method is computationally expensive. In our work, we have used the FSSH-TDKS method within a classical path approximation (FSSH-CPA) to reduce the computational cost.[38] The classical path approximation assumes that the nuclear dynamics of the system is not affected by the dynamics of electronic degrees of freedom but that the electron dynamics is driven by the nuclear dynamics.[38] So, the electronic Hamiltonian depends parametrically along a predetermined classical molecular dynamics trajectory. A large number of stochastic realizations of the FSSH algorithm can be computed along the ground state MD

trajectory which drastically decreases the computational cost. The quantum classical correlation is not included in FSSH-CPA.

The hop rejection and velocity rescaling of standard FSSH are replaced in FSSH-CPA by using a Boltzmann factor $b_{i\to j}(t)$ to scale the transition probabilities $g_{i\to j}(t)$. It ensures the detailed balance condition in FSSH-CPA by making the transitions up in energy less probable.

$$g_{i\to j}(t) \to g_{i\to j}(t) b_{i\to j}(t) \tag{2.34}$$

$$b_{i\to j}(t) = \begin{cases} exp\left(-\frac{E_j - E_i}{k_B T}\right) & E_j > E_i \\ 1 & E_j \leq E_i \end{cases} \tag{2.35}$$

E_j and E_i are the energies of states j and i respectively.

In the full quantum description, the wave function of the system loses the phase coherence due to the interactions with bath degrees of freedom. FSSH-CPA is a quantum classical calculation where the electrons are treated quantum mechanically and the nuclei are treated classically. So, the bath induced quantum coherence loss should be explicitly introduced.[39-41]

In FSSH-CPA, decoherence can be incorporated according to decoherence-induced surface hopping (DISH) algorithm.[42-43] In this algorithm, the decoherence times τ_a for each state are given by:

$$\frac{1}{\tau_a}(t) = \sum_{i\neq\alpha}^{N} |c_i(t)|^2 r_{\alpha i} \tag{2.36}$$

where N is the number of adiabatic states and the coefficients $c_i(t)$ are obtained by solving quantum classical equation (2.32). $r_{\alpha i}$ gives the decoherence rates between the pairs of electronic states. The decoherence times define the time at which the electronic coherences dissolve due to

interaction with the environment. Our calculations have incorporated the decoherence via the DISH algorithm as implemented in the PYXAID program.[38, 43]

In the PYXAID program, nonadiabatic coupling (H_{ij}) is evaluated numerically using the scheme proposed by Hammes-Schiffer and Tully[44]:

$$H_{ij}\left(t+\frac{dt}{2}\right) = -i\hbar\frac{\langle\Psi_i(t)|\Psi_j(t+dt)\rangle - \langle\Psi_i(t+dt)|\Psi_j(t)\rangle}{2.dt} \tag{2.37}$$

2.6 Basis set

The electronic wavefunction Ψ can be constructed as a linear combination of the basis functions χ_i; this set of basis functions is called the basis set.[1]

$$\Psi = \sum_{i=1}^{N} a_i\chi_i \tag{2.38}$$

Each basis function has coefficient a_i associated with it and N is the number of basis functions (N). An infinite basis set needs to be used to reach the complete basis set limit, which is not practical. So, researchers are identifying the mathematical functions that allow the wave functions to reach close to the infinite basis set limit in an efficient manner.

Basis sets used in this dissertation are of two types: atomic basis sets and plane wave basis sets. Atomic basis sets are composed of atomic orbitals, which can be Slater-type orbitals (STOs) or Gaussian-type orbitals. The mathematical form of STOs is:

$$\varphi(r,\theta,\emptyset;n,l,m) = Nr^{n-1}e^{-\varsigma r}Y_l^m(\theta,\Psi) \tag{2.39}$$

where r is the distance of the electron from the atomic nucleus; n, l, m are the quantum numbers; N is the normalization constant; ς is the exponent that depends on atomic number and controls the

width of orbitals; and $Y_l^m(\theta, \Psi)$ refer to the spherical harmonic functions. STOs give the correct exponential decay with increasing r and the 1s orbital has a cusp at the nucleus, as it should. But, there is no analytical solution available for the four center integrals in STOs, and hence the four center integrals need to be computed numerically. This makes STOs computationally expensive. So, an alternative to the STOs called the Gaussian-type orbital (GTO) is used, where the radial decay of wavefunction is changed from e^{-r} to e^{-r^2}. Since an analytical solution can be obtained for the integrals associated with GTOs, they are faster than STOs. The mathematical form of a GTO in Cartesian coordinates is:

$$\varphi(x, y, z; \alpha, i, j, k) = N x^i y^j z^k e^{-\varsigma r^2} \tag{2.40}$$

where α is the exponent that controls the width of the GTO and i, j, k are the integers that describe the type of orbitals. Since the decay of GTOs is exponential in r^2, there is a rapid reduction in amplitude with distance and therefore these functions cannot describe the atomic orbitals properly far from the nucleus. Also, GTOs do not have a cusp at the nucleus and hence cannot describe the orbital properly. In order to account for these deficiencies of GTOs, STOs are often constructed from a linear combination of GTOs. In this dissertation, ADF[45] calculations use STOs and the Gaussian[46] calculations use GTOs. Polarization and diffuse functions can be added to the basis functions to improve the accuracy. Polarization functions are important to model the bonding since they give the correct shape of molecular orbitals. Diffuse functions are important when considering anions, Rydberg states and other long range interactions.

Plane wave basis sets are not centered on atoms and are used for periodic infinite systems.[1, 47] According to the Bloch theorem, the electronic wavefunction at every k-point can be expanded

in terms of a discrete plane wave basis set. The electronic wavefunction φ_n is represented as a combination of periodic part $u_n(r)$ and plane wave part/phase factor $e^{ik.r}$ with wave vector k.

$$\varphi_n(r) = e^{ik.r} u_n(r) \tag{2.41}$$

Upon Fourier transform, the periodic part $u_n(r)$ can be written as:

$$u_n(r) = \sum_G c_{n,G} e^{iG.r} \tag{2.42}$$

where $c_{n,G}$ are plane wave coefficients and G is the reciprocal lattice vector. So, from (41) and (42), the plane wave basis set can be written as:

$$\varphi_n(r) = \sum_G c_{n,(k+G)} e^{i(k+G).r} \tag{2.43}$$

where $c_{n,(k+G)}$ is the expansion coefficient. An infinite number of plane waves are needed to describe the wavefunction accurately, but this is not practical. So, we need to make approximations to select the most useful plane waves. One of those approximations is to use the plane waves up to a cutoff energy E_{cut} according to the relation:

$$E_{cut} = \frac{\hbar^2}{2m} \vec{G}_{cut}^2 \tag{2.44}$$

where $\hbar = \frac{h}{2\pi}$ and h is Planck's constant. So, the size of the plane wave basis set is independent of the number of atoms but depends on the volume of the box and the cutoff energy.

Plane wave basis sets require pseudopotentials to reduce the computational cost. Since the core electrons are chemically inert, pseudopotential methods are developed that replace core electrons by a pseudopotential that acts on a set of pseudo wavefunctions. This potential can be represented with only a small number of Fourier coefficients. The valence electrons are represented with full wavefunctions. This dissertation uses the projector augmented wave (PAW)[48] pseudopotential that is available in VASP.[49]

2.7 Relativistic effects

The innermost electrons that penetrate to the nucleus (s and p electrons) of heavier elements have higher speeds. The average radial velocity $< V_r >$ of the electron in the 1s shell can be obtained using $< V_r > /c = Z\alpha$ where c is the speed of light, Z is the atomic number and α is the fine structure constant (1/137). On using this equation for the mercury atom of atomic number 80, one finds that the radial velocity of the 1s electron is 58% of the velocity of light.[50] When an electron speed is comparable to the speed of light, the mass of the electron m increases according to:

$$m = \frac{m_e}{\sqrt{1 - \left({}^{v_e}/_{c}\right)^2}} \tag{2.45}$$

where m_e, v_e, and c are the rest mass of the electron, the velocity of the electron and the speed of light respectively. So, as the velocity becomes close to the speed of light, a correction in mass is required. So, the relativistic effect imposes a limit on the maximum speed of particles.

Due to this relativistic effect, the s-shell contracts and the s-electrons are very strongly bound to the nucleus. The p-shell electrons also contract but they contract to a lesser extent compared to the s-shell. Due to the shielding from s and p electrons, the d and f electrons are less bound to the nucleus. This leads to a change in the electronic structure of the elements heavier than lanthanides.[51-53] So, the relativistic effects are very important for heavier atoms (e.g. gold) used in this dissertation. In this dissertation, scalar relativistic effects are included in ADF calculations through ZORA (zeroth order regular approximation).[54-55] In the VASP software calculations, the scalar relativistic effects are included through the pseudopotentials.[56]

2.8 References

1. Cramer, C. J., *Essentials of Computational Chemistry: Theories and Models*. Wiley: 2004.

2. Hohenberg, P.; Kohn, W., Inhomogeneous Electron Gas. *Phys. Rev.* **1964,** *136* (3B), B864-B871.

3. Kohn, W.; Sham, L. J., Self-Consistent Equations Including Exchange and Correlation Effects. *Phys. Rev.* **1965,** *140* (4A), A1133-A1138.

4. Bao, J. L.; Gagliardi, L.; Truhlar, D. G., Self-Interaction Error in Density Functional Theory: An Appraisal. *J. Phys. Chem. Lett.* **2018,** *9* (9), 2353-2358.

5. Perdew, J. P.; Schmidt, K., Jacob's Ladder of Density Functional Approximations for the Exchange-Correlation Energy. *AIP Conf. Proc.* **2001,** *577* (1), 1-20.

6. Vosko, S. H.; Wilk, L.; Nusair, M., Accurate Spin-Dependent Electron Liquid Correlation Energies for Local Spin Density Calculations: a Critical Analysis. *Can. J. Phys.* **1980,** *58* (8), 1200-1211.

7. Perdew, J. P.; Burke, K.; Ernzerhof, M., Generalized Gradient Approximation Made Simple. *Phys. Rev. Lett.* **1996,** *77* (18), 3865-3868.

8. Tao, J.; Perdew, J. P.; Staroverov, V. N.; Scuseria, G. E., Climbing the Density Functional Ladder: Nonempirical Meta--Generalized Gradient Approximation Designed for Molecules and Solids. *Phys. Rev. Lett.* **2003,** *91* (14), 146401.

9. Lee, C.; Yang, W.; Parr, R. G., Development of the Colle-Salvetti Correlation-Energy Formula into a Functional of the Electron Density. *Phys. Rev. B* **1988,** *37* (2), 785-789.

10. Tirado-Rives, J.; Jorgensen, W. L., Performance of B3LYP Density Functional Methods for a Large Set of Organic Molecules. *J. Chem. Theory Comput.* **2008,** *4* (2), 297-306.

11. Borioni, J. L.; Puiatti, M.; Vera, D. M. A.; Pierini, A. B., In Search of the Best DFT Functional for Dealing with Organic Anionic Species. *Phys. Chem. Chem. Phys.* **2017,** *19* (13), 9189-9198.

12. Runge, E.; Gross, E. K. U., Density-Functional Theory for Time-Dependent Systems. *Phys. Rev. Lett.* **1984,** *52* (12), 997-1000.

13. Dreuw, A.; Head-Gordon, M., Single-Reference ab Initio Methods for the Calculation of Excited States of Large Molecules. *Chem. Rev.* **2005,** *105* (11), 4009-4037.

14. van Leeuwen, R., Mapping from Densities to Potentials in Time-Dependent Density-Functional Theory. *Phys. Rev. Lett.* **1999,** *82* (19), 3863-3866.

15. Provorse, M. R.; Isborn, C. M., Electron Dynamics with Real-Time Time-Dependent Density Functional Theory. *Int. J. Quantum Chem.* **2016,** *116* (10), 739-749.

16. Casida, M. E., Time-Dependent Density Functional Response Theory for Molecules. In *Recent Advances in Density Functional Methods*, WORLD SCIENTIFIC: 1995; Vol. Volume 1, pp 155-192.

17. Byun, Y.-M.; Ullrich, C. A., Excitons in Solids from Time-Dependent Density-Functional Theory: Assessing the Tamm-Dancoff Approximation. *Computation* **2017,** *5* (1).

18. Lopata, K.; Govind, N., Modeling Fast Electron Dynamics with Real-Time Time-Dependent Density Functional Theory: Application to Small Molecules and Chromophores. *J. Chem. Theory Comput.* **2011,** *7* (5), 1344-1355.

19. Gómez Pueyo, A.; Marques, M. A. L.; Rubio, A.; Castro, A., Propagators for the Time-Dependent Kohn–Sham Equations: Multistep, Runge–Kutta, Exponential Runge–Kutta, and Commutator Free Magnus Methods. *J. Chem. Theory Comput.* **2018,** *14* (6), 3040-3052.

20. Isborn, C. M.; Li, X.; Tully, J. C., Time-Dependent Density Functional Theory Ehrenfest Dynamics: Collisions Between Atomic Oxygen and Graphite Clusters. *J. Chem. Phys.* **2007,** *126* (13), 134307.

21. Ding, F.; Guidez, E. B.; Aikens, C. M.; Li, X., Quantum Coherent Plasmon in Silver Nanowires: A Real-time TDDFT Study. *J. Chem. Phys.* **2014,** *140* (24), 244705.

22. Persico, M.; Granucci, G., An Overview of Nonadiabatic Dynamics Simulations Methods, with Focus on the Direct Approach Versus the Fitting of Potential Energy Surfaces. *Theor. Chem. Acc.* **2014,** *133* (9), 1526.

23. Sawada, S.-I.; Nitzan, A.; Metiu, H., Mean-Trajectory Approximation for Charge- and Energy-Transfer Processes at Surfaces. *Phys. Rev. B* **1985,** *32* (2), 851-867.

24. Micha, D. A., A Self-Consistent Eikonal Treatment of Electronic Transitions in Molecular Collisions. *J. Chem. Phys.* **1983,** *78* (12), 7138-7145.

25. C. Tully, J., Mixed Quantum–Classical Dynamics. *Faraday Discuss.* **1998,** *110* (0), 407-419.

26. Li, X.; Tully, J. C.; Schlegel, H. B.; Frisch, M. J., Ab Initio Ehrenfest Dynamics. *J. Chem. Phys.* **2005,** *123* (8), 084106.

27. Li, X.; Smith, S. M.; Markevitch, A. N.; Romanov, D. A.; Levis, R. J.; Schlegel, H. B., A Time-Dependent Hartree–Fock Approach for Studying the Electronic Optical Response of Molecules in Intense Fields. *Phys. Chem. Chem. Phys.* **2005,** *7* (2), 233-239.

28. Tully, J. C.; Preston, R. K., Trajectory Surface Hopping Approach to Nonadiabatic Molecular Collisions: The Reaction of H^+ with D_2. *J. Chem. Phys.* **1971,** *55* (2), 562-572.

29. Kuntz, P. J., Classical Path Surface-Hopping Dynamics. I. General Theory and Illustrative Trajectories. *J. Chem. Phys.* **1991,** *95* (1), 141-155.

30. Parlant, G.; Gislason, E. A., An Exact Trajectory Surface Hopping Procedure: Comparison with Exact Quantal Calculations. *J. Chem. Phys.* **1989,** *91* (7), 4416-4418.

31. Gersonde, I. H.; Gabriel, H., Molecular Dynamics of Photodissociation in Matrices including Nonadiabatic Processes. *J. Chem. Phys.* **1993,** *98* (3), 2094-2106.

32. Coker, D. F.; Xiao, L., Methods for Molecular Dynamics with Nonadiabatic Transitions. *J. Chem. Phys.* **1995,** *102* (1), 496-510.

33. Tully, J. C., Molecular Dynamics with Electronic Transitions. *J. Chem. Phys.* **1990,** *93* (2), 1061-1071.

34. Parandekar, P. V.; Tully, J. C., Mixed Quantum-Classical Equilibrium. *J. Chem. Phys.* **2005,** *122* (9), 094102.

35. Schmidt, J. R.; Parandekar, P. V.; Tully, J. C., Mixed Quantum-Classical Equilibrium: Surface Hopping. *J. Chem. Phys.* **2008,** *129* (4), 044104.

36. Carof, A.; Giannini, S.; Blumberger, J., Detailed Balance, Internal Consistency, and Energy Conservation in Fragment Orbital-Based Surface Hopping. *J. Chem. Phys.* **2017,** *147* (21), 214113.

37. Craig, C. F.; Duncan, W. R.; Prezhdo, O. V., Trajectory Surface Hopping in the Time-Dependent Kohn-Sham Approach for Electron-Nuclear Dynamics. *Phys. Rev. Lett.* **2005,** *95* (16), 163001.

38. Akimov, A. V.; Prezhdo, O. V., The PYXAID Program For Non-adiabatic Molecular Dynamics in Condensed Matter Systems. *J. Chem. Theory Comput.* **2013,** *9* (11), 4959-4972.

39. Prezhdo, O. V.; Rossky, P. J., Evaluation of Quantum Transition Rates from Quantum-Classical Molecular Dynamics Simulations. *J. Chem. Phys.* **1997,** *107* (15), 5863-5878.

40. Prezhdo, O. V.; Rossky, P. J., Relationship between Quantum Decoherence Times and Solvation Dynamics in Condensed Phase Chemical Systems. *Phys. Rev. Lett.* **1998,** *81* (24), 5294-5297.

41. Schwartz, B. J.; Bittner, E. R.; Prezhdo, O. V.; Rossky, P. J., Quantum Decoherence and the Isotope Effect in Condensed Phase Nonadiabatic Molecular Dynamics Simulations. *J. Chem. Phys.* **1996,** *104* (15), 5942-5955.

42. Jaeger, H. M.; Fischer, S.; Prezhdo, O. V., Decoherence-Induced Surface Hopping. *J. Chem. Phys.* **2012,** *137* (22), 22A545.

43. Akimov, A. V.; Prezhdo, O. V., Advanced Capabilities of the PYXAID Program: Integration Schemes, Decoherence Effects, Multiexcitonic States, and Field-Matter Interaction. *J. Chem. Theory Comput.* **2014,** *10* (2), 789-804.

44. Hammes-Schiffer, S.; Tully, J. C., Proton Transfer in Solution: Molecular Dynamics with Quantum Transitions. *J. Chem. Phys.* **1994,** *101* (6), 4657-4667.

45. te Velde, G.; Bickelhaupt, F. M.; Baerends, E. J.; Fonseca Guerra, C.; van Gisbergen, S. J. A.; Snijders, J. G.; Ziegler, T., Chemistry with ADF. *J. Comput. Chem.* **2001,** *22* (9), 931-967.

46. Frisch, M.; Trucks, G.; Schlegel, H.; Scuseria, G.; Robb, M.; Cheeseman, J.; Scalmani, G.; Barone, V.; Mennucci, B.; Petersson, G., Gaussian 09 (Gaussian, Inc., Wallingford, CT). *Revision D* **2009,** *1*.

47. Payne, M. C.; Teter, M. P.; Allan, D. C.; Arias, T. A.; Joannopoulos, J. D., Iterative Minimization Techniques for Ab Initio Total-Energy Calculations: Molecular Dynamics and Conjugate Gradients. *Rev. Mod. Phys.* **1992,** *64* (4), 1045-1097.

48. Blöchl, P. E., Projector Augmented-Wave Method. *Phys. Rev. B* **1994,** *50* (24), 17953-17979.

49. Kresse, G.; Furthmüller, J., Efficiency of Ab-Initio Total Energy Calculations for Metals and Semiconductors Using a Plane-Wave Basis Set. *Comput. Mater. Sci.* **1996,** *6* (1), 15-50.

50. Pradeep, T.; Anshup, Noble Metal Nanoparticles for Water Purification: A Critical Review. *Thin Solid Films* **2009,** *517* (24), 6441-6478.

51. Pitzer, K. S., Relativistic Effects on Chemical Properties. *Acc. Chem. Res.* **1979,** *12* (8), 271-276.

52. Bartlett, N., Relativistic Effects and the Chemistry of Gold. *Gold Bulletin* **1998,** *31* (1), 22-25.

53. Pyykko, P.; Desclaux, J. P., Relativity and the Periodic System of Elements. *Acc. Chem. Res.* **1979,** *12* (8), 276-281.

54. van Lenthe, E.; Snijders, J. G.; Baerends, E. J., The Zero-Order Regular Approximation for Relativistic Effects: The Effect of Spin–Orbit Coupling in Closed Shell Molecules. *J. Chem. Phys.* **1996,** *105* (15), 6505-6516.

55. van Lenthe, E.; Ehlers, A.; Baerends, E.-J., Geometry Optimizations in the Zero Order Regular Approximation for Relativistic Effects. *J. Chem. Phys.* **1999,** *110* (18), 8943-8953.

56. Hafner, J., Ab-initio simulations of materials using VASP: Density-functional theory and beyond. *J. Comput. Chem.* **2008,** *29* (13), 2044-2078.

Chapter 3 - Nonradiative Relaxation Dynamics in the $[Au_{25-n}Ag_n(SH)_{18}]^{-1}$ (n = 1, 12, 25) Thiolate-protected Nanoclusters

Reproduced with permission from:

Pandeya, P.; Aikens, C. M., *J. Chem. Phys.* **2021**, *154*, 184303.

3.1 Abstract

Evaluation of the electron-nuclear dynamics and relaxation mechanisms of gold and silver nanoclusters and their alloys is important for future photocatalytic, light harvesting and photoluminescence applications of these systems. In this work, the effect of silver doping on the nonradiative excited state relaxation dynamics of the atomically precise thiolate-protected gold nanocluster $[Au_{25-n}Ag_n(SH)_{18}]^{-1}$ (n = 1, 12, 25) is studied theoretically. Time-dependent density functional theory is used to study excited states lying in the energy range 0.0-2.5 eV. The fewest switches surface hopping method with decoherence correction was used to investigate the dynamics of these states. The HOMO-LUMO gap increases significantly upon doping of 12 silver atoms but decreases for the pure silver nanocluster. Doped clusters show a different response for ground state population increase lifetimes and excited state population decay times in comparison to the undoped system. The ground state recovery times of the S_1-S_6 states in the first excited peak were found to be longer for $[Au_{13}Ag_{12}(SH)_{18}]^{-1}$ than the corresponding recovery times of other studied nanoclusters, suggesting that this partially doped nanocluster is best for preserving electrons in an excited state. The decay time constants were in the range of 2.0-20 ps for the six lowest energy excited states. Among the higher excited states, S_7 has the slowest decay time constant although it occurs more quickly than S_1 decay. Overall, these clusters follow common

decay time constant trends and relaxation mechanisms due to the similarities in their electronic structures.

3.2 Introduction

Small thiolate-stabilized gold nanoclusters with core diameters of less than 2 nm are of great importance due to their future applications in solar cells, light harvesting and photoluminescence.[1-18] Understanding radiative and nonradiative relaxation of these nanoclusters is key to fulfilling their potential in these applications. Numerous experimental studies have been performed on thiolate-protected gold nanoclusters to understand their nonradiative relaxation mechanisms[15-17, 19-25] but fewer theoretical studies have been undertaken.[26-30] $Au_{25}(SR)_{18}$ is the most frequently studied nanocluster[31-35] because it has higher chemical and thermodynamic stability than clusters of other sizes.[31, 36, 37] Doping of thiolate-protected gold nanoclusters with cheaper metals like silver that possess distinct physical and chemical properties compared to those of gold, is useful to study to improve properties due to synergy of the different component metals.[38] Since gold and silver have a similar outermost valence electronic configuration (gold:$6s^1$; silver:$5s^1$), and nearly identical lattice constants, these atoms can be mixed in various proportions.[39] Silver-doped Au_{25} nanoclusters have the same framework as their homo-metal counterparts, but their optical, structural, and electronic properties can be tuned.[39-41]

A great number of atomically precise, monolayer-protected gold clusters have been characterized using X-ray crystallography and diffractometric analysis over the past years,[1, 33, 42-50] [1, 33, 42-50] whereas only a few silver clusters have been crystallized.[51-59] After the discovery of the $[Au_{25}(SR)_{18}]^{-1}$ cluster (abbreviated as Au_{25} in the text), the electronic structure of related $[Ag_{25}(SH)_{18}]^{-1}$ and $[Au_{13}Ag_{12}(SH)_{18}]^{-1}$ clusters were described using the time dependent density

functional theory method.[41, 60] In 2015, Bakr and co-workers crystallized a thiolate-protected silver nanocluster $[Ag_{25}(SR)_{18}]^{-1}$ that is an exact analog of $[Au_{25}(SR)_{18}]^{-1}$ in terms of size, superatom electronic configuration, charge and composition.[61] Thus, this allowed researchers to perform a direct comparison of properties of thiolate-protected silver nanoclusters. This cluster consists of an Ag_{13} icosahedral core protected by six V-shaped -S-Ag-S-Ag-S- staple motifs with an overall quasi-T_h symmetry similar to the gold analog.[61]

Previous works on doping indicate that the most favorable place for doping a single silver atom is on the surface of the nanocluster core compared to doping in the center of the core and in the staple motifs (e.g. Ref. 39 and references therein). Researchers have been able to dope ~24 silver atoms into $[Au_{25}(SR)_{18}]^{-1}$ experimentally.[62] Theoretically, Guidez et al. examined the absorption spectra of a series of $[Au_{25-n}Ag_n(SH)_{18}]^{-1}$ (n = 1, 2, 4, 6, 8, 10, 12) bimetallic nanoparticles[39] where the silver atoms were substituted in different positions of the gold cluster core. That work also confirmed that silver tends to occupy positions on the outer shell of the core. They also noticed that the optical peaks shift to higher energy with increasing numbers of silver atoms, the intensity of the absorption peak at 2.5 eV increases as the number of silver dopants increases due to the increasing contributions of superatom 1P→1D and 1P→2S transitions, and some additional orbital splitting occurs due to breaking of symmetry of nanocluster. Thus, they concluded that it is possible to tune optical properties if one can control the number of silver atoms in the nanoparticle.

Many experimental nonradiative relaxation dynamics investigations on thiolate-protected noble metal nanoclusters have been performed on the $[Au_{25}(SR)_{18}]^{-1}$ nanocluster.[15-17, 19-22] Various research groups have proposed several different mechanisms for the nonradiative relaxation mechanism of $[Au_{25}(SR)_{18}]^{-1}$.[15-17, 20-22] Moran and co-workers[17] observed an extremely rapid

internal conversion process, taking place on the order of 200 fs in $[Au_{25}(SCH_2CH_2Ph)_{18}]^{-1}$. Knappenberger and co-workers[20] studied the relaxation dynamics in the anionic and neutral $Au_{25}L_{18}$ clusters. They observed few picosecond time scale dynamics for a nonradiative nanocluster core-to-ligand energy transfer process following the internal conversion. Experimental work has also been performed on a luminescent rod-shaped, silver-doped $Au_{25-n}Ag_n$ cluster to understand its ultrafast relaxation dynamics.[24] An ultrafast excited state relaxation (~0.58 ps), which is an internal conversion process, and a subsequent nuclear relaxation (~20.7 ps) were reported in $Au_{25-n}Ag_n$. A faster nuclear relaxation was observed in doped systems compared to that in undoped.

A recent theoretical study using ab initio real-time nonadiabatic molecular dynamics (NA-MD) simulations was performed by our group to understand the electron relaxation dynamics of the Au_{25} cluster.[27] In this study, the time constants observed experimentally[17] were found to arise from nanocluster core-to-core transitions rather than from a core-to-staple motif transition; no staple-based or other states were observed at lower energy than the nanocluster core-based S_1 state.[27]

Although it has been concluded that many atoms of silver can be doped in gold nanoclusters and properties such as the visible absorption spectrum can be tuned, few experimental studies have been done to investigate the nonradiative excited state relaxation of the silver doped $[Au_{25}(SR)_{18}]^{-1}$ nanocluster.[63, 64] Insights into the radiative properties of the Ag_{25} and single silver atom doped Au_{25} system can be obtained from our earlier work on the luminescence of these systems;[65] however, there are no reports of theoretical work performed to understand the nonradiative relaxation dynamics of the thiolate-protected silver nanocluster that is an exact analog of a thiolate-protected gold nanocluster, which is required in order to understand the excited state electron

dynamics relevant in energy transfer and photocatalytic processes. With the discovery of the "golden" silver nanoparticle $[Ag_{25}(SR)_{18}]^{-1}$,[61] it will be important to assess the applicability of the relaxation mechanism proposed for the $[Au_{25}(SR)_{18}]^{-1}$ nanocluster to its silver analog. It is essential to have deeper atomic level understanding of nonradiative relaxation in nanoalloys and in the "golden" silver nanoparticle $[Ag_{25}(SR)_{18}]^{-1}$ in order to design new atomically precise nanoalloys with more uses and applications.

Herein, the $[Au_{25}(SH)_{18}]^{-1}$ cluster has been doped with one or twelve silver atoms where the silver atoms are doped on the outer surface of the nanocluster core. Then, we perform electron-nuclear dynamics to reveal the nonradiative relaxation mechanism for excited electrons in the doped clusters, $[Au_{24}Ag(SH)_{18}]^{-1}$ and $[Au_{13}Ag_{12}(SH)_{18}]^{-1}$, as well as in the "golden" silver nanoparticle $[Ag_{25}(SR)_{18}]^{-1}$.

3.3 Computational details

Real-time ab initio nonadiabatic molecular dynamics (NA-MD) simulations have been performed to study the nonadiabatic dynamics in the $[Au_{24}Ag(SH)_{18}]^{-1}$, $[Au_{13}Ag_{12}(SH)_{18}]^{-1}$, and $[Ag_{25}(SH)_{18}]^{-1}$ nanoclusters. These nanoclusters will be abbreviated as $Au_{24}Ag$, $Au_{13}Ag_{12}$, and Ag_{25}, respectively, throughout the text. The procedure used is similar to our previous study of $[Au_{25}(SH)_{18}]^{-1}$ relaxation dynamics.[27]

Geometry optimizations were performed using the conjugate gradient method implemented in the Amsterdam Density Functional (ADF) package[66] to obtain the relaxed geometries at 0K (Figure 3-1). Core electrons were treated using a frozen core approximation to reduce the computational burden while a triple-ζ polarized basis set (TZP) was used for the valence electrons. Electron exchange and correlation were included using the GGA Perdew−

Burke−Ernzerhof (PBE) exchange-correlation functional.[67] Optimization was performed in the gas phase. Although previous work in our group has employed the LB94 and SAOP functionals to examine the optical absorption spectra of these systems,[41] the current work employs the PBE functional for consistency with the dynamics calculations described below. Scalar relativistic effects were included using the zeroth-order regular approximation (ZORA).[68-70] Electronic transitions and absorption spectra were obtained using linear response time-dependent density functional theory (TDDFT) and convoluted with a Gaussian function with a full width at half maximum of 0.2 eV. Electronic excited states that contribute to the two main peaks in the range of 0.0-2.5 eV were studied in detail.

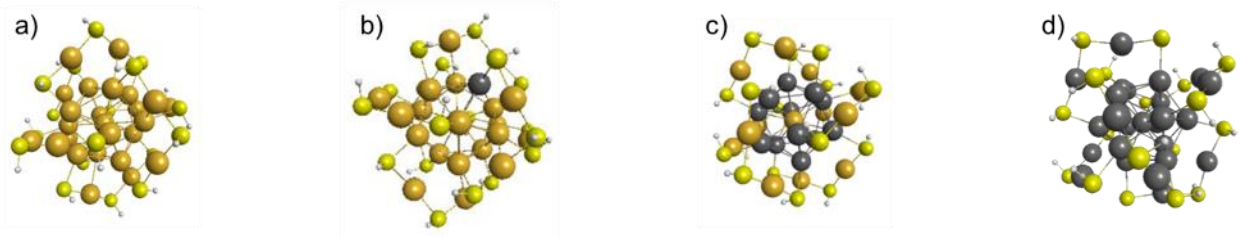

Figure 3-1 Optimized geometries of (a) $[Au_{25}(SH)_{18}]^{-1}$, (b) $[Au_{24}Ag(SH)_{18}]^{-1}$, (c) $[Au_{13}Ag_{12}(SH)_{18}]^{-1}$ and (d) $[Ag_{25}(SH)_{18}]^{-1}$ at the PBE/TZP level of theory. Yellow: gold; gray: silver; light green: sulfur; white: hydrogen.

Next, optimized structures were heated to room temperature (300 K) and molecular dynamics trajectories were computed with the Vienna Ab initio Simulation Package (VASP).[71] Trajectories were computed for 5 ps assuming a microcanonical ensemble and using the Verlet algorithm[72] with a 1 fs time step. The simulation box size used was 24 Å to avoid contacts between the clusters. We used projector-augmented wave (PAW)[73] pseudopotentials. A kinetic energy cutoff value of 402.0 eV was used for the temperature ramping calculation and a 301.8 eV energy cutoff value was employed for the MD and NA coupling calculations. We used gamma points and

the PBE functional in all VASP calculations. An MD trajectory was computed for 5 ps length which provides nuclear coordinates at each time step.

Then, nonadiabatic coupling matrix elements were computed using the nuclear coordinates at each time step along the MD trajectory by employing the fewest-switches surface hopping (FSSH) method of Tully and Hammes-Schiffer[74] with a numerical approach from Prezhdo and co-workers.[75] The decoherence-induced surface hopping (DISH)[76] scheme was used to correct the overcoherent nature of the FSSH approach. Computationally efficient approaches like the classical path approximation and the time-dependent Kohn-Sham description of electronic states (FSSH-TDKS)[75] were utilized, which have been found to be appropriate for solid-state systems where nuclear dynamics are not significantly affected by electronic transitions. FSSH requires statistical averaging over an ensemble of trajectories to give well-converged statistics of electronic transitions. So, 10 different starting geometries were taken along the entire 5 ps molecular dynamics trajectory; 3.5 ps length sub-trajectories were considered and 1000 electron dynamics trajectories were performed for each sub-trajectory. All NA-MD calculations were computed using the PYXAID program.[77, 78]

Finally, the excited state population decay time and ground state population increase time were calculated by fitting to the following equations respectively:

$$\boldsymbol{f(t)=exp(-t/\tau)} \qquad (1)$$

$$\boldsymbol{f(t)=1-exp(-t/\tau)} \qquad (2)$$

These decay times were calculated both with and without an energy correction to the calculated excited state energies. These energy corrections are used to compensate for underestimation or overestimation in the calculated density functional theory (DFT) band gaps compared to the experimental gaps. An energy correction was considered for several excited states in order to

evaluate its impact on the excited state dynamics and this comparison is presented in the Supporting Information; no energy correction is used in the main text. All states considered in this work are singlet states.

3.4 Results and discussion

3.4.1 Optical absorption spectra

The PBE/TZP absorption spectra of $Au_{24}Ag$, $Au_{13}Ag_{12}$, and Ag_{25} are shown in Figure 3-2. The first peak in the absorption spectra is found to originate from nanocluster core-to-core transitions (HOMO through HOMO-2 into LUMO and LUMO+1) for all three systems similar to the Au_{25} nanocluster, where the HOMO is nearly triply degenerate and LUMO is nearly doubly degenerate. These three highest occupied orbitals have superatomic P orbital character and the lowest unoccupied orbitals have superatomic D orbital character; these orbitals look similar to atomic p and d orbitals except that they are delocalized throughout the nanocluster core. Transitions arising from electronic excitation between these orbitals are described as core-to-core transitions because the orbitals are primarily spatially located in the nanocluster core. The first peak blue-shifts from about 1.41 eV in Au_{25} (Ref. 27) up to 1.9 eV for $Au_{13}Ag_{12}$ (Figure 3-2). This blue shift is due to an increase in the HOMO-LUMO gap upon doping of 12 silver atoms as also found in our previous studies.[39] This blue shift of the first peak on doping silver atoms is also observed experimentally.[35] The second peak at ~2.5 eV for Au_{25} is seen to be unaffected upon doping of one and twelve silver atoms. For Ag_{25}, its energy remains the same but an additional shoulder is seen at the lower energy side. Thus, the second peak for Ag_{25} can be considered to be red-shifted compared to the second peak of Au_{25} which is also observed in the experimental spectra.[61] The peak positions of Ag_{25} obtained in the current study are similar to the peak positions

obtained for $[Ag_{25}(SH)_{18}]^{-1}$ using the SAOP/TZP level of theory.[41] The theoretical peak positions of Ag_{25} are red-shifted compared to the main peaks observed experimentally at 1.84, 2.53 and 3.18 eV.[61] The red-shift of the theoretical peaks compared to experiment has also been reported for the well-known Au_{25} cluster.[33] However, the red-shifting of the first peak in the silver cluster is less than that of the gold cluster.

The intensities of the peaks also vary depending on the degree of silver doping. The spectrum is broader for $Au_{24}Ag$ than for the others which could be due to breaking of the symmetry of the system upon doping of a single silver atom. The intensity of the second peak increases significantly upon doping of twelve silver atoms. The intensity of the first peak is a little higher for Ag_{25} than for the other systems.

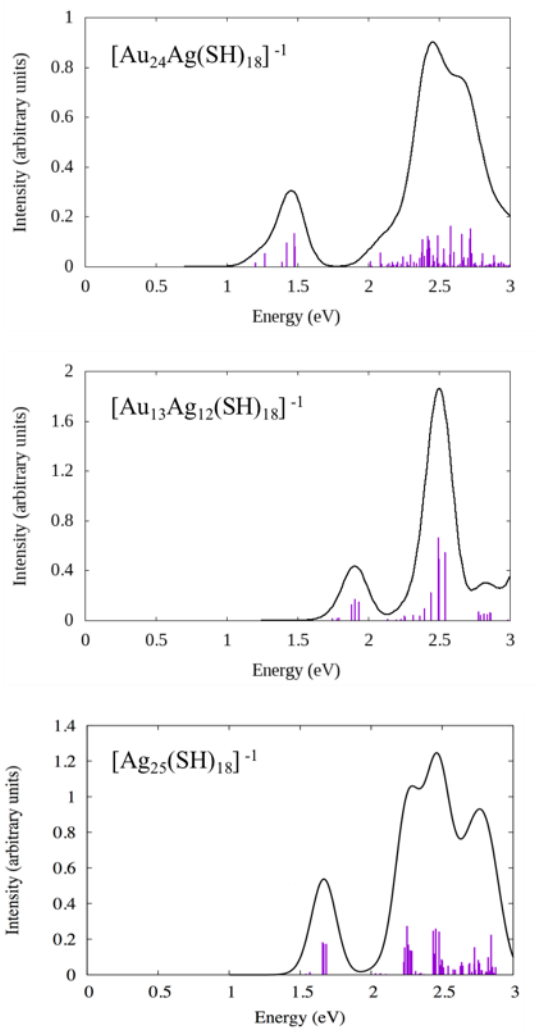

Figure 3-2 PBE/TZP optical absorption spectra of $[Au_{24}Ag(SH)_{18}]^{-1}$, $[Au_{13}Ag_{12}(SH)_{18}]^{-1}$, and $[Ag_{25}(SH)_{18}]^{-1}$.

3.4.2 Electronic relaxation dynamics of the first peak in the absorption spectra of the three studied clusters

In the following sections, the electronic relaxations of the nanoclusters are analyzed. In this section, the first peak of all three clusters is examined in order to understand its nonradiative relaxations. Tables 3-1, 3-2 and 3-3 show the important excitations involved in the first peak based on their oscillator strengths and weights. These clusters have similar electronic structure to Au_{25}, and also have similarities in the transitions responsible for their low-energy excited states. Three

main excitations involving the HOMO-2 to LUMO+1 orbitals in the most probable transitions give rise to the first peak, which was also the case for the Au_{25} cluster.

Table 3-1 Transitions with the highest weights for the prominent excited states that contribute to the first peak arising from the TDDFT calculation for $[Au_{24}Ag(SH)_{18}]^{-1}$

Excited state	Energy (eV)	Oscillator strength	Weight	Most weighted transitions
4	1.43	0.0200	0.6069	HOMO-1 → LUMO
			0.2167	HOMO-1 → LUMO+1
			0.1122	HOMO-2 → LUMO
5	1.47	0.0277	0.5119	HOMO-2 → LUMO
			0.2773	HOMO-1 → LUMO+1
			0.1091	HOMO-2 → LUMO+1
6	1.48	0.0163	0.8192	HOMO-2 → LUMO+1
			0.1018	HOMO-2 → LUMO

Table 3-2 Transitions with the highest weights for the prominent excited states that contribute to the first peak arising from the TDDFT calculation for $[Au_{13}Ag_{12}(SR)_{18}]^{-1}$

Excited state	Energy (eV)	Oscillator strength	Weight	Most weighted transitions
4	1.88	0.0200	0.3958	HOMO-2 → LUMO
			0.1634	HOMO → LUMO+1
			0.1604	HOMO-2 → LUMO+1
5	1.90	0.0350	0.5476	HOMO-1 → LUMO
			0.1968	HOMO-1 → LUMO+1
			0.1443	HOMO → LUMO+1
6	1.93	0.0300	0.5440	HOMO-2 → LUMO+1
			0.2722	HOMO-2 → LUMO

Table 3-3 Transitions with the highest weights for the prominent excited states that contribute to the first peak arising from the TDDFT calculation for $[Ag_{25}(SR)_{18}]^{-1}$

Excited state	Energy (eV)	Oscillator strength	Weight	Most weighted transitions
4	1.66	0.0389	0.3386	HOMO-2 → LUMO
			0.2451	HOMO-2 → LUMO+1
			0.145	HOMO → LUMO
			0.1026	HOMO-1 → LUMO
5	1.67	0.0372	0.2869	HOMO → LUMO+1

			0.2217	HOMO-2 → LUMO
			0.1525	HOMO-2 → LUMO+1
			0.1252	HOMO-1 → LUMO+1
			0.1236	HOMO-1 → LUMO
6	1.68	0.0370	0.5256	HOMO-1 → LUMO+1
			0.2674	HOMO → LUMO+1
			0.0624	HOMO-2 → LUMO
			0.0611	HOMO-2 → LUMO+1

Because the HOMO, HOMO-1, and HOMO-2 are nearly triply degenerate and the LUMO and LUMO+1 are nearly doubly degenerate, we can use the same FSSH-TDKS defined excited states (S_1 - S_6) as in our previous Au_{25} simulations.[27] A list of excited states and corresponding transitions used in the FSSH-TDKS calculations is given in Table 3-4. The HOMO-2 to LUMO+1 orbitals are all nanocluster core-based orbitals.

Table 3-4 Excited states with the corresponding transitions for FSSH-TDKS calculations

Excited state	Transitions
S_1	HOMO → LUMO
S_2	HOMO → LUMO+1
S_3	HOMO-1 → LUMO
S_4	HOMO-1 → LUMO+1
S_5	HOMO-2→ LUMO
S_6	HOMO-2 → LUMO+1

The orbital energy variations occurring in all clusters during the MD simulation are shown in Figure 3-3. The near degeneracies of the HOMO, HOMO-1, HOMO-2 and LUMO, LUMO+1 orbitals are apparent, similar to Au_{25}. The HOMO-LUMO gap varies around 1.10, 1.49, and 1.15 eV for $Au_{24}Ag$, $Au_{13}Ag_{12}$, and Ag_{25} respectively during the MD simulation. The orbital energies of all three clusters during the MD simulation (Figure 3-3) show the approximate triple degeneracy between the HOMO, HOMO−1, and HOMO−2 and the approximate double degeneracy between the LUMO and LUMO+1. This behavior is consistent with the nature of orbitals in the $Au_{25}(SR)_{18}^-$

^{1} cluster.[27] The HOMO-LUMO gap is seen to have increased significantly upon doping of 12 silver atoms but is similar for Au_{25} and Ag_{25} systems.

In our previous work on Au_{25}, we compared results with an energy correction of 0.55 eV to match with the experimental data and account for the theoretical underestimation of the first peak energy to results without an energy correction.[27] Inclusion of an energy correction typically lengthens the ground state growth time due to an increase in the energy gap between the excited states and the ground state, but the population relaxation times between the individual excited states remain mostly unchanged. In this work, we consider energy corrections to the excited state energies, but see only minor effects on excited state lifetimes (see Supporting Information). No energy corrections are included in the main text.

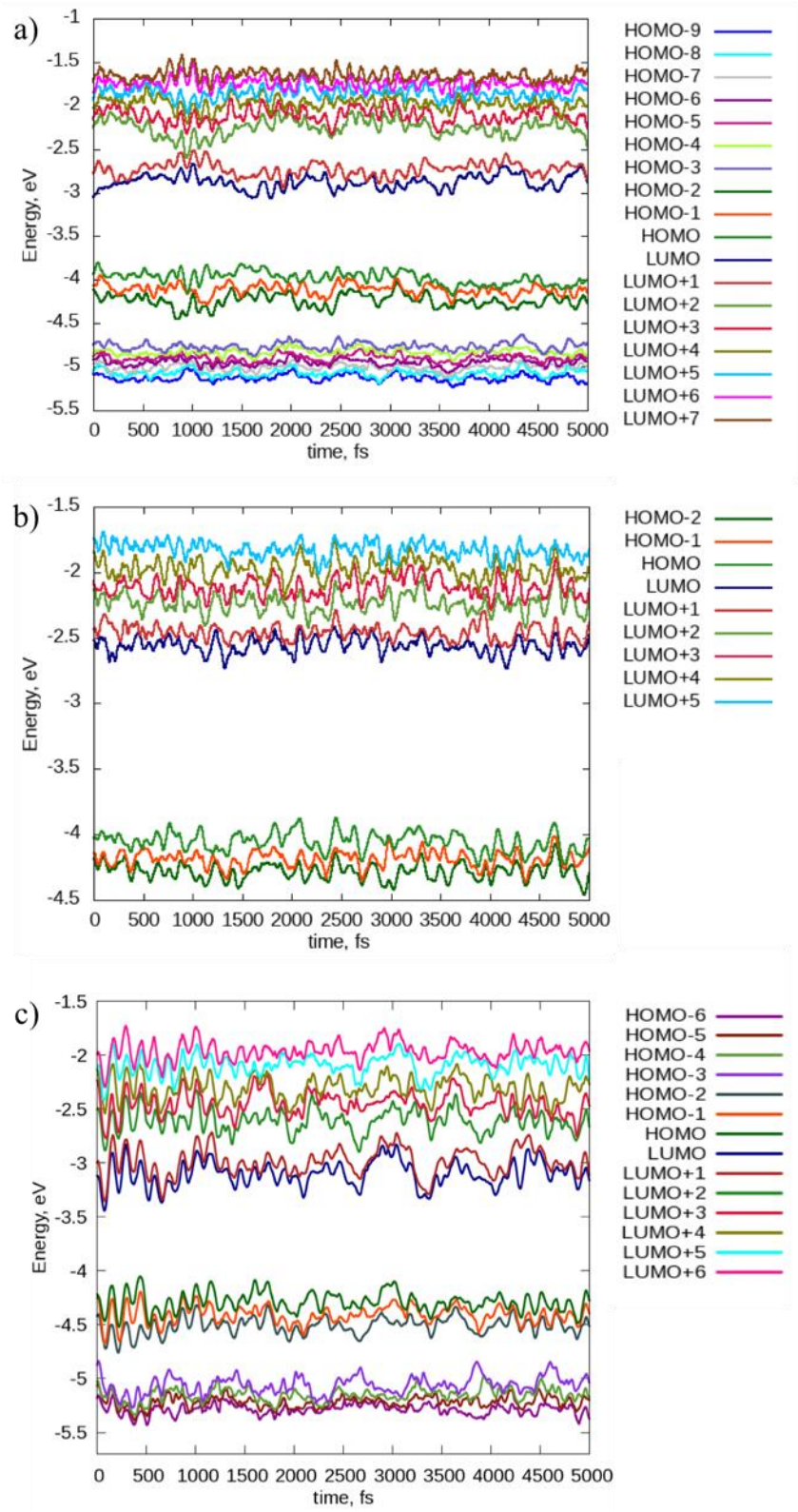

Figure 3-3 Variation of PBE orbital energies with time for (a) $[Au_{24}Ag(SH)_{18}]^{-1}$, (b) $[Au_{13}Ag_{12}(SH)_{18}]^{-1}$ and (c) $[Ag_{25}(SH)_{18}]^{-1}$.

The population relaxation dynamics of the first six excited states, S_1 to S_6, that contribute to the first peak of the studied clusters are shown in Figures 4, 5 and 6. The surface hopping (SH) populations of the states as computed from the FSSH approach are determined as a function of the simulation time after exciting an excited state of interest. The corresponding ground state recovery times (Table 3-5) and excited state population decay times (Table 3-6) have been calculated for all systems.

The population relaxation curves for the S_1-S_6 states of Ag_{25} (Figure 3-6) sometimes show "step relaxation" behavior where the population of a state transfers rapidly to another state. For example, the S_2 (HOMO→ LUMO+1) state quickly transfers its population to the S_1 (HOMO → LUMO) state during the 2700-3200 fs timeframe in Figure 3-6(b). There are also rapid population transfers from S_5 (HOMO-2 → LUMO) to S_3 (HOMO-1→ LUMO) (Figure 3-6(e)) and S_6 (HOMO-2 → LUMO+1) to S_4 (HOMO-1 → LUMO+1) (Figure 3-6(f)) during the 1000-2000 fs timeframes. A rapid population transfer could arise due to near-degeneracies that appear in the orbitals that are involved in these states during the MD simulation (Figure 3-3(c)). For example, during the ~2600-3400 fs timeframe in the MD simulations, near-degeneracy can be observed between the LUMO and LUMO+1 orbitals. During that time frame, the S_2 and S_1 states have close energies which therefore promotes a rapid population transfer among these states. Similar explanations can be given to population transfers from S_5 to S_3 and from S_6 to S_4. During the ~1100-2100 fs timeframe, the HOMO-1 and HOMO-2 orbitals show degeneracies which will stimulate the S_5 to S_3 and S_6 to S_4 population transfers. The relaxation patterns of states S_1 and S_2 are similar to the relaxation in the Au_{25} cluster whereas states S_3-S_6 demonstrate slight differences. (The population relaxation curves of the first six excited states of the Au_{25} cluster are shown in Figure A-3.) For example, the S_5 state more rapidly transfers its population to the S_3 state (Figure

3-6(e)) and the S_6 state relaxes more quickly to S_4 (Figure 3-6(f)) compared to the dynamics in the Au_{25} cluster.

The population relaxation of the S_1-S_4 states of $Au_{24}Ag$ (Figure 3-4) are slower than those of Au_{25}. In contrast, the S_5 and S_6 states more rapidly transfer electron population to S_3 and S_4 states in $Au_{24}Ag$ (Figure 3-4) compared to the population transfer of these states in Au_{25}.

Comparing the relaxation curves of $Au_{13}Ag_{12}$ (Figure 3-5) with those of Au_{25} (Figure A-3), population transfer from all S_1-S_6 states of $Au_{13}Ag_{12}$ to other higher or lower lying states occurs more quickly than the population transfer of the respective states in Au_{25}. This suggests that the time in which the excited population remains in any particular excited state might be the least for $Au_{13}Ag_{12}$ compared to the other studied clusters. However, its relaxation time to the ground state is the slowest of the clusters considered in this work (Table 3-5), which may suggest that the electrons in this system may be the best for harvesting in solar cell and photocatalytic applications.

Overall, the ground state (GS) population recovery lifetime decreases upon doping of a single silver atom and increases to a great extent upon doping of 12 silver atoms compared to the time constants of Au_{25} (Table 3-5). The GS growth times for the singly doped cluster are shorter compared to the others, which can be related to the smaller HOMO-LUMO gap in the singly doped system (~1.10 eV) compared to that of other systems (Figure 3-3(a)). The long GS recovery lifetimes of the $Au_{13}Ag_{12}$ system are logical because this cluster has the largest HOMO-LUMO gap (~ 1.49 eV, Figure 3-3(b)). In addition, the GS population recovery lifetimes are also long for Ag_{25}. In this case, the average HOMO-LUMO gap of the Ag_{25} cluster is around ~1.15 eV, whereas the Au_{25} cluster had a slightly lower gap of ~1.09 eV, so the HOMO-LUMO gap does not appear to explain the long GS lifetimes. Instead, this could be due to electron population transfer among

the S_1-S_6 states. Since the population relaxes to other higher lying excited states before reaching to the ground state, it takes a long time for the population to increase in the ground state.

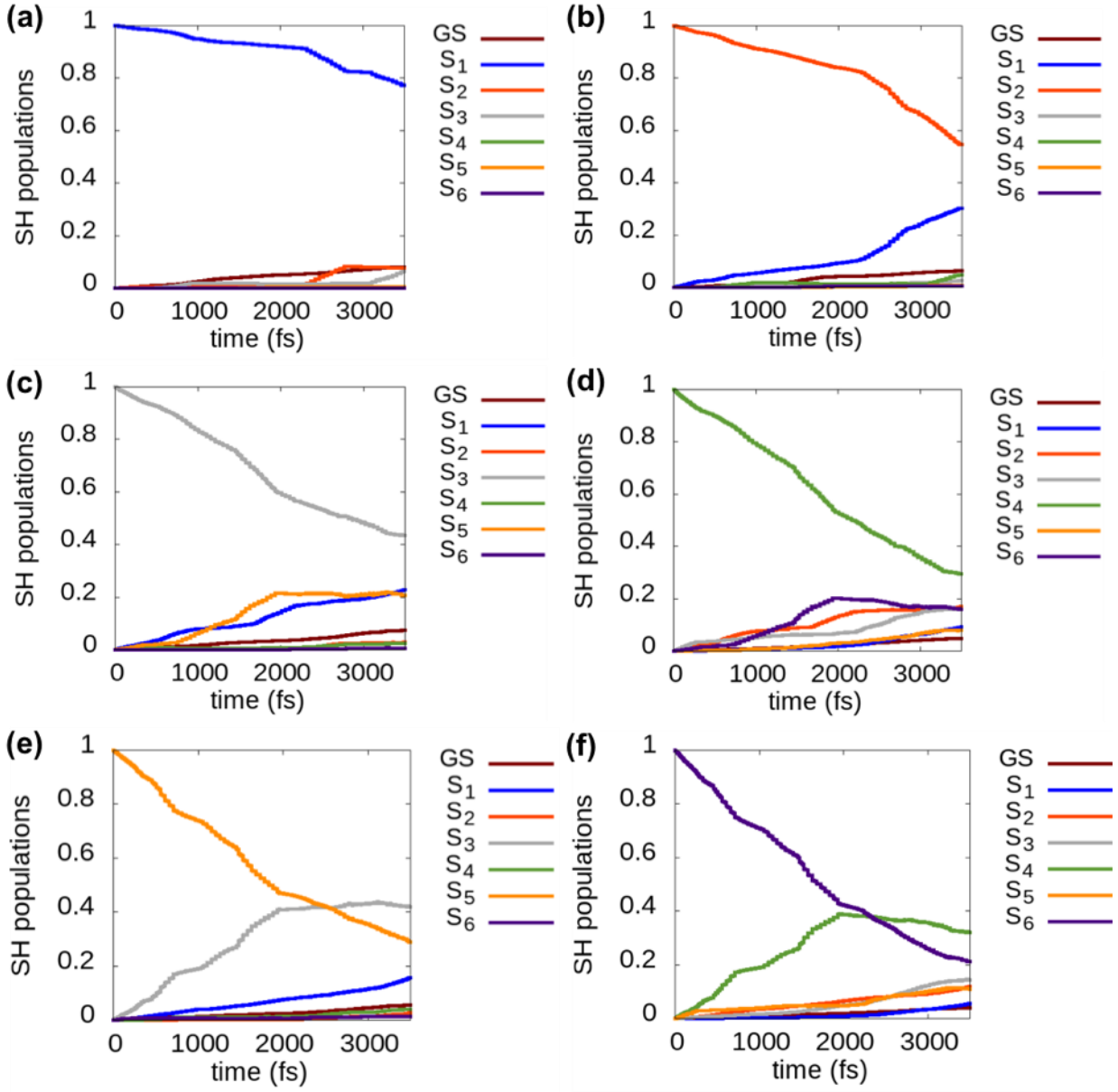

Figure 3-4 Evolution of populations of (a) S_1, (b) S_2, (c) S_3, (d) S_4, (e) S_5, (f) S_6 states for $[Au_{24}Ag(SH)_{18}]^{-1}$.

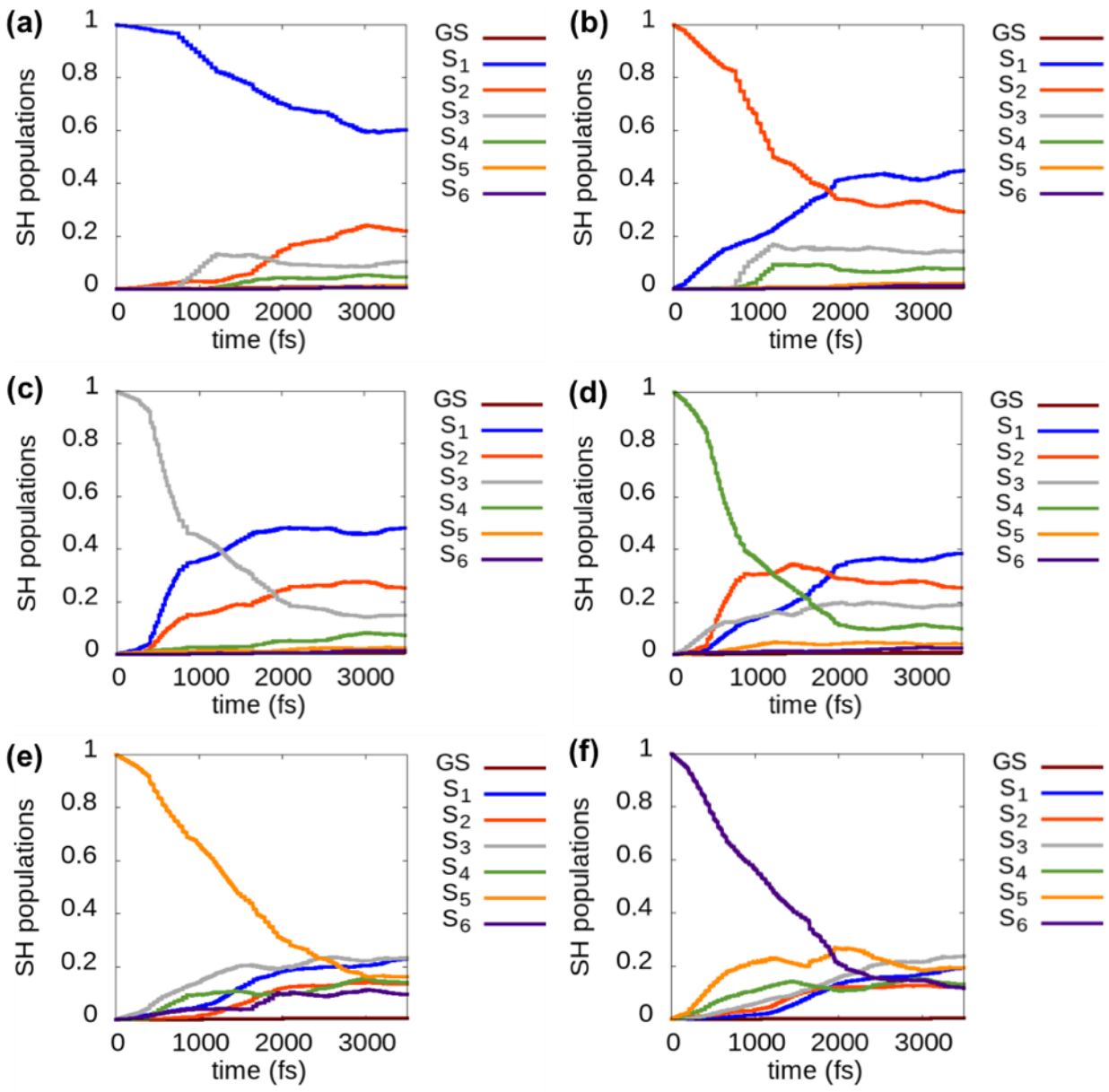

Figure 3-5 Evolution of populations of (a) S_1, (b) S_2, (c) S_3, (d) S_4, (e) S_5, (f) S_6 states for $[Au_{13}Ag_{12}(SH)_{18}]^{-1}$.

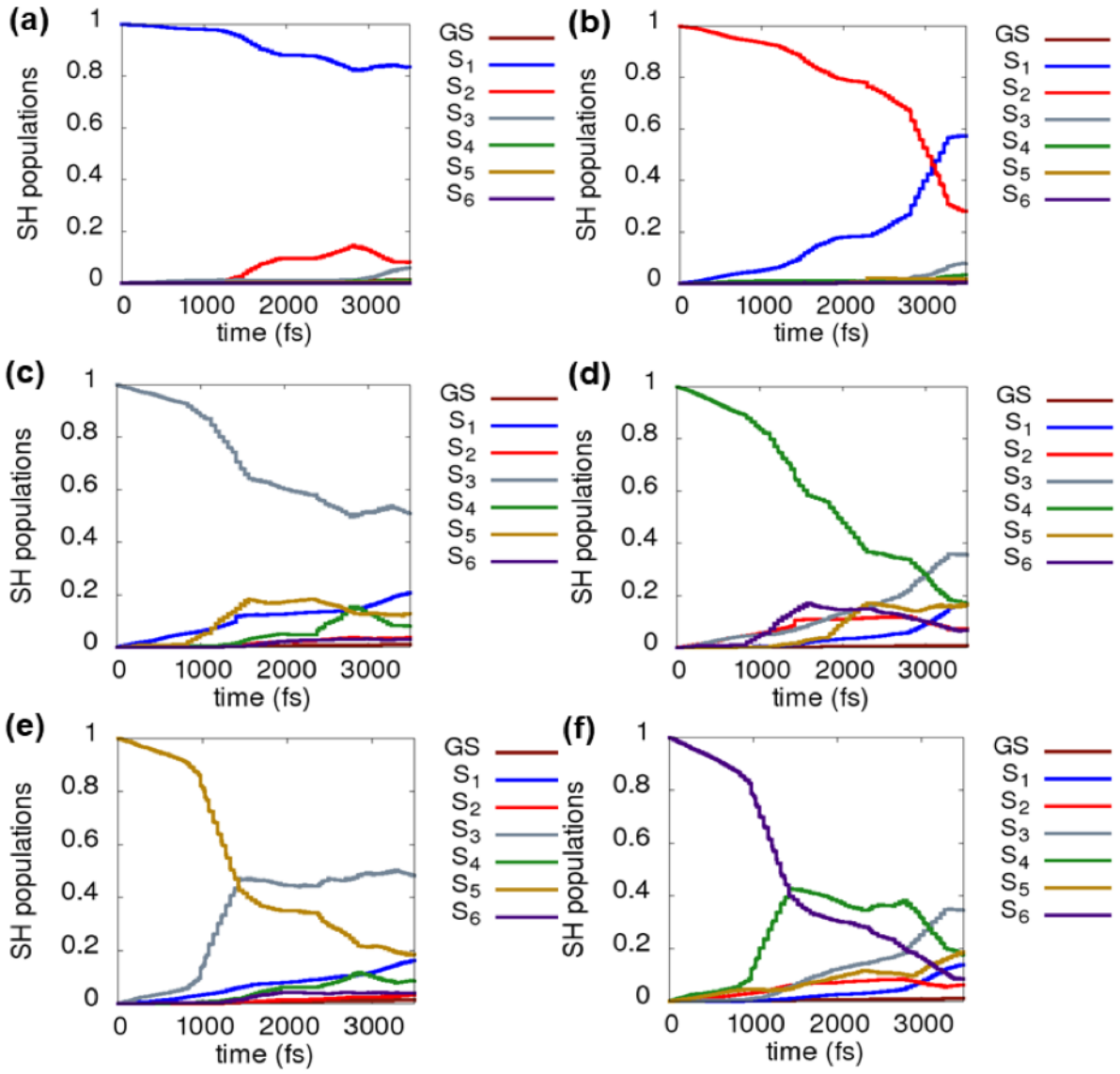

Figure 3-6 Evolution of populations of (a) S_1, (b) S_2, (c) S_3, (d) S_4, (e) S_5, (f) S_6 states for $[Ag_{25}(SH)_{18}]^{-1}$.

Table 3-5 Ground state population increase lifetimes after excitation to the first six excited states that contribute to the first peak in the optical absorption spectrum

Excited State	GS growth time (ps)			
	$[Au_{25}(SH)_{18}]^{-1}$ (Ref 27)	$[Au_{24}Ag(SH)_{18}]^{-1}$	$[Au_{13}Ag_{12}(SH)_{18}]^{-1}$	$[Ag_{25}(SH)_{18}]^{-1}$
S_1	73	40	313	251
S_2	71	56	389	317

S_3	81	51	370	334
S_4	120	80	383	411
S_5	96	72	578	270
S_6	158	97	795	371

Table 3-6 Decay times of the excited state population of the six excited states contributing to the first peak in the optical absorption spectrum

Excited State	Excited state decay time (ps)			
	$[Au_{25}(SH)_{18}]^{-1}$ (Ref 27)	$[Au_{24}Ag(SH)_{18}]^{-1}$	$[Au_{13}Ag_{12}(SH)_{18}]^{-1}$	$[Ag_{25}(SH)_{18}]^{-1}$
S_1	15.0	18.0	6.5	18.0
S_2	3.2	9.1	2.2	6.1
S_3	3.0	4.4	1.5	4.6
S_4	1.9	3.4	1.1	2.8
S_5	2.6	2.9	1.9	2.2
S_6	1.9	2.5	1.6	2.0

In all nanoclusters, a general trend appears: a higher initial excitation leads to a slower repopulation of the ground state due to the gap between that state and the GS. One exception occurs in S_4 of Ag_{25} because the S_4 ground state growth time is longer compared to that of S_6. A high initial excitation implies the existence of a large number of intermediate states which typically leads to a longer ground state recovery time. However, in Ag_{25} the unexpected longer ground state growth time of S_4 may be explained because there is a close energetic proximity between the S_4 and S_6 states of Ag_{25} (based on energy differences from Figure 3-3(c)) unlike in $Au_{24}Ag$ and $Au_{13}Ag_{12}$ (Figure 3-3(a) and 3-3(b)). Thus, S_4 state can transfer its population to higher states S_6 and S_5 before relaxing into lower states (Figure 3-6(d)), which could slow down the repopulation of the GS. Overall, the orbitals in Ag_{25} and $Au_{13}Ag_{12}$ are closer in energy than in Au_{25} (Ref [27]) and $Au_{24}Ag$ clusters. Because of this, there can be rapid population transfers between the nanocluster core states in Ag_{25} and $Au_{13}Ag_{12}$ compared to Au_{25} and $Au_{24}Ag$, which makes the repopulation of the GS harder for the latter two systems. For example, S_1 state population transfers into the S_2 state

and then the S_2 population is transferred back to the S_1 much faster in Ag_{25} than in $Au_{24}Ag$ (Figures 4 and 6). Overall, relaxation friction caused by the intermediate states affects the overall excited state relaxation dynamics and GS repopulation times.

Returning to the decay times of the excited state populations, these decay times increase slightly with the doping of a single silver atom into Au_{25} but decrease more significantly upon doping of 12 silver atoms (Table 3-6) compared to the decay times of Au_{25}. The excited state populations in $Au_{13}Ag_{12}$ (Figure 3-5) relax faster compared to the population relaxations in $Au_{24}Ag$ (Figure 3-4). The decay times of Ag_{25} (Figure 3-6) are similar to the decay times of $Au_{24}Ag$. On examining Table 3-5 and Table 3-6, it can be seen that the decay times of the excited state population are ultrafast despite the slow ground state repopulation dynamics. For example, the ground state repopulation times after excitation of S_1 are much larger than the decay times for the S_1 state for all three clusters (40 ps vs. 18 ps for $Au_{24}Ag$, 313 ps vs. 6.5 ps for $Au_{13}Ag_{12}$, and 251 ps vs. 18 ps for Ag_{25}). Again, this occurs because the intermediate states play an important role in the decay dynamics. From Figure 3-4, we can see in the case of $Au_{24}Ag$ that the S_1 state population transfers to the S_2 state much faster than the population transfers to the ground state. In the case of $Au_{13}Ag_{12}$ (Figure 3-5), S_1 state population transfers to the S_2, S_3, S_4 and S_5 states much faster than the population transfers to the ground state. Similarly, S_1 population transfer to S_2 and S_3 states is much faster in Ag_{25} than the population transfer to the ground state (Figure 3-6). This population transfer to the intermediate states may assist in causing longer ground state repopulation times compared to the decay time of each excited state population. Similarly, it is evident that as the population goes to a larger number of intermediate states, the time it takes to return to the ground state becomes longer.

Figure 3-7 displays how the decay time constant trend varies among the first six states for these clusters. Au_{25}, $Au_{24}Ag$, and Ag_{25} generally follow a similar trend among the first six states. However, the Ag_{25} and $Au_{24}Ag$ decay times are slightly slower than the decay times of Au_{25}. The decay times of $Au_{13}Ag_{12}$ are the fastest out of these four systems.

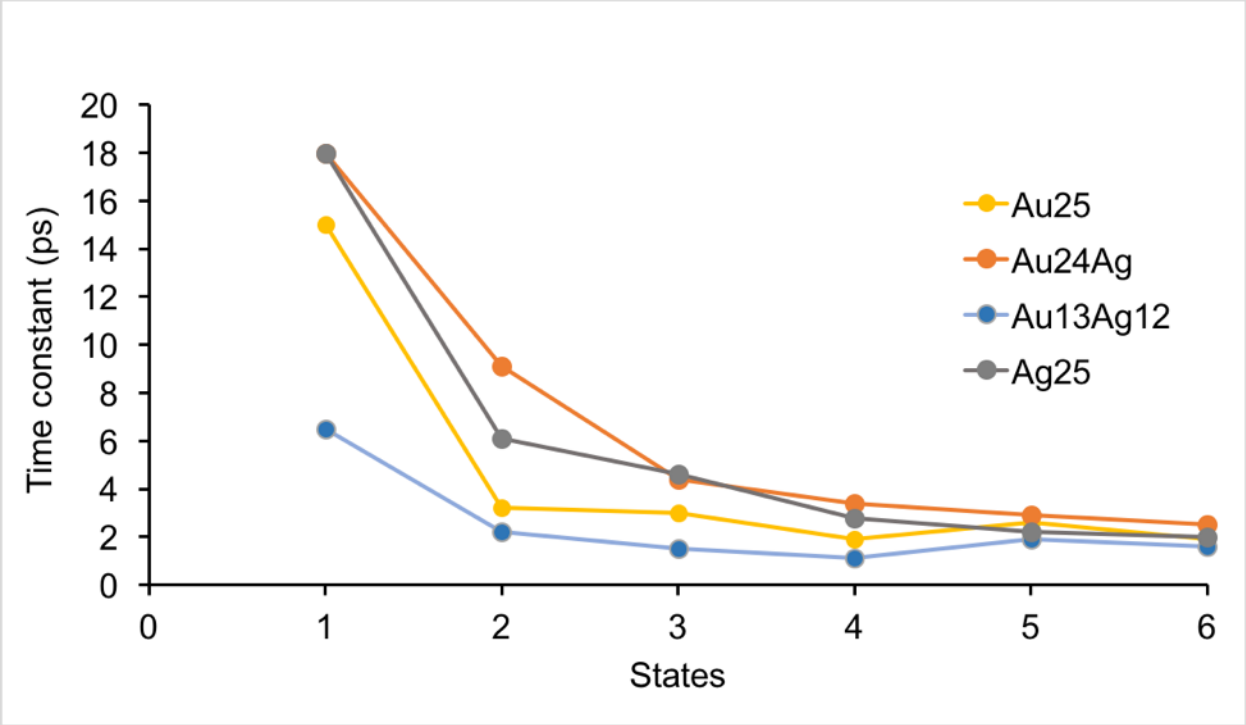

Figure 3-7 The decay time constants arising from excitation into the first six excited states for $[Au_{25}(SH)_{18}]^{-1}$, $[Au_{24}Ag(SH)_{18}]^{-1}$, $[Au_{13}Ag_{12}(SH)_{18}]^{-1}$ and $[Ag_{25}(SH)_{18}]^{-1}$.

3.4.3 Electronic relaxation dynamics of higher excited states

In this section, the relaxation dynamics of the higher excited states will be analyzed. Eighty, eighteen and forty-two higher excited states were included in the calculations for $Au_{24}Ag$, $Au_{12}Ag_{13}$, and Ag_{25} respectively which account for peaks up to ~2.5 eV in energy. The HOMO-9 to LUMO+7, HOMO-2 to LUMO+5 and HOMO-6 to LUMO+5 orbitals are the orbitals involved in the most probable transitions for the $Au_{24}Ag$, $Au_{12}Ag_{13}$, and Ag_{25} systems respectively based on their high oscillator strengths and transition dipole moments (Tables A-3, A-4, A-5). Hence, all

possible single particle transitions were considered for those orbitals in the FSSH-TDKS calculations (Tables A-6, A-7, A-8). S_1–S_6 have the same definitions as stated above and in our previous Au_{25} study.[27] Other possible transitions for higher excited states of $[Au_{24}Ag(SR)_{18}]^{-1}$ and $[Au_{13}Ag_{12}(SR)_{18}]^{-1}$ are assigned accordingly. Overall, the population relaxation of the S_1 to S_6 states for these clusters show similar relaxation patterns with only minor changes when additional states are included in the calculation (Figures S4-S6).

The S_1 state has the slowest decay time constant out of all the states considered in this study. The S_1 decay was calculated to have time constants of 19.2 ps, 6.6 ps and 17.0 ps for $Au_{24}Ag$ (Table A-9), $Au_{13}Ag_{12}$ (Table 3-7) and Ag_{25} (Table A-10) respectively with the inclusion of additional higher states, which are very close to the values of 18.0 ps, 6.5 ps, and 18.0 ps found during simulations that only considered the first six excited states (Table 3-6). The S_2-S_6 decay constant trends in the presence of higher states are also similar to the decay constant trends observed when only the S_1-S_6 states are considered. Overall, the decay time constants in the presence of higher excited states showed almost no difference to the decay time constants when only six states were considered.

Among the higher excited states, S_7 has a relatively long decay time both with and without an energy gap correction to the S_1−S_6 states. The S_7 decay times are calculated to be 15.5 ps, 5.6 ps, and 11.0 ps for $Au_{24}Ag$, $Au_{13}Ag_{12}$ and Ag_{25}, respectively (see Table A-9 for $Au_{24}Ag$, Table 3-7 for $Au_{13}Ag_{12}$, and Table A-10 for Ag_{25}), which are similar to the S_7 decay time of 9.9 ps for Au_{25}.[27] The longer lifetimes in S_7 compared to the other higher states are likely due to the large energy gap between the S_7 and S_6 states in all of these systems which makes population transfer difficult between these two states. The gap between the LUMO+1 and LUMO+2 orbitals results in the energy gap between the S_6 and S_7. In general, the higher excited states have much faster

decay times than the lower energy states. Overall, the decay time constant trend in all clusters is similar to Au_{25}. Similar electronic structures in these nanoclusters result in similar relaxation dynamics.

Table 3-7 The decay times of the excited state population of S_1 to S_{18} states in the presence of higher excited states for $[Au_{13}Ag_{12}(SH)_{18}]^{-1}$

Excited state	Decay time (ps)
S_1	6.6
S_2	2.4
S_3	1.5
S_4	1.2
S_5	2.3
S_6	1.6
S_7	5.6
S_8	1.8
S_9	1.3
S_{10}	2.1
S_{11}	1.4
S_{12}	0.9
S_{13}	0.8
S_{14}	1.3
S_{15}	1.7
S_{16}	1.1
S_{17}	1.0
S_{18}	1.6

3.5 Conclusion

The electron-nuclear dynamics of the $[Au_{24}Ag(SH)_{18}]^{-1}$, $[Au_{13}Ag_{12}(SH)_{18}]^{-1}$ and $[Ag_{25}(SH)_{18}]^{-1}$ thiolate-protected nanoparticles have been investigated using the FSSH-TDKS approach. The electron-nuclear relaxation dynamics of the nanoclusters have been compared with the relaxations of their gold analog, the well-known $[Au_{25}(SH)_{18}]^{-1}$ nanocluster. The HOMO-LUMO gap increases significantly upon doping 12 silver atoms into the gold cluster. However, the gap decreases a little for $Au_{24}Ag$ and Ag_{25} compared to that of Au_{25}. The first peak in each

absorption spectrum is blue-shifted compared to that of Au_{25}; the highest energy first peak is found for $Au_{13}Ag_{12}$ at ~1.9 eV.

The nonradiative relaxation dynamics are affected by the doping of silver atoms. Ultrafast relaxation time constants in the range of 2.0-20.0 ps were observed for the S_1−S_6 excited state population decays. These fast decay time constants are observed for the S_1−S_6 states because population can transfer to other excited states in addition to the GS. The excited state population decays fastest upon doping of 12 silver atoms compared to the time constants of other clusters. This could be due to the presence of other intermediate states in $Au_{13}Ag_{12}$ that are close in energy. Nevertheless, these clusters conserve similar trends in decay times among the first six excited states.

The time scales for the GS recovery were found to be larger than the relaxation time scales of the S_1−S_6 excited states, which was also the case in $[Au_{25}(SH)_{18}]^{-1}$. The ground state population recovery lifetime is shorter for $Au_{24}Ag$ and longer for $Au_{13}Ag_{12}$ compared to the time constants of Au_{25}. Again, this could be due to the population being transferred to other intermediate states in $Au_{13}Ag_{12}$. The GS recovery times are slower for the S_2-S_6 states compared to S_1, suggesting recovery of the GS population is hindered by the effective "friction" due to the presence of intermediate electronic states. The GS recovery times of the S_1-S_6 states for Ag_{25} were found to be longer than the corresponding GS recovery times of Au_{25} and $Au_{24}Ag$. Addition of an energy correction to the energy gaps did not greatly affect the excited state decay times although it did increase the GS recovery times.

The relaxation dynamics of higher excited states with energy up to ~2.5 eV preserved the relaxation trends observed for the S_1−S_6 states. Among the higher excited states, S_7 has a

comparatively long decay time. The energy gap between the S_6 and S_7 states may result in the relatively long S_7 decay, although the decay is faster than the decay from the S_1 state.

In general, the basic physics and qualitative insights for all four clusters are similar. They each follow a relaxation mechanism equivalent to the $[Au_{25}(SH)_{18}]^{-1}$ nanocluster where no states involving orbitals based on the staple motifs are observed at lower energy than the nanocluster core-based S_1 state; thus, electron dynamics in the lowest excited states occurs primarily in the cluster core. Decay time constant trends in these clusters are also similar to the Au_{25} nanocluster. However, doping of the nanoclusters does affect the quantitative values of the decay times, suggesting that doping represents a feasible and controllable method to tune nonradiative dynamics in nanoclusters. In this study, $Au_{13}Ag_{12}$ has the fastest excited state dynamics and the slowest decay of excited state population back to the ground state, suggesting that it may be the best candidate for solar cell sensitizers out of the four clusters examined here.

3.6 Acknowledgements

This material is based on work supported by National Science Foundation under grant CHE-1507909 and by the Department of Energy under grant DE-SC0012273. The computing for this project was performed on the Beocat Research Cluster at Kansas State University, which is funded in part by NSF grants CHE-1726332, CNS-1006860, EPS-1006860, and EPS-0919443 and Extreme Science and Engineering Discovery Environment (XSEDE),[79] which is supported by National Science Foundation grant number ACI-1053575. Beocat Application Scientist Dr. Dave Turner provided valuable technical expertise. The authors are grateful to Prof. Alexey V. Akimov for his support and valuable discussions on PYXAID.

3.7 Dedication

This paper is dedicated to Prof. Patricia Thiel for her kind mentorship of C.M.A. in the Preparing Future Faculty program at Iowa State University. Prof. Thiel was an excellent surface scientist and role model who contributed substantially to the physical chemistry community.

3.8 References

1. Jin, R., Atomically Precise Metal Nanoclusters: Stable Sizes and Optical Properties. Nanoscale **2015,** 7 (5), 1549-1565.

2. Valden, M.; Lai, X.; Goodman, D. W., Onset of Catalytic Activity of Gold Clusters on Titania with the Appearance of Nonmetallic Properties. Science **1998,** 281 (5383), 1647-1650.

3. Zhu, Y.; Qian, H.; Drake, B. A.; Jin, R., Atomically Precise $Au_{25}(SR)_{18}$ Nanoparticles as Catalysts for the Selective Hydrogenation of α,β-Unsaturated Ketones and Aldehydes. Angew. Chem. Int. Ed. **2010,** 49 (7), 1295-1298.

4. Ramakrishna, G.; Varnavski, O.; Kim, J.; Lee, D.; Goodson, T., Quantum-Sized Gold Clusters as Efficient Two-Photon Absorbers. J. Am. Chem. Soc. **2008,** 130 (15), 5032-5033.

5. Ramakrishna, G.; Varnavski, O.; Kim, J.; Lee, D.; Goodson, T. In Nonlinear Optical Properties of Quantum Sized Gold Clusters, Photonic Devices + Applications, SPIE: 2008; p 12.

6. Stamplecoskie, K. G.; Kamat, P. V., Size-Dependent Excited State Behavior of Glutathione-Capped Gold Clusters and Their Light-Harvesting Capacity. J. Am. Chem. Soc. **2014,** 136 (31), 11093-11099.

7. Chen, Y.-S.; Choi, H.; Kamat, P. V., Metal-Cluster-Sensitized Solar Cells. A New Class of Thiolated Gold Sensitizers Delivering Efficiency Greater Than 2%. J. Am. Chem. Soc. **2013,** 135 (24), 8822-8825.

8. Kogo, A.; Sakai, N.; Tatsuma, T., Photocatalysis of Au_{25}-Modified TiO_2 Under Visible and Near Infrared Light. Electrochem. Commun. **2010,** 12 (7), 996-999.

9. Kogo, A.; Sakai, N.; Tatsuma, T., Photoelectrochemical Analysis of Size-dependent Electronic Structures of Gold Clusters Supported on TiO_2. Nanoscale **2012,** 4 (14), 4217-4221.

10. Yu, C.; Li, G.; Kumar, S.; Kawasaki, H.; Jin, R., Stable $Au_{25}(SR)_{18}/TiO_2$ Composite Nanostructure with Enhanced Visible Light Photocatalytic Activity. J. Phys. Chem. Lett. **2013,** 4 (17), 2847-2852.

11. Subramanian, V.; Wolf, E. E.; Kamat, P. V., Catalysis with TiO_2/Gold Nanocomposites. Effect of Metal Particle Size on the Fermi Level Equilibration. J. Am. Chem. Soc. **2004,** 126 (15), 4943-4950.

12. Qian, K.; Sweeny, B. C.; Johnston-Peck, A. C.; Niu, W.; Graham, J. O.; DuChene, J. S.; Qiu, J.; Wang, Y.-C.; Engelhard, M. H.; Su, D., Surface Plasmon-Driven Water Reduction: Gold Nanoparticle Size Matters. J. Am. Chem. Soc. **2014,** 136 (28), 9842-9845.

13. Gomes Silva, C. u.; Juárez, R.; Marino, T.; Molinari, R.; García, H., Influence of Excitation Wavelength (UV or Visible Light) on the Photocatalytic Activity of Titania Containing Gold Nanoparticles for the Generation of Hydrogen or Oxygen from Water. J. Am. Chem. Soc. **2010,** 133 (3), 595-602.

14. Primo, A.; Marino, T.; Corma, A.; Molinari, R.; Garcia, H., Efficient Visible-Light Photocatalytic Water Splitting by Minute Amounts of Gold Supported on Nanoparticulate CeO_2 Obtained by a Biopolymer Templating Method. J. Am. Chem. Soc. **2011,** 133 (18), 6930-6933.

15. Stamplecoskie, K. G.; Chen, Y.-S.; Kamat, P. V., Excited-state Behavior of Luminescent Glutathione-Protected Gold Clusters. J. Phys. Chem. C **2014,** 118 (2), 1370-1376.

16. Link, S.; El-Sayed, M. A.; Schaaff, T. G.; Whetten, R. L., Transition from Nanoparticle to Molecular Behavior: a Femtosecond Transient Absorption Study of a Size-Selected 28 Atom Gold Cluster. Chem. Phys. Lett. **2002,** 356 (3-4), 240-246.

17. Miller, S. A.; Womick, J. M.; Parker, J. F.; Murray, R. W.; Moran, A. M., Femtosecond Relaxation Dynamics of $Au_{25}L_{18}^-$ Monolayer-protected Clusters. J. Phys. Chem. C **2009,** 113 (22), 9440-9444.

18. Lee, D.; Donkers, R. L.; Wang, G.; Harper, A. S.; Murray, R. W., Electrochemistry and Optical Absorbance and Luminescence of Molecule-like Au_{38} Nanoparticles. J. Am. Chem. Soc. **2004,** 126 (19), 6193-6199.

19. Devadas, M. S.; Kim, J.; Sinn, E.; Lee, D.; Goodson III, T.; Ramakrishna, G., Unique Ultrafast Visible Luminescence in Monolayer-Protected Au_{25} Clusters. J. Phys. Chem. C **2010,** 114 (51), 22417-22423.

20. Green, T. D.; Knappenberger, K. L., Relaxation Dynamics of $Au_{25}L_{18}$ Nanoclusters Studied by Femtosecond Time-resolved Near Infrared Transient Absorption Spectroscopy. Nanoscale **2012,** 4 (14), 4111-4118.

21. Yau, S. H.; Varnavski, O.; Goodson III, T., An Ultrafast Look at Au Nanoclusters. Acc. Chem. Res. **2013,** 46 (7), 1506-1516.

22. Stoll, T.; Sgrò, E.; Jarrett, J. W.; Réhault, J.; Oriana, A.; Sala, L.; Branchi, F.; Cerullo, G.; Knappenberger Jr, K. L., Superatom State-Resolved Dynamics of the $Au_{25}(SC_8H_9)_{18}^-$ Cluster from Two-dimensional Electronic Spectroscopy. J. Am. Chem. Soc. **2016,** 138 (6), 1788-1791.

23. Zhou, M.; Tian, S.; Zeng, C.; Sfeir, M. Y.; Wu, Z.; Jin, R., Ultrafast Relaxation Dynamics of $Au_{38}(SC_2H_4Ph)_{24}$ Nanoclusters and Effects of Structural Isomerism. J. Phys. Chem. C **2017,** 121 (20), 10686-10693.

24. Zhou, M.; Zhong, J.; Wang, S.; Guo, Q.; Zhu, M.; Pei, Y.; Xia, A., Ultrafast Relaxation Dynamics of Luminescent Rod-Shaped, Silver-Doped Ag_xAu_{25-x} Clusters. J. Phys. Chem. C **2015,** 119 (32), 18790-18797.

25. Sfeir, M. Y.; Qian, H.; Nobusada, K.; Jin, R., Ultrafast Relaxation Dynamics of Rod-Shaped 25-Atom Gold Nanoclusters. J. Phys. Chem. C **2011,** 115 (14), 6200-6207.

26. Chen, X.; Prezhdo, O. V.; Ma, Z.; Hou, T.; Guo, Z.; Li, Y., Ab initio Phonon-coupled Nonadiabatic Relaxation Dynamics of $[Au_{25}(SH)_{18}]^-$ Clusters. Phys. Status Solidi B **2016,** 253 (3), 458-462.

27. Senanayake, R. D.; Akimov, A. V.; Aikens, C. M., Theoretical Investigation of Electron and Nuclear Dynamics in the $[Au_{25}(SH)_{18}]^{-1}$ Thiolate-Protected Gold Nanocluster. J. Phys. Chem. C **2016,** 121 (20), 10653-10662.

28. Senanayake, R. D.; Aikens, C. M., Electronic Relaxation Dynamics in $[Au_{25}(SR)_{18}]^{-1}$ (R = CH_3, C_2H_5, C_3H_7, MPA, PET) Thiolate-Protected Nanoclusters. Phys. Chem. Chem. Phys. **2020,** 22 (9), 5272-5285.

29. Senanayake, R. D.; Aikens, C. M., Theoretical Investigation of Relaxation Dynamics in the $Au_{18}(SH)_{14}$ Thiolate-Protected Gold Nanocluster. J. Chem. Phys. **2019,** 151 (9), 094702.

30. Senanayake, R. D.; Guidez, E. B.; Neukirch, A. J.; Prezhdo, O. V.; Aikens, C. M., Theoretical Investigation of Relaxation Dynamics in $Au_{38}(SH)_{24}$ Thiolate-Protected Gold Nanoclusters. J. Phys. Chem. C **2018,** 122 (28), 16380-16388.

31. Kang, X.; Chong, H.; Zhu, M., $Au_{25}(SR)_{18}$: the Captain of the Great Nanocluster Ship. Nanoscale **2018,** 10 (23), 10758-10834.

32. Zhu, M.; Aikens, C. M.; Hendrich, M. P.; Gupta, R.; Qian, H.; Schatz, G. C.; Jin, R., Reversible Switching of Magnetism in Thiolate-Protected Au25 Superatoms. J. Am. Chem. Soc. **2009,** 131 (7), 2490-2492.

33. Zhu, M.; Aikens, C. M.; Hollander, F. J.; Schatz, G. C.; Jin, R., Correlating the Crystal Structure of a Thiol-protected Au_{25} Cluster and Optical Properties. J. Am. Chem. Soc. **2008,** 130 (18), 5883-5885.

34. Wu, Z.; Jin, R., Stability of the Two Au−S Binding Modes in $Au_{25}(SG)_{18}$ Nanoclusters Probed by NMR and Optical Spectroscopy. ACS Nano **2009,** 3 (7), 2036-2042.

35. Negishi, Y.; Iwai, T.; Ide, M., Continuous Modulation of Electronic Structure of Stable Thiolate-Protected Au_{25} Cluster by Ag Doping. Chem. Commun. **2010,** 46 (26), 4713-4715.

36. Negishi, Y.; Chaki, N. K.; Shichibu, Y.; Whetten, R. L.; Tsukuda, T., Origin of Magic Stability of Thiolated Gold Clusters: A Case Study on $Au_{25}(SC_6H_{13})_{18}$. J. Am. Chem. Soc. **2007,** 129 (37), 11322-11323.

37. Shichibu, Y.; Negishi, Y.; Tsunoyama, H.; Kanehara, M.; Teranishi, T.; Tsukuda, T., Extremely High Stability of Glutathionate-Protected Au_{25} Clusters Against Core Etching. Small **2007,** 3 (5), 835-839.

38. Yan, N.; Liao, L.; Yuan, J.; Lin, Y.-j.; Weng, L.-h.; Yang, J.; Wu, Z., Bimetal Doping in Nanoclusters: Synergistic or Counteractive? Chem. Mater. **2016,** 28 (22), 8240-8247.

39. Guidez, E. B.; Mäkinen, V.; Häkkinen, H.; Aikens, C. M., Effects of Silver Doping on the Geometric and Electronic Structure and Optical Absorption Spectra of the $Au_{25-n}Ag_n(SH)_{18}^-$ (n = 1, 2, 4, 6, 8, 10, 12) Bimetallic Nanoclusters. J. Phys. Chem. C **2012,** 116 (38), 20617-20624.

40. Krishnadas, K. R.; Baksi, A.; Ghosh, A.; Natarajan, G.; Pradeep, T., Structure-Conserving Spontaneous Transformations Between Nanoparticles. Nat. Commun. **2016,** 7 (1), 13447.

41. Aikens, C. M., Origin of Discrete Optical Absorption Spectra of $M_{25}(SH)_{18}^-$ Nanoparticles (M= Au, Ag). J. Phys. Chem. C **2008,** 112 (50), 19797-19800.

42. Negishi, Y.; Nobusada, K.; Tsukuda, T., Glutathione-Protected Gold Clusters Revisited: Bridging the Gap Between Gold (I)− thiolate Complexes and Thiolate-protected Gold Nanocrystals. J. Am. Chem. Soc. **2005,** 127 (14), 5261-5270.

43. Lopez-Acevedo, O.; Tsunoyama, H.; Tsukuda, T.; Hakkinen, H.; Aikens, C. M., Chirality and Electronic Structure of the Thiolate-protected Au_{38} Nanocluster. J. Am. Chem. Soc. **2010,** 132 (23), 8210-8218.

44. Jadzinsky, P. D.; Calero, G.; Ackerson, C. J.; Bushnell, D. A.; Kornberg, R. D., Structure of a Thiol Monolayer-Protected Gold Nanoparticle at 1.1 Å Resolution. Science **2007,** 318 (5849), 430-433.

45. Zeng, C.; Chen, Y.; Kirschbaum, K.; Appavoo, K.; Sfeir, M. Y.; Jin, R., Structural Patterns at All Scales in a Nonmetallic Chiral $Au_{133}(SR)_{52}$ Nanoparticle. Sci. Adv. **2015,** 1 (2), e1500045.

46. Dass, A.; Theivendran, S.; Nimmala, P. R.; Kumara, C.; Jupally, V. R.; Fortunelli, A.; Sementa, L.; Barcaro, G.; Zuo, X.; Noll, B. C., $Au_{133}(SPh\text{-}t\ Bu)_{52}$ Nanomolecules: X-ray Crystallography, Optical, Electrochemical, and Theoretical Analysis. J. Am. Chem. Soc. **2015,** 137 (14), 4610-4613.

47. Hoque, M. M.; Mayer, K. M.; Ponce, A.; Alvarez, M. M.; Whetten, R. L., Toward Smaller Aqueous-Phase Plasmonic Gold Nanoparticles: High-Stability Thiolate-Protected ~4.5 nm Cores. Langmuir **2019,** 35 (32), 10610-10617.

48. Li, H.; Song, Y.; Lv, Y.; Yun, Y.; Lv, X.; Yu, H.; Zhu, M., Unexpected Observation of Heavy Monomeric Motifs in a Basket-like $Au_{26}Ag_{22}$ Nanocluster. Inorg. Chem. **2019,** 58 (3), 1724-1727.

49. Guan, Z.-J.; Hu, F.; Li, J.-J.; Liu, Z.-R.; Wang, Q.-M., Homoleptic Alkynyl-Protected Gold Nanoclusters with Unusual Compositions and Structures. Nanoscale **2020,** 12 (25), 13346-13350.

50. Narouz, M. R.; Takano, S.; Lummis, P. A.; Levchenko, T. I.; Nazemi, A.; Kaappa, S.; Malola, S.; Yousefalizadeh, G.; Calhoun, L. A.; Stamplecoskie, K. G.; Häkkinen, H.; Tsukuda, T.; Crudden, C. M., Robust, Highly Luminescent Au_{13} Superatoms Protected by N-Heterocyclic Carbenes. J. Am. Chem. Soc. **2019,** 141 (38), 14997-15002.

51. Desireddy, A.; Conn, B. E.; Guo, J.; Yoon, B.; Barnett, R. N.; Monahan, B. M.; Kirschbaum, K.; Griffith, W. P.; Whetten, R. L.; Landman, U., Ultrastable Silver Nanoparticles. Nature **2013,** 501 (7467), 399.

52. Yang, H.; Wang, Y.; Huang, H.; Gell, L.; Lehtovaara, L.; Malola, S.; Häkkinen, H.; Zheng, N., All-thiol-stabilized Ag_{44} and $Au_{12}Ag_{32}$ Nanoparticles with Single-crystal Structures. Nat. Commun. **2013,** 4, 2422.

53. Yang, H.; Wang, Y.; Zheng, N., Stabilizing Subnanometer Ag (0) Nanoclusters by Thiolate and Diphosphine Ligands and their Crystal structures. Nanoscale **2013,** 5 (7), 2674-2677.

54. AbdulHalim, L. G.; Bootharaju, M. S.; Tang, Q.; Del Gobbo, S.; AbdulHalim, R. G.; Eddaoudi, M.; Jiang, D.-e.; Bakr, O. M., $Ag_{29}(BDT)_{12}(TPP)_4$: A Tetravalent Nanocluster. J. Am. Chem. Soc. **2015,** 137 (37), 11970-11975.

55. Dhayal, R. S.; Liao, J. H.; Liu, Y. C.; Chiang, M. H.; Kahlal, S.; Saillard, J. Y.; Liu, C., $[Ag_{21}\{S_2P(OiPr)_2\}_{12}]^+$: An Eight-Electron Superatom. Angew. Chem. Int. Ed. **2015,** 54 (12), 3702-3706.

56. Yang, H.; Lei, J.; Wu, B.; Wang, Y.; Zhou, M.; Xia, A.; Zheng, L.; Zheng, N., Crystal Structure of a Luminescent Thiolated Ag Nanocluster with an Octahedral Ag_{64}^+ Core. Chem. Commun. **2013,** 49 (3), 300-302.

57. Dar, W. A.; Bodiuzzaman, M.; Ghosh, D.; Paramasivam, G.; Khatun, E.; Sugi, K. S.; Pradeep, T., Interparticle Reactions between Silver Nanoclusters Leading to Product Cocrystals by Selective Cocrystallization. ACS Nano **2019,** 13 (11), 13365-13373.

58. Liu, J.-Y.; Alkan, F.; Wang, Z.; Zhang, Z.-Y.; Kurmoo, M.; Yan, Z.; Zhao, Q.-Q.; Aikens, C. M.; Tung, C.-H.; Sun, D., Different Silver Nanoparticles in One Crystal: $Ag_{210}(^{i}PrPhS)_{71}(Ph_3P)_5Cl$ and $Ag_{211}(^{i}PrPhS)_{71}(Ph_3P)_6Cl$. Angew. Chem. Int. Ed. **2019,** 58 (1), 195-199.

59. Bodiuzzaman, M.; Ghosh, A.; Sugi, K. S.; Nag, A.; Khatun, E.; Varghese, B.; Paramasivam, G.; Antharjanam, S.; Natarajan, G.; Pradeep, T., Camouflaging Structural Diversity: Co-crystallization of Two Different Nanoparticles Having Different Cores But the Same Shell. Angew. Chem. Int. Ed. **2019,** 58 (1), 189-194.

60. Bakr, O. M.; Amendola, V.; Aikens, C. M.; Wenseleers, W.; Li, R.; Dal Negro, L.; Schatz, G. C.; Stellacci, F., Silver Nanoparticles with Broad Multiband Linear Optical Absorption. Angew. Chem. **2009,** 121 (32), 6035-6040.

61. Joshi, C. P.; Bootharaju, M. S.; Alhilaly, M. J.; Bakr, O. M., $[Ag_{25}(SR)_{18}]^{-}$: The "golden" Silver Nanoparticle. J. Am. Chem. Soc. **2015,** 137 (36), 11578-11581.

62. Jin, R.; Zhao, S.; Liu, C.; Zhou, M.; Panapitiya, G.; Xing, Y.; Rosi, N. L.; Lewis, J. P.; Jin, R., Controlling Ag-doping in $[Ag_xAu_{25-x}(SC_6H_{11})_{18}]^{-}$ Nanoclusters: Cryogenic Optical, Electronic and Electrocatalytic Properties. Nanoscale **2017,** 9 (48), 19183-19190.

63. Yuan, Q.; Kang, X.; Hu, D.; Qin, C.; Wang, S.; Zhu, M., Metal Synergistic Efect on Cluster Optical Properties: Based on Ag_{25} Series Nanoclusters. Dalton Trans. **2019,** 48 (35), 13190-13196.

64. Bootharaju, M. S.; Joshi, C. P.; Parida, M. R.; Mohammed, O. F.; Bakr, O. M., Templated Atom-Precise Galvanic Synthesis and Structure Elucidation of a $[Ag_{24}Au(SR)_{18}]^{-}$ Nanocluster. Angew. Chem. Int. Ed. **2016,** 55 (3), 922-926.

65. Weerawardene, K. L. D. M.; Aikens, C. M., Origin of Photoluminescence of $Ag_{25}(SR)_{18}^{-}$ Nanoparticles: Ligand and Doping Effect. J. Phys. Chem. C **2018,** 122 (4), 2440-2447.

66. Te Velde, G. t.; Bickelhaupt, F. M.; Baerends, E. J.; Fonseca Guerra, C.; van Gisbergen, S. J.; Snijders, J. G.; Ziegler, T., Chemistry with ADF. J. Comput. Chem. **2001,** 22 (9), 931-967.

67. Perdew, J. P.; Burke, K.; Ernzerhof, M., Generalized Gradient Approximation Made Simple. Phys. Rev. Lett. **1996,** 77 (18), 3865.

68. Lenthe, E. v.; Baerends, E.-J.; Snijders, J. G., Relativistic Regular Two-Component Hamiltonians. J. Chem. Phys. **1993,** 99 (6), 4597-4610.

69. van Lenthe, E.; Snijders, J. G.; Baerends, E. J., The Zero-Order Regular Approximation for Relativistic Effects: The Effect of Spin–Orbit Coupling in Closed Shell Molecules. J. Chem. Phys. **1996,** 105 (15), 6505-6516.

70. van Lenthe, E.; Baerends, E. J.; Snijders, J. G., Relativistic Total Energy Using Regular Approximations. J. Chem. Phys. **1994,** 101 (11), 9783-9792.

71. Kresse, G.; Furthmüller, J., Efficiency of Ab-initio Total Energy Calculations for Metals and Semiconductors using a Plane-wave Basis Set. Comput. Mater. Sci. **1996,** 6 (1), 15-50.

72. Verlet, L., Computer "Experiments" on Classical Fluids. I. Thermodynamical Properties of Lennard-Jones Molecules. Phys. Rev. **1967,** 159 (1), 98-103.

73. Kresse, G.; Joubert, D., From Ultrasoft Pseudopotentials to the Projector Augmented-wave Method. Phys. Rev. B **1999,** 59 (3), 1758.

74. Hammes-Schiffer, S.; Tully, J. C., Proton Transfer in Solution: Molecular Dynamics with Quantum Transitions. J. Chem. Phys. **1994,** 101 (6), 4657-4667.

75. Craig, C. F.; Duncan, W. R.; Prezhdo, O. V., Trajectory Surface hopping in the Time-dependent Kohn-Sham Approach for electron-nuclear Dynamics. Phys. Rev. Lett. **2005,** 95 (16), 163001.

76. Jaeger, H. M.; Fischer, S.; Prezhdo, O. V., Decoherence-Induced Surface Hopping. J. Chem. Phys. **2012,** 137 (22), 22A545.

77. Akimov, A. V.; Prezhdo, O. V., The PYXAID Program For Non-adiabatic Molecular Dynamics in Condensed Matter Systems. J. Chem. Theory Comput. **2013,** 9 (11), 4959-4972.

78. Akimov, A. V.; Prezhdo, O. V., Advanced Capabilities of the PYXAID Program: Integration Schemes, Decoherence Effects, Multiexcitonic States, and Field-Matter Interaction. J. Chem. Theory Comput. **2014,** 10 (2), 789-804.

79. Towns, J.; Cockerill, T.; Dahan, M.; Foster, I.; Gaither, K.; Grimshaw, A.; Hazlewood, V.; Lathrop, S.; Lifka, D.; Peterson, G. D.; Roskies, R.; Scott, J. R.; Wilkins-Diehr, N., XSEDE: Accelerating Scientific Discovery. Computing in Science & Engineering **2014,** 16 (5), 62-74.

Chapter 4 - Theoretical study of radiative and nonradiative relaxation of excited electrons in $Au_{20}(SCH_3)_{16}$

4.1 Abstract

In this work, we study the absorption and emission spectra of the $Au_{20}(SCH_3)_{16}$ nanocluster. Two structures of $Au_{20}(SR)_{16}$ have been proposed that differ in having an octameric ring or a hexameric ring. Using density functional theory, we have first compared the two structures and determined that the structure with an octameric ring is the lowest energy structure. We have investigated the origin of the experimentally observed luminescence in the nanocluster. The experimentally observed luminescence matches with the luminescence from S_6 without considering the underestimation from GGA functionals. Upon considering the underestimation, S_2 luminescence also matches the experimental luminescence. We have analyzed the electronic structure and the geometrical changes in the excited states. The ring and the trimeric staple motif of the cluster are found to have the most geometrical distortion upon optimization of these states. The core and other staple motifs do not become significantly distorted in the excited states. We also examined the nonradiative electron relaxation from higher excited states. During the nonradiative relaxation, a stepwise electron relaxation mechanism is observed after an initial hole relaxation. Electron relaxation from the S_1 state has the longest decay time constant due to a large gap between the HOMO and LUMO orbitals.

4.2 Introduction

Gold nanoclusters have received significant attention due to their unique optical properties.[1-3] Luminescent gold nanoparticles have found applications in various fields including catalysis,[4] sensing,[5] and medicine.[6] Luminescence from gold nanoclusters is found to depend on the size, composition and on the ligands of the nanoclusters.[5, 7-22] Some gold nanoclusters have high quantum yields; Pyo et al. prepared a folate-functionalized Au_{22} cluster that exhibited a luminescence quantum yield of 42%.[20] This cluster was prepared by the surface functionalization of $Au_{22}(SG)_{18}$ (SG=glutathione). Because the luminescence from nanoclusters is dependent on various factors that determine its potential applications, it is very important to understand the radiative and nonradiative relaxation of excited electrons in nanoclusters. Understanding of the relaxation mechanism in the nanoclusters will be helpful to find an appropriate cluster for a given application involving excited electrons. In a study by Chen et al., gold nanoclusters are found to enhance photocatalytic yields upon visible light irradiation and can be used as sensitizers in a solar cell.[23] Thus, studies of the relaxation of excited electrons will help determine the applicability of the cluster as a solar cell sensitizer by finding out the origin of its photo-enhancement.

Various studies of the radiative and nonradiative relaxation of excited electrons in gold nanoclusters have been performed.[24-29] Green et al. found the non-radiative core-to-ligand energy transfer process as a dominant electron relaxation mechanism in $[Au_{25}(SR)_{18}]^-$ and $[Au_{25}(SR)_{18}]^0$.[25] Later, Senanayake et al. performed a theoretical study on $[Au_{25}(SH)_{18}]^-$ to find that the experimentally observed time constants in the picoseconds range could arise from core-to-core transitions rather than from a core-to-semiring transition.[27] Similarly, Weerawardene et al.[30] found that the core-based orbitals in $[Au_{25}(SR)_{18}]^-$ (R = H, CH_3,C_2H_5, and C_3H_7) are involved

in the experimentally observed emission rather than the charge transfer states[31] and ligand based states.[32]

The Au_{20} dimer connected by diglyme ligands ($Au_{20}(SC_2H_4Ph)_{15}$-diglyme-$Au_{20}(SC_2H_4Ph)_{15}$) is found to have strong visible photoluminescence which is absent for the monomer.[22, 33] In order to investigate this interesting property, herein we initially study the radiative and nonradiative relaxation mechanism of excited electrons in $Au_{20}(SCH_3)_{16}$. $Au_{20}(SCH_2CH_2Ph)_{16}$ was first synthesized by Jin and co-workers in 2009.[34] They found the cluster to be extraordinarily robust against excess thiol etching and to have a large HOMO−LUMO gap of 2.15 eV. The main absorption peak was observed at 2.56 eV and two additional features were observed at 2.95 eV and 3.5 eV. A broadband femtosecond transient absorption study of the cluster was performed by Zhou et al. in which the fluorescence peaks were obtained at 1.51 eV and 1.61 eV.[35] After its discovery, many works have been undertaken to determine its geometrical structure. Early theoretical studies from Zeng and co-workers[36] and Jiang et al.[37] reported the $Au_{20}(SCH_3)_{16}$ cluster to have a prolate-shaped Au_8 core with four level-3 staple motifs (i.e. -RS-Au-RS-Au-RS-Au-RS-). In 2014, Jin and co-workers[38] performed an X-ray crystallographic analysis of $Au_{20}(TBBT)_{16}$ (TBBT = SPh-^{t}Bu) and found the cluster to have a vertex-sharing Au_7 bi-tetrahedral core, $Au_8(SR)_8$ octameric ring, and two monomeric and one trimeric staple motifs. The ring was found to encircle the Au_7 core. At this point, it was not clear whether different structures of Au_{20} were obtained due to the use of aliphatic vs. aromatic ligands. Later, Weerawardene and Aikens theoretically studied the effects of aliphatic and aromatic ligands on the geometrical and electronic structure of the cluster.[39] They found that the Au_{20} geometrical structure is independent of the type of ligand used and described minor effects on its electronic structure. Their study also showed that the structure obtained by Jin group[38] was more stable than the previously predicted

structures.[36-37] Recently, the Pei group suggested that this cluster has a slightly different structure depending on the ligand used.[40] Using dispersion-corrected density functional theory, they found a structure with a Au_7 core, $Au_6(SR)_6$ ring, one trimeric staple motif and two dimeric staple motifs for $Au_{20}(SCH_2CH_2Ph)_{16}$. Because there are very limited studies focused on understanding the structure and optical properties of this nanocluster, it is still essential to determine the exact structure of the cluster and its optical properties.

4.3 Computational details

Structures are optimized with the Amsterdam Density Functional (ADF) package.[41] We have used the BP86 functional which is a generalized gradient approximation (GGA) type functional.[42-43] Double zeta (DZ) and triple zeta (TZ) basis sets are used. We have also performed some of the calculations including the D3 dispersion correction by Grimme et al.[44] and polarization (P) functions (Table 4-1). DZP(non-Au) in Table 4-1 means that we have used the DZ basis set for Au and DZP for S, C, and H. Absorption spectra are obtained with linear response time-dependent density functional theory (LR-TDDFT).[45] The absorption spectra are obtained using DZ and TZP basis sets. We performed additional calculations that add the D3 dispersion correction and polarization functions on the DZ and TZ basis sets, and also include the presence of tetrahydrofuran (THF) as a solvent. Calculation in solution is performed using the conductor-like screening model (COSMO).[46] Absorption spectra are convoluted with Gaussian functions with a full width at half-maximum value of 0.2 eV. Scalar relativistic effects are included using the zeroth-order regular approximation (ZORA).[47-48] Molecular structures are visualized using MacMolPlt[49] and the orbitals with ADF GUI with a contour value of 0.02.

The excited state geometries are optimized by calculating the excited state gradients. The energy and gradient convergence criteria are set to 1×10^{-4} and 1×10^{-3}. The radiative lifetimes τ_i are calculated using the following equation:[50]

$$\frac{1}{\tau_i} = \frac{4}{3t_0}\alpha_0^3(\Delta E_i)^3 \sum_{\alpha\in(x,y,z)} |M_\alpha^i|^2 \tag{4.1}$$

where ΔE_i is the excitation energy; M_α^i is the transition dipole moment in the *x*, *y*, or *z* direction; α_0 is the fine structure constant; and $t_0 = (4\pi\epsilon_0)^2\hbar^3/m_e e^4$. In this equation, ϵ_0 is the dielectric constant of vacuum, $\hbar$ is the Planck constant divided by 2π, m_e is the mass of the electron, and e is the charge of the electron.

For the nonadiabatic calculations, the optimized geometries are equilibrated to 300K in the Vienna Ab initio Simulation Package (VASP).[51] This calculation uses the PBE functional with projector-augmented wave pseudopotentials,[52] gamma k-points, and the microcanonical ensemble. A kinetic energy cut-off value of 400 eV is used and the simulation box size is 24 Å. After equilibration, a molecular dynamics (MD) trajectory of 5 ps is obtained with a time step of 1 fs. Then, nonadiabatic coupling elements are computed along the MD trajectory using the same method we used in our previous studies.[27] Finally, fewest switches surface hopping (FSSH)[53] simulations are performed in the PYXAID program.[54-55] The FSSH simulations use the classical path approximation and a time-dependent Kohn−Sham (FSSH−TDKS)[56] description of electronic states. Decoherence is included using the decoherence-induced surface hopping (DISH) algorithm.[57] The decay times of excited electrons are calculated with equation (2):

$$f(t) = \exp\left(-\frac{t}{\tau}\right) \tag{4.2}$$

4.4 Results and discussions

Two $Au_{20}(SCH_3)_{16}$ structures are compared to determine the lowest energy structure: the structures are based on the recent geometry proposed from the Pei group[40] (structure 1) and the crystal structure from the Jin group[38] (structure 2). As discussed in the introduction, structure 1 has an Au_7 core, $Au_6(SR)_6$ ring, one trimeric staple motif and two dimeric staple motifs whereas structure 2 has an Au_7 core, $Au_8(SR)_8$ octameric ring, two monomeric staple motifs and one trimeric staple motif. Overall, we found structure 2 to be more stable than structure 1 (Table 4-1). Structure 1 is predicted to be slightly more stable than structure 2 only for the BP86/TZP level of theory examined here, but the difference is very small. Therefore, we have used structure 2 for further calculations.

Table 4-1 Energy difference of $Au_{20}(SCH_3)_{16}$ structures.

	$\Delta E = E_1 - E_2$(kcal/mol)
BP86/DZ	14.91
BP86+D3/DZ	28.20
BP86/DZ(Au), DZP(non-Au)	7.89
BP86/TZP	-3.60
BP86+D3/TZP	10.05

After determining the structure of the $Au_{20}(SCH_3)_{16}$ system, we obtained the absorption spectra of the cluster with different levels of theory (Figure 4-1). The spectra are compared with the experimental absorption spectrum of the cluster which shows the most prominent peak at 2.56 eV.[34] The most prominent peaks with the BP86/DZ, BP86+D3/DZ, BP86+D3/TZP, and BP86/DZ/solvent(THF) levels of theory are obtained at 2.26 eV, 2.38 eV, 2.57 eV, and 2.26 eV, respectively. BP86+D3/TZP accurately reproduces the experimentally observed most prominent absorption peak. The theoretically obtained excitation energies with other functional/basis set combinations are slightly underestimated. The calculated underestimations are 0.3 eV, 0.18 eV

and 0.3 eV with BP86/DZ, BP86+D3/DZ, and BP86/DZ/solvent(THF), respectively. GGA functionals are known to underestimate excitation energies. Figure 4-1 shows that the absorption spectra do not change significantly by using different functional/basis set combinations. The main features of the experimental absorption spectrum are obtained even with only the DZ basis set. In addition, the HOMO−LUMO gaps obtained with all these methods are similar. Theoretically obtained HOMO−LUMO gaps are 1.62 eV, 1.58 eV, 1.97 eV, and 1.66 eV on using BP86/DZ, BP86+D3/DZ, BP86+D3/TZP, and BP86/DZ/solvent(THF), respectively. These HOMO−LUMO gaps are similar to the experimentally observed HOMO−LUMO gap of 2.15 eV, which is determined by extrapolating the energy of the first optical peak.[34] So, the HOMO−LUMO gaps are underestimated by 0.53 eV, 0.57 eV, 0.18 eV, and 0.49 eV on using BP86/DZ, BP86+D3/DZ, BP86+D3/TZP, and BP86/DZ/solvent(THF), respectively; however, it should be noted that extrapolation of an experimental optical gap can overestimate the HOMO-LUMO gap. Although the best results for the first peak position and the HOMO−LUMO gap are obtained using BP86+D3/TZP, BP86/DZ is also able to reproduce the experimental features with a slight underestimation in excitation energies and the HOMO−LUMO gap. Thus, we have used BP86/DZ to perform the excited state calculations in order to reduce the experimental cost. We also note that the spectral features are enhanced in the presence of solvent; the oscillator strengths of the peak at 2.26 eV increase about three times compared to calculations without solvent.

Overall, at the BP86/DZ level of theory, $Au_{20}(SCH_3)_{16}$ has a small peak at 1.83 eV and a more prominent peak at 2.26 eV (Figure 4-1). Experimentally, the main peaks were found at 2.56, 2.95, and 3.50 eV.[34] The fourth and sixteenth excited states correspond to the strong peaks at 1.83 eV and 2.26 eV, respectively (Table 4-2). The HOMO-3 → LUMO transition is the main transition

that corresponds to the peak at 1.83 eV. The HOMO-2 → LUMO+1 transition is the dominant contribution to the 2.26 eV peak.

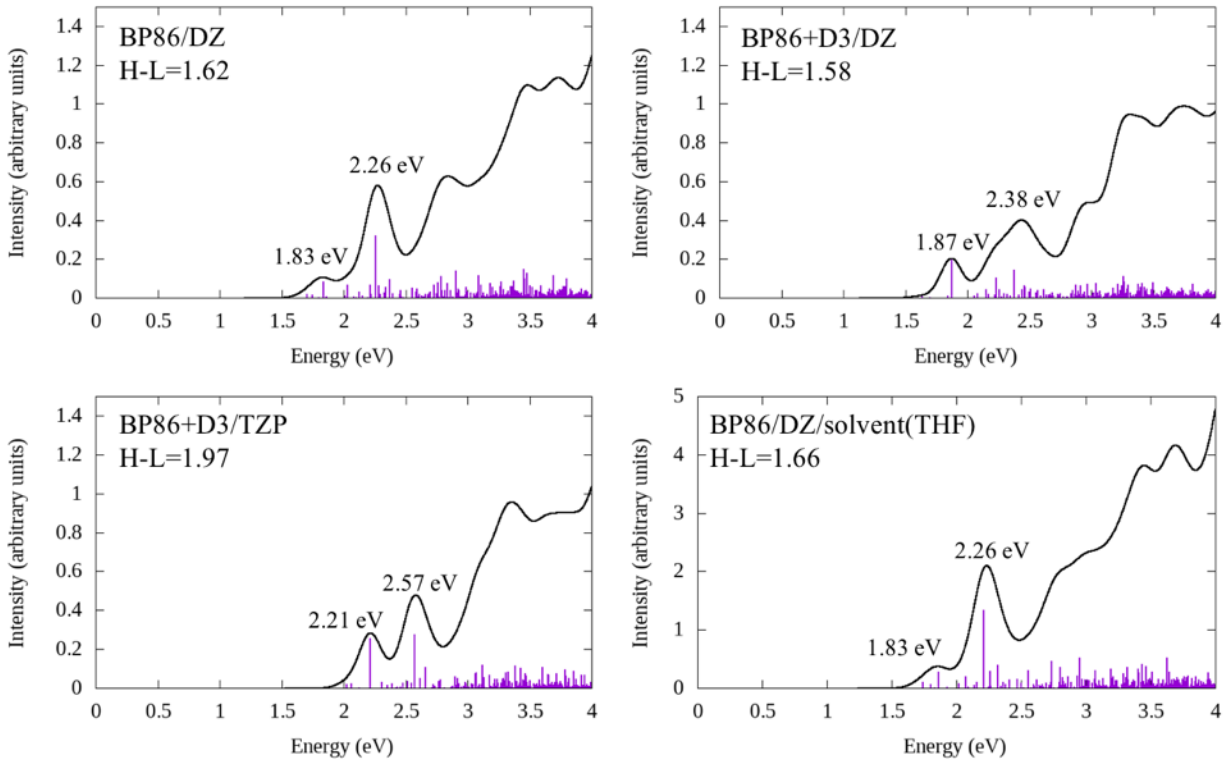

Figure 4-1 Absorption spectra of $Au_{20}(SCH_3)_{16}$ obtained by using the given levels of theory. 'H-L' in each figure refers to the HOMO−LUMO gap.

Table 4-2 Transitions with highest weight and transition dipole moment that correspond to the first six and the sixteenth excited states from the BP86/DZ TDDFT calculation. H and L refer to the HOMO and LUMO orbitals respectively.

Excited state	Energy (eV)	Oscillator strength (au)	Most weighted transitions	Weight	Transition dipole moment (au)		
					x	y	z
1	1.70	0.0034	H→L H-3→L	0.9311 0.0350	0.0003 -0.0007	-1.4149 0.4432	-0.0012 -0.0006
2	1.75	0.0026	H-1→L H-4→L	0.9593 0.0157	1.0087 -0.0677	0.0029 -0.0002	0.2247 -0.0346
3	1.80	0.0002	H-2→L H-4→L	0.9487 0.0276	0.1603 -0.0886	0.0133 -0.0003	0.1846 -0.0452
4	1.83	0.0175	H-3→L H→L H-5→L H→L+1	0.9038 0.0307 0.0198 0.0192	-0.0035 -0.0001 -0.0000 0.0002	2.1698 0.2476 -0.2472 -0.1109	-0.0028 0.0002 0.0000 0.0015

5	1.86	0.0012	H-4→L H-2→L H-1→L	0.9477 0.0220 0.0158	-0.5099 -0.0240 -0.1255	-0.0016 -0.0020 -0.0004	-0.2603 -0.0276 -0.0280
6	2.01	0.0014	H-5→L H→L+1	0.5749 0.3965	-0.0002 -0.0009	-1.2702 0.4815	0.0000 -0.0064
16	2.26	0.0672	H-2→L+1 H-4→L+1 H-10→L H-3→L+2 H-1→L+1 H→L+3 H-9→L	0.6096 0.1231 0.0836 0.0826 0.0311 0.0120 0.0115	0.0331 0.0948 0.1181 0.0043 -0.1061 0.1080 -0.1266	0.0024 0.0000 0.0000 0.0056 0.0002 -0.0025 -0.0014	3.4386 0.0101 -0.2825 0.1547 0.2427 -0.1989 0.0651

4.4.1 Ground state (S_0) structure

The optimized ground state structure of $Au_{20}(SCH_3)_{16}$ has a vertex-sharing bi-tetrahedral Au_7 core, a chair shaped $Au_8(SR)_8$ octameric ring, two monomeric staple motifs and one trimeric staple motif (Figure 4-2). The octameric ring circles the Au_7 core. The monomeric and trimeric staple motifs are attached to the core via Au-S bonds whereas the ring interacts with the core via Au-Au bonds.

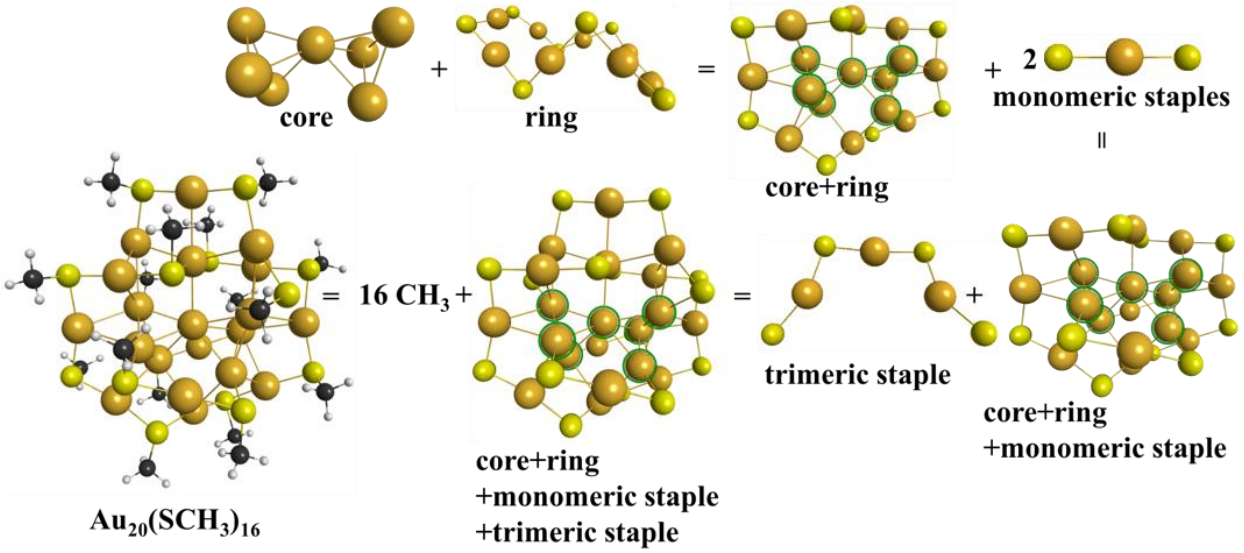

Figure 4-2 Structure of $Au_{20}(SCH_3)_{16}$ and its components: Au_7 core, a chair shaped $Au_8(SR)_8$ octameric ring, two monomeric staple motifs and one trimeric staple motif. The yellow, green, black, and white atoms refer to Au, S, C, and H atoms respectively. The Au_7 core is highlighted in green circles.

The average bond lengths and bond angles are calculated for the optimized structure (Table 4-3). The bond lengths and bond angles obtained with BP86/DZ are similar to but slightly different from those obtained using PBE/TZP.[39] The average Au-Au bond length in the core is 2.79 ± 0.04 with BP86/DZ which is very close to 2.80 ± 0.04 obtained with PBE/TZP. The average Au_{core}–S_{staple} and Au_{staple}–S_{staple} bond lengths of 2.50 ± 0.01 and 2.43 ± 0.02 respectively obtained with BP86/DZ are about 0.08 Å longer compared to the bond lengths of 2.42 ± 0.02 and 2.35 ± 0.01 obtained with PBE/TZP. The Au_{ring}–Au_{core} bond length of 2.93 ± 0.04 obtained with BP86/DZ is ~0.27 Å shorter than the bond length of 3.20 ± 0.32 obtained with PBE/TZP. This is the bond that shows the largest difference in bond length between different functionals. Au_{ring}–S_{ring} bond lengths of 2.43 ± 0.02 obtained with BP86/DZ are 0.07 Å longer compared to the 2.36 ± 0.01 bond length obtained with PBE/TZP. The bond angles with BP86/DZ are smaller compared to the bond angles with PBE/TZP. ∠Au_{ring}–SR–Au_{ring} is ~ 7.34 degrees smaller whereas the ∠SR–Au_{ring}–SR is ~ 2.98 degrees smaller. Although the bond lengths and angles obtained with BP86/DZ and PBE/TZP are not exactly same, the overall cluster structure is still similar.

Table 4-3 Geometrical parameters for the BP86/DZ optimized $Au_{20}(SCH_3)_{16}$ in the ground state (S_0). The bond lengths are given in Å and the bond angles are given in degrees.

Bond length/ bond angle	Average (bond length/ bond angle)
Au_{core}–Au_{core}	2.79 ± 0.04
Au_{core}–S_{staple}	2.50 ± 0.01
Au_{staple}–S_{staple}	2.43 ± 0.02
Au_{ring}–Au_{core}	2.93 ± 0.04
Au_{ring}–S_{ring}	2.43 ± 0.02
∠Au_{ring}–SR–Au_{ring}	93.65 ± 5.65
∠SR–Au_{ring}–SR	168.18 ± 3.50

4.4.2 Radiative relaxation of excited electrons

We have optimized several excited states to achieve an understanding of radiative relaxation in $Au_{20}(SCH_3)_{16}$. We performed optimizations up to the sixth singlet excited state (S_6); however, optimizations were only possible for the first (S_1), second (S_2) and sixth (S_6) excited states due to state crossings in the other states, suggesting that radiative relaxation would only potentially be observed from S_1, S_2, or S_6. According to Kasha's rule, photon emission occurs in appreciable yield from the lowest excited state of a given multiplicity.[58] However exceptions have been found to this rule which is nicely described in a review paper by Chou and co-workers.[59] So, we have studied the luminescence from excited states higher than S_1 as well.

From the ground state, an optimization of S_1 yields a structure that has a radiative emission energy of 0.41 eV. We also tried to optimize S_2 from the ground state, but S_2 crosses the S_1 state. Thus, S_2 is expected to non-radiatively relax to S_1. Because S_2 crosses with S_1, we then performed an optimization of S_1 starting from the S_2 structure at the crossing. This again gives the optimized S_1 structure that has radiative emission energy of 0.41 eV. So, if the states cross during optimization of higher excited states, non-radiative relaxation is possible from the higher state into the lower state; then, radiative emission is possible from that excited state. Overall, we find that S_2 non-radiatively relaxes to the S_1, then S_1 radiatively relaxes to the ground state with an emission energy of 0.41 eV.

On the other hand, an optimization of S_3 starting from the ground state structure non-radiatively relaxes to S_2 and then to S_1. This successive relaxation to lower excited states is defined as 'stepwise relaxation' in this text. Then, S_1 relaxes radiatively with an emission energy of 0.68 eV. So, we have observed two different S_1 structures: one with an emission energy of 0.41 eV and the other with an emission energy of 0.68 eV. We tightened the gradient convergence criteria to

2×10^{-4} and re-optimized the S_1 structure that shows emission at higher energy (0.68 eV). The re-optimized structure also gives an emission energy at 0.68 eV. This kind of dual luminescence was also observed by Jin and co-workers in Au_{24}(S-TBBM)$_{20}$, $Au_{14}Cd_1$(S-Adm)$_{12}$, and Au_{24}(S-PET)$_{20}$, where S-TBBM=4-tertbutyl-phenylmethancan, S-Adm=1-adamantanethiol, and S-PET=2-phenylethanethiol.[60] Dual luminescence has been observed in other nanoparticles as well.[2, 61-64]

S_4 also shows non-radiative stepwise relaxation similar to the relaxation process observed during relaxation from S_3; the higher excited states successively relax to nearby lower states. So, S_4 relaxes finally to S_2 and S_2 can relax to the ground state with an emission energy of 0.91 eV. Similarly, S_5 relaxes non-radiatively to S_1 (emission energy of 0.41 eV), S_6 relaxes non-radiatively to S_2 (emission energy of 0.91 eV), and S_7 relaxes non-radiatively to S_6 (emission energy of 1.50 eV). This emission energy of 1.50 eV matches the experimentally observed emission energy of 1.51 eV.[35] However, as discussed before, the BP86/DZ absorption peak position is underestimated by 0.3 eV compared to the experimental peak position. On adding the 0.3 eV underestimation to the S_2 emission energy of 0.91 eV, we get 1.21 eV, which is reasonably close to the experimentally observed emission at 1.50 eV. So, the experimentally observed luminescence could also arise from this S_2 structure. The emission energy from both S_1 structures is smaller even on adding a correction for the calculated underestimation (S_{1a}: 0.41 eV + 0.3 eV = 0.71 eV, S_{1b}: 0.68 eV + 0.3 eV = 0.98 eV). Thus, the experimentally observed emission may not arise from either of the S_1 structures.

4.4.2.1 S_1 structures

As discussed above, we have observed dual luminescence from the S_1 state: at 0.41 eV (referred to as S_{1a}) and at 0.68 eV (referred to as S_{1b}). The vertical excitation energy of S_1 is 1.70

eV and hence emission from S_1 gives a large Stokes shift. The Stokes shifts are calculated to be 1.42 eV and 1.02 eV for S_{1a} and S_{1b}, respectively. Radiative lifetimes of S_{1a} and S_{1b} are 0.64×10^{-3} seconds and 0.23×10^{-4} seconds, respectively.

The electronic structures of both S_{1a} and S_{1b} (along with the ground state electronic structure) are shown in Figure 4-3. The HOMO−LUMO gap decreases significantly in both S_1 states compared to the gap in the ground state. The gap is larger for S_{1b} (0.61 eV) than for S_{1a} (0.37 eV). The HOMO → LUMO transition is the primary contribution to both S_{1a} and S_{1b} states (Table 4-4). The HOMO is a core based orbital in both S_1 states. The LUMO in S_{1a} is mainly located on the $Au_8(SR)_8$ octameric ring and the trimeric staple motif, although it is also located slightly in the core. For the S_{1b} state, the LUMO is located mainly on the core and the $Au_8(SR)_8$ octameric ring. Thus, the two S_1 structures differ in the type of LUMO orbital involved for each, which indicates that a diabatic state crossing has occurred between these two structures. Orbitals for the S_0 state are also presented in Figure 4-3c.

Table 4-4 Transitions with highest weight and transition dipole moment that correspond to S_{1a} and S_{1b} states. H and L refer to the HOMO and LUMO orbitals respectively.

Excited state	Energy (eV)	Oscillator strength (au)	Most weighted transitions	Weight	Transition dipole moment (au)		
					x	y	z
S_{1a}	0.41	0.0002	H→L	0.9982	-0.4450	-0.2835	0.3064
S_{1b}	0.68	0.0022	H→L	0.9954	-0.1722	-0.0260	-1.2126

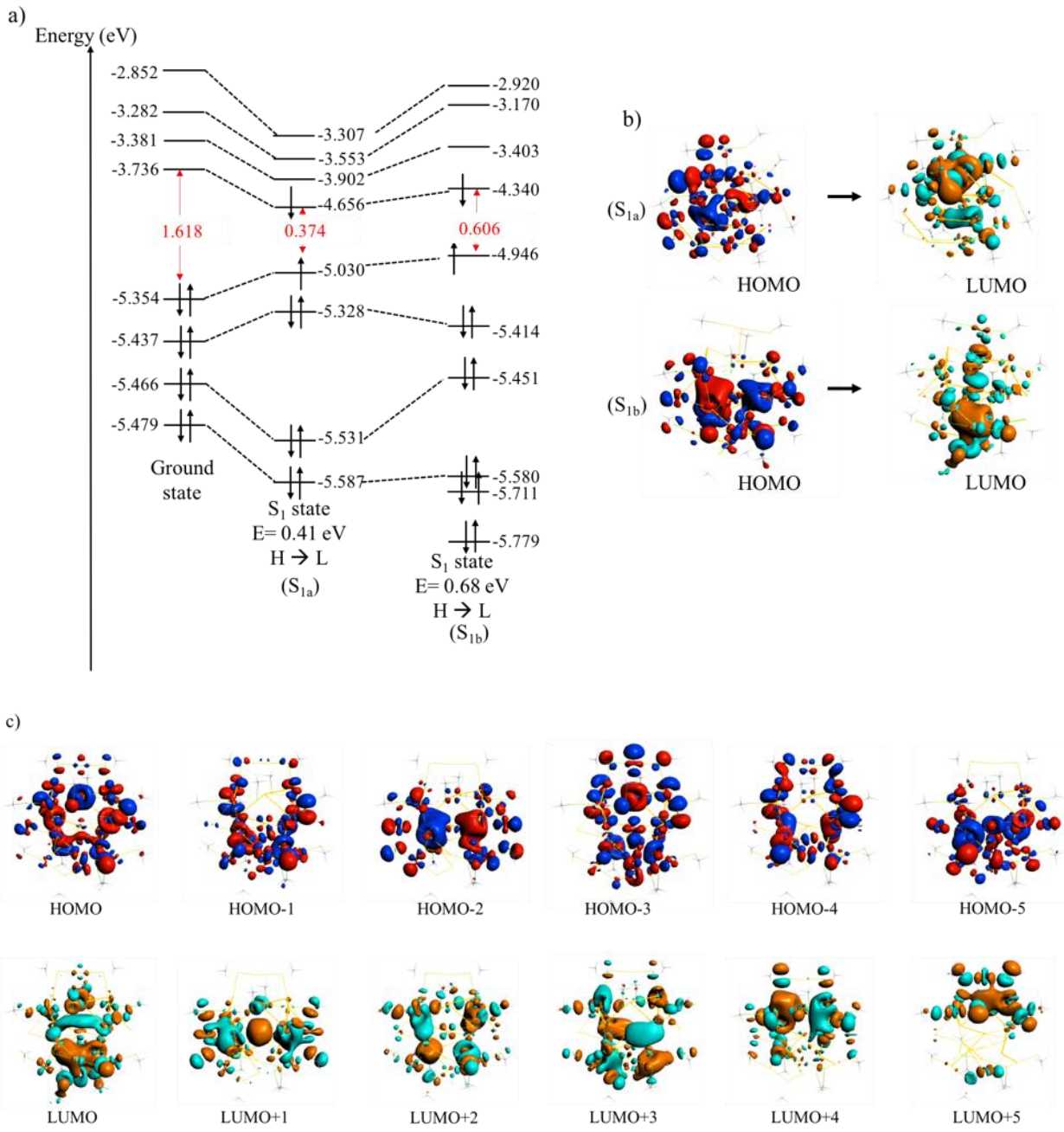

Figure 4-3 a) Comparison of energy levels of frontier orbitals in S_0, S_{1a} and S_{1b} states. The HOMO−LUMO gap is shown in red. H and L refer to the HOMO and LUMO orbitals respectively. b) HOMO and LUMO orbitals in S_{1a} and S_{1b} states. c) Frontier orbitals in S_0.

We also examined the geometrical structures of the two S_1 states (Figure 4-4). The Au_7 core gets distorted in both S_{1a} and S_{1b}. The distance between the two tetrahedrons (bond highlighted in red in Figure 4-4) is shortened from 3.96 Å in S_0 to 2.91 Å in S_{1a} and to 2.78 Å in S_{1b}. Distortion is also observed in the trimeric staple motif and the $Au_8(SR)_8$ octameric ring of S_{1a}. A terminal Au-S bond on the trimeric staple motif of S_{1a} (highlighted by a red circle in Figure 4-4) becomes elongated from 2.47 Å to 2.75 Å. Similarly, another Au-S bond length in the ring increases from 2.47 Å in the ground state geometry to 4.00 Å in the S_{1a} geometry (green circle, Figure 4-4). Due to this distortion, the average bond lengths and bond angles that include the ring and trimeric staple motifs show more deviation for S_{1a} compared to the deviation for S_{1b} (Table 4-5). No large distortion is observed in the S_{1b} structure.

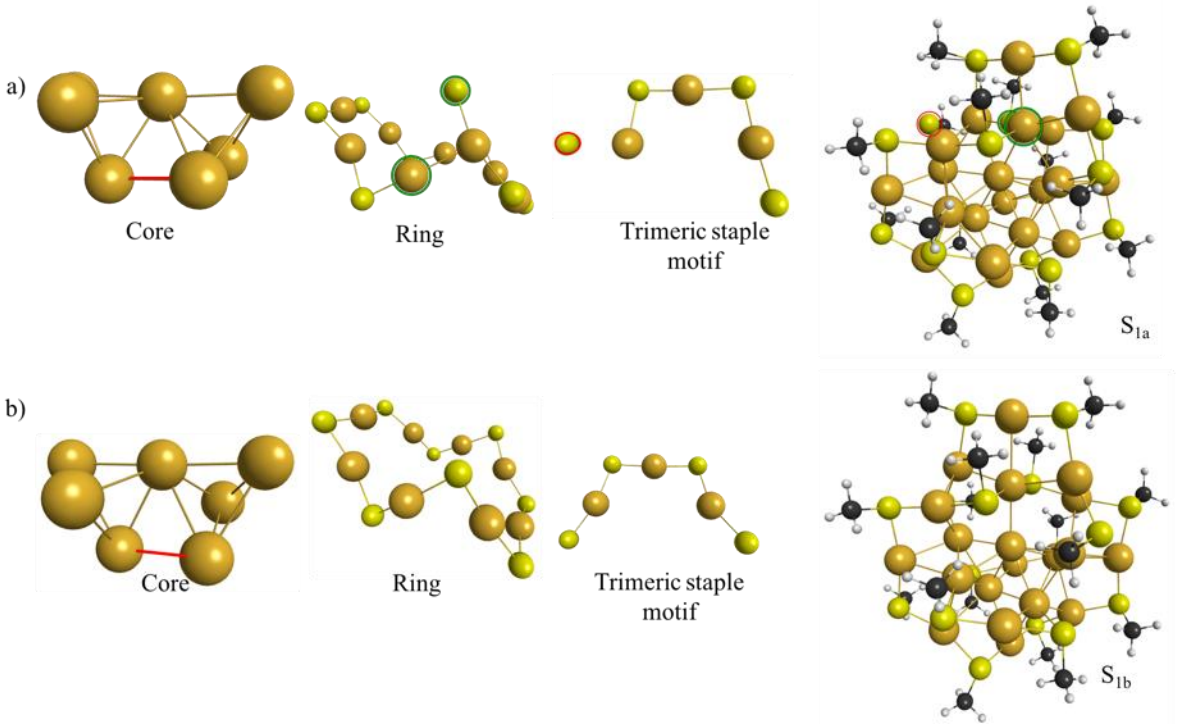

Figure 4-4 Structure of core, ring, trimeric staple motif components and entire $Au_{20}(SCH_3)_{16}$ nanocluster for a) S_{1a} and b) S_{1b}. Atoms are circled in green and red to denote the most distorted atoms in the entire cluster and in the staple motifs.

Table 4-5 Geometrical parameters for the optimized S_{1a} and S_{1b} structures. The bond lengths are given in Å and the bond angles are given in degrees.

Bond length/ bond angle	Average (bond length/ bond angle)	
	S_{1a}	S_{1b}
Au_{core}–Au_{core}	2.82 ± 0.04	2.83 ± 0.08
Au_{core}–S_{staple}	2.53 ± 0.04	2.53 ± 0.05
Au_{staple}–S_{staple}	2.47 ± 0.11	2.43 ± 0.02
Au_{ring}–Au_{core}	2.99 ± 0.11	2.95 ± 0.07
Au_{ring}–S_{ring}	2.54 ± 0.38	2.44 ± 0.02
∠Au_{ring}–SR–Au_{ring}	88.00 ± 17.16	91.26 ± 7.25
∠SR–Au_{ring}–SR	161.04 ± 11.17	165.86 ± 3.93

4.4.2.2 S_2 and S_6 structures

The HOMO-1 → LUMO transition is the primary contribution to S_2 whereas S_6 has main contributions from HOMO-4 → LUMO and HOMO-5 → LUMO transitions (Table 4-6). The orbitals corresponding to the main transitions are shown in Figure 4-5. The HOMO-1 in S_2 is spread out over the trimeric and monomeric staple motifs whereas the LUMO is located mainly on the core and ring structure. For S_6, the LUMO is located mainly on the core and ring structure similar to S_2. The HOMO-4 is delocalized throughout the cluster (but mainly on the trimeric staple motif) and the HOMO-5 is mainly on monomeric staple motifs. These transitions suggest charge transfer from the outside shell to inner core of the nanocluster, which was also observed before.[35] The HOMO−LUMO gaps of S_2 and S_6 are 0.77 eV and 1.19 eV, respectively. The radiative lifetimes of S_2 and S_6 are calculated to be 0.70×10^{-5} seconds and 0.59×10^{-6} seconds, respectively. These times are smaller compared to the lifetimes of both S_1 structures (S_{1a}: 0.64×10^{-3} seconds and S_{1b}: 0.23×10^{-4} seconds). The shorter lifetimes arise because of the larger transition dipole moment and hence the larger oscillator strengths for S_2 and S_6 (comparing Tables 4-4 and 4-6). The distortions in S_2 are similar to the S_{1b} structure whereas the S_6 structure is similar to the optimized structure (Table 4-3, Table 4-5, Table 4-7).

Table 4-6 Transitions with highest weight and transition dipole moment that correspond to S_2 and S_6 states. H and L refer to the HOMO and LUMO orbitals respectively.

Excited state	Energy (eV)	Oscillator strength (au)	Most weighted transitions	Weight	Transition dipole moment (au)		
					x	y	z
S_2	0.91	0.0039	H-1→L	0.9424	0.1399	-1.2703	0.5437
			H→L	0.0434	0.0345	0.0287	0.2100
S_6	1.59	0.0155	H-5→L	0.6901	0.0613	-0.7611	0.0076
			H-4→L	0.2428	-0.1401	-1.2755	-0.0512
			H-1→L+1	0.0165	0.0241	0.3593	0.0757

Table 4-7 Geometrical parameters for the optimized S_2 and S_6 structures. The bond lengths are given in Å and the bond angles are given in degrees.

Bond length/ bond angle	Average (bond length/ bond angle)	
	S_2	S_6
Au_{core}–Au_{core}	2.83 ± 0.09	2.80 ± 0.06
Au_{core}–S_{staple}	2.54 ± 0.04	2.53 ± 0.03
Au_{staple}–S_{staple}	2.44 ± 0.04	2.45 ± 0.04
Au_{ring}–Au_{core}	2.95 ± 0.07	2.94 ± 0.07
Au_{ring}–S_{ring}	2.44 ± 0.03	2.44 ± 0.03
∠Au_{ring}–SR–Au_{ring}	92.01 ± 7.71	92.58 ± 5.10
∠SR–Au_{ring}–SR	166.57 ± 3.55	167.98 ± 2.49

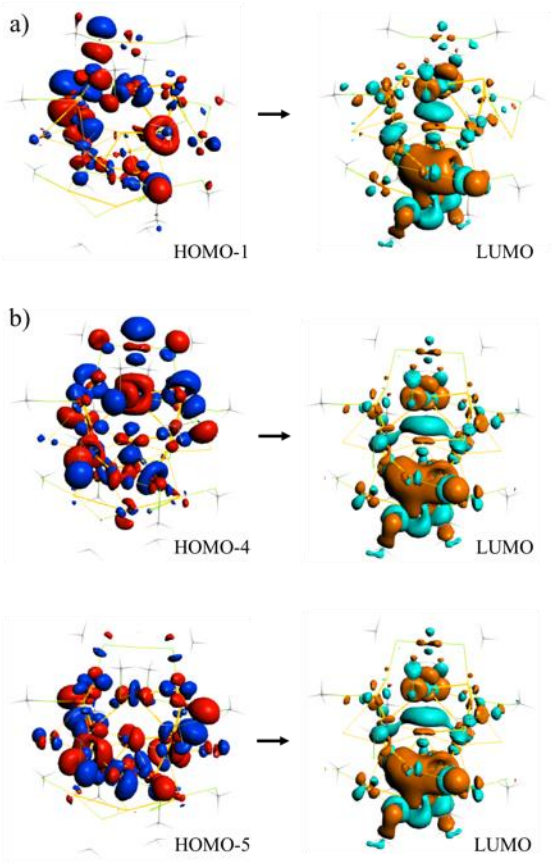

Figure 4-5 Main transitions and orbitals corresponding to a) S_2 and b) S_6.

4.4.3 Non-radiative relaxation of excited electrons

As shown in Table 4-2, HOMO-10 to LUMO+3 orbitals contribute up to the second peak in the absorption spectrum of the cluster at 2.26 eV. In this section, we calculate nonadiabatic coupling matrix elements between HOMO-10 through LUMO+10 orbitals and perform the FSSH nonadiabatic dynamics on the HOMO-10 to LUMO+6 orbitals. Analysis of more orbitals helps to get a better picture of the dynamics. We have studied the excitations up to 2.37 eV in the absorption spectrum to study the non-radiative relaxation of excited electrons.

The variation of orbital energies during the MD simulation is plotted in Figure 4-6. It shows that the occupied orbitals are closer in energy to each other compared to the energy differences

between the virtual orbitals. This is the reason that many occupied orbitals (compared to the number of virtual orbitals) contribute to the prominent absorption peaks as discussed before. The average HOMO−LUMO gap during the MD simulation is 1.71 eV, which is close to the ground state HOMO−LUMO gap obtained from the ADF calculation using BP86/DZ (1.62 eV).

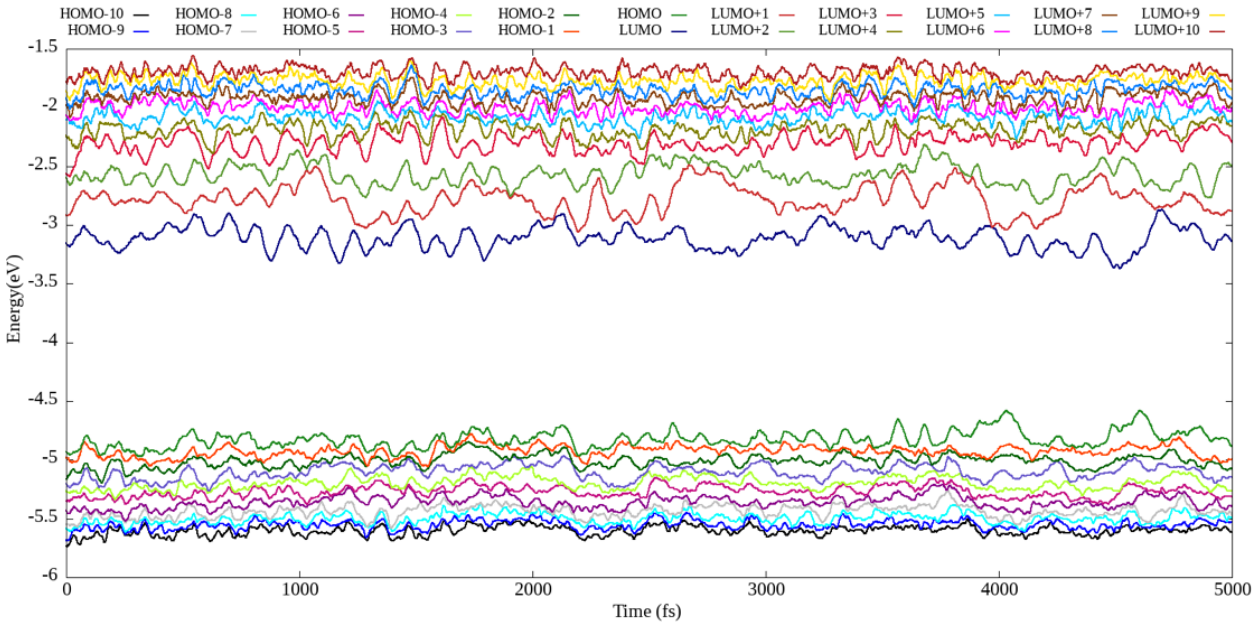

Figure 4-6 Orbital energy variation during molecular dynamics.

For the FSSH−TDKS calculation, the excited states are defined as shown in Table 4-8. It should be noted that the FSSH-TDKS states are single determinants and are defined differently than the states that arise from TDDFT calculations. In our FSSH-TDKS calculation, the electrons are excited into unoccupied orbitals and then the relaxation mechanisms of these excited electrons to the ground state or other excited states are studied.

Table 4-8 Excited states and the transitions defined for FSSH−TDKS calculation. H and L refer to the HOMO and LUMO orbitals respectively.

Excited state	Transitions	Excited state	Transitions	Excited state	Transitions	Excited state	Transitions
S_1	H → L	S_{21}	H-2 → L+6	S_{41}	H-5 → L+5	S_{61}	H-8 → L+4
S_2	H → L+1	S_{22}	H-3 → L	S_{42}	H-5 → L+6	S_{62}	H-8 → L+5
S_3	H → L+2	S_{23}	H-3 → L+1	S_{43}	H-6 → L	S_{63}	H-8 → L+6
S_4	H → L+3	S_{24}	H-3 → L+2	S_{44}	H-6 → L+1	S_{64}	H-9 → L
S_5	H → L+4	S_{25}	H-3 → L+3	S_{45}	H-6 → L+2	S_{65}	H-9 → L+1
S_6	H → L+5	S_{26}	H-3 → L+4	S_{46}	H-6 → L+3	S_{66}	H-9 → L+2
S_7	H → L+6	S_{27}	H-3 → L+5	S_{47}	H-6 → L+4	S_{67}	H-9 → L+3
S_8	H-1 → L	S_{28}	H-3 → L+6	S_{48}	H-6 → L+5	S_{68}	H-9 → L+4
S_9	H-1 → L+1	S_{29}	H-4 → L	S_{49}	H-6 → L+6	S_{69}	H-9 → L+5
S_{10}	H-1 → L+2	S_{30}	H-4 → L+1	S_{50}	H-7 → L	S_{70}	H-9 → L+6
S_{11}	H-1 → L+3	S_{31}	H-4 → L+2	S_{51}	H-7 → L+1	S_{71}	H-10 → L
S_{12}	H-1 → L+4	S_{32}	H-4 → L+3	S_{52}	H-7 → L+2	S_{72}	H-10 → L+1
S_{13}	H-1 → L+5	S_{33}	H-4 → L+4	S_{53}	H-7 → L+3	S_{73}	H-10 → L+2
S_{14}	H-1 → L+6	S_{34}	H-4 → L+5	S_{54}	H-7 → L+4	S_{74}	H-10 → L+3
S_{15}	H-2 → L	S_{35}	H-4 → L+6	S_{55}	H-7 → L+5	S_{75}	H-10 → L+4
S_{16}	H-2 → L+1	S_{36}	H-5 → L	S_{56}	H-7 → L+6	S_{76}	H-10 → L+5
S_{17}	H-2 → L+2	S_{37}	H-5 → L+1	S_{57}	H-8 → L	S_{77}	H-10 → L+6
S_{18}	H-2 → L+3	S_{38}	H-5 → L+2	S_{58}	H-8 → L+1		
S_{19}	H-2 → L+4	S_{39}	H-5 → L+3	S_{59}	H-8 → L+2		
S_{20}	H-2 → L+5	S_{40}	H-5 → L+4	S_{60}	H-8 → L+3		

After exciting the electrons to higher excited states, we then calculate the decay time constants of each of the excited states (Table 4-9). The decay time constant of an excited state refers to the time taken by the electronic population in that state to decay to other states. We observed the longest decay times for S_1 and S_2. States that arise from transitions from the orbitals HOMO, HOMO-1 and HOMO-2 into unoccupied orbitals (i.e., S_1 to S_{18}) give slightly longer time constants compared to the states arising from transitions out of lower occupied orbitals. For these transitions, the longest time constants are obtained when the transition is to the virtual orbitals from LUMO to LUMO+4. This occurs because these orbitals are loosely packed and transfer of electronic population to nearby orbitals is more difficult than if the orbitals were closely packed.

The time constants for higher excited states are smaller compared to the time constants obtained for these states.

The relaxation dynamics of the electronic population from each of the excited states S_1 through S_9 are presented in Figure 4-7. Relaxation curves are also obtained for the population relaxation from higher excited states, but they are not shown in this text. From these relaxation curves, a hole relaxation mechanism is observed for the excited population. For example, S_1 (HOMO → LUMO) population transfers to S_8 (HOMO-1 → LUMO); only the occupied orbitals (which correspond to the holes) are changed in this process. Similarly, S_2 (HOMO → LUMO+1) population is observed to transfer first to S_9 (HOMO-1 → LUMO+1), which is also a hole relaxation process. Then the population relaxes to S_1, and then finally relaxes to the ground state. So, there is a gradual relaxation of population from the higher state to ground state, i.e., relaxation occurs sequentially from higher state to lower state (stepwise relaxation) after the first hole relaxation. This stepwise relaxation after the first hole relaxation is the electron relaxation mechanism observed in our study. During the relaxation process from S_3 (HOMO → LUMO+2), population first transfers to S_{10} (HOMO-1 → LUMO+2) and then to S_2, S_1 and ground state, which is again both hole and stepwise relaxation.

Table 4-9 Decay times of excited states

States	Decay time (ps)	States	Decay time (ps)	States	Decay time (ps)	States	Decay time (ps)
S_1	17.0	S_{21}	0.5	S_{41}	0.3	S_{61}	0.2
S_2	11.1	S_{22}	0.8	S_{42}	0.3	S_{62}	0.2
S_3	1.8	S_{23}	0.9	S_{43}	0.4	S_{63}	0.2
S_4	3.2	S_{24}	0.6	S_{44}	0.4	S_{64}	0.3
S_5	1.5	S_{25}	0.7	S_{45}	0.4	S_{65}	0.3
S_6	1.0	S_{26}	0.5	S_{46}	0.4	S_{66}	0.2
S_7	0.7	S_{27}	0.4	S_{47}	0.3	S_{67}	0.2
S_8	2.5	S_{28}	0.4	S_{48}	0.3	S_{68}	0.2
S_9	3.3	S_{29}	0.5	S_{49}	0.3	S_{69}	0.2
S_{10}	1.2	S_{30}	0.6	S_{50}	0.3	S_{70}	0.2
S_{11}	1.7	S_{31}	0.5	S_{51}	0.3	S_{71}	0.3

S_{12}	1.0	S_{32}	0.5	S_{52}	0.3	S_{72}	0.3
S_{13}	0.7	S_{33}	0.4	S_{53}	0.3	S_{73}	0.3
S_{14}	0.6	S_{34}	0.3	S_{54}	0.3	S_{74}	0.3
S_{15}	1.5	S_{35}	0.3	S_{55}	0.2	S_{75}	0.3
S_{16}	2.0	S_{36}	0.5	S_{56}	0.2	S_{76}	0.2
S_{17}	1.0	S_{37}	0.5	S_{57}	0.3	S_{77}	0.2
S_{18}	1.3	S_{38}	0.4	S_{58}	0.3		
S_{19}	0.8	S_{39}	0.4	S_{59}	0.3		
S_{20}	0.6	S_{40}	0.4	S_{60}	0.2		

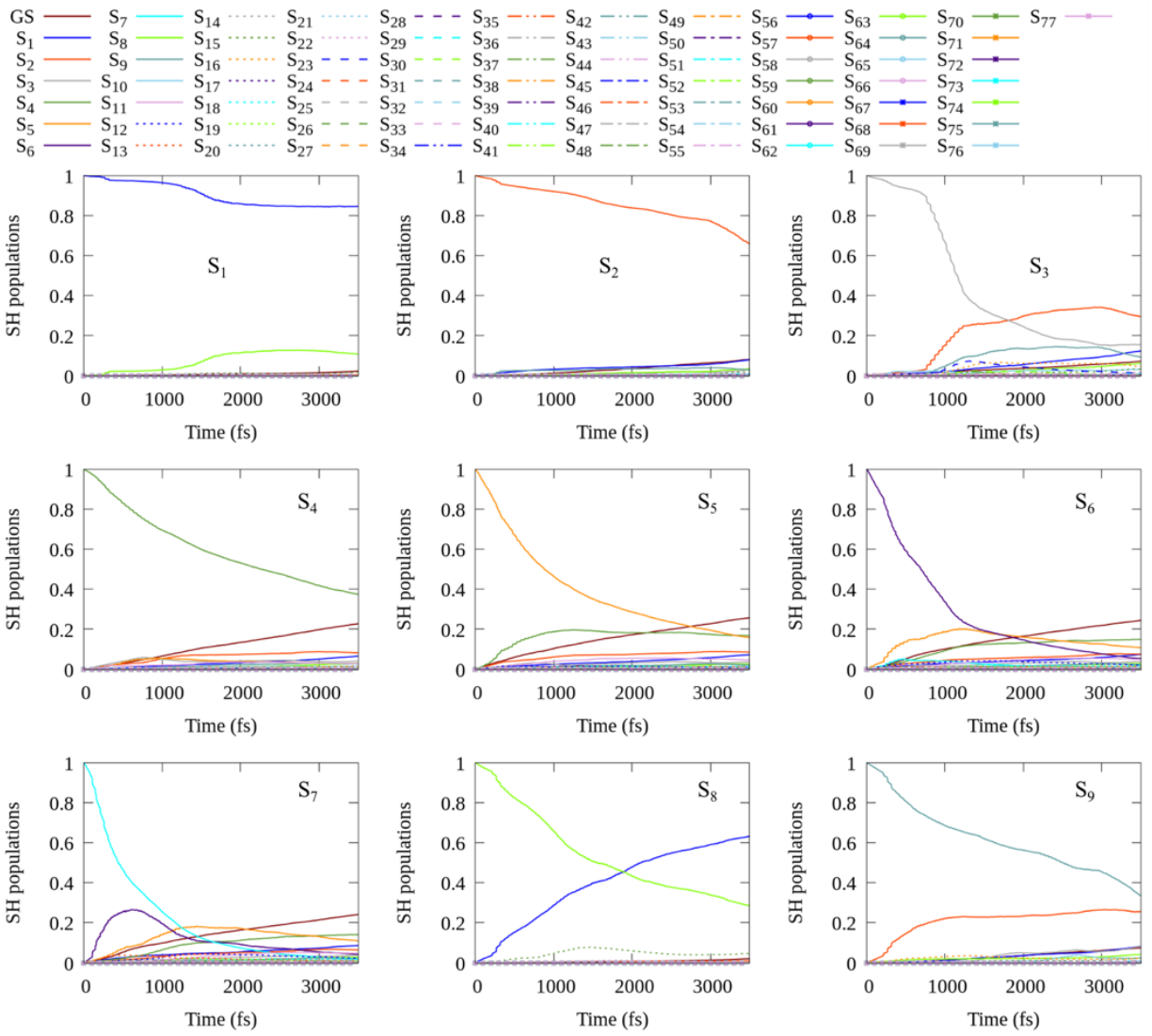

Figure 4-7 Relaxation mechanism of electrons excited to S_1, S_2, S_3, S_4, S_5, S_6, S_7, S_8 and S_9 states.

Because the theoretical peak obtained in our calculation is at 2.26 eV (Figure 4-1) which is underestimated by 0.3 eV compared to the experimental peak observed at 2.56 eV,[34] we performed additional FSSH calculations by adding an energy correction of 0.3 eV to all 77 states. The decay times obtained with the addition of the energy correction are presented in Table 4-10. Addition of this energy correction leads to only minor changes to the decay time constants; the time constants get slightly smaller on including the energy correction. The largest difference is observed for S_2; the decay time constant decreases by 2.7 ps on adding the energy correction. On adding the energy correction, the population relaxes faster to the ground state than without the correction. This causes slightly smaller decay times on adding the energy correction (compare Figure 4-7 and 4-8).

Table 4-10 Decay times of excited states with energy correction

States	Decay time (ps)	States	Decay time (ps)	States	Decay time (ps)	States	Decay time (ps)
S_1	16.0	S_{21}	0.5	S_{41}	0.3	S_{61}	0.2
S_2	8.4	S_{22}	0.8	S_{42}	0.3	S_{62}	0.2
S_3	1.7	S_{23}	0.8	S_{43}	0.4	S_{63}	0.2
S_4	2.7	S_{24}	0.6	S_{44}	0.4	S_{64}	0.3
S_5	1.3	S_{25}	0.7	S_{45}	0.4	S_{65}	0.3
S_6	1.0	S_{26}	0.5	S_{46}	0.4	S_{66}	0.2
S_7	0.7	S_{27}	0.4	S_{47}	0.3	S_{67}	0.2
S_8	2.5	S_{28}	0.3	S_{48}	0.3	S_{68}	0.2
S_9	3.0	S_{29}	0.5	S_{49}	0.3	S_{69}	0.2
S_{10}	1.2	S_{30}	0.6	S_{50}	0.3	S_{70}	0.2
S_{11}	1.5	S_{31}	0.5	S_{51}	0.3	S_{71}	0.3
S_{12}	0.9	S_{32}	0.5	S_{52}	0.3	S_{72}	0.3
S_{13}	0.7	S_{33}	0.4	S_{53}	0.3	S_{73}	0.3
S_{14}	0.5	S_{34}	0.3	S_{54}	0.2	S_{74}	0.3
S_{15}	1.5	S_{35}	0.3	S_{55}	0.2	S_{75}	0.2
S_{16}	1.9	S_{36}	0.5	S_{56}	0.2	S_{76}	0.2
S_{17}	1.0	S_{37}	0.5	S_{57}	0.3	S_{77}	0.2
S_{18}	1.2	S_{38}	0.4	S_{58}	0.3		
S_{19}	0.8	S_{39}	0.4	S_{59}	0.3		
S_{20}	0.6	S_{40}	0.3	S_{60}	0.2		

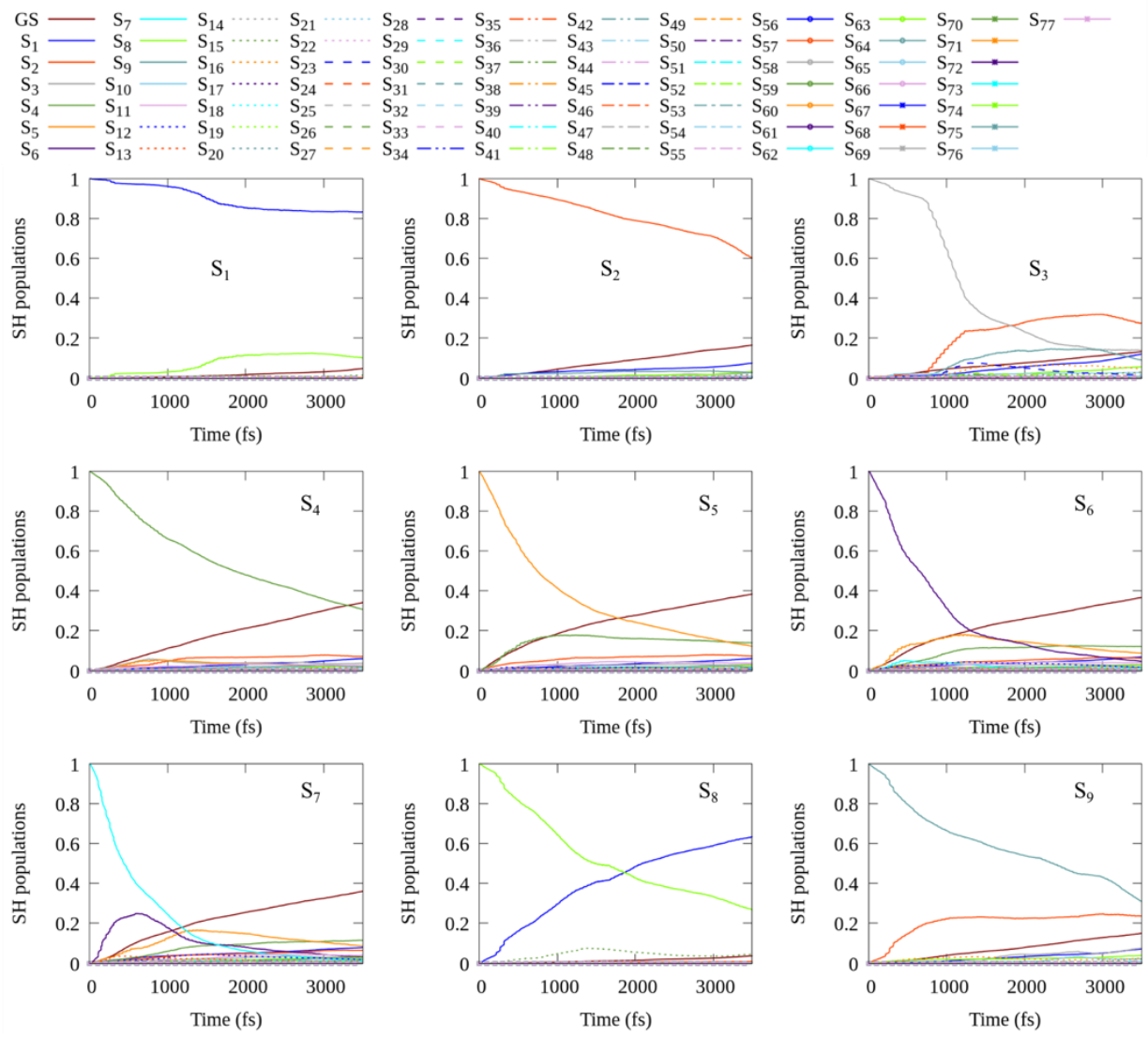

Figure 4-8 Relaxation mechanism of electrons excited to S_1, S_2, S_3, S_4, S_5, S_6, S_7, S_8 and S_9 states on adding energy correction of 0.3 eV.

4.5 Conclusion

We have theoretically studied the geometrical and electronic structure of $Au_{20}(SCH_3)_{16}$. The most stable structure of the cluster is found to have a vertex sharing Au_7 bi-tetrahedral core, two monomeric staple motifs, one trimeric staple motif, and one $Au_8(SR)_8$ octameric ring that encircles the core. This structure arises from the crystal structure reported by Jin and coworkers.[38]

The cluster has a small absorption peak at 1.83 eV and a more prominent peak at 2.26 eV. The HOMO−LUMO gap is found to be 1.62 eV, which is smaller than the experimental HOMO−LUMO gap.[34]

We also investigated the radiative and nonradiative relaxation of excited electrons in $Au_{20}(SCH_3)_{16}$. We observed luminescence from the S_1, S_2, and S_6 states whereas the experimentally observed luminescence at 1.51 eV[35] matches with the emission energy of 1.50 eV from S_6 state. Upon taking the underestimation of peak position and HOMO−LUMO gap into consideration, the experimentally observed luminescence energy also matches with the S_2 state luminescence. Dual luminescence is observed from S_1 at 0.41 eV and 0.68 eV. In general, the geometrical structures are distorted in the excited states compared to the structure in the ground state. The most structural distortion is observed for the S_1 state that gives an emission energy at 0.41 eV and for the S_2 structure. For the nonradiative relaxation of excited electrons, the longest decay times are obtained for the states corresponding to HOMO → LUMO and HOMO → LUMO+1 transitions. The decay times for the higher states are shorter. Stepwise relaxation mechanisms (after the initial hole relaxation) are observed for the nonradiative decay of excited electrons.

4.6 Acknowledgements

This material is based on work supported by the National Science Foundation under grant CHE-1905048. The computing for this project was performed on the Beocat Research Cluster at Kansas State University, which is funded in part by NSF grants CHE-1726332, CNS-1006860, EPS-1006860, and EPS-0919443.

4.7 References

1. Chen, L.-Y.; Wang, C.-W.; Yuan, Z.; Chang, H.-T., Fluorescent Gold Nanoclusters: Recent Advances in Sensing and Imaging. *Anal. Chem.* **2015,** *87* (1), 216-229.

2. Link, S.; Beeby, A.; FitzGerald, S.; El-Sayed, M. A.; Schaaff, T. G.; Whetten, R. L., Visible to Infrared Luminescence from a 28-Atom Gold Cluster. *J. Phys. Chem. B* **2002,** *106* (13), 3410-3415.

3. Wyrwas, R. B.; Alvarez, M. M.; Khoury, J. T.; Price, R. C.; Schaaff, T. G.; Whetten, R. L., The Colours of Nanometric Gold. *Eur. Phys. J. D* **2007,** *43* (1), 91-95.

4. Primo, A.; Corma, A.; García, H., Titania Supported Gold Nanoparticles as Photocatalyst. *Phys. Chem. Chem. Phys.* **2011,** *13* (3), 886-910.

5. Si, P.; Razmi, N.; Nur, O.; Solanki, S.; Pandey, C. M.; Gupta, R. K.; Malhotra, B. D.; Willander, M.; de la Zerda, A., Gold Nanomaterials for Optical Biosensing and Bioimaging. *Nanoscale Advances* **2021,** *3* (10), 2679-2698.

6. Yang, X.; Yang, M.; Pang, B.; Vara, M.; Xia, Y., Gold Nanomaterials at Work in Biomedicine. *Chem. Rev.* **2015,** *115* (19), 10410-10488.

7. Wilcoxon, J. P.; Martin, J. E.; Parsapour, F.; Wiedenman, B.; Kelley, D. F., Photoluminescence From Nanosize Gold Clusters. *J. Chem. Phys.* **1998,** *108* (21), 9137-9143.

8. Aikens, C. M., Electronic and Geometric Structure, Optical Properties, and Excited State Behavior in Atomically Precise Thiolate-Stabilized Noble Metal Nanoclusters. *Acc. Chem. Res.* **2018,** *51* (12), 3065-3073.

9. Tahmasbi Rad, A.; Bao, Y.; Jang, H.-S.; Xia, Y.; Sharma, H.; Dormidontova, E. E.; Zhao, J.; Arora, J.; John, V. T.; Tang, B. Z.; Dainese, T.; Hariri, A.; Jokerst, J. V.; Maran, F.; Nieh, M.-P., Aggregation-Enhanced Photoluminescence and Photoacoustics of Atomically Precise Gold Nanoclusters in Lipid Nanodiscs ($NANO^2$). *Adv. Funct. Mater.* **2021,** *31* (10), 2009750.

10. Olesiak-Banska, J.; Waszkielewicz, M.; Obstarczyk, P.; Samoc, M., Two-Photon Absorption and Photoluminescence of Colloidal Gold Nanoparticles and Nanoclusters. *Chem. Soc. Rev.* **2019,** *48* (15), 4087-4117.

11. Huang, Y.; Fuksman, L.; Zheng, J., Luminescence Mechanisms of Ultrasmall Gold Nanoparticles. *Dalton Trans.* **2018,** *47* (18), 6267-6273.

12. Xie, J.; Zheng, Y.; Ying, J. Y., Protein-Directed Synthesis of Highly Fluorescent Gold Nanoclusters. *J. Am. Chem. Soc.* **2009,** *131* (3), 888-889.

13. Pyo, K.; Thanthirige, V. D.; Kwak, K.; Pandurangan, P.; Ramakrishna, G.; Lee, D., Ultrabright Luminescence from Gold Nanoclusters: Rigidifying the Au(I)–Thiolate Shell. *J. Am. Chem. Soc.* **2015,** *137* (25), 8244-8250.

14. Yu, Y.; Luo, Z.; Chevrier, D. M.; Leong, D. T.; Zhang, P.; Jiang, D.-e.; Xie, J., Identification of a Highly Luminescent $Au_{22}(SG)_{18}$ Nanocluster. *J. Am. Chem. Soc.* **2014,** *136* (4), 1246-1249.

15. Huang, T.; Murray, R. W., Visible Luminescence of Water-Soluble Monolayer-Protected Gold Clusters. *J. Phys. Chem. B* **2001,** *105* (50), 12498-12502.

16. Song, X.-R.; Goswami, N.; Yang, H.-H.; Xie, J., Functionalization of Metal Nanoclusters for Biomedical Applications. *Analyst* **2016,** *141* (11), 3126-3140.

17. Goswami, N.; Yao, Q.; Luo, Z.; Li, J.; Chen, T.; Xie, J., Luminescent Metal Nanoclusters with Aggregation-Induced Emission. *J. Phys. Chem. Lett.* **2016,** *7* (6), 962-975.

18. Perić, M.; Sanader Maršić, Ž.; Russier-Antoine, I.; Fakhouri, H.; Bertorelle, F.; Brevet, P.-F.; le Guével, X.; Antoine, R.; Bonačić-Koutecký, V., Ligand Shell Size Effects on One- And Two- Photon Excitation Fluorescence of Zwitterion Functionalized Gold Nanoclusters. *Phys. Chem. Chem. Phys.* 2019, *21* (43), 23916-23921.

19. Zheng, J.; Zhou, C.; Yu, M.; Liu, J., Different Sized Luminescent Gold Nanoparticles. *Nanoscale* **2012,** *4* (14), 4073-4083.

20. Pyo, K.; Ly, N. H.; Yoon, S. Y.; Shen, Y.; Choi, S. Y.; Lee, S. Y.; Joo, S.-W.; Lee, D., Highly Luminescent Folate-Functionalized Au_{22} Nanoclusters for Bioimaging. *Adv. Healthc. Mater.* **2017,** *6* (16), 1700203.

21. Yuan, X.; Luo, Z.; Zhang, Q.; Zhang, X.; Zheng, Y.; Lee, J. Y.; Xie, J., Synthesis of Highly Fluorescent Metal (Ag, Au, Pt, and Cu) Nanoclusters by Electrostatically Induced Reversible Phase Transfer. *ACS Nano* **2011,** *5* (11), 8800-8808.

22. Herbert, P. J.; Yi, C.; Compel, W. S.; Ackerson, C. J.; Knappenberger, K. L., Relaxation Dynamics of Electronically Coupled $Au_{20}(SC_8H_9)_{15}$-n-glyme-$Au_{20}(SC_8H_9)_{15}$ Monolayer-Protected Cluster Dimers. *J. Phys. Chem. C* **2018,** *122* (33), 19251-19258.

23. Chen, Y.-S.; Choi, H.; Kamat, P. V., Metal-Cluster-Sensitized Solar Cells. A New Class of Thiolated Gold Sensitizers Delivering Efficiency Greater Than 2%. *J. Am. Chem. Soc.* **2013,** *135* (24), 8822-8825.

24. Stamplecoskie, K. G.; Chen, Y.-S.; Kamat, P. V., Excited-state Behavior of Luminescent Glutathione-Protected Gold Clusters. *J. Phys. Chem. C* **2014,** *118* (2), 1370-1376.

25. Green, T. D.; Knappenberger, K. L., Relaxation Dynamics of $Au_{25}L_{18}$ Nanoclusters Studied by Femtosecond Time-resolved Near Infrared Transient Absorption Spectroscopy. *Nanoscale* **2012,** *4* (14), 4111-4118.

26. Senanayake, R. D.; Aikens, C. M., Electronic Relaxation Dynamics in $[Au_{25}(SR)_{18}]^{-1}$ (R = CH_3, C_2H_5, C_3H_7, MPA, PET) Thiolate-Protected Nanoclusters. *Phys. Chem. Chem. Phys.* **2020,** *22* (9), 5272-5285.

27. Senanayake, R. D.; Akimov, A. V.; Aikens, C. M., Theoretical Investigation of Electron and Nuclear Dynamics in the $[Au_{25}(SH)_{18}]^{-1}$ Thiolate-Protected Gold Nanocluster. *J. Phys. Chem. C* **2016,** *121* (20), 10653-10662.

28. Senanayake, R. D.; Aikens, C. M., Theoretical Investigation of Relaxation Dynamics in the $Au_{18}(SH)_{14}$ Thiolate-Protected Gold Nanocluster. *J. Chem. Phys.* **2019,** *151* (9), 094702.

29. Senanayake, R. D.; Guidez, E. B.; Neukirch, A. J.; Prezhdo, O. V.; Aikens, C. M., Theoretical Investigation of Relaxation Dynamics in $Au_{38}(SH)_{24}$ Thiolate-Protected Gold Nanoclusters. *J. Phys. Chem. C* **2018,** *122* (28), 16380-16388.

30. Weerawardene, K. D. M.; Aikens, C. M., Theoretical Insights into the Origin of Photoluminescence of $Au_{25}(SR)_{18}^{-}$Nanoparticles. *J. Am. Chem. Soc.* **2016,** *138* (35), 11202-11210.

31. Wu, Z.; Jin, R., On the Ligand's Role in the Fluorescence of Gold Nanoclusters. *Nano Lett.* **2010,** *10* (7), 2568-2573.

32. Devadas, M. S.; Bairu, S.; Qian, H.; Sinn, E.; Jin, R.; Ramakrishna, G., Temperature-Dependent Optical Absorption Properties of Monolayer-Protected Au_{25} and Au_{38} Clusters. *J. Phys. Chem. Lett.* **2011,** *2* (21), 2752-2758.

33. Compel, W. S.; Wong, O. A.; Chen, X.; Yi, C.; Geiss, R.; Häkkinen, H.; Knappenberger, K. L.; Ackerson, C. J., Dynamic Diglyme-Mediated Self-Assembly of Gold Nanoclusters. *ACS Nano* **2015,** *9* (12), 11690-11698.

34. Zhu, M.; Qian, H.; Jin, R., Thiolate-Protected Au_{20} Clusters with a Large Energy Gap of 2.1 eV. *J. Am. Chem. Soc.* **2009,** *131* (21), 7220-7221.

35. Zhou, M.; Vdović, S.; Long, S.; Zhu, M.; Yan, L.; Wang, Y.; Niu, Y.; Wang, X.; Guo, Q.; Jin, R.; Xia, A., Intramolecular Charge Transfer and Solvation Dynamics of Thiolate-Protected $Au_{20}(SR)_{16}$ Clusters Studied by Ultrafast Measurement. *J. Phys. Chem. A* **2013,** *117* (40), 10294-10303.

36. Pei, Y.; Gao, Y.; Shao, N.; Zeng, X. C., Thiolate-Protected $Au_{20}(SR)_{16}$ Cluster: Prolate Au_8 Core with New $[Au_3(SR)_4]$ Staple Motif. *J. Am. Chem. Soc.* **2009,** *131* (38), 13619-13621.

37. Jiang, D.-e.; Chen, W.; Whetten, R. L.; Chen, Z., What Protects the Core When the Thiolated Au Cluster is Extremely Small? *J. Phys. Chem. C* **2009,** *113* (39), 16983-16987.

38. Zeng, C.; Liu, C.; Chen, Y.; Rosi, N. L.; Jin, R., Gold–Thiolate Ring as a Protecting Motif in the $Au_{20}(SR)_{16}$ Nanocluster and Implications. *J. Am. Chem. Soc.* **2014,** *136* (34), 11922-11925.

39. Weerawardene, K. L. D. M.; Aikens, C. M., Effect of Aliphatic Versus Aromatic Ligands on the Structure and Optical Absorption of $Au_{20}(SR)_{16}$. *J. Phys. Chem. C* **2016,** *120* (15), 8354-8363.

40. Wang, P.; Sun, X.; Liu, X.; Xiong, L.; Ma, Z.; Wang, Y.; Pei, Y., A Revisit to the Structure of $Au_{20}(SCH_2CH_2Ph)_{16}$: a Cubic Nanocrystal-Like Gold Kernel. *Nanoscale* **2018,** *10* (22), 10357-10364.

41. te Velde, G.; Bickelhaupt, F. M.; Baerends, E. J.; Fonseca Guerra, C.; van Gisbergen, S. J. A.; Snijders, J. G.; Ziegler, T., Chemistry with ADF. *J. Comput. Chem.* **2001,** *22* (9), 931-967.

42. Becke, A. D., Density-Functional Exchange-Energy Approximation with Correct Asymptotic Behavior. *Phys. Rev. A* **1988,** *38* (6), 3098-3100.

43. Perdew, J. P., Density-Functional Approximation for the Correlation Energy of the Inhomogeneous Electron Gas. *Phys. Rev. B* **1986,** *33* (12), 8822-8824.

44. Grimme, S.; Ehrlich, S.; Goerigk, L., Effect of the Damping Function in Dispersion Corrected Density Functional Theory. *J. Comput. Chem.* **2011,** *32* (7), 1456-1465.

45. Casida, M. E., Time-Dependent Density Functional Response Theory for Molecules. In *Recent Advances in Density Functional Methods*, WORLD SCIENTIFIC: 1995; Vol. Volume 1, pp 155-192.

46. Klamt, A.; Schüürmann, G., COSMO: a New Approach to Dielectric Screening in Solvents with Explicit Expressions for the Screening Energy and its Gradient. *J. Chem. Soc., Perkin Trans. 2* **1993,** (5), 799-805.

47. van Lenthe, E.; Snijders, J. G.; Baerends, E. J., The Zero-Order Regular Approximation for Relativistic Effects: The Effect of Spin–Orbit Coupling in Closed Shell Molecules. *J. Chem. Phys.* **1996,** *105* (15), 6505-6516.

48. Lenthe, E. v.; Baerends, E.-J.; Snijders, J. G., Relativistic Regular Two-Component Hamiltonians. *J. Chem. Phys.* **1993,** *99* (6), 4597-4610.

49. Bode, B. M.; Gordon, M. S., Macmolplt: a Graphical User Interface for GAMESS. *J. Mol. Graphics Modell.* **1998,** *16* (3), 133-138.

50. Mori, K.; Goumans, T. P. M.; van Lenthe, E.; Wang, F., Predicting Phosphorescent Lifetimes and Zero-Field Splitting of Organometallic Complexes with Time-Dependent Density Functional Theory Including Spin–Orbit Coupling. *Phys. Chem. Chem. Phys.* **2014,** *16* (28), 14523-14530.

51. Kresse, G.; Furthmüller, J., Efficiency of Ab-Initio Total Energy Calculations for Metals and Semiconductors Using a Plane-Wave Basis Set. *Comput. Mater. Sci.* **1996,** *6* (1), 15-50.

52. Kresse, G.; Joubert, D., From Ultrasoft Pseudopotentials to the Projector Augmented-wave Method. *Phys. Rev. B* **1999,** *59* (3), 1758.

53. Tully, J., Mixed Quantum–Classical Dynamics. *Faraday Discuss.* **1998,** *110*, 407-419.

54. Akimov, A. V.; Prezhdo, O. V., The PYXAID Program For Non-adiabatic Molecular Dynamics in Condensed Matter Systems. *J. Chem. Theory Comput.* **2013,** *9* (11), 4959-4972.

55. Akimov, A. V.; Prezhdo, O. V., Advanced Capabilities of the PYXAID Program: Integration Schemes, Decoherence Effects, Multiexcitonic States, and Field-Matter Interaction. *J. Chem. Theory Comput.* **2014,** *10* (2), 789-804.

56. Craig, C. F.; Duncan, W. R.; Prezhdo, O. V., Trajectory Surface hopping in the Time-dependent Kohn-Sham Approach for electron-nuclear Dynamics. *Phys. Rev. Lett.* **2005,** *95* (16), 163001.

57. Jaeger, H. M.; Fischer, S.; Prezhdo, O. V., Decoherence-Induced Surface Hopping. *J. Chem. Phys.* **2012,** *137* (22), 22A545.

58. Kasha, M., Characterization of Electronic Transitions in Complex Molecules. *Discuss. Faraday Soc.* **1950,** *9* (0), 14-19.

59. Demchenko, A. P.; Tomin, V. I.; Chou, P.-T., Breaking the Kasha Rule for More Efficient Photochemistry. *Chem. Rev.* **2017,** *117* (21), 13353-13381.

60. Li, Q.; Zhou, D.; Chai, J.; So, W. Y.; Cai, T.; Li, M.; Peteanu, L. A.; Chen, O.; Cotlet, M.; Wendy Gu, X.; Zhu, H.; Jin, R., Structural Distortion and Electron Redistribution in Dual-Emitting Gold Nanoclusters. *Nat. Commun.* **2020,** *11* (1), 2897.

61. Ai, P.; Mauro, M.; Danopoulos, A. A.; Muñoz-Castro, A.; Braunstein, P., Dual Emission of a Cyclic Hexanuclear Gold(I) Complex. Interplay between Au_3 and Au_2 Ligand-Supported Luminophores. *J. Phys. Chem. C* **2019,** *123* (1), 915-921.

62. Chen, D.; Li, B.; Cai, S.; Wang, P.; Peng, S.; Sheng, Y.; He, Y.; Gu, Y.; Chen, H., Dual Targeting Luminescent Gold Nanoclusters for Tumor Imaging and Deep Tissue Therapy. *Biomaterials* **2016,** *100*, 1-16.

63. Wen, X.; Yu, P.; Toh, Y.-R.; Tang, J., Structure-Correlated Dual Fluorescent Bands in BSA-Protected Au_{25} Nanoclusters. *J. Phys. Chem. C* **2012,** *116* (21), 11830-11836.

64. Xu, Q.-Q.; Dong, X.-Y.; Huang, R.-W.; Li, B.; Zang, S.-Q.; Mak, T. C. W., A Thermochromic Silver Nanocluster Exhibiting Dual Emission Character. *Nanoscale* **2015,** *7* (5), 1650-1654.

Chapter 5 - Theoretical Analysis of Optical Absorption Spectra of Parallel Nanowire Dimers and Dolmen Trimers

Reproduced with permission from:

Pandeya, P.; Aikens, C. M., *J. Phys. Chem. C* ***2020,*** *124 (24),* 13495-13507.

5.1 Abstract

Plasmonic nanoparticles are well known for their properties of electromagnetic field enhancement and surface spectroscopy enhancement. We used the plasmon hybridization method and group theory to study parallel dimers and dolmen trimers of Ag_n (n = 4, 6, 10) nanoparticles. Interactions between the plasmon modes were studied with decreasing inter-particle separation distances. Time dependent density functional calculations are performed on the structures using the BP86/DZ level of theory. In dimers, the decrease of the inter-particle separation blue-shifts the longitudinal peak but the transverse peak position is not affected significantly. In trimers, a new peak is also observed as a shoulder of the longitudinal peak. When the inter-particle separation reduces to 0.6 nm in dimers and trimers, a new peak emerges between the longitudinal and transverse peaks. This new peak red-shifts and increases in intensity upon further decreasing the inter-particle separation. Analysis of the transition densities and symmetries for the respective peaks shows that the new peak arises from a charge-transfer excitation.

5.2 Introduction

A localized surface plasmon resonance is a collective oscillation of free electrons in metallic nanoparticles upon interaction with electromagnetic radiation. The oscillation frequency depends on the shape, size and dielectric environment of the nanoparticles.[1] Plasmonic nanoparticles are of great interest as they enhance the local electromagnetic fields and are very important for surface spectroscopy.[2] Experiments have shown enhancements as large as 10−14 orders of magnitude, enabling spectroscopic detection of a single molecule.[3-5] Different shapes of nanoparticles have been studied such as nano shells,[6-7] rods,[8-9] disks,[10] cubes,[11] cylinders,[12] triangles[13] and rings.[14] Among them, cylindrical nanowires and nanorods have received a lot of interest because their optical properties are very sensitive to their aspect ratio.[15-17] Arrays of nanoparticles are ideal for different applications like biosensing,[18-19] nanolasing,[20] spectroscopy[21-22] and as optical waveguides.[23-25] In consequence, a number of interesting studies have been performed on ordered arrays of nanoparticles[26-34] such as dolmen trimers[35-38] and end-to-end and side-by-side arrangements of nanorods.[39-44]

The optical properties of nanoparticle assemblies are dramatically influenced by the coupling of the plasmon resonances of nearby nanoparticles. Symmetry breaking often accompanies formation of nanoparticle assemblies, and the nanoparticle coupling leads to different bright and dark modes.[45] Plasmonic modes of individual particles hybridize to form new collective modes in multiparticle systems.[46] Plasmon coupling has advantages in surface-enhanced Raman scattering (SERS)[47] and tip-enhanced Raman scattering.[48] Nanoparticle dimers are the most versatile and simple multiparticle structures studied so far. Many experimental and theoretical studies have already been performed on nanoparticle homo and hetero-dimers.[49-55] Dimers have found applications ranging from sensing and spectroscopy[46, 56] to nonlinear optics.[57]

Nordlander and Prodan have developed a plasmon hybridization model[58] that helps to elucidate the plasmon resonances present in an array of nanostructures. This approach is similar to the interaction of atomic orbitals to form molecular orbitals; the plasmon modes of the constituent nanoparticles hybridize to form composite plasmon modes. Plasmons of composite nanoparticles can thus be described as bonding and antibonding combinations arising from hybridization of the individual nanoparticle plasmons. The method has been used successfully to describe the plasmon resonances in concentric spherical metallic nanoparticles,[59] nanoparticle dimers,[60] and various other geometries like nanoshell, nanoeggs, nanomatryushkas, nanorice, nanoparticle trimers, nanoparticle quadrumers, and a semi-infinite surface or a metallic film.[61]

Numerous studies examine nanoparticles in close proximity.[39, 62-72] The most widely used approach for analyzing excitation energy transfer in nanoparticle assemblies involves classical methods such as finite difference time domain (FDTD)[73-74] calculations or similar methods based on solving Maxwell's equations.[25, 73, 75-76] But, because quantum effects play a major role when small inter-particle dimensions are present, researchers have proposed quantum-corrected models to the classical electro-magnetic simulations for these systems.[77-78] Several studies have shown that classical electrodynamics simulations fail for small nanoparticles and nanoparticle assemblies with small separations.[46, 78-81] As these models do not give an atomistic treatment of the systems, quantum mechanical methods such as density functional theory (DFT) are essential to predict the quantum effects at small separation distances. In consequence, studies have been performed on nanoparticle assemblies using quantum mechanical methods. Quantum effects such as surface scattering, electron spill-out at the surface, coupling of plasmons to single particle excitations and the nonlocality of electronic response play a dominant role for nano sized structures.[79, 82] A quantum mechanical study can give a realistic description of the overlap and tunneling of plasmons

for closely separated nanoparticles.[83-84] Tunneling breaks down the local field enhancement predicted by classical theory at the subnanometer regime and leads to the formation of a charge transfer plasmon.[65, 78, 85-86] A charge transfer plasmon is observed where there is direct charge transfer from one nanoparticle to another, when the nanoparticles touch each other, or when a conductive junction is established between them.[87-88] Savage et al. used a quantum corrected model to predict the onset of quantum tunneling effects at around 0.3 nm particle separation.[81] They have shown that the quantum regime starts with a blue shift of hybridized modes in coupled nanoparticles. Zhang et al. showed that the atomic structure of the metal clusters plays a key role in determining accurately both the absorption cross section and electric field enhancement and the effect is more critical when the distance between the nanoparticles is smaller than around 0.3 nm[89] which is also discussed in the review article by Varas et al.[90]

In this paper, we investigate small silver nanowires, their dimers (parallel side-by-side arrangement) and trimers (dolmen structure). We use a quantum mechanical time-dependent density functional theory (TDDFT)[91] method that offers the possibility to address the optical response of plasmonic systems at the fully quantum ab initio level. Although these nanowires are small, the excitations in similar nanowire systems have previously been shown to be plasmonic using approaches that scale e.g. the electron-electron interactions.[92-93] We look into the evolution of the optical absorption spectra of silver nanowire dimers and trimers with different monomer lengths and changing inter-particle distances. We use group theory considerations and the plasmon hybridization method to explain the origin of a new peak in the optical absorption spectra of the nanowire assemblies with decreasing inter-particle distance. We also examine the transition electron densities in dimers and trimers and show that these transition densities are very helpful to describe the evolution of new peaks in the absorption spectra with the decrease in inter-particle

separation. The study of these nanowire assemblies is important to understand the mechanism of interaction of plasmons in composite systems.

5.3 Computational details

All calculations are performed with the Amsterdam Density Functional (ADF)[94] 2017 package. Geometry optimizations on the monomer nanowires are performed with linear symmetry using the generalized gradient approximation (GGA) Becke–Perdew (BP86)[95-97] exchange-correlation functional with a large frozen core double-zeta (DZ) basis set; the optimized coordinates are provided in Table B-1. It should be noted that these geometries do not represent global minima, but are useful model systems for understanding the properties of larger nanorods. Scalar relativistic effects are included with the zeroth-order regular approximation (ZORA).[98] Excitation spectra are calculated using linear response time-dependent density functional theory (TDDFT).[99-102] Unless otherwise noted, the exchange correlation functional used for the TDDFT calculations is the Perdew-Burke-Ernzerhof (PBE) GGA.[103] Time dependent Hartree Fock (TDHF)[104-105] calculations are also carried out on dimers and trimers in order to analyze the charge transfer plasmon. The absorption spectra are convoluted with a Gaussian with a full width at half maximum (FWHM) of 0.2 eV. Multiple excited states may contribute to each plasmon peak; each excited state may be expressed as a linear combination of excited determinants, where each excited determinant can be expressed as an occupied-to-virtual orbital transition. Transition electron densities are computed, which determine how electron density changes between the ground state and an excited state. Orbitals are represented in the ADF-GUI with a contour value of 0.02 and the transition density plots are obtained with an iso-value of 0.02 unless otherwise stated.

The monomers, dimers and trimers of Ag_4, Ag_6 and Ag_{10} nanowires are studied at different inter-particle distances. For dimers, the two monomers are arranged in a side-to-side fashion to form a dimer with D_{2h} symmetry. For trimers, the third monomer is placed on the top of dimer to form a dolmen structure with C_{2v} symmetry. The structures of the studied assemblies of nanowires are shown in Figure 5-1. Only homo-dimers and homo-trimers are considered in this work. To construct these structures, we set the monomers at separation distances (d) of 2 nm, 1.5 nm, 1 nm, 0.9 nm, 0.8 nm, 0.7 nm, 0.6 nm, 0.55 nm, 0.5 nm, 0.45 nm, and 0.4 nm from each other.

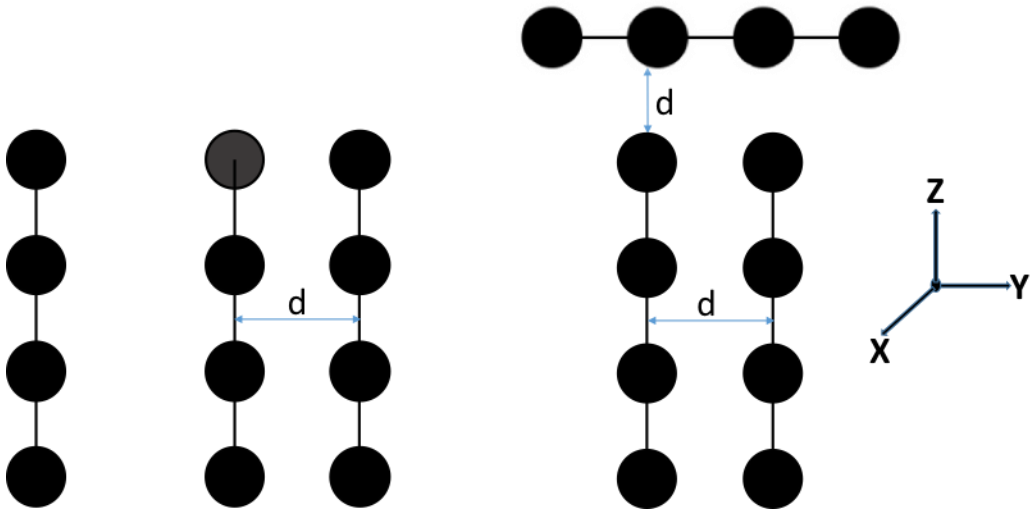

Figure 5-1 Nanowires assemblies examined in this work: monomer, parallel dimer, and dolmen trimer.

5.4 Results and discussion

We first consider the absorption spectra of Ag_n (n = 4, 6, 10) monomers, then discuss the absorption spectra of dimers and trimers. We look in detail into the changes in absorption spectra with the change of aspect ratio for the monomers and also with respect to the change in monomer separation distance for the dimers and trimers. Then, we study the main transitions, symmetry representations and types of orbitals corresponding to the main absorption peaks of the monomers,

dimers, and trimers. We also examine the transition electron densities to describe the observed spectral behavior.

5.4.1 Absorption spectra for monomers of Ag_n (n = 4, 6, 10)

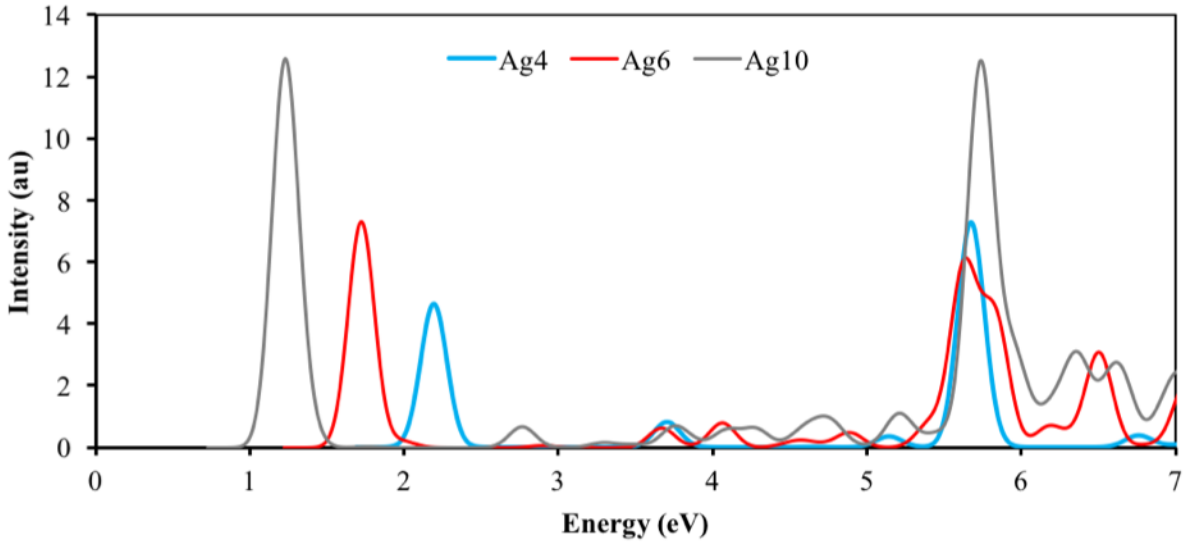

Figure 5-2 Absorption spectra for Ag_4, Ag_6 and Ag_{10} monomer nanowires.

As shown in Figure 5-2, nanowire monomers exhibit two major peaks in their absorption spectra. The sharp peak at lower energies is the longitudinal peak which arises mainly from plasmon oscillation along the long axis of nanowires. This peak originates from the HOMO → LUMO transition and has Σ_u symmetry. These orbitals can also be represented as Σ_n, in which n represents the axial quantum number of the orbital (i.e. the number of axial nodes + 1) as if it were a delocalized particle-in-a-cylinder orbital.[106] The main transitions and the orbitals involved in the longitudinal peak of nanowire monomers are shown in Table 5-1. $\Sigma_n \rightarrow \Sigma_{n+1}$ transitions are primarily responsible for the longitudinal peak in all nanowire monomers. The shapes of the orbitals that contribute to the longitudinal peak of the Ag_4, Ag_6 and Ag_{10} nanowires are shown in

Figure 5-3. The intensity of the longitudinal peak increases from Ag_4 to Ag_{10} (Figure 5-2) as determined by the increasing oscillator strength of the state responsible for this peak (Table 5-1). This is due to the increase in the number of electrons with the increase in system size, which causes a stronger plasmon oscillation.[106] This linear increase of oscillator strength with the chain length has also been observed in previous studies.[107] Note that the signs associated with the transition dipole moments in Tables 5-1 and 5-2 are the signs printed in the TDDFT calculations, so the absolute signs do not matter for a given system; however, within a given excitation, the relative signs are meaningful for different contributions to the excitation.

Table 5-1 Main transitions, excited state energies, oscillator strengths, and transition dipole moments for the longitudinal peak of monomer nanowires.

Nanowire	Transitions (Symmetry representation)	Transitions (Delocalized orbital notation)	Energy (eV)	Oscillator Strength (a.u.)	Transition Dipole Moment (a.u.)
Ag_4	$3\sigma_u \rightarrow 4\sigma_g$	$\Sigma_2 \rightarrow \Sigma_3$	2.19	0.99	-4.82
Ag_6	$5\sigma_g \rightarrow 5\sigma_u$	$\Sigma_3 \rightarrow \Sigma_4$	1.72	1.55	6.46
Ag_{10}	$8\sigma_g \rightarrow 8\sigma_u$	$\Sigma_5 \rightarrow \Sigma_6$	1.23	2.61	-9.48

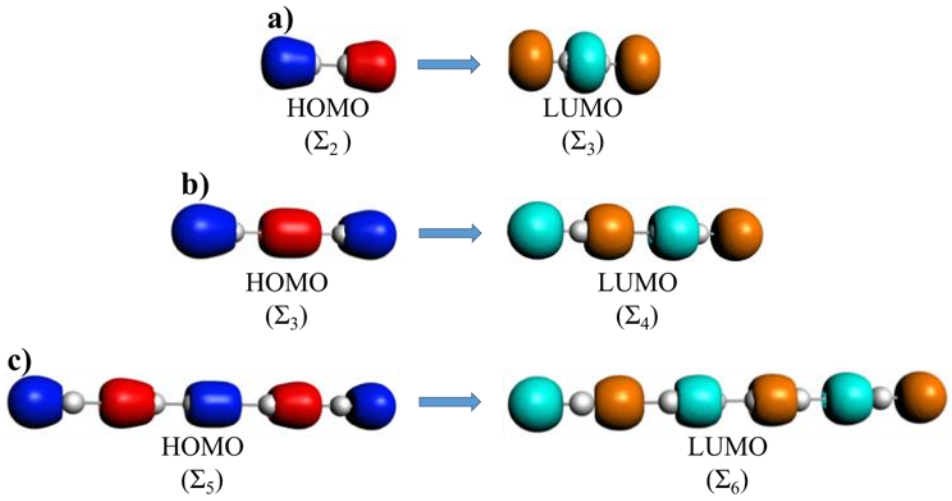

Figure 5-3 Orbitals primarily responsible for the longitudinal peak of a) Ag_4, b) Ag_6 and c) Ag_{10} nanowires.

On comparing the monomer spectra of different chain lengths (Figure 5-2), the longitudinal peak is seen to be sensitive to aspect ratio of the nanowire which was also observed in previous studies.[108] This peak shows a significant redshift as the length of the wire chain increases from Ag_4 to Ag_{10}. This behavior can be explained in accordance with the particle-in-a-cylinder model, which demonstrates why a linear relationship between the aspect ratio of the nanowire (which is proportional to nanowire length for a given nanowire diameter) and the longitudinal plasmon wavelength is typically observed.[106]

The peak at higher energy in the absorption spectra is the transverse peak. It arises due to the plasmon oscillation along the short axis of nanowire and exhibits Π_u symmetry. The transverse peak arises mainly from transitions between Σ and Π levels of the nanowires as shown in Figure 5-4 for the Ag_4 nanowire. Our results on the study of longitudinal and transverse peaks of monomers match with the previous studies on nanowires[107, 109-110] and are included in this paper for the purpose of completeness. The transverse peak is broader compared to the longitudinal peak as it involves multiple $\Sigma \rightarrow \Pi$ transitions, each with lower dipole moment contributions compared to the longitudinal peak, as shown in Tables 5-1 and 5-2. Transition dipole moments increase as the length of nanowire increases. An absorption spectrum for the Ag_6 monomer is shown in Figure B-1 which clearly shows the multiple transitions involved in the transverse peak and a single strong transition for longitudinal peak. The main transitions and the types of orbitals involved for transverse peak of the monomers are shown in Table 5-2. The change of aspect ratio has a negligible effect on the transverse peak position (Figure 5-2).

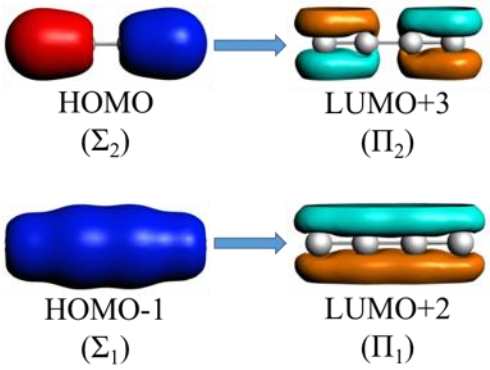

Figure 5-4 Orbitals primarily responsible for the transverse peak of the Ag_4 nanowire.

Table 5-2 Energies, oscillator strengths, main transitions, and transition dipole moments for the transverse peak of monomer nanowires.

Nanowire	Energy (eV)	Oscillator Strength (a.u.)	Transitions (Symmetry representation)	Transitions (Delocalized orbital notation)	Transition Dipole Moment (a.u.)
Ag_4	5.67	0.76	$3\sigma_u \rightarrow 3\pi_g$ $3\sigma_g \rightarrow 3\pi_u$	$\Sigma_2 \rightarrow \Pi_2$ $\Sigma_1 \rightarrow \Pi_1$	-1.65 -1.45
Ag_6	5.62	0.57	$5\sigma_g \rightarrow 5\pi_u$ $4\sigma_u \rightarrow 4\pi_g$ $4\sigma_g \rightarrow 4\pi_u$ $2\pi_u \rightarrow 6\sigma_g$	$\Sigma_3 \rightarrow \Pi_3$ $\Sigma_2 \rightarrow \Pi_2$ $\Sigma_1 \rightarrow \Pi_1$ d-band $\rightarrow \Sigma_5$	1.11 1.00 0.86 -0.28
	5.74	0.14	$5\sigma_g \rightarrow 5\pi_u$ $4\sigma_u \rightarrow 4\pi_g$ $4\sigma_g \rightarrow 4\pi_u$ $4\sigma_g \rightarrow 5\pi_u$	$\Sigma_3 \rightarrow \Pi_3$ $\Sigma_2 \rightarrow \Pi_2$ $\Sigma_1 \rightarrow \Pi_1$ $\Sigma_1 \rightarrow \Pi_3$	0.47 0.62 0.19 -0.13
	5.84	0.38	$5\sigma_g \rightarrow 5\pi_u$ $4\sigma_u \rightarrow 4\pi_g$ $4\sigma_g \rightarrow 4\pi_u$ $2\pi_u \rightarrow 6\sigma_g$	$\Sigma_3 \rightarrow \Pi_3$ $\Sigma_2 \rightarrow \Pi_2$ $\Sigma_1 \rightarrow \Pi_1$ d-band $\rightarrow \Sigma_5$	0.78 0.57 0.64 0.32
Ag_{10}	5.74	1.22	$8\sigma_g \rightarrow 8\pi_u$ $7\sigma_u \rightarrow 7\pi_g$ $7\sigma_g \rightarrow 7\pi_u$ $6\sigma_u \rightarrow 6\pi_g$ $6\sigma_g \rightarrow 6\pi_u$ $2\pi_g \rightarrow 9\sigma_u$	$\Sigma_5 \rightarrow \Pi_5$ $\Sigma_4 \rightarrow \Pi_4$ $\Sigma_3 \rightarrow \Pi_3$ $\Sigma_2 \rightarrow \Pi_2$ $\Sigma_1 \rightarrow \Pi_1$ d-band $\rightarrow \Sigma_8$	1.03 0.87 0.84 0.75 0.67 -0.19

	5.92	0.13	$8\sigma_g \rightarrow 8\pi_u$ $7\sigma_u \rightarrow 7\pi_g$ $7\sigma_g \rightarrow 7\pi_u$ $6\sigma_u \rightarrow 6\pi_g$ $6\sigma_g \rightarrow 6\pi_u$ $2\pi_g \rightarrow 9\sigma_u$ $6\sigma_g \rightarrow 8\pi_u$	$\Sigma_5 \rightarrow \Pi_5$ $\Sigma_4 \rightarrow \Pi_4$ $\Sigma_3 \rightarrow \Pi_3$ $\Sigma_2 \rightarrow \Pi_2$ $\Sigma_1 \rightarrow \Pi_1$ d-band $\rightarrow \Sigma_8$ $\Sigma_1 \rightarrow \Pi_5$	-0.30 -0.27 -0.30 -0.14 -0.16 -0.26 0.03
	5.95	0.12	$8\sigma_g \rightarrow 8\pi_u$ $7\sigma_u \rightarrow 7\pi_g$ $7\sigma_g \rightarrow 7\pi_u$ $6\sigma_u \rightarrow 6\pi_g$ $6\sigma_g \rightarrow 6\pi_u$ $2\pi_g \rightarrow 9\sigma_u$ $6\sigma_g \rightarrow 8\pi_u$	$\Sigma_5 \rightarrow \Pi_5$ $\Sigma_4 \rightarrow \Pi_4$ $\Sigma_3 \rightarrow \Pi_3$ $\Sigma_2 \rightarrow \Pi_2$ $\Sigma_1 \rightarrow \Pi_1$ d-band $\rightarrow \Sigma_8$ $\Sigma_1 \rightarrow \Pi_5$	-0.27 -0.25 -0.12 -0.27 -0.15 -0.28 -0.03

5.4.2 Absorption spectra of dimers

In this section, we analyze the changes in the optical absorption spectra of the dimers compared to the spectrum of the monomer as a function of inter-particle distance. For this, we examine the evolution of the absorption spectra as the separation distance decreases from 2 nm to 0.4 nm using increments of 0.1 nm (Figure 5-5). When the monomers are separated by large distances from each other (i.e. above approximately 0.7 nm), the dimer spectrum are similar to the spectrum of the monomer except that the intensities of both longitudinal and transverse peaks are doubled due to the presence of two monomers. However, when the separation between the monomers is less than 0.7 nm, a new peak (called a charge transfer peak in this text, which will be verified later in this work) begins to emerge between the longitudinal and the transverse peak for all investigated systems (Ag_4, Ag_6 and Ag_{10}). This peak emerges between 4 eV and 5 eV for every system. It increases in intensity and red-shifts from its initial position as the separation between monomers further decreases. Correspondingly, the intensity of the transverse peak also decreases.

In order to study the origin of the charge transfer peak, such as whether or not it is part of transverse peak that has red shifted from the transverse peak position, we computed the spectra at additional separation distances between 0.7 nm and 0.6 nm. Spectra at some of these distances are included in Figure 5-5b for the Ag_6 dimer. These spectra show that the peak does not shift continuously from the transverse peak position. It appears between 4 eV and 5 eV for every system as the distance decreases; upon further decreasing the inter-particle distance, the charge-transfer peak starts to red-shift from its position and increases in intensity.

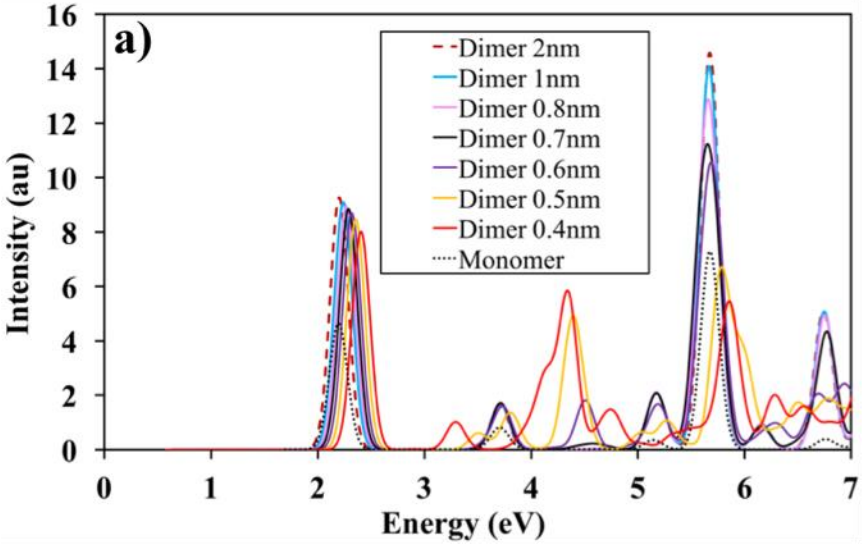
a)
Dimer 2nm
Dimer 1nm
Dimer 0.8nm
Dimer 0.7nm
Dimer 0.6nm
Dimer 0.5nm
Dimer 0.4nm
Monomer
Intensity (au)
Energy (eV)

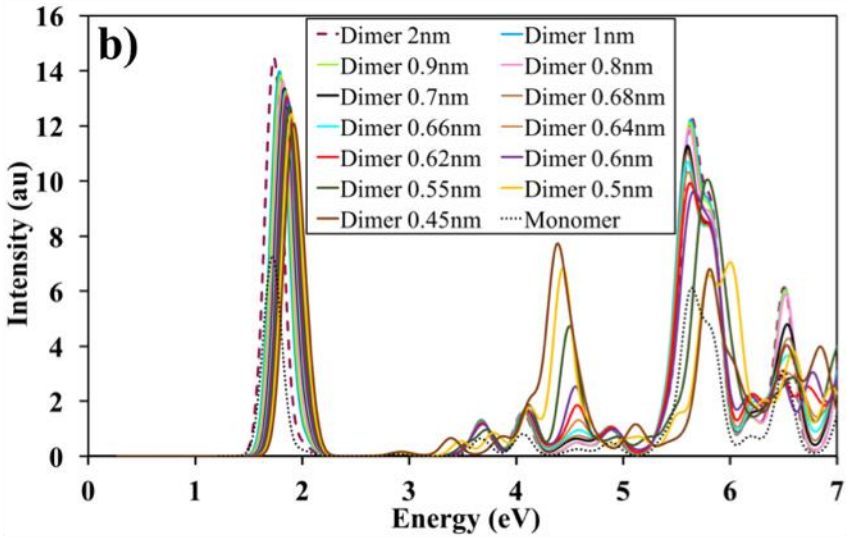
b)
Dimer 2nm
Dimer 1nm
Dimer 0.9nm
Dimer 0.8nm
Dimer 0.7nm
Dimer 0.68nm
Dimer 0.66nm
Dimer 0.64nm
Dimer 0.62nm
Dimer 0.6nm
Dimer 0.55nm
Dimer 0.5nm
Dimer 0.45nm
Monomer
Intensity (au)
Energy (eV)

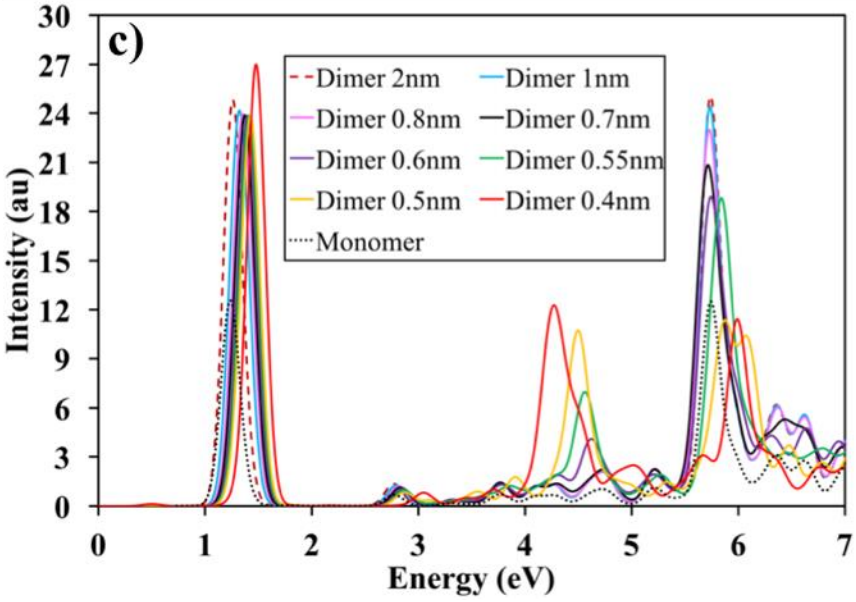
c)
Dimer 2nm
Dimer 1nm
Dimer 0.8nm
Dimer 0.7nm
Dimer 0.6nm
Dimer 0.55nm
Dimer 0.5nm
Dimer 0.4nm
Monomer
Intensity (au)
Energy (eV)

Figure 5-5 Absorption spectra for the dimers of a) Ag_4, b) Ag_6 and c) Ag_{10} nanowires. Spectra for only selected inter-particle distances are shown for clarity.

The longitudinal peak of the dimer blue-shifts slightly with decreasing gap distance (Figure 5-5). The intensity of this peak decreases as the inter-particle separation decreases. The blue-shift of longitudinal peak can be well explained using the concept of plasmon hybridization.[58] Plasmons can couple based on the dipole-dipole interaction model as shown in Figure 5-6. Hybridization results from coupling of plasmon modes analogous to bonding and antibonding interactions of molecular orbitals. The blue-shift of the longitudinal peak with the decrease in the gap is due to the bright mode being higher in energy which is a result of the repulsive dipole-dipole interaction between nanowires as shown in Figure 5-6. As the separation between monomers decreases, the interaction between the nanowires leads to a greater separation between bright and dark modes. Since the higher energy mode is the bright mode, the longitudinal peak blue-shifts on decreasing the separation between the monomers.

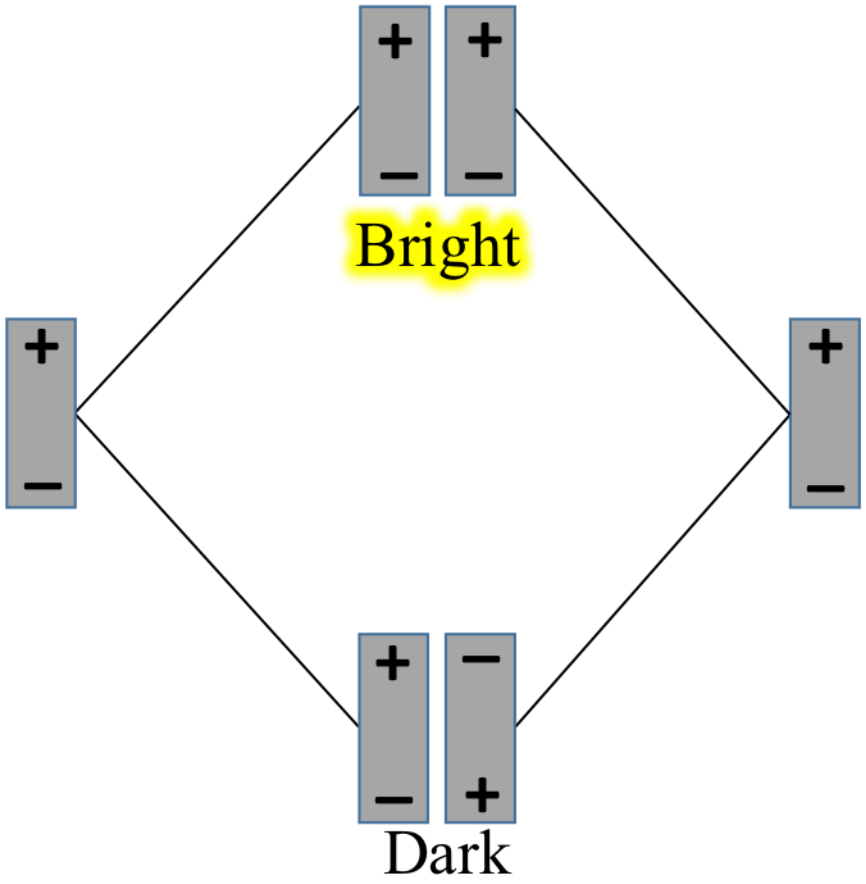

Figure 5-6 Longitudinal plasmon interaction that cause blue-shift in peak position in decreasing the gap between monomers.

Symmetry analysis of individual peaks shows that the longitudinal peak has B_{1u} (*z*-polarized) symmetry while the transverse peak has both B_{2u} (*y*-polarized) and B_{3u} (*x*-polarized) symmetry. If one examines the orbital transitions and the symmetry of the charge transfer peak, it can be seen that the charge transfer peak has only a B_{2u} symmetry contribution. The appearance of the charge transfer peak becomes more clear by studying the transverse plasmons in each nanowire monomer and the interaction between them. The inter-particle interactions between the B_{2u} and B_{3u} plasmon modes that contribute to the transverse plasmon peak are shown schematically in Figure 5-7. The *x*-polarized plasmon and *y*-polarized plasmon interactions yield a bright mode for

the higher and lower energy levels, respectively. The charge transfer peak has B_{2u} symmetry, similar to the *y*-polarized transverse mode. Because of the geometrical considerations, the interaction between the *y*-polarized transverse modes is stronger compared to the interaction between *x*-polarized transverse modes as the gap distance decreases between monomers. As a result, the *y*-polarized plasmon peak exhibits more splitting of its energy levels which causes its bright mode to red-shift. The interaction between the *x*-polarized plasmon increases upon decreasing the separation, but it is less compared to that of the *y*-polarized plasmon. In consequence, the plasmon peak with B_{3u} symmetry shifts slightly towards the higher energy side but this shift is less compared to that of the B_{2u} plasmon peak.

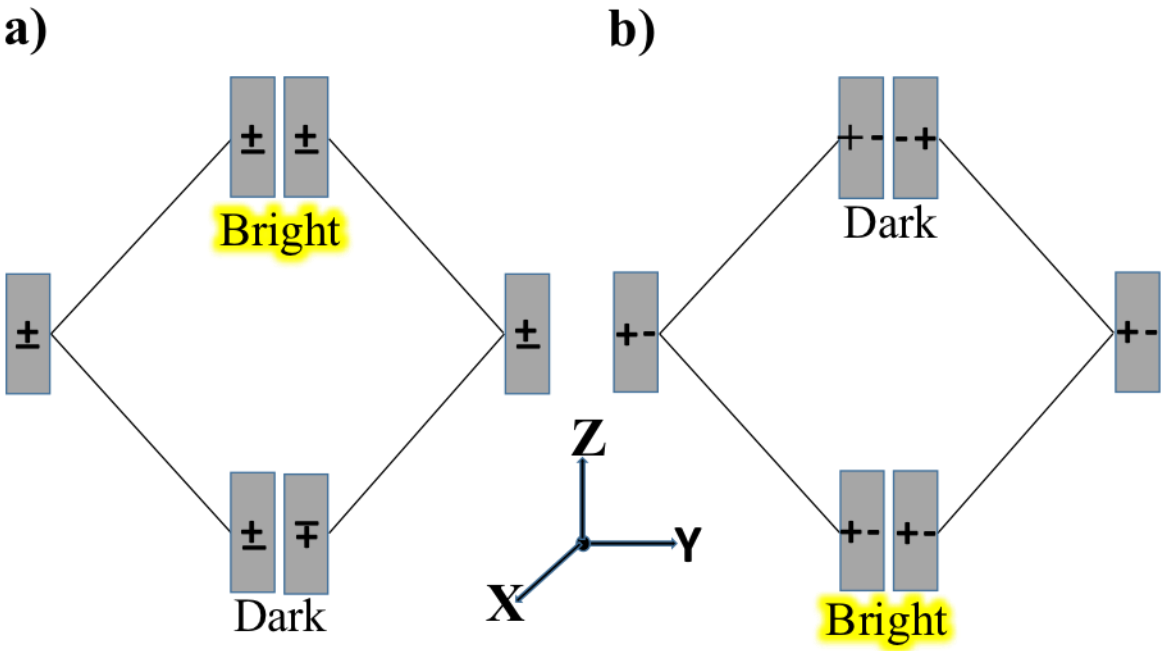

Figure 5-7 Transverse plasmon interaction in nanowires a) *x*-polarized, b) *y*-polarized. The long axis of the nanowires lies along the z-axis and the inter-particle axis is the y-axis.

When we look at the optical absorption spectrum for each dimer (Figure 5-5), the new feature in the spectrum (the charge-transfer peak) grows as the inter-particle separation is decreased. The charge transfer peak increases in intensity whereas the transverse peak decreases in intensity upon decreasing the separation between monomers. This supports the idea that this peak is related to the transverse plasmon mode, although it is not simply a red-shifted transverse peak.

To investigate further, we plotted separate absorption spectra for each of the symmetries (plasmon polarization directions) that contribute to the overall absorption spectra for the dimers of Ag_4, Ag_6 and Ag_{10} nanowires (Figures S2 and S3). The charge transfer peak has only B_{2u} symmetry which is the symmetry group of the *y*-polarized transverse mode of the plasmon (i.e. the transverse mode that is polarized along the inter-particle axis). The transverse peak around 5.7 eV does not continuously red-shift with decreasing inter-particle distance to create the charge transfer peak near 4.3 eV. Instead, the charge transfer appears when the inter-particle distance is approximately 0.7 nm, and increases in intensity dramatically and red-shifts slightly as the inter-particle distance decreases; in contrast, at separation distances below 0.7 nm, the *y*-polarized transverse mode near 5.7 eV shifts to higher energy (reversing its previous trend toward lower energy) and decreases in intensity.

We also see from Figure 5-5 that the intensity of the longitudinal peak becomes smaller with decreasing gap distance in all dimers. Similarly, Figure B-2 and Figure B-3 show that the B_{1u} peak is shifting to higher energy at smaller inter-particle distance. On looking at the spectra of Ag_{10} at the 0.4 nm inter-particle distance in Figure 5-5, we see that the intensity increases instead of decreasing unlike in other dimer systems and at other inter-particle separations. The cause of this can be understood by considering the peak contributions. Symmetry contribution plots for

Ag_{10} (Figure B-3) show that B_{2u} symmetry also contributes to the longitudinal peak at the 0.4 nm inter-particle distance for this nanowire. However in other systems, there is no other symmetry contribution to the longitudinal peak except B_{1u} at any separation. This extra B_{2u} may have increased the intensity of Ag_{10} at 0.4 nm.

Overall, in the case of larger gap distances, the quantum mechanical effects can be neglected. However, as the gap distance become less than 0.7 nm, quantum mechanical effects become important. We see that the new charge transfer peaks appear at small monomer separations which is likely caused due to the overlapping of the electron densities of the two closely placed nanoparticles (Figure 5-5).

5.4.2.1 Symmetries, transitions and orbitals for the main absorption peaks in dimers

Table 5-3 lists the main transitions, symmetry and orbitals for the longitudinal peak of Ag_4, Ag_6 and Ag_{10} nanowire dimers. It is clear from the table that the longitudinal peak of all nanowire dimers have $\Sigma \rightarrow \Sigma$ transitions with B_{1u} symmetry. For dimers at all separations, the longitudinal peak arises due to $\Sigma_n^* \rightarrow \Sigma_{n+1}^*$ and $\Sigma_n \rightarrow \Sigma_{n+1}$ transitions with B_{1u} symmetry. The symmetry contribution (B_{1u}) and the type of orbital transitions ($\Sigma \rightarrow \Sigma$) that corresponds to the longitudinal peak of dimers do not change with the change in inter-particle distance. So, the symmetry and transitions given in Table 5-3 are applicable to the dimers at all inter-particle separation. However, it should be noted that a small B_{2u} contribution does arise at 0.4 nm for the Ag_{10} dimer as seen in Figure B-3.

Symmetry contributions to the transverse peak are different at large and small inter-particle distances, unlike for the longitudinal peak. Table 5-4 shows the transitions that contribute to the transverse peak of Ag_4 dimer at large (2 nm) and small (0.4 nm) inter-particle distance. B_{2u} and

B_{3u} symmetries contribute to the transverse peak at large separation whereas at small separation, only the B_{3u} symmetry contributes to the transverse peak. Table 5-4 shows that the transverse peak in dimers is due to $\Sigma_n^* \rightarrow \Pi_n^*$and $\Sigma_n \rightarrow \Pi_n$ with B_{3u} symmetry as well as $\Sigma_n \rightarrow \Pi_n^*$ and $\Sigma_n^* \rightarrow \Pi_n$ transitions with B_{2u} symmetry at large inter-particle separation (2 nm). At interacting inter-particle distance (0.4 nm), only transitions with B_{3u} symmetry contribute to the transverse peak and B_{2u} symmetry transitions no longer contribute to the transverse peak. Ag_6 and Ag_{10} dimers have the same symmetry contributions and similar transitions including some additional transitions in between the orbitals having more number of nodes. For the naming of orbitals, the Greek letter and the subscript denote the delocalized monomer orbitals involved in the dimer orbital and a "*" denotes an inter-particle antibonding nature of the monomer orbitals as shown in Figure 5-8. Overall, the transitions in Table 5-3, Table 5-4 and Table 5-5 show that the $\Sigma \rightarrow \Sigma$ transitions contribute to the longitudinal peak whereas the transverse and charge transfer peak have $\Sigma \rightarrow \Pi$ transitions. Figure 5-8 shows some of the orbitals that contribute to these peaks.

Table 5-3 Symmetry, main transitions and orbital contributions for the longitudinal peak of dimers.

Nanowire	Symmetry	Transitions (Symmetry representation)	Transitions (Delocalized orbital notation)
Ag_4	B_{1u}	$7b_{3g} \rightarrow 8b_{2u}$	$\Sigma_2^* \rightarrow \Sigma_3^*$
		$7b_{1u} \rightarrow 8a_g$	$\Sigma_2 \rightarrow \Sigma_3$
Ag_6	B_{1u}	$11b_{2u} \rightarrow 11b_{3g}$	$\Sigma_3^* \rightarrow \Sigma_4^*$
		$11a_g \rightarrow 11b_{1u}$	$\Sigma_3 \rightarrow \Sigma_4$
Ag_{10}	B_{1u}	$18b_{2u} \rightarrow 18b_{3g}$	$\Sigma_5^* \rightarrow \Sigma_6^*$
		$18a_g \rightarrow 18b_{1u}$	$\Sigma_5 \rightarrow \Sigma_6$

Table 5-4 Symmetry, main transitions and orbital contributions for the transverse peak of Ag_4 dimer at large and small separation.

Separation	Symmetry	Transitions	Transitions

		(Symmetry representation)	(Delocalized orbital notation)
2 nm	B_{3u}	$7b_{1u} \rightarrow 5b_{2g}$ $7b_{3g} \rightarrow 5a_u$ $7a_g \rightarrow 5b_{3u}$ $7b_{2u} \rightarrow 5b_{1g}$	$\Sigma_2 \rightarrow \Pi_2$ $\Sigma_2^* \rightarrow \Pi_2^*$ $\Sigma_1 \rightarrow \Pi_1$ $\Sigma_1^* \rightarrow \Pi_2^*$
	B_{2u}	$7b_{1u} \rightarrow 9b_{3g}$ $7b_{3g} \rightarrow 9b_{1u}$ $7a_g \rightarrow 9b_{2u}$ $7b_{2u} \rightarrow 9a_g$	$\Sigma_2 \rightarrow \Pi_2^*$ $\Sigma_2^* \rightarrow \Pi_2$ $\Sigma_1 \rightarrow \Pi_1^*$ $\Sigma_1^* \rightarrow \Pi_1$
0.4 nm	B_{3u}	$7b_{1u} \rightarrow 5b_{2g}$ $7a_g \rightarrow 5b_{3u}$ $7b_{3g} \rightarrow 5a_u$ $7b_{2u} \rightarrow 5b_{1g}$	$\Sigma_2 \rightarrow \Pi_2$ $\Sigma_1 \rightarrow \Pi_1$ $\Sigma_2^* \rightarrow \Pi_2^*$ $\Sigma_1^* \rightarrow \Pi_1^*$

Table 5-5 Symmetry, main transitions and orbital contributions for the charge transfer peak of dimers at 0.5 nm.

Nanowire	Symmetry	Transitions (Symmetry representation)	Transitions (Delocalized orbital notation)
Ag_4	B_{2u}	$7b_{3g} \rightarrow 9b_{1u}$	$\Sigma_2^* \rightarrow \Pi_2$
		$7b_{2u} \rightarrow 9a_g$	$\Sigma_2^* \rightarrow \Pi_2$
Ag_6	B_{2u}	$11b_{2u} \rightarrow 14a_g$	$\Sigma_3^* \rightarrow \Pi_3$
		$10b_{3g} \rightarrow 13b_{1u}$ $10b_{2u} \rightarrow 13a_g$	$\Sigma_2^* \rightarrow \Pi_2$ $\Sigma_1^* \rightarrow \Pi_1$
Ag_{10}	B_{2u}	$18b_{2u} \rightarrow 24a_g$	$\Sigma_5^* \rightarrow \Pi_5$
		$17b_{3g} \rightarrow 22b_{1u}$ $17b_{2u} \rightarrow 22a_g$ $16b_{3g} \rightarrow 20b_{1u}$ $16b_{2u} \rightarrow 21a_g$	$\Sigma_4 \rightarrow \Pi_4$ $\Sigma_3^* \rightarrow \Pi_3$ $\Sigma_2^* \rightarrow \Pi_2$ $\Sigma_1^* \rightarrow \Pi_1$

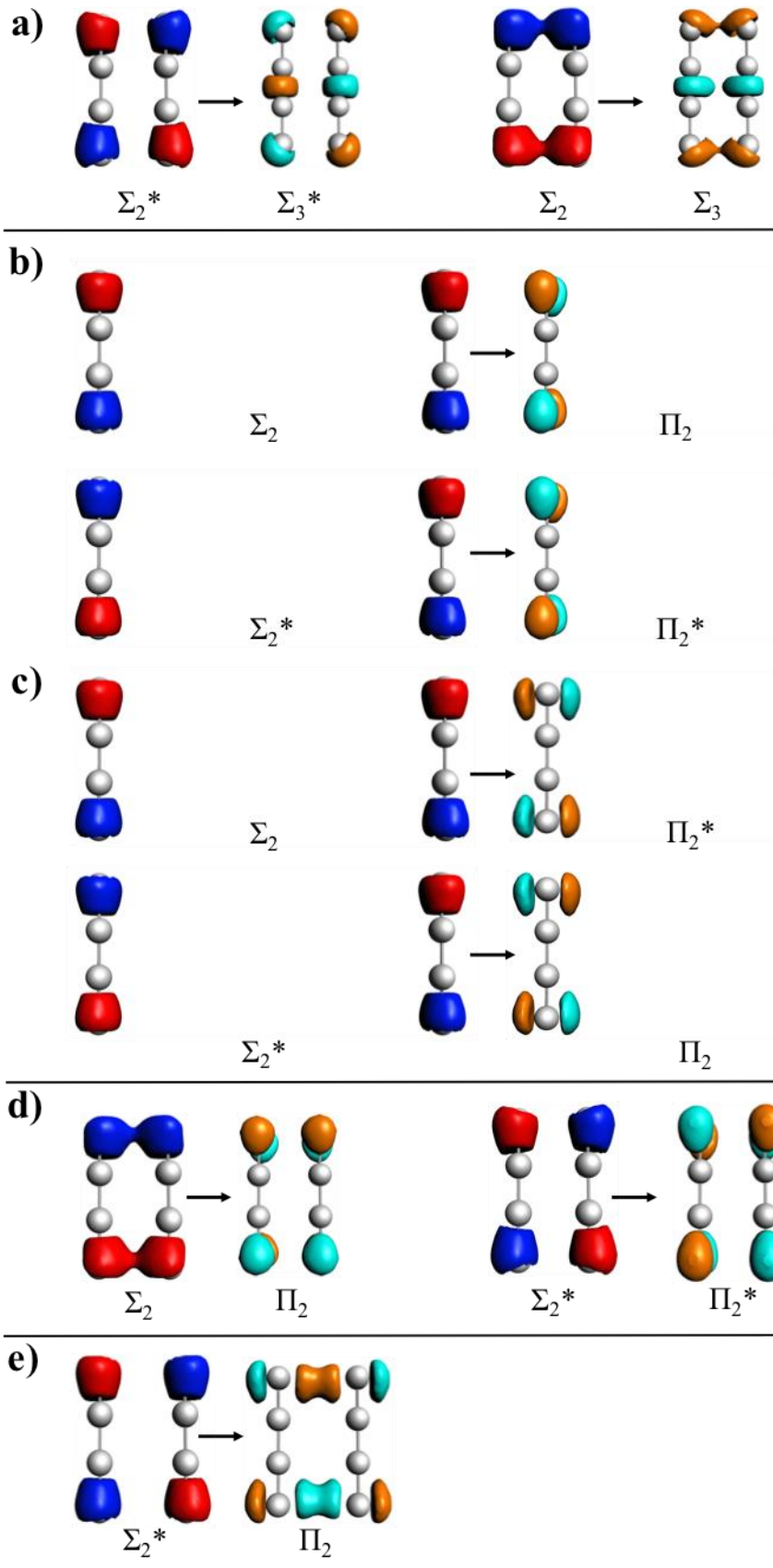
a)
Σ_2*
Σ_3*
Σ_2
Σ_3
b)
Σ_2
Π_2
Σ_2*
Π_2*
c)
Σ_2
Π_2*
Σ_2*
Π_2
d)
Σ_2
Π_2
Σ_2*
Π_2*
e)
Σ_2*
Π_2

Figure 5-8 Examples of occupied-to-virtual orbital transitions contributing to the (a) longitudinal peak of Ag_4 dimer as shown in Table 5-3, (b) transverse peak of Ag_4 dimer at 2 nm separation and with B_{3u} symmetry as shown in Table 5-4, (c) transverse peak of Ag_4 dimer at 2 nm separation and with B_{2u} symmetry as shown in Table 5-4, (d) transverse peak of Ag_4 dimer at 0.4 nm separation as shown in Table 5-4, (e) charge transfer peak of the Ag_4 dimer at 0.5 nm as shown in Table 5-4 drawn with a contour value of 0.03.

5.4.2.2 Transition electron densities

In order to understand more about the types of transitions that make up the different peaks in the absorption spectra, we studied the transition densities for the strongest excited state (i.e. the excited state with the highest oscillator strength) corresponding to each plasmon peak (Figure 5-9). These transition densities are shown for inter-particle distances of 2 nm (large separation between the monomers) and 0.5 nm (small separation between the monomers) for the Ag_4 nanowire dimer. Transition densities were similarly studied for other separations as well (not shown). The transition densities of other close-lying excitations with smaller oscillator strengths are similar to those of the strong excitations as shown in the Supporting Information (Figure B-4).

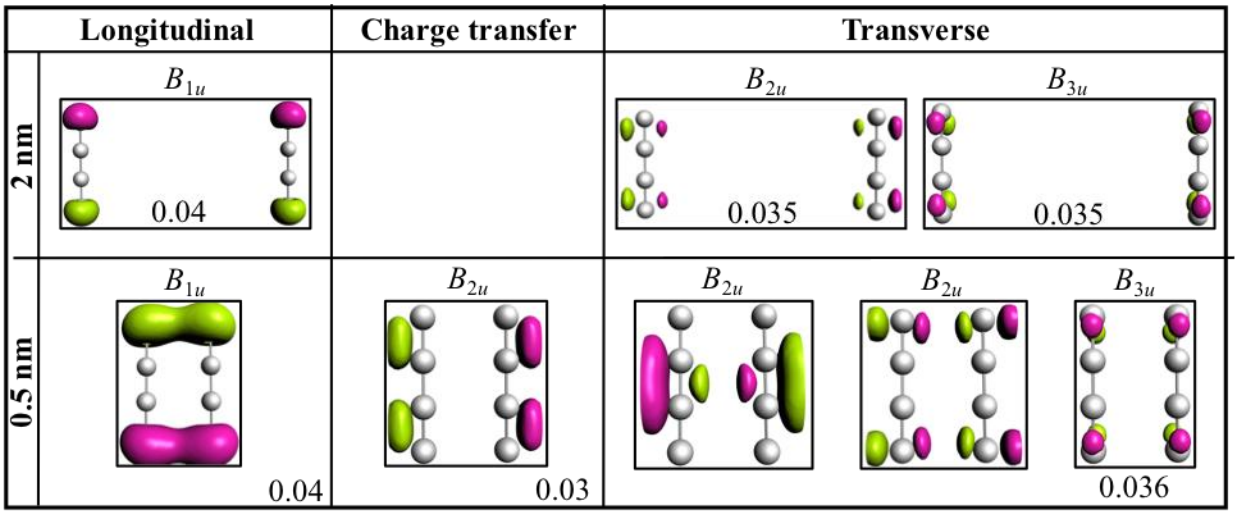

Figure 5-9 Transition electron densities for the strongest peaks of Ag_4 dimer at the iso-value of 0.02 unless stated in inset.

In Figure 5-9, transition electron densities for the longitudinal peak at both large and small separation show longitudinal character (i.e. the movement of electron density along the long axis). Similarly, the transition electron densities for the transverse peaks at all separations show transverse character where the movement of electron density is perpendicular to the long axis. The charge transfer peak does not appear when the inter-particle distance is large (e.g. 2 nm), whereas it appears for small inter-particle distances (e.g. 0.5 nm). The transition densities demonstrate that this peak has charge transfer character because the movement of electron density occurs from one wire to the other. Transition electron densities for the middle peak of Ag_6 and Ag_{10} are given in the supporting information (Figure B-5) which show similar charge transfer character.

Overall, from 2 nm until 0.7 nm, there is very little coupling between the nanowires. After 0.7 nm, the coupling between the nanowires favors the tunneling of electrons between the two monomers. In consequence, quantum mechanical effects are especially necessary to include at small separation distances.

Because calculations with pure GGA functional are known to overestimate charge transfer,[111] we also performed calculations using the time-dependent Hartree-Fock (TDHF) approximation to examine whether any charge transfer artifacts arise due to the use of the GGA functional (Figure 5-10). Although the longitudinal and transverse peak positions obtained with TDHF are somewhat shifted compared to the peak positions obtained with the GGA functional, both levels of theory agree on the formation of a charge transfer peak with B_{2u} symmetry that occurs between 4 eV and 5 eV and has charge transfer character in the transition electron density (Figure 5-10). A picture of the spectra obtained with TDHF calculation at different monomer separations along with their transition density plots are shown in Figure B-6. One noticeable difference between the TDDFT calculations (with a pure GGA functional) and the TDHF

calculations is that the charge transfer peak shifts gradually during the TDHF calculations, unlike in the TDDFT calculations; this is likely due to differences in the interaction term between the excited determinants as previously observed in TDHF and TDDFT calculations on nanowires arranged in an end-to-end fashion.[88] This suggests that the sudden appearance of the charge-transfer peak in calculations using a pure GGA functional may be an artifact, although the existence of the charge-transfer peak is not.

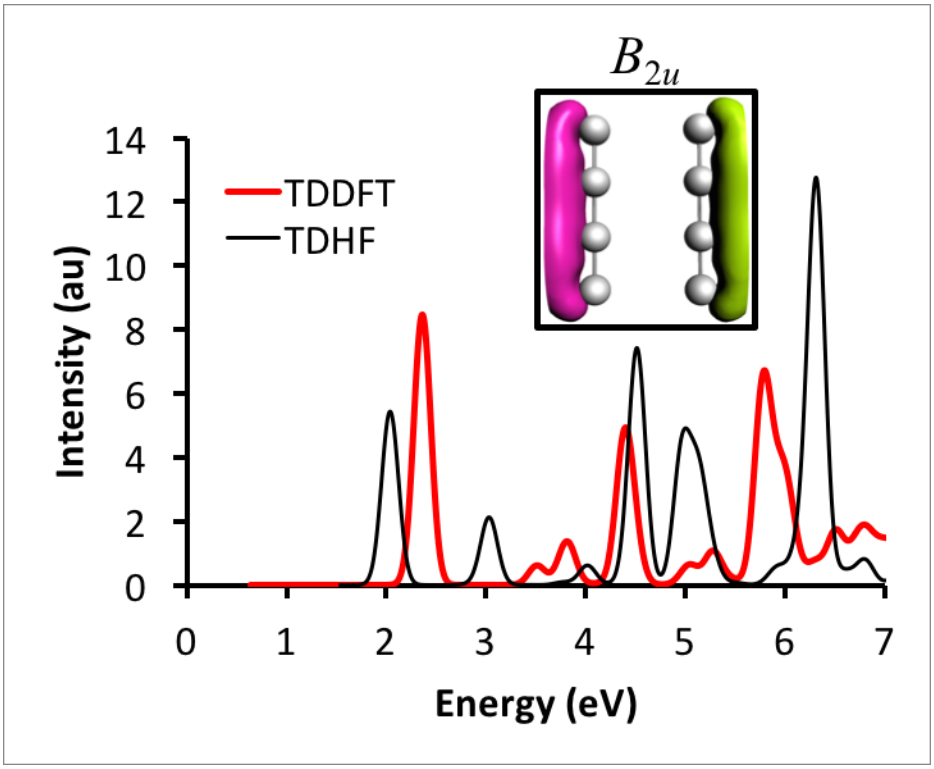

Figure 5-10 Optical absorption spectra showing the main peaks computed with TDDFT (red plot) and TDHF (black plot). The inset shows the TDHF transition electron density (iso-value = 0.03) for the charge transfer peak between 4 eV and 5 eV with B_{2u} symmetry.

5.4.3 Absorption spectra of trimers

Absorption spectra are also obtained for trimers of Ag_n (n = 4, 6, 10) in the dolmen structure with C_{2v} symmetry. Spectra for the Ag_4 trimer at inter-particle distances of 2 nm to 0.4 nm are

shown in Figure 5-11. Spectra for Ag_6 and Ag_{10} trimers at different inter-particle separations have similar trends (Figure B-7). Throughout this section, the Ag_6 and Ag_{10} trimers yield the same results as Ag_4 and are not discussed in detail.

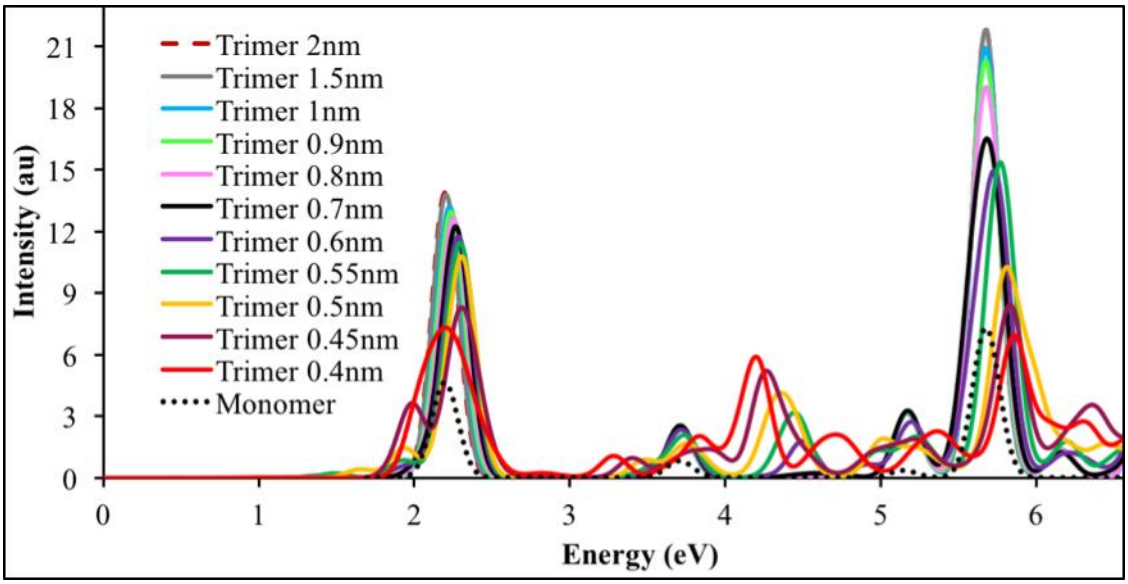

Figure 5-11 Absorption spectra for Ag_4 trimer

A blue-shift of the longitudinal peak is apparent in the trimer similar to the dimer, but additional shoulder peaks are also seen on the lower energy side when the monomer separation is 0.6 nm or less. The intensity of the shoulder peak increases upon decreasing the separation between the monomers. At 0.45 nm, the peak no longer blue-shifts and instead its energy remains constant. At 0.4 nm, the shoulder peak is not noticeable due to the employed smoothing, but it is still present. The intensity of the longitudinal peak decreases more for the trimers when compared to the case in the dimers for decreasing gap distance.

For the dimer structure, both nanowires lie on the z-axis, so there is interaction only between the two *z*-polarized plasmons for the longitudinal peak of the dimer. In the trimer, one difference compared to the longitudinal peak of the dimer is that there are many possible

interactions between the different plasmon modes in the three nanowires (Figure B-8). Because the parallel dimer is aligned on the z-axis, the longitudinal peak is the *z*-polarized plasmon. However, because the long axis of the capping monomer lies on the y-axis in the trimer, the *y*-polarized plasmon also contributes to the longitudinal peak as also observed in the absorption spectrum. At small separation distances, there are significant interactions between the monomer plasmons that give different symmetries for the longitudinal peak. These interactions give rise to other unique features in the trimer spectra compared to the dimer spectra. For the C_{2v} trimer, two symmetries contribute to the longitudinal peak in the trimer: A_1 (*z*-polarized) from the parallel dimer and B_2 (*y*-polarized) from the capping nanowire. The transition electron densities of the most important excitations that that contribute to the longitudinal peak of the Ag_4 trimer obtained at different inter-particle separations are given in Figure B-9. Absorption spectra for the individual symmetry contributions of the Ag_4 trimer are also plotted which clearly show the symmetry contributions to the different peaks (Figure B-10).

Similarly, the transverse plasmons have different polarization directions. Unlike in the dimer transverse peak, a *z*-polarized excitation also contributes to the transverse peak of the trimer because it is the transverse plasmon peak of the capping nanowire (Figure 5-12a). The transverse plasmon oscillations in capping nanowires interact with the bright and dark modes obtained from the transverse oscillations in dimer nanowires. An interaction picture of the bright modes from Figure 5-7 with different possible plasmon oscillations of the capping nanowire is illustrated in Figure 5-12. The *y*-polarized transverse dimer plasmon interacts with the *y*-polarized plasmon in the capping nanowire; similarly, the *x*-polarized plasmon from the dimer interacts with the *x*-polarized plasmon in the capping nanowire. Overall, the transverse peak in trimer has A_1 (from *z*-polarized transverse plasmon of capping monomer as shown in Figure 5-12), B_1 (from *x*-polarized

plasmon contribution of both dimer and capping monomer) and B_2 (from *y*-polarized transverse plasmon in dimers and capping monomer) symmetry contributions.

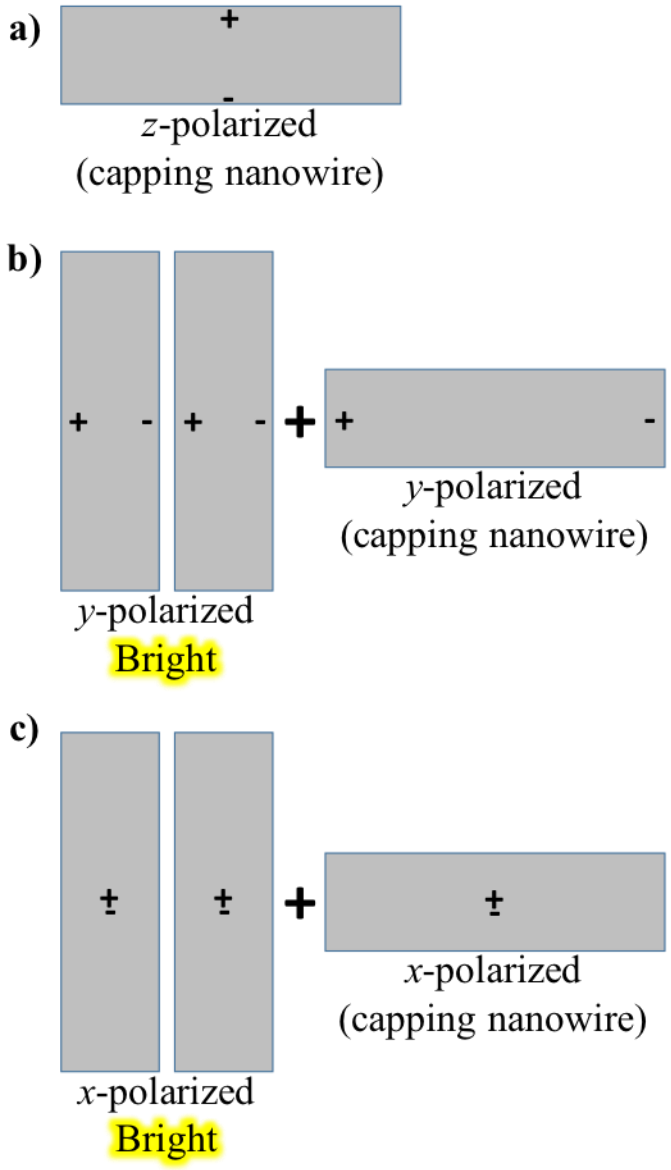

Figure 5-12 a) The *z*-polarized transverse plasmon in the capping nanowire which also contributes to the transverse absorption peak in the trimer system. Interaction of bright b) *y*-polarized and c) *x*-polarized transverse dimer plasmons shown in Figure 5-7 with *y*- and *x*-plasmon excitations from the capping nanowire, respectively.

Similar to the charge transfer peak in the dimer, the charge transfer peak in the trimer appears for monomer gaps of 0.6 nm or less and is *y*-polarized (B_2 symmetry). Upon further decreasing the inter-particle separation, the charge transfer peak red-shifts and increases in intensity while the transverse peak slightly blue-shifts and decreases in intensity, similar to the dimer spectra. It should be noted that the capping monomer plasmon has an insignificant contribution to the charge transfer peak compared to the dimer subsystem.

5.4.3.1 Symmetry, transitions and orbitals for the main peaks in trimers

Table 5-6 Symmetry, main transitions and orbital contributions for the longitudinal peak of Ag_4 trimer at large and small inter-particle separation.

Separation	Symmetry	Transitions (Symmetry representation)	Transitions (Delocalized orbital notation)
2 nm	B_2	$20b_2 \rightarrow 22a_1$	$^{cap}\Sigma_2 \rightarrow {}^{cap}\Sigma_3$
	A_1	$21b_2 \rightarrow 22b_2$ $21a_1 \rightarrow 23a_1$	$^{dimer}\Sigma_2{*} \rightarrow {}^{dimer}\Sigma_3{*}$ $^{dimer}\Sigma_2 \rightarrow {}^{dimer}\Sigma_3$
0.4 nm	B_2	$19b_2 \rightarrow 22a_1$	$^{cap}\Sigma_2 \rightarrow {}^{cap}\Sigma_3$
	A_1	$21a_1 \rightarrow 23a_1$ $21b_2 \rightarrow 22b_2$	$^{dimer}\Sigma_2 \rightarrow {}^{dimer}\Sigma_3$ *and* $^{cap}\Sigma_1$ $^{dimer}\Sigma_2{*} \rightarrow {}^{dimer}\Sigma_3{*}$

From Table 5-6, at large separations the transitions do not mix; they occur from cap to cap or from dimer to dimer. However, at small inter-particle separation (e.g. 0.4 nm), there is interaction between the capped monomer and the dimer subsystem. This kind of interaction is observed for other investigated systems Ag_6 and Ag_{10}: the interaction between the cap and the dimer part is seen only at small separation distances and is not observed at all at large separations. Thus, the capped monomer does not interact with the dimer as strongly as the two monomers in dimers interact although they are at the same separation distance.

5.4.3.2 Transition electron densities

Transition electron densities for the main peaks of the Ag_4 trimer are shown in Figure 5-13. The longitudinal peak arises from plasmon oscillation along the long axis of the parallel nanowire dimer (*z*-polarized plasmon) and in the long axis of the capping nanowire (*y*-polarized plasmon). Interaction between the dimer and the capping monomer appears at the smaller inter-particle distance of 0.5 nm but not at the larger separation. Similarly, the transition electron densities for the transverse peak of the trimer show *x*-, *y*-, and *z*- polarized plasmon contributions. The peak obtained in between 4 eV and 5 eV in the trimer has charge transfer character similar to the charge transfer peak in the dimer. Other systems (Ag_6 and Ag_{10}) have similar transition electron densities as the Ag_4 trimer system. We also performed TDHF calculations with the trimer which similarly yielded a new feature between 4 eV and 5 eV having charge transfer character. Thus, both the dimer and the dolmen trimer exhibit a new charge transfer peak for small inter-particle separations. The unique feature of the dolmen trimer compared to the dimer is the appearance of a new shoulder peak on the lower energy side of longitudinal peak. The TDDFT and TDHF transition electron densities for that peak are shown in Figure 5-14. We can see that TDDFT predicts that both the A_1 and B_2 symmetry contribute to this peak whereas TDHF only predicts a B_2 symmetry contribution. The transition densities with A_1 symmetry from TDDFT show charge transfer between the parallel dimer and capping monomer. However, the transition density plots with B_2 symmetry obtained from both TDDFT and TDHF do not show charge transfer character. Because charge transfer character of the longitudinal peak with A_1 symmetry is not obtained with TDHF, TDDFT appears to overestimate the charge transfer for this peak.

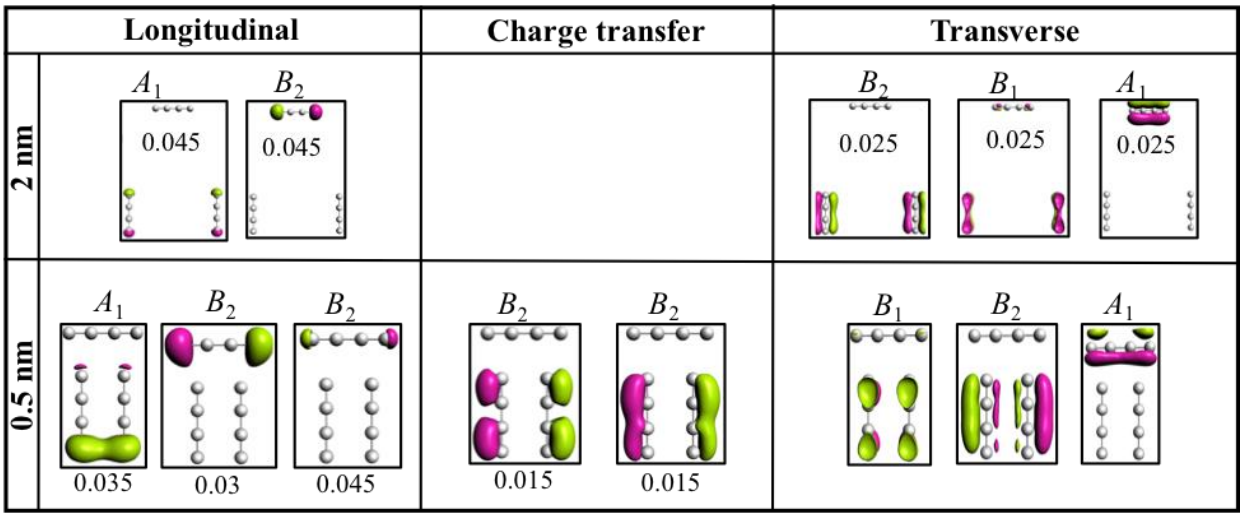

Figure 5-13 Transition electron densities for major peaks of Ag_4 trimer at 2 nm and 0.5 nm inter-particle distance obtained at iso-value of 0.02 unless stated.

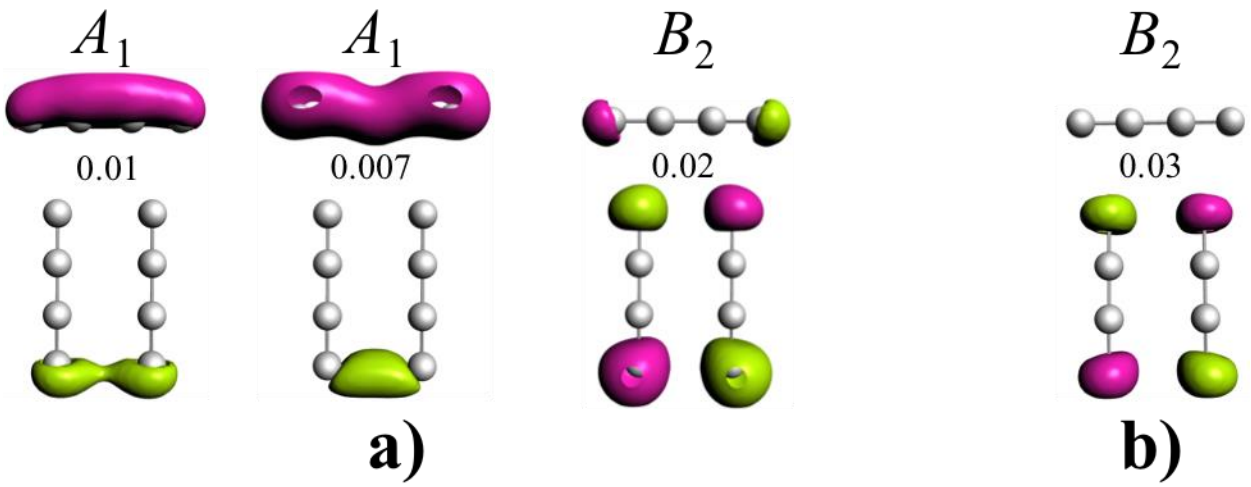

Figure 5-14 Transition electron density plots for the shoulder on the lower energy side of the longitudinal peak of the Ag_4 trimer at 0.5 nm interparticle distance obtained with an iso-value of 0.005 (a) from TDDFT (b) from TDHF.

5.5 Conclusion

In nanowire monomers, the longitudinal peak (Σ symmetry) is due to Σ → Σ transitions and the transverse peak (Π symmetry) arises due to Σ → Π transitions. The longitudinal peak red-

shifts upon increasing the chain length. For dimers at all separations, the longitudinal peak arises due to $\Sigma_n^* \rightarrow \Sigma_{n+1}^*$ and $\Sigma_n \rightarrow \Sigma_{n+1}$ transitions with B_{1u} symmetry. The transverse peak in dimers is due to $\Sigma_n^* \rightarrow \Pi_n^*$ and $\Sigma_n \rightarrow \Pi_n$ transitions having B_{3u} symmetry and $\Sigma_n \rightarrow \Pi_n^*$ and $\Sigma_n^* \rightarrow \Pi_n$ transitions having B_{2u} symmetry at large separation; at closer interparticle distances, only B_{3u} contributes. For trimers, the longitudinal peak has contributions from B_2 and A_1 symmetry at all separation distances. At large inter-particle distances, the transitions are ${}^{cap}\Sigma_n \rightarrow {}^{cap}\Sigma_{n+1}$ with B_2 symmetry. The longitudinal peak also has ${}^{dimer}\Sigma_n^* \rightarrow {}^{dimer}\Sigma_{n+1}^*$ and ${}^{dimer}\Sigma_n \rightarrow {}^{dimer}\Sigma_{n+1}$ transitions with A_1 symmetry when the separation is large between the monomers. Thus, the transitions occur within the same subsystem at large separation distances. When the separation between the monomers is small, transitions between the capping monomer and dimer subsystem also occur as shown in Table 5-6 for an interparticle distance of 0.4 nm. The transverse peak arises from B_2, B_1 and A_1 transitions at large separation distances, but only arises from B_1 and A_1 at small separations.

Overall, we used the plasmon hybridization model and electron transition densities to analyze different features in the absorption spectra of parallel dimers and dolmen trimers of linear nanowires. Plasmon resonances of composite systems are found to arise from hybridized modes of individual nanoparticle plasmons which can be helpful to tune the optical properties. The plasmon hybridization model explains the shift of plasmon peaks for different inter-particle separations. We studied the possible bright and dark modes that can arise upon interaction of nanowire monomers at different separation distances. We found that the strong coupling between the nanowires and the tunneling of electrons at short inter-particle distances in nanowire dimers and trimers favors the creation of a new charge transfer peak. At interacting inter-particle distances, the charge transfer peak originates from $\Sigma_n^* \rightarrow \Pi_n$ transitions with B_{2u} and B_2 symmetry for the

dimer and trimer respectively. Time-dependent Hartree-Fock calculations confirmed the presence of the charge transfer peak in Ag_4.

We hope this study will generate new avenues in the study of plasmonics and will initiate additional research on the nature of plasmonic peaks that arise at small inter-particle distances. This study may offer a way to advance rational engineering of the desired optical response to improve light harvesting and sensing properties, thus leading to selective control of charge localization and transport.

5.6 Acknowledgements

This material is based on work supported by the Air Force Office of Scientific Research under Grant FA9550-15-0114. The computing for this project was performed on the Beocat Research Cluster at Kansas State University, which is funded in part by NSF Grants CHE-1726332, CNS-1006860, EPS-1006860, and EPS-0919443.

5.7 References

1. Kelly, K. L.; Coronado, E.; Zhao, L. L.; Schatz, G. C., The Optical Properties of Metal Nanoparticles: The Influence of Size, Shape, and Dielectric Environment. *J. Phys. Chem. C* **2003,** *107*, 668-677.

2. Aroca, R.; Price, B., A New Surface for Surface-Enhanced Infrared Spectroscopy: Tin Island Films. *J. Phys. Chem. B* **1997,** *101* (33), 6537-6540.

3. Wang, Z.; Pan, S.; Krauss, T. D.; Du, H.; Rothberg, L. J., The Structural Basis for Giant Enhancement Enabling Single-Molecule Raman Scattering. *Proc. Natl. Acad. Sci. U.S.A* **2003,** *100* (15), 8638-8643.

4. Nie, S.; Emory, S. R., Probing Single Molecules and Single Nanoparticles by Surface-Enhanced Raman Scattering. *Science* **1997,** *275* (5303), 1102-6.

5. Michaels, A. M.; Nirmal, M.; Brus, L. E., Surface Enhanced Raman Spectroscopy of Individual Rhodamine 6G Molecules on Large Ag Nanocrystals. *J. Am. Chem. Soc.* **1999,** *121* (43), 9932-9939.

6. Oldenburg, S. J.; Averitt, R. D.; Westcott, S. L.; Halas, N. J., Nanoengineering of Optical Resonances. *Chem. Phys. Lett.* **1998,** *288* (2), 243-247.

7. Graf, C.; van Blaaderen, A., Metallodielectric Colloidal Core−Shell Particles for Photonic Applications. *Langmuir* **2002,** *18* (2), 524-534.

8. Nicewarner-Peña, S. R.; Freeman, R. G.; Reiss, B. D.; He, L.; Peña, D. J.; Walton, I. D.; Cromer, R.; Keating, C. D.; Natan, M. J., Submicrometer Metallic Barcodes. *Science* **2001,** *294* (5540), 137-141.

9. Jana, N. R.; Gearheart, L.; Murphy, C. J., Wet Chemical Synthesis of High Aspect Ratio Cylindrical Gold Nanorods. *J. Phys. Chem. B* **2001,** *105* (19), 4065-4067.

10. Maillard, M.; Giorgio, S.; Pileni, M.-P., Tuning the Size of Silver Nanodisks with Similar Aspect Ratios: Synthesis and Optical Properties. *J. Phys. Chem. B* **2003,** *107* (11), 2466-2470.

11. Sun, Y.; Xia, Y., Shape-Controlled Synthesis of Gold and Silver Nanoparticles. *Science* **2002,** *298* (5601), 2176-2179.

12. Szymańska-Chargot, M.; Gruszecka, A.; Smolira, A.; Bederski, K.; Głuch, K.; Cytawa, J.; Michalak, L., Formation of Nanoparticles and Nanorods via UV Irradiation of $AgNO_3$ Solutions. *J. Alloys Compd.* **2009,** *486* (1), 66-69.

13. Kasture, M.; Sastry, M.; Prasad, B. L. V., Halide ion Controlled Shape Dependent Gold Nanoparticle Synthesis with Tryptophan as Reducing Agent: Enhanced Fluorescent Properties and White Light Emission. *Chem. Phys. Lett.* **2010,** *484* (4), 271-275.

14. Aizpurua, J.; Hanarp, P.; Sutherland, D. S.; Käll, M.; Bryant, G. W.; García de Abajo, F. J., Optical Properties of Gold Nanorings. *Phys. Rev. Lett.* **2003,** *90* (5), 057401.

15. Al-Sherbini, E.-S. A. M., UV–visible Light Reshaping of Gold Nanorods. *Mater. Chem. Phys.* **2010,** *121* (1), 349-353.

16. Ni, W.; Ambjörnsson, T.; Apell, S. P.; Chen, H.; Wang, J., Observing Plasmonic−Molecular Resonance Coupling on Single Gold Nanorods. *Nano Lett.* **2010,** *10* (1), 77-84.

17. Schmucker, A. L.; Harris, N.; Banholzer, M. J.; Blaber, M. G.; Osberg, K. D.; Schatz, G. C.; Mirkin, C. A., Correlating Nanorod Structure with Experimentally Measured and Theoretically Predicted Surface Plasmon Resonance. *ACS Nano* **2010,** *4* (9), 5453-5463.

18. Olofsson, L.; Rindzevicius, T.; Pfeiffer, I.; Käll, M.; Höök, F., Surface-Based Gold-Nanoparticle Sensor for Specific and Quantitative DNA Hybridization Detection. *Langmuir* **2003,** *19* (24), 10414-10419.

19. McFarland, A. D.; Van Duyne, R. P., Single Silver Nanoparticles as Real-Time Optical Sensors with Zeptomole Sensitivity. *Nano Lett.* **2003,** *3* (8), 1057-1062.

20. Noginov, M. A.; Zhu, G.; Belgrave, A. M.; Bakker, R.; Shalaev, V. M.; Narimanov, E. E.; Stout, S.; Herz, E.; Suteewong, T.; Wiesner, U., Demonstration of a Spaser-Based Nanolaser. *Nature* **2009,** *460* (7259), 1110-1112.

21. Xu, H.; Bjerneld, E. J.; Käll, M.; Börjesson, L., Spectroscopy of Single Hemoglobin Molecules by Surface Enhanced Raman Scattering. *Phys. Rev. Lett.* **1999,** *83* (21), 4357-4360.

22. Nie, S.; Emory, S. R., Probing Single Molecules and Single Nanoparticles by Surface-Enhanced Raman Scattering. *Science* **1997,** *275* (5303), 1102-1106.

23. Quinten, M.; Leitner, A.; Krenn, J. R.; Aussenegg, F. R., Electromagnetic Energy Transport Via Linear Chains of Silver Nanoparticles. *Opt. Lett.* **1998,** *23* (17), 1331-1333.

24. Maier, S. A.; Kik, P. G.; Atwater, H. A.; Meltzer, S.; Harel, E.; Koel, B. E.; Requicha, A. A. G., Local Detection of Electromagnetic Energy Transport Below the Diffraction Limit in Metal Nanoparticle Plasmon Waveguides. *Nat. Mater.* **2003,** *2* (4), 229-232.

25. Brongersma, M. L.; Hartman, J. W.; Atwater, H. A., Electromagnetic Energy Transfer and Switching in Nanoparticle Chain Arrays Below the Diffraction Limit. *Phys. Rev. B* **2000,** *62* (24), R16356-R16359.

26. Vasilantonakis, N.; Nasir, M. E.; Dickson, W.; Wurtz, G. A.; Zayats, A. V., Bulk Plasmon-Polaritons in Hyperbolic Nanorod Metamaterial Waveguides. *Laser Photonics Rev.* **2015,** *9* (3), 345-353.

27. Gotschy, W.; Vonmetz, K.; Leitner, A.; Aussenegg, F. R., Thin Films by Regular Patterns of Metal Nanoparticles: Tailoring the Optical Properties by Nanodesign. *Appl. Phys. B* **1996,** *63* (4), 381-384.

28. Haynes, C. L.; McFarland, A. D.; Zhao, L.; Van Duyne, R. P.; Schatz, G. C.; Gunnarsson, L.; Prikulis, J.; Kasemo, B.; Käll, M., Nanoparticle Optics: The Importance of Radiative Dipole Coupling in Two-Dimensional Nanoparticle Arrays. *J. Phys. Chem. B* **2003,** *107* (30), 7337-7342.

29. Lamprecht, B.; Schider, G.; Lechner, R. T.; Ditlbacher, H.; Krenn, J. R.; Leitner, A.; Aussenegg, F. R., Metal Nanoparticle Gratings: Influence of Dipolar Particle Interaction on the Plasmon Resonance. *Phys. Rev. Lett.* **2000,** *84* (20), 4721-4724.

30. Kahl, M.; Voges, E., Analysis of Plasmon Resonance and Surface-Enhanced Raman Scattering on Periodic Silver Structures. *Phys. Rev. B* **2000,** *61* (20), 14078-14088.

31. Félidj, N.; Aubard, J.; Lévi, G.; Krenn, J. R.; Salerno, M.; Schider, G.; Lamprecht, B.; Leitner, A.; Aussenegg, F. R., Controlling the Optical Response of Regular Arrays of Gold Particles for Surface-Enhanced Raman Scattering. *Phys. Rev. B* **2002,** *65* (7), 075419.

32. Billot, L.; Lamy de la Chapelle, M.; Grimault, A. S.; Vial, A.; Barchiesi, D.; Bijeon, J. L.; Adam, P. M.; Royer, P., Surface Enhanced Raman Scattering on Gold Nanowire Arrays: Evidence of Strong Multipolar Surface Plasmon Resonance Enhancement. *Chem. Phys. Lett.* **2006,** *422* (4), 303-307.

33. Laurent, G.; Félidj, N.; Aubard, J.; Lévi, G.; Krenn, J. R.; Hohenau, A.; Schider, G.; Leitner, A.; Aussenegg, F. R., Surface Enhanced Raman Scattering Arising from Multipolar Plasmon Excitation. *J. Chem. Phys.* **2004,** *122* (1), 011102.

34. Félidj, N.; Aubard, J.; Lévi, G.; Krenn, J. R.; Hohenau, A.; Schider, G.; Leitner, A.; Aussenegg, F. R., Optimized Surface-Enhanced Raman Scattering on Gold Nanoparticle Arrays. *Appl. Phys. Lett.* **2003,** *82* (18), 3095-3097.

35. Biswas, S.; Duan, J.; Nepal, D.; Pachter, R.; Vaia, R., Plasmonic Resonances in Self-Assembled Reduced Symmetry Gold Nanorod Structures. *Nano Lett.* **2013,** *13* (5), 2220-2225.

36. Verellen, N.; Sonnefraud, Y.; Sobhani, H.; Hao, F.; Moshchalkov, V. V.; Dorpe, P. V.; Nordlander, P.; Maier, S. A., Fano Resonances in Individual Coherent Plasmonic Nanocavities. *Nano Lett.* **2009,** *9* (4), 1663-1667.

37. Zhang, S.; Genov, D. A.; Wang, Y.; Liu, M.; Zhang, X., Plasmon-Induced Transparency in Metamaterials. *Phys. Rev. Lett.* **2008,** *101* (4), 047401.

38. Halpin, A.; Mennes, C.; Bhattacharya, A.; Gómez Rivas, J., Visualizing Near-Field Coupling in Terahertz Dolmens. *Appl. Phys. Lett.* **2017,** *110* (10), 101105.

39. Vincenot, J.; Aikens, C. M., Quantum Mechanical Examination of Optical Absorption Spectra of Silver Nanorod Dimers. In *Advances in the Theory of Atomic and Molecular Systems: Dynamics, Spectroscopy, Clusters, and Nanostructures*, Piecuch, P.; Maruani, J.; Delgado-Barrio, G.; Wilson, S., Eds. Springer Netherlands: Dordrecht, 2009; Vol. 20, pp 253-264.

40. Wang, W.; Zheng, L.; Xiong, L.; Qi, J.; Li, B., High Q-Factor Multiple Fano Resonances for High-Sensitivity Sensing in all-Dielectric Metamaterials. *OSA Continuum* **2019,** *2* (10), 2818-2825.

41. Wang, X.; Yao, L.; Chen, X.; Dai, H.; Wang, M.; Zhang, L.; Ni, Y.; Xiao, L.; Han, J.-B., Gap-Induced Giant Third-Order Optical Nonlinearity and Long Electron Relaxation Time in Random-Distributed Gold Nanorod Arrays. *ACS Appl. Mater. Interfaces* **2019,** *11* (35), 32469-32474.

42. Mercadal, P. A.; Encina, E. R.; Coronado, E. A., Colloidal SERS Substrate for the Ultrasensitive Detection of Biotinylated Antibodies Based on Near-Field Gradient within the Gap of Au Nanoparticle Dimers. *J. Phys. Chem. C* **2019,** *123* (38), 23577-23585.

43. Pachidis, P.; Cote, B. M.; Ferry, V. E., Tuning the Polarization and Directionality of Photoluminescence of Achiral Quantum Dot Films with Chiral Nanorod Dimer Arrays: Implications for Luminescent Applications. *ACS Appl. Nano Mater.* **2019,** *2* (9), 5681-5687.

44. Smith, K. C.; Olafsson, A.; Hu, X.; Quillin, S. C.; Idrobo, J. C.; Collette, R.; Rack, P. D.; Camden, J. P.; Masiello, D. J., Direct Observation of Infrared Plasmonic Fano Antiresonances by a Nanoscale Electron Probe. *Phys. Rev. Lett.* **2019,** *123* (17), 177401.

45. Hao, F.; Sonnefraud, Y.; Dorpe, P. V.; Maier, S. A.; Halas, N. J.; Nordlander, P., Symmetry Breaking in Plasmonic Nanocavities: Subradiant LSPR Sensing and a Tunable Fano Resonance. *Nano Lett.* **2008,** *8* (11), 3983-3988.

46. Halas, N. J.; Lal, S.; Chang, W.-S.; Link, S.; Nordlander, P., Plasmons in Strongly Coupled Metallic Nanostructures. *Chem. Rev.* **2011,** *111* (6), 3913-3961.

47. Gersten, J.; Nitzan, A., Electromagnetic Theory of Enhanced Raman Scattering by Molecules Adsorbed on Rough Surfaces. *J. Chem. Phys.* **1980,** *73* (7), 3023-3037.

48. Hartschuh, A.; Sánchez, E. J.; Xie, X. S.; Novotny, L., High-Resolution Near-Field Raman Microscopy of Single-Walled Carbon Nanotubes. *Phys. Rev. Lett.* **2003,** *90* (9), 095503.

49. Schmeits, M.; Dambly, L., Fast-Electron Scattering by Bispherical Surface-Plasmon Modes. *Phys. Rev. B* **1991,** *44* (23), 12706-12712.

50. Tamaru, H.; Kuwata, H.; Miyazaki, H. T.; Miyano, K., Resonant Light Scattering from Individual Ag Nanoparticles and Particle Pairs. *Appl. Phys. Lett.* **2002,** *80* (10), 1826-1828.

51. Rechberger, W.; Hohenau, A.; Leitner, A.; Krenn, J. R.; Lamprecht, B.; Aussenegg, F. R., Optical Properties of Two Interacting Gold Nanoparticles. *Opt. Commun.* **2003,** *220* (1), 137-141.

52. Su, K. H.; Wei, Q. H.; Zhang, X.; Mock, J. J.; Smith, D. R.; Schultz, S., Interparticle Coupling Effects on Plasmon Resonances of Nanogold Particles. *Nano Lett.* **2003,** *3* (8), 1087-1090.

53. Futamata, M.; Maruyama, Y.; Ishikawa, M., Local Electric Field and Scattering Cross Section of Ag Nanoparticles under Surface Plasmon Resonance by Finite Difference Time Domain Method. *J. Phys. Chem. B* **2003,** *107* (31), 7607-7617.

54. Olk, P.; Renger, J.; Wenzel, M. T.; Eng, L. M., Distance Dependent Spectral Tuning of Two Coupled Metal Nanoparticles. *Nano Lett.* **2008,** *8* (4), 1174-1178.

55. Brown, L. V.; Sobhani, H.; Lassiter, J. B.; Nordlander, P.; Halas, N. J., Heterodimers: Plasmonic Properties of Mismatched Nanoparticle Pairs. *ACS Nano* **2010,** *4* (2), 819-832.

56. Schnell, M.; García-Etxarri, A.; Huber, A. J.; Crozier, K.; Aizpurua, J.; Hillenbrand, R., Controlling the Near-Field Oscillations of Loaded Plasmonic Nanoantennas. *Nat. Photonics* **2009,** *3*, 287-291.

57. Kim, S.; Jin, J.; Kim, Y.-J.; Park, I.-Y.; Kim, Y.; Kim, S.-W., High-Harmonic Generation by Resonant Plasmon Field Enhancement. *Nature* **2008,** *453*, 757-760.

58. Prodan, E.; Radloff, C.; Halas, N. J.; Nordlander, P., A Hybridization Model for the Plasmon Response of Complex Nanostructures. *Science* **2003,** *302* (5644), 419-22.

59. Prodan, E.; Nordlander, P., Plasmon Hybridization in Spherical Nanoparticles. *J. Chem. Phys.* **2004,** *120* (11), 5444-54.

60. Nordlander, P.; Oubre, C.; Prodan, E.; Li, K.; Stockman, M. I., Plasmon Hybridization in Nanoparticle Dimers. *Nano Lett.* **2004,** *4* (5), 899-903.

61. Wang, H.; Brandl, D. W.; Nordlander, P.; Halas, N. J., Plasmonic Nanostructures: Artificial Molecules. *Acc. Chem. Res.* **2007,** *40* (1), 53-62.

62. Scholl, J. A.; García-Etxarri, A.; Koh, A. L.; Dionne, J. A., Observation of Quantum Tunneling between Two Plasmonic Nanoparticles. *Nano Lett.* **2013,** *13* (2), 564-569.

63. Ciracì, C.; Hill, R. T.; Mock, J. J.; Urzhumov, Y.; Fernández-Domínguez, A. I.; Maier, S. A.; Pendry, J. B.; Chilkoti, A.; Smith, D. R., Probing the Ultimate Limits of Plasmonic Enhancement. *Science* **2012,** *337* (6098), 1072-1074.

64. Toscano, G.; Raza, S.; Jauho, A.-P.; Mortensen, N. A.; Wubs, M., Modified Field Enhancement and Extinction by Plasmonic Nanowire Dimers due to Nonlocal Response. *Opt. Express* **2012,** *20* (4), 4176-4188.

65. Zuloaga, J.; Prodan, E.; Nordlander, P., Quantum Description of the Plasmon Resonances of a Nanoparticle Dimer. *Nano Lett.* **2009,** *9* (2), 887-891.

66. Song, P.; Nordlander, P.; Gao, S., Quantum Mechanical Study of the Coupling of Plasmon Excitations to Atomic-Scale Electron Transport. *J. Chem. Phys.* **2011,** *134* (7), 074701.

67. Mao, L.; Li, Z.; Wu, B.; Xu, H., Effects of Quantum Tunneling in Metal Nanogap on Surface-Enhanced Raman Scattering. *Appl. Phys. Lett.* **2009,** *94* (24), 243102.

68. Alkan, F.; Aikens, C. M., TD-DFT and TD-DFTB Investigation of the Optical Properties and Electronic Structure of Silver Nanorods and Nanorod Dimers. *J. Phys. Chem. C* **2018,** *122* (41), 23639-23650.

69. Bae, G.-T.; Aikens, C. M., TDDFT and CIS Studies of Optical Properties of Dimers of Silver Tetrahedra. *J. Phys. Chem. A* **2012,** *116* (31), 8260-8269.

70. Chen, X.; Moore, J. E.; Zekarias, M.; Jensen, L., Atomistic Electrodynamics Simulations of Bare and Ligand-Coated Nanoparticles in the Quantum Size Regime. *Nat. Commun.* **2015,** *6*, 8921.

71. Chen, X.; Jensen, L., Morphology Dependent Near-Field Response in Atomistic Plasmonic Nanocavities. *Nanoscale* **2018,** *10* (24), 11410-11417.

72. Liu, P.; Chulhai, D. V.; Jensen, L., Single-Molecule Imaging Using Atomistic Near-Field Tip-Enhanced Raman Spectroscopy. *ACS Nano* **2017,** *11* (5), 5094-5102.

73. Solis, D.; Willingham, B.; Nauert, S. L.; Slaughter, L. S.; Olson, J.; Swanglap, P.; Paul, A.; Chang, W.-S.; Link, S., Electromagnetic Energy Transport in Nanoparticle Chains via Dark Plasmon Modes. *Nano Lett.* **2012,** *12* (3), 1349-1353.

74. Willingham, B.; Link, S., Energy Transport in Metal Nanoparticle Chains Via Sub-Radiant Plasmon Modes. *Opt. Express* **2011,** *19* (7), 6450-6461.

75. Solis, D.; Paul, A.; Olson, J.; Slaughter, L. S.; Swanglap, P.; Chang, W.-S.; Link, S., Turning the Corner: Efficient Energy Transfer in Bent Plasmonic Nanoparticle Chain Waveguides. *Nano Lett.* **2013,** *13* (10), 4779-4784.

76. Maier, S. A.; Kik, P. G.; Atwater, H. A., Optical Pulse Propagation in Metal Nanoparticle Chain Waveguides. *Phys. Rev. B* **2003,** *67* (20), 205402.

77. Hohenester, U., Quantum Corrected Model for Plasmonic Nanoparticles: A Boundary Element Method Implementation. *Phys. Rev. B* **2015,** *91* (20), 205436.

78. Esteban, R.; Borisov, A. G.; Nordlander, P.; Aizpurua, J., Bridging Quantum and Classical Plasmonics with a Quantum-Corrected Model. *Nat. Commun.* **2012,** *3*, 825.

79. Scholl, J. A.; Koh, A. L.; Dionne, J. A., Quantum Plasmon Resonances of Individual Metallic Nanoparticles. *Nature* **2012,** *483*, 421-427.

80. Zhu, W.; Crozier, K. B., Quantum Mechanical Limit to Plasmonic Enhancement as Observed by Surface-Enhanced Raman Scattering. *Nat. Commun.* **2014,** *5*, 5228.

81. Savage, K. J.; Hawkeye, M. M.; Esteban, R.; Borisov, A. G.; Aizpurua, J.; Baumberg, J. J., Revealing the Quantum Regime in Tunnelling Plasmonics. *Nature* **2012,** *491*, 574-577.

82. Raza, S.; Stenger, N.; Kadkhodazadeh, S.; Fischer Søren, V.; Kostesha, N.; Jauho, A.-P.; Burrows, A.; Wubs, M.; Mortensen, N. A., Blueshift of the Surface Plasmon Resonance in Silver Nanoparticles Studied with EELS. *Nanophotonics* **2013,** *2* (2), 131-138.

83. Prodan, E.; Car, R., Tunneling Conductance of Amine-Linked Alkyl Chains. *Nano Lett.* **2008,** *8* (6), 1771-1777.

84. García de Abajo, F. J., Nonlocal Effects in the Plasmons of Strongly Interacting Nanoparticles, Dimers, and Waveguides. *J. Phys. Chem. C* **2008,** *112* (46), 17983-17987.

85. Romero, I.; Aizpurua, J.; Bryant, G. W.; Abajo, F. J. G. d., Plasmons in Nearly Touching Metallic Nanoparticles: Singular Response in the Limit of Touching Dimers. *Opt. Express* **2006,** *14* (21), 9988-9999.

86. Lassiter, J. B.; Aizpurua, J.; Hernandez, L. I.; Brandl, D. W.; Romero, I.; Lal, S.; Hafner, J. H.; Nordlander, P.; Halas, N. J., Close Encounters Between Two Nanoshells. *Nano Lett.* **2008,** *8* (4), 1212-1218.

87. Zhu, W.; Esteban, R.; Borisov, A. G.; Baumberg, J. J.; Nordlander, P.; Lezec, H. J.; Aizpurua, J.; Crozier, K. B., Quantum Mechanical Effects in Plasmonic Structures with Subnanometre Gaps. *Nat. Commun.* **2016,** *7*, 11495.

88. Alkan, F.; Aikens, C. M., Understanding Plasmon Coupling in Nanoparticle Dimers Using Molecular Orbitals and Configuration Interaction. *Phys. Chem. Chem. Phys.* **2019,** *21* (41), 23065-23075.

89. Zhang, P.; Feist, J.; Rubio, A.; García-González, P.; García-Vidal, F. J., Ab Initio Nanoplasmonics: The Impact of Atomic Structure. *Phys. Rev. B* **2014,** *90* (16), 161407.

90. Alejandro, V.; Pablo, G.-G.; Johannes, F.; García-Vidal, F. J.; Angel, R., Quantum Plasmonics: from Jellium Models to ab Initio Calculations. *Nanophotonics* **2016,** *5* (3), 409-426.

91. Marques, M. A. L.; Gross, E. K. U., TIME-DEPENDENT DENSITY FUNCTIONAL THEORY. *Annu. Rev. Phys. Chem.* **2004,** *55* (1), 427-455.

92. Krauter, C. M.; Bernadotte, S.; Jacob, C. R.; Pernpointner, M.; Dreuw, A., Identification of Plasmons in Molecules with Scaled Ab Initio Approaches. *J. Phys. Chem. C* **2015,** *119* (43), 24564-24573.

93. Bernadotte, S.; Evers, F.; Jacob, C. R., Plasmons in Molecules. *J. Phys. Chem. C* **2013,** *117* (4), 1863-1878.

94. te Velde, G.; Bickelhaupt, F. M.; Baerends, E. J.; Fonseca Guerra, C.; van Gisbergen, S. J. A.; Snijders, J. G.; Ziegler, T., Chemistry with ADF. *J. Comput. Chem.* **2001,** *22* (9), 931-967.

95. Becke, A. D., Density-Functional Exchange-Energy Approximation with Correct Asymptotic Behavior. *Phys. Rev. A* **1988,** *38* (6), 3098-3100.

96. Perdew, J. P., Density-Functional Approximation for the Correlation Energy of the Inhomogeneous Electron Gas. *Phys. Rev. B* **1986,** *33* (12), 8822-8824.

97. Perdew, J. P., Erratum: Density-Functional Approximation for the Correlation Energy of the Inhomogeneous Electron Gas. *Phys. Rev. B* **1986,** *34* (10), 7406-7406.

98. Lenthe, E. v.; Baerends, E. J.; Snijders, J. G., Relativistic regular two-component Hamiltonians. *J. Chem. Phys.* **1993,** *99* (6), 4597-4610.

99. Runge, E.; Gross, E. K. U., Density-Functional Theory for Time-Dependent Systems. *Phys. Rev. Lett.* **1984,** *52* (12), 997-1000.

100. Casida, M. E.; Jamorski, C.; Casida, K. C.; Salahub, D. R., Molecular Excitation Energies to High-Lying Bound States from Time-Dependent Density-Functional Response Theory: Characterization and Correction of the Time-Dependent Local Density Approximation Ionization Threshold. *J. Chem. Phys.* **1998,** *108* (11), 4439-4449.

101. Gross, E. K. U.; Kohn, W., Local Density-Functional Theory of Frequency-Dependent Linear Response. *Phys. Rev. Lett.* **1985,** *55* (26), 2850-2852.

102. Casida, M. E. *Recent Advances in Density Functional Methods*; World Scientific: 1995; pp 155-192.

103. Perdew, J. P.; Burke, K.; Ernzerhof, M., Generalized Gradient Approximation Made Simple. *Phys. Rev. Lett.* **1996,** *77* (18), 3865-3868.

104. Jørgensen, P.; Linderberg, J., Time-dependent Hartree–Fock calculations in the Pariser–Parr–Pople model. Applications to aniline, azulene and pyridine. *Int. J. Quantum Chem.* **1970,** *4* (6), 587-602.

105. Olsen, J.; Jensen, H. J. A.; Jørgensen, P., Solution of the Large Matrix Equations Which Occur in Response Theory. *J. Comput. Phys.* **1988,** *74* (2), 265-282.

106. Johnson, H. E.; Aikens, C. M., Electronic Structure and TDDFT Optical Absorption Spectra of Silver Nanorods. *J. Phys. Chem. A* **2009,** *113* (16), 4445-4450.

107. Guidez, E. B.; Aikens, C. M., Theoretical Analysis of the Optical Excitation Spectra of Silver and Gold Nanowires. *Nanoscale* **2012,** *4* (14), 4190-4198.

108. López-Lozano, X.; Barron, H.; Mottet, C.; Weissker, H.-C., Aspect-Ratio- and Size-Dependent Emergence of the Surface-Plasmon Resonance in Gold nanorods – an Ab Initio TDDFT Study. *Phys. Chem. Chem. Phys.* **2014,** *16* (5), 1820-1823.

109. Guidez, E. B.; Aikens, C. M., Quantum Mechanical Origin of the Plasmon: from Molecular Systems to Nanoparticles. *Nanoscale* **2014,** *6* (20), 11512-11527.

110. Lian, K.-Y.; Sałek, P.; Jin, M.; Ding, D., Density-Functional Studies of Plasmons in Small Metal Clusters. *J. Chem. Phys.* **2009,** *130* (17), 174701.

111. Dreuw, A.; Weisman, J. L.; Head-Gordon, M., Long-Range Charge-Transfer Excited States in Time-Dependent Density Functional Theory Require Non-Local Exchange. *J. Chem. Phys.* **2003,** *119* (6), 2943-2946.

Chapter 6 - RT-TDDFT Examination of Nanowire Arrays for the Plasmonic Enhanced Dissociation of Dinitrogen

6.1 Abstract

Because the breaking of the triple bond in dinitrogen is the most difficult step in the Haber-Bosch process, researchers strive to find a way to activate/dissociate this bond without the use of high pressure and temperature conditions. In this work, we have theoretically studied the plasmon induced dissociation of dinitrogen on linear Ag_4 nanowire dimers via the application of electric fields of various intensities and frequencies. We use the side-by-side and end-to-end orientations of nanowires where the nitrogen molecule is positioned either at the end of the wires or between the wires. Then, we observe the influence of the applied fields on the N-N bond length. In this work, the LC-ωPBE exchange correlation functional with the LANL2DZ basis set are used in real-time time-dependent density functional theory calculations with Ehrenfest dynamics. We have found that there is a higher possibility of N-N bond dissociation by using the end-to-end orientation of nanowires than by using the side-by-side nanowires. A higher chance of dissociation is observed for nanowires with small inter-particle separation (0.50 nm and smaller) and also with high field strengths (0.04 au or higher).

6.2 Introduction

Plasmonic noble metals like gold and silver nanoparticles have already found use in photochemistry,[1] bio imaging,[2] and solar cells.[3] Recent studies show that the plasmonic materials can also be used in hydrogen dissociation, carbon dioxide reduction, water splitting and so on.[4-6]

Mukherjee et al. observed the room temperature dissociation of hydrogen molecule on gold nanoparticles.[4] They found that the hot electrons released after the plasmon decay mechanism transfer to the hydrogen molecule to cause its dissociation. Similarly, Yan et al. studied the water splitting on gold nanoparticles using real-time time-dependent density functional theory and observed that the rate of water splitting is dependent on quantum oscillation mode of plasmonic excitation. They found that the splitting rate is higher with odd plasmon modes compared to the even plasmon modes. Recently, Wu et al. theoretically investigated the mechanism of photocatalytic hydrogen dissociation on an Au_6 model cluster.[7] From the quantum dynamics simulation on diabatic potential energy surfaces, they found that the hydrogen dissociation is possible due to the crossing between hot electron and charge transfer diabatic states. They reported plasmonic materials to have a higher concentration of hot electron states due to their larger absorption cross section compared to the nonplasmonic materials and hence be more important for plasmonic catalysis.

Dissociation of the dinitrogen bond is the rate-limiting step of the Haber-Bosch process, where N_2 is catalytically converted to NH_3. Because dinitrogen is a stable molecule, high temperature and pressure are typically required in this step. Thus, researchers are also interested to find alternate ways so that this process can be done under ambient conditions.

Researchers have observed the activation of nitrogen molecule on nanoparticles composed of plasmon-supporting metals, although many of these studies examined only ground-state catalysis.[8-13] For example, Aguado and co-workers observed the dissociative chemisorption of a N_2 molecule that was oriented side-by-side on the $Al_{44}^{+/-}$ cluster.[8] Schleyer and co-workers have shown that N-N elongation varies with the cluster size; Li_8 is the smallest cluster that can dissociate the N-N bond.[14] The plasmonic property of the nanoparticles has been found to help to dissociate

the N_2 molecule under mild conditions.[15-16] Carter and coworkers showed that the reaction barrier for dinitrogen dissociation is lowered due to plasmon local field enhancement on using a Mo-doped Au surface.[15] Carter et. al. found that the presence of Fe and Mo substituents in the Au(111) surface improves the dissociation of N_2 by 3.2 eV and 4.7 eV respectively.[17] Similarly, Hull et al. showed that 0.05 au electric field can dissociate the N_2 molecule on silver nanowire monomer system.[18] Overall, plasmon-enhanced photocatalytic nitrogen dissociation is getting significant attraction because it does not produce harmful greenhouse gases (e.g. carbon dioxide) and renewable solar energy can be used to drive the process.

All of these structures discussed above are either single nanoparticle clusters or surfaces. The study of the possibility of N_2 dissociation with nanoparticle dimers is essential because these structures may have more potential to break the N-N bond due to the electromagnetic field enhancement from the assemblies. Plasmonic assemblies may have optical hotspots which can help to enhance the molecular properties that depend on the intensity of applied field.[19] Since the plasmon coupling is stronger at smaller inter-particle separation and electrons can tunnel between the assemblies,[20] N-N dissociation may get favored due to charge transfer to the nitrogen virtual orbitals. Also because silver is one of the strongest plasmonic metals, we have investigated the plasmonic mediated photocatalysis with silver nanoparticles.

In this paper we have investigated the plasmon mediated photocatalytic dissociation of dinitrogen on model Ag_4 nanowire dimers using electric field strength of 0.01 au – 0.05 au. Since we have previously observed the dinitrogen dissociation on silver wire monomers on using an electric field with an intensity of 0.05 au,[18] in this project, we investigate if there is any possibility of N_2 dissociation on dimers using an electric field intensity less than 0.05 au. We have studied the dissociation probability using an Ag_4 dimer at large and small inter-particle separations of 1.00

nm, 0.75 nm and 0.50 nm. This study will help us to understand the effect of the applied field strengths and inter-particle separations on N_2 dissociation.

6.3 Computational methods

We have used the LC-ωPBE[21] exchange correlation functional with the LANL2DZ[22-24] basis set for the geometry optimization, linear response time dependent density functional theory (LR-TDDFT)[25] and real time TDDFT[26-28] calculations on the studied systems. Absorption spectra obtained from LR-TDDFT are convoluted with a Gaussian broadening with a full-width at half-maximum of 0.2 eV. The unrestricted method is used for Ehrenfest molecular dynamics[29-31] calculations. A trapezoid electric field is applied which is turned off at 20 fs (Figure 6-1) while the simulation is run until 200 fs. The benefit of using the trapezoid function is that we can selectively excite only certain frequencies, similar to application of a continuous wave electric field. We used an electronic time step of 0.00025 fs and a nuclear time step of 0.1 fs. The silver atoms in the nanowires are frozen during the Ehrenfest calculation. Random initial velocities are used in these calculations. All of the calculations are performed with the development version of the Gaussian program.[32] The transition electron density plots and molecular orbitals are obtained with VESTA[33] and Jmol[34] respectively.

The orientations of the dimers with the N_2 molecule studied for this project are presented in Figure 6-2. In constructing these arrays, the coordinates of the first Ag_4 nanowire are optimized (coordinates provided in Table C-1). Then, we add N_2 on one end of the wire and optimize this system (Table C-2). Both of these optimizations are done without any symmetry constraints and have 4 imaginary frequencies. Thus, the structures are not in their local minimum, but these geometries have previously been found to yield good models of the physics in larger nanowires.[35-

[36] After optimization, the molecule was translated so that the center of mass of the molecule lies at the origin (Table C-3). Throughout the text, this translated Ag_4N_2 is taken as the monomer structure. Then, a second Ag_4 unit is added without optimization; the Ag_4 coordinates are taken from Ag_4N_2. In the first orientation (a), the second Ag_4 nanowire is placed side-by-side to Ag_4N_2 with a separation of d (Table C-4). For the second orientation (b), the second Ag_4 nanowire is placed at a distance d from the Ag end of the Ag_4N_2 (Table C-5). Because the center of mass of (b) is very far from the origin, the coordinates are then translated to the origin. For the third orientation (c), the N_2 molecule is at a distance d from an Ag atom in a hotspot between two end-to-end Ag_4 nanowires (Table C-6). In addition, structure (c) at the optimized distance (0.26 nm) is analyzed. For this, the hotspot structure with d = 1.00 nm is optimized, which gives a Ag-N bond length of 0.26 nm on both sides (Table C-7). For simplicity, orientations (a), (b), and (c) will be called side-by-side, end-to-end, and hotspot, respectively, from now onwards. Again, the nanowire monomers and arrays studied in this work are model systems that do not occur in linear fashion in their local minimum geometry.

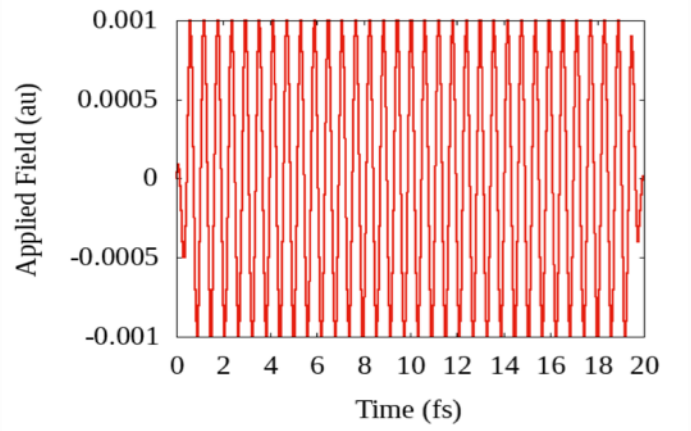

Figure 6-1 Trapezoid field of strength 0.001 au.

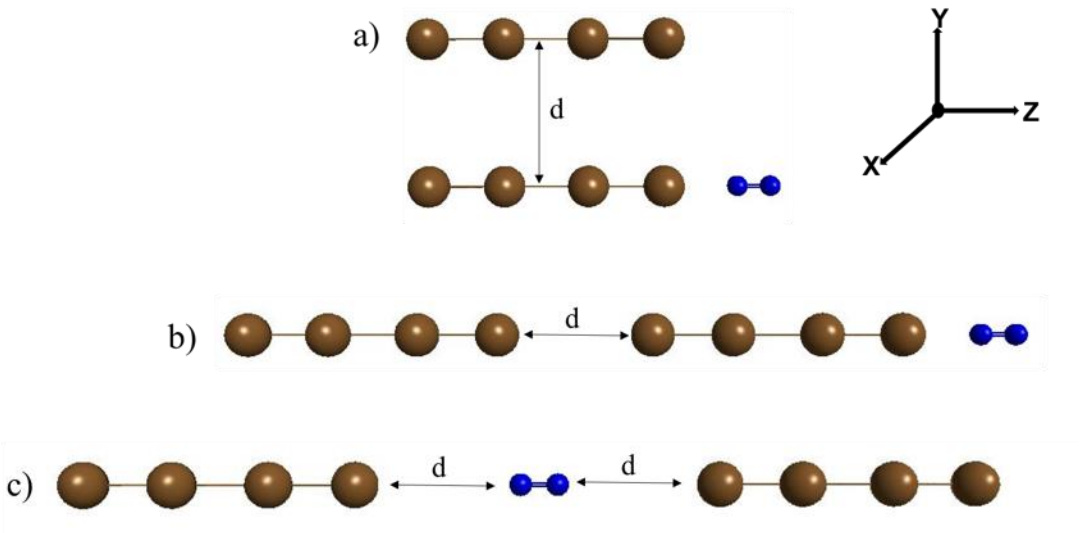

Figure 6-2 Structures of silver nanowire arrays with dinitrogen studied in this work, where d = 0.50 nm, 0.75 nm and 1.00 nm for each of these orientations. Color key: Blue = nitrogen, brown = silver.

6.4 Results

6.4.1 N_2

First, we have studied the nitrogen molecule as a control system; we investigate the minimum frequency and intensity of the applied field to dissociate the nitrogen molecule when the silver nanowires are not present. The absorption spectrum of N_2 exhibits peaks at 14.0 eV, 15.3 eV, and 18.4 eV (Figure 6-3). The main transitions that contribute to each of these peaks are given in Table 6-1. The first peak is the transverse peak while the two other peaks are longitudinal peaks. This is clearly evidenced by the transition electron density plots in Figure 6-3: state 6 and state 7 (which are degenerate contributions to the first significant absorption peak) show the transition electron density along short axis of the N_2 molecule whereas states 8 and 9 exhibit transition electron densities aligned along the long axis of the N_2 molecule. A molecular orbital diagram of the nitrogen molecule is given in Figure C-1. Transitions 4 → 8 ($1\sigma^* \rightarrow 2\pi_y^*$) and 4 → 9 ($1\sigma^* \rightarrow 2\pi_x^*$) contribute equally to the first peak. The second peak has the largest number of transitions

that contribute to it, along with some de-excitations (shown with blue arrows). It has the highest oscillator strength among three peaks and hence is the highest peak in the absorption spectrum (Figure 6-3). Only one transition contributes to the third peak. States from 1 to 5 have zero oscillator strength and hence do not give peaks in the absorption spectrum (Table C-8).

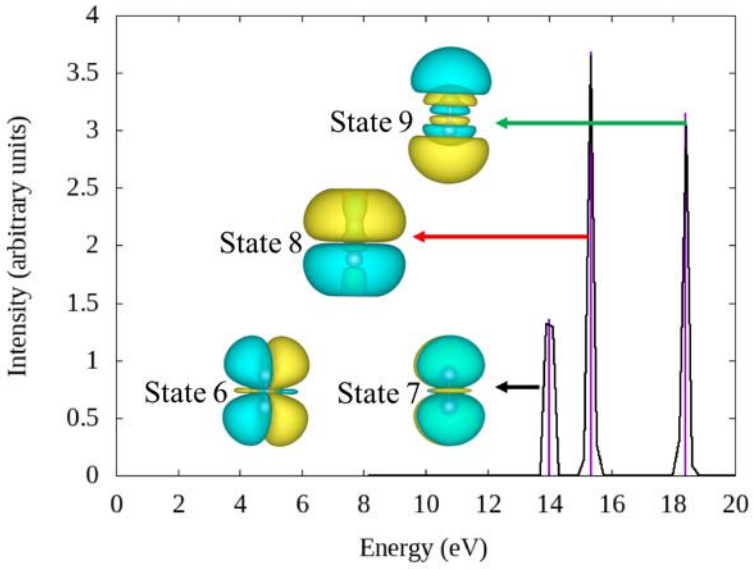

Figure 6-3 Absorption spectrum of N_2 obtained with LR-TDDFT. Insets are the transition electron densities for the states that correspond to each of the peaks with iso-values of 0.001.

Table 6-1 The transitions corresponding to each of the peaks in the absorption spectrum of N_2

Excited State	Energy (eV)	Oscillator strength (au)	Transitions	Weight
6	14.0049	0.2882	4 → 8 ($1\sigma^*$ → $2\pi_y^*$) 4 → 9 ($1\sigma^*$ → $2\pi_x^*$)	0.66690 0.23921
7	14.0049	0.2882	4 → 8 ($1\sigma^*$ → $2\pi_y^*$) 4 → 9 ($1\sigma^*$ → $2\pi_x^*$)	0.23921 0.66690
8	15.3490	0.7826	5 → 9 ($1\pi_y$ → $2\pi_x^*$) 6 → 8 ($1\pi_x$ → $2\pi_y^*$) 7 → 17 (2σ → hybrid) 5 ← 9 ($1\pi_y$ ← $2\pi_x^*$) 6 ← 8 ($1\pi_x$ ← $2\pi_y^*$)	0.49346 0.49346 -0.14818 -0.10920 -0.10920
9	18.3903	0.6705	7 → 10 (2σ →$2\sigma^*$)	0.69829

We studied the possibility of N_2 activation/dissociation upon applying both resonant and non-resonant fields and intensities of 0.01 au, 0.02 au, 0.03 au, 0.04 au and 0.05 au (Figure 6-4). Because the second peak has the highest oscillator strength, we expect N_2 dissociation to have its maximum potential upon applying the electric field corresponding to its frequency (15.35 eV).

The equilibrium N-N distance in the N_2 molecule is 1.12 Å at the LC-ωPBE/LANL2DZ level of theory. Similarly, the N-N double and single bonds obtained at the same level of theory for N_2H_2 and N_2H_4 are 1.26 Å and 1.39 Å, respectively. In this text, the N_2 molecule is said to be dissociated if the N-N bond length is more than 2.0 Å during the course of the simulation. The bond is said to have activated (but not dissociated) if the bond length is more than the equilibrium N-N bond length of 1.12. So, we consider the N-N bond to be activated if it is in the range of 1.2 – 2.0 Å.

Figure 6-4 shows that N_2 dissociates on using the resonant field with field intensity of 0.02 au and higher. Certain abnormalities are observed on applying the field corresponding to the frequency of 18.39 eV. For example, analysis of the N-N bond length up to 20 fs shows that the bond length is more elongated on using a 0.04 au field than on using a 0.05 au field. This is because of the random initial velocities used in our calculations. We performed an additional set of calculation with zero initial velocities which shows the expected behavior (Figure C-2).

Dissociation is also observed with non-resonant excitation, even several eV away from the 15 eV peak. For example, N_2 dissociates on applying an electric field corresponding to the frequency of 10 eV (Figure 6-4(e)) and 12 eV (Figure 6-4(f)). However, the N-N distance only oscillates around the equilibrium N_2 bond length of 1.12 Å when using the field that corresponds to the frequency of 8 eV. Calculations with these non-resonant fields to determine their effect on N-N bond length are performed using the field intensity of 0.04 au only.

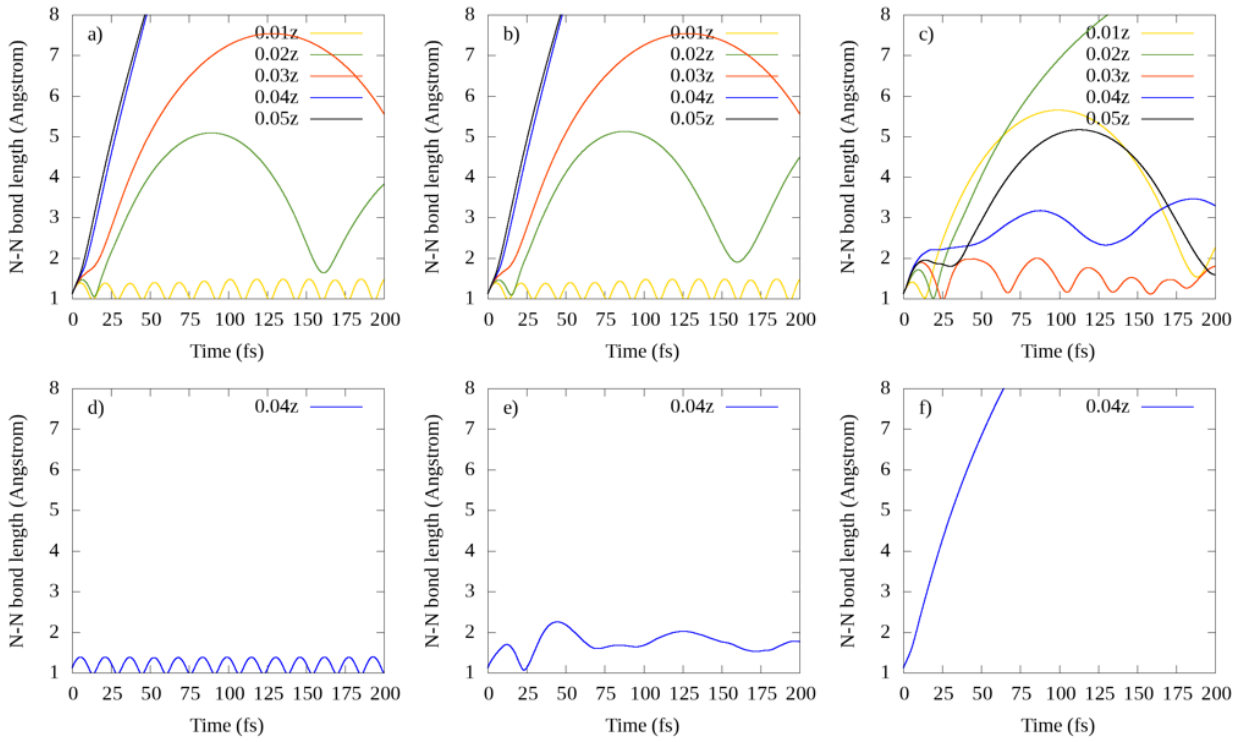

Figure 6-4 N-N bond length in the N_2 molecule as a function of time for electric fields applied along the z direction with various field strengths and frequencies. Applied electric fields correspond to the frequencies of a) 14.00 eV, b) 15.35 eV, c) 18.39 eV, d) 8.00 eV, e) 10.00 eV and f) 12.00 eV.

In order to investigate the reason for dissociation/activation upon applying non-resonant fields corresponding to frequencies of 10 or 12 eV, we studied the electron-only dynamics of the system using RT-TDDFT without Ehrenfest dynamics. We analyzed the Fourier transforms (FTs) of the dipole moment during different time ranges: 0-20 fs (corresponding to the time during which the field is applied) and 20-240 fs (Figure C-3). On applying the fields corresponding to frequencies of 10 eV and 12 eV, the FT peak for 0-20 fs is mainly obtained at the applied field frequency (10 eV or 12 eV, respectively) whereas the FT peak for 20-240 fs (after the field is turned off) is positioned at ~15 eV. Thus, non-resonant excitation even up to 5 eV away leads to excitation at a natural resonance (absorption) in the system. Because the 0.04 au field

corresponding to the frequency of ~15 eV causes N-N dissociation (Figure 6-4(b)), excitation of this peak upon applying the fields corresponding to 10 and 12 eV might have led to N_2 dissociation during the 20-240 fs timescale. However, upon applying the field corresponding to a frequency of 8 eV, the FT peak for 20-240 fs is obtained mainly at ~18 eV. Since N-N bond elongation is comparatively smaller when using a 0.04 au field with a frequency corresponding to ~18 eV (Figure 6-4(c)), this excitation does not lead to dissociation.

6.4.2 Monomer and dimers

Our goal in this project is to use the plasmonic properties of Ag_4 nanowire dimers for the possible dissociation of dinitrogen bond. Our recent work shows that N_2 dissociation is possible on exciting the longitudinal excitation and on applying electric field frequency that corresponds to nanowire's longitudinal peak frequency with an intensity of 0.05 au.[18] We are interested to investigate whether the electric fields with intensity lower than 0.05 au lead to dinitrogen dissociation when we use nanowire dimers instead of monomers. As shown in Figure 6-4, the dissociation of N_2 without the aid of the plasmonic property of nanoparticles requires a very high energy of at least 10 eV and a field intensity of 0.04 au. We now investigate the possibility of dissociation on using less intense electric field with the help of plasmonic property of nanowire dimers.

The binding energies of these systems are positive suggesting that these clusters are energetically favorable (Table C-9). Note that the binding energies of these systems are calculated using the equation $E(Ag_8N_2) - E(Ag_8) - E(N_2)$.

6.4.2.1 Absorption spectra

Figure 6-5 shows the absorption spectra of the monomer and dimer systems studied in this work. For the side-by-side dimer (red), the longitudinal peak blueshifts and the transverse peak redshifts as observed in our previous study.[20] The longitudinal and transverse peaks of the dimers with the N_2 molecule in the hotspot (green) slightly redshift compared to the monomer peaks. In the hotspot orientation, the peak positions do not change significantly with the change in inter-particle distance. A new feature appears between the longitudinal and transverse peaks for the optimized distance (0.26 nm) in the hotspot orientation at 3.48 eV. The transitions to nitrogen antibonding orbitals mainly correspond to this peak. A redshift of the longitudinal and the transverse peaks is also observed for the end-to-end orientation (blue). Among all orientations, the maximum shift of the longitudinal peak is observed to occur for the 0.50 nm distance in the end-to-end orientation.

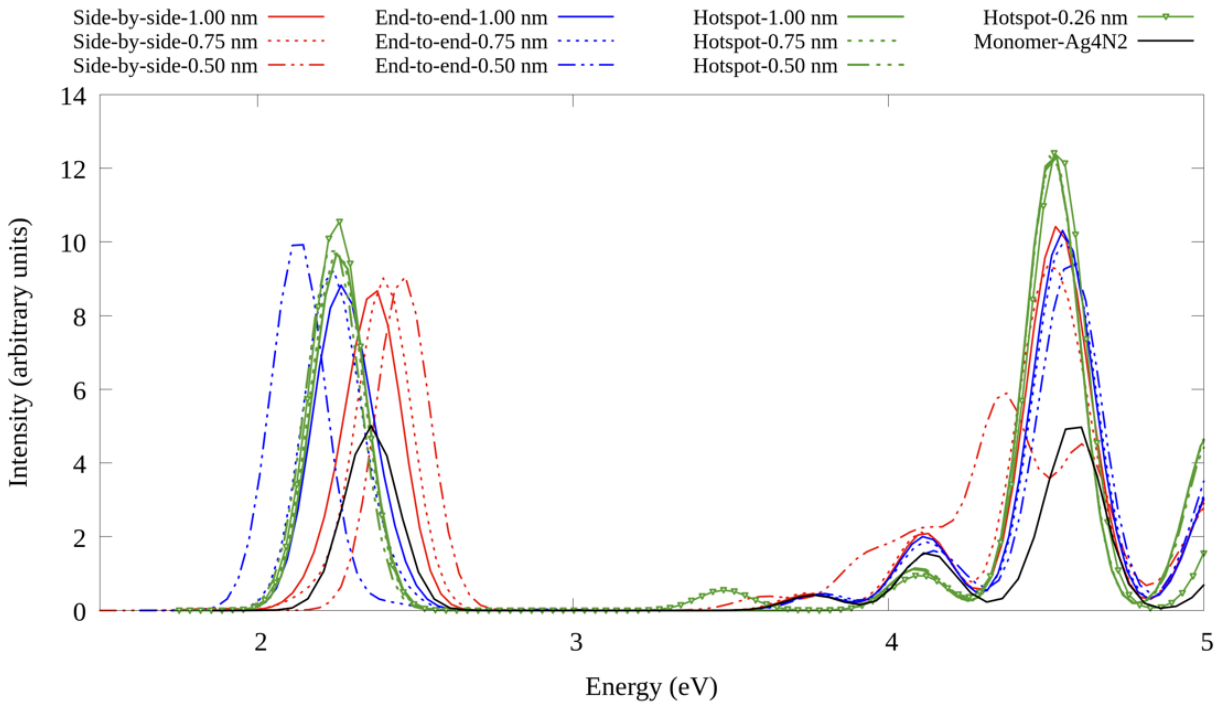

Figure 6-5 Absorption spectra of monomer Ag_4N_2 and the dimers at different inter-particle separations as shown in the figure legend.

Because the dimer peak positions of the studied systems only slightly shift from the monomer peak positions, we first investigate the possible N_2 dissociation using the longitudinal peak frequency of the Ag_4N_2 monomer (2.36 eV). This means that we excite all systems using an electric field with a frequency corresponding to 2.36 eV. Using the same excitation frequency on all dimers helps to compare the efficiency of field intensity and polarization direction for the nitrogen dissociation. Later we also analyze the dissociation possibility upon exciting the molecule with the perfectly resonant longitudinal peak frequency of each of the dimers at each inter-particle separations.

6.4.2.2 Plasmon-mediated photocatalysis

In this section, we study the nitrogen activation/dissociation probability for all dimer orientations at different inter-particle separations and field strengths (Figure 6-6). For side-by-side dimers, the N-N bond activation increases on increasing field strength at each of the inter-particle separations. However, the N-N bond activation at the same field strength does not increase on decreasing the separation distance. For end-to-end dimers, N_2 activation/dissociation is more probable than with any other studied orientations. The 0.05 au field dissociates the N-N bond at all of the inter-particle separations investigated for the end-to-end orientation. At 0.50 nm, even the 0.04 au field leads to the dissociation of N_2. We do not observe a significant effect of the inter-particle separation on N-N activation from 1.00 nm to 0.75 nm. For the hotspot orientation, the field strength alone cannot change the N-N bond length if the inter-particle separation is very large, which is observed for the separation of 1 nm. The effect of field intensity is pronounced only at smaller inter-particle separations of 0.75 nm and 0.50 nm. We also observed that the smallest inter-particle separation causes a more elongated N-N bond length by comparing the results from 0.75

nm and 0.50 nm. Additional calculations have been performed on the hotspot orientation at inter-particle separations smaller than 0.50 nm (Figure C-4). Because the optimized hotspot orientation has a Ag-N distance of 0.26 nm on both ends, we analyzed the effects on the N-N bond length upon using an electric field on this orientation. On using the optimized distance, N-N dissociation is observed even with a field strength of 0.04 au. We have also investigated the N-N dissociation for a hotspot dimer that has Ag-N distances of 0.26 nm and 0.50 nm.

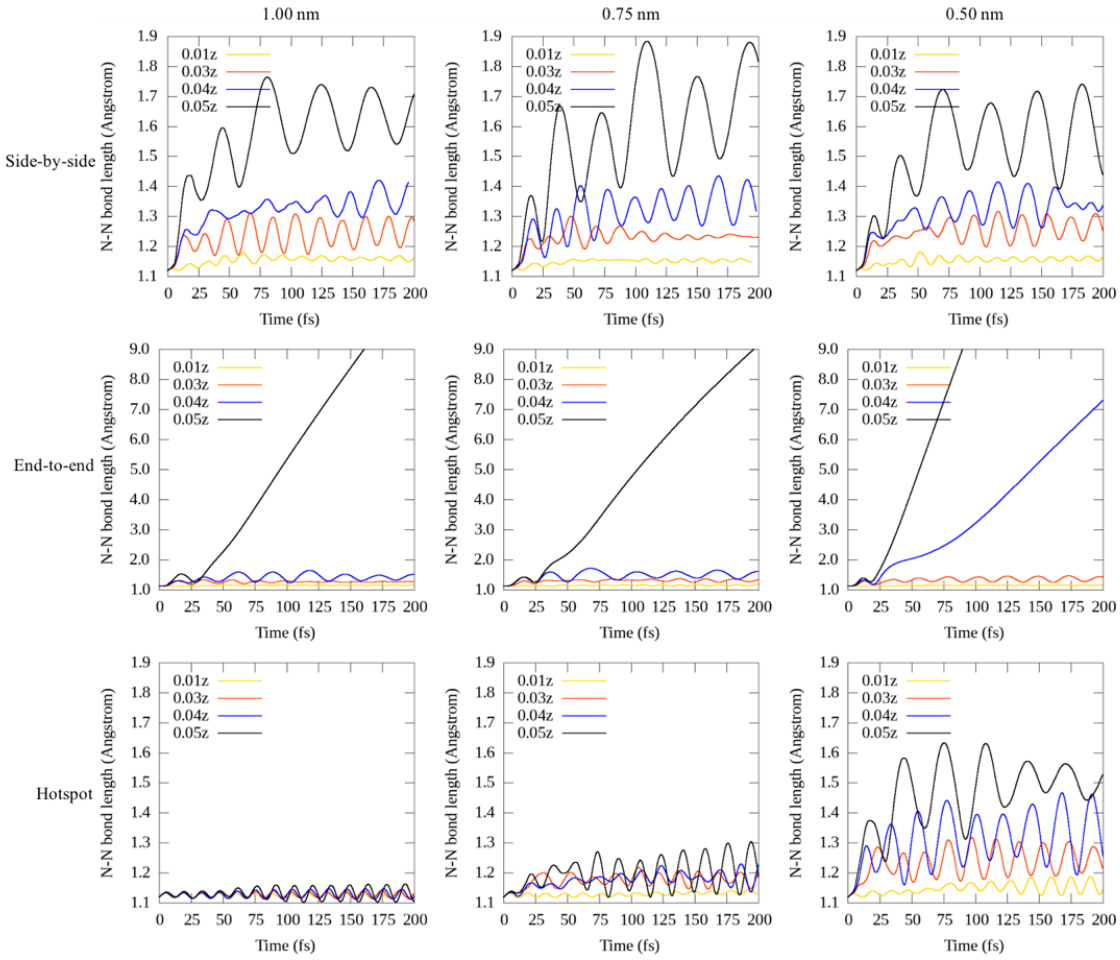

Figure 6-6 Variation of N-N bond length with time for different dimer-N_2 orientations (row) and at different inter-particle separations (columns). The graphs are obtained using z-polarized fields with field strengths of 0.01 au, 0.03 au, 0.04 au and 0.05 au as shown in the figures. The applied field has a frequency corresponding to 2.36 eV (i.e., the longitudinal peak frequency of the Ag_4N_2 monomer). Note that the y-axis scale is different for the middle row (i.e., the end-to-end orientation).

Overall, we observed that the possibility of N-N dissociation is higher when using an end-to-end orientation of the dimer compared to using the side-by-side or hotspot orientations of dimers. As expected, the N_2 bond length is more elongated with higher field strengths than with lower field strengths for all dimer orientations.

In order to determine the types of orbitals that become significantly occupied in order to dissociate N_2, we analyzed the electronic populations of the virtual orbitals. Because N_2 on the end-to-end dimer with an inter-particle distance of 0.50 nm dissociates with an applied field with a field strength of 0.05 au field but not with a field strength of 0.01 au, we have analyzed the populations on the virtual orbitals of this dimer upon application of 0.01 au and 0.05 au fields using RT-TDDFT calculations without Ehrenfest dynamics (Figure 6-7, C-5). The molecular orbital diagram of this dimer is given in Figure C-6. We observed more significant population on wire-based orbitals (i.e. the orbitals that are mainly localized on Ag wires) than on N_2-based orbitals (i.e. the orbitals that are mainly localized on N_2-molecule). Also, on applying the 0.01 au field, the population on wire-based orbitals drops after the applied field is turned off at 20 fs. However, on applying the 0.05 au field, the population on the wire-based orbitals does not drop, but rather keeps increasing even after the field is turned off at 20 fs. This suggests that a higher intensity field is required for the N_2 bond dissociation which is able to excite the population to virtual orbitals even after the applied field is turned off.

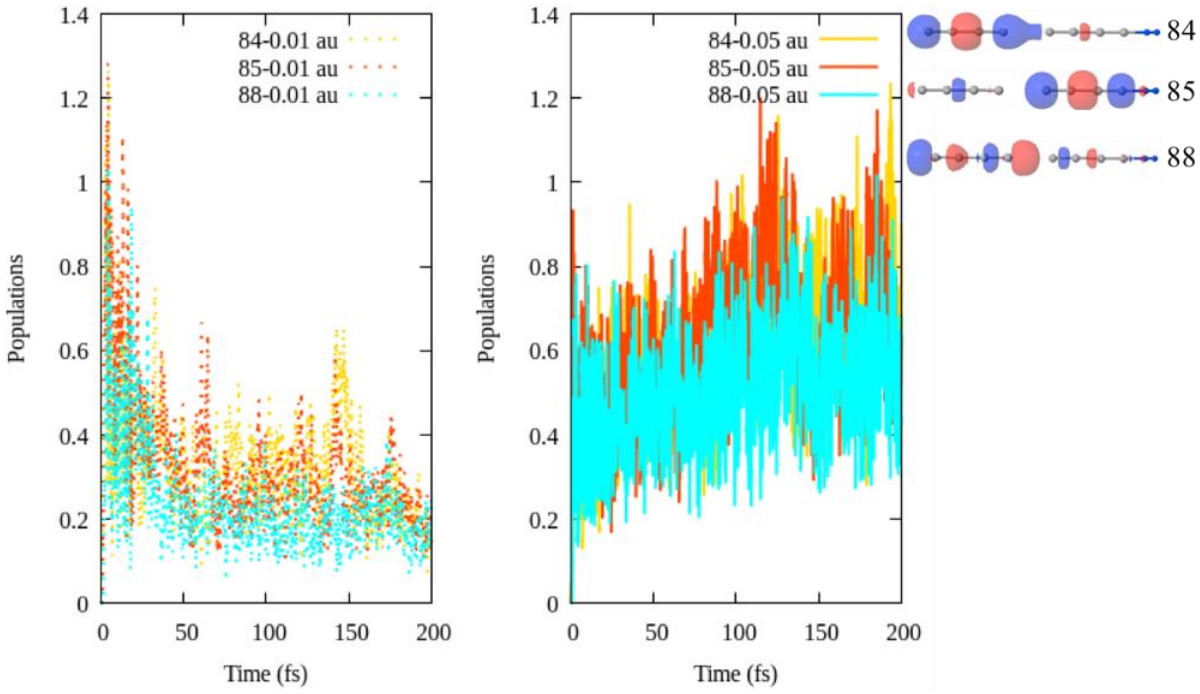

Figure 6-7 Variation of population in virtual molecular orbitals 84, 85, and 88 throughout the simulation time upon applying an electric field corresponding to 2.36 eV and an electric field intensity of 0.01 au and 0.05 au. This plot is obtained for the end-to-end system with an inter-particle distance of 0.50 nm.

In order to confirm whether the observed N-N elongation is due to the effect of plasmonic nanowires and not due to the strong applied fields, we applied the electric field corresponding to the monomer longitudinal frequency (2.36 eV) on the nitrogen molecule only (Figure C-7). In the absence of nanowires, the N-N distance oscillates around the average N-N bond length. The N-N distance does not increase throughout the whole simulation time even with the strongest applied field of intensity 0.05 au. Thus, the dissociation observed in Figure 6-6 and Figure C-4 is due to the plasmonic activity of the nanowires; it is not only due to the high intensity of the applied field.

We also studied the possibility of N_2 dissociation using applied electric fields with frequencies that correspond to the longitudinal peak energies of each dimer (Figure C-8, C-9). We observed that the effect of field strength and inter-particle separation upon N_2 dissociation is

similar on using the dimer longitudinal peak frequency and the monomer longitudinal peak frequency. In both cases, N_2 dissociation is more probable when using the end-to end orientation of the monomers compared to using other dimers.

Because the N_2 molecule is situated on the z-axis in all of the studied systems and the longitudinal plasmon of the silver nanowires is activated, only a z-polarized applied field dissociates the N_2 bond. x- and y-polarized electric fields do not dissociate the N_2 molecule (N-N bond distance vs. time plots are not shown for this case).

We also applied an electric field with a frequency corresponding to the transverse peak energy of the Ag_4N_2 monomer (4.60 eV). We excited both the longitudinal and transverse excitations with applied fields corresponding to the frequency of 4.60 eV (Figure C-10). The transverse excitations polarized along the x- and y-directions do not cause N-N dissociation. Interestingly, we found that the N-N bond dissociates upon using a z-polarized 4.60 eV applied field although it is not resonant with the longitudinal plasmon peak of the systems. Further studies to investigate the reason for this dissociation are needed in the future.

It should be noted that in all of the orientations we have studied, the nitrogen molecule moves away from the nanowires during the simulation. The nitrogen molecule does not continue to bind to the dimer. For example, when the nitrogen molecule is present in the hotspot, the N_2 molecule escapes from the hotspot (without getting adsorbed) and then dissociates. This is in agreement with previous observations.[18]

6.5 Conclusions

The minimum strength of the electric field required to dissociate an isolated N_2 molecule is 0.04 au with a frequency that corresponds to 10 eV. Less intense fields are needed to cause N_2

dissociation on Ag_xN_2 assemblies due to the plasmon-enhancement from the silver wires. Furthermore, dissociation occurs with lower field frequencies. N-N dissociation is most probable with an end-to-end orientation of nanowires compared to other orientations. Higher field intensities and smaller inter-particle separations have higher probability to cause more N-N elongation in all of the dimer orientations. For the hotspot dimer with 1.00 nm inter-particle separation, the N-N bond length on applying field strength of 0.05 au is similar to the N-N bond length on applying 0.01 au field. This could be due to the large gap between the nanowires; the Ag-N distance is 1.00 nm on each of the sides in the hotspot orientation. This suggests that plasmonic enhancement is negligible if the inter-particle separation is very large.

In order to dissociate the N-N bond, the applied field should be strong enough to excite the electronic population into virtual orbitals even after the field is switched off. If the population on virtual orbital drops as the field is turned off, the N-N bond does not become dissociated. The population increases on Ag-based orbitals rather than on N_2 antibonding orbitals when N_2 becomes dissociated. Dissociation is observed upon excitation of longitudinal modes using both the perfectly resonant and slightly off-resonant frequency fields. However, no dissociation occurs on exciting the transverse mode with x- or y-polarized fields. For all of the dimers, the N_2 molecule does not rebind to the nanowires after dissociation.

6.6 References

1. Zhang, Y.; He, S.; Guo, W.; Hu, Y.; Huang, J.; Mulcahy, J. R.; Wei, W. D., Surface-Plasmon-Driven Hot Electron Photochemistry. *Chem. Rev.* **2018,** *118* (6), 2927-2954.

2. Zhou, C.; Hao, G.; Thomas, P.; Liu, J.; Yu, M.; Sun, S.; Öz, O. K.; Sun, X.; Zheng, J., Near-Infrared Emitting Radioactive Gold Nanoparticles with Molecular Pharmacokinetics. *Angew. Chem. Int. Ed.* **2012,** *51* (40), 10118-10122.

3. Ginting, R. T.; Kaur, S.; Lim, D.-K.; Kim, J.-M.; Lee, J. H.; Lee, S. H.; Kang, J.-W., Plasmonic Effect of Gold Nanostars in Highly Efficient Organic and Perovskite Solar Cells. *ACS Appl. Mater. Interfaces* **2017,** *9* (41), 36111-36118.

4. Mukherjee, S.; Libisch, F.; Large, N.; Neumann, O.; Brown, L. V.; Cheng, J.; Lassiter, J. B.; Carter, E. A.; Nordlander, P.; Halas, N. J., Hot Electrons Do the Impossible: Plasmon-Induced Dissociation of H_2 on Au. *Nano Lett.* **2013,** *13* (1), 240-247.

5. Kumari, G.; Zhang, X.; Devasia, D.; Heo, J.; Jain, P. K., Watching Visible Light-Driven CO_2 Reduction on a Plasmonic Nanoparticle Catalyst. *ACS Nano* **2018,** *12* (8), 8330-8340.

6. Yan, L.; Wang, F.; Meng, S., Quantum Mode Selectivity of Plasmon-Induced Water Splitting on Gold Nanoparticles. *ACS Nano* **2016,** *10* (5), 5452-5458.

7. Wu, Q.; Zhou, L.; Schatz, G. C.; Zhang, Y.; Guo, H., Mechanistic Insights into Photocatalyzed H_2 Dissociation on Au Clusters. *J. Am. Chem. Soc.* **2020,** *142* (30), 13090-13101.

8. Cao, B.; Starace, A. K.; Judd, O. H.; Bhattacharyya, I.; Jarrold, M. F.; López, J. M.; Aguado, A., Activation of Dinitrogen by Solid and Liquid Aluminum Nanoclusters: A Combined Experimental and Theoretical Study. *J. Am. Chem. Soc.* **2010,** *132* (37), 12906-12918.

9. Kulkarni, B. S.; Krishnamurty, S.; Pal, S., Size- and Shape-Sensitive Reactivity Behavior of Al_n (n = 2–5, 13, 30, and 100) Clusters Toward the N_2 Molecule: A First-Principles Investigation. *J. Phys. Chem. C* **2011,** *115* (30), 14615-14623.

10. Martirez, J. M. P.; Carter, E. A., Excited-State N_2 Dissociation Pathway on Fe-Functionalized Au. *J. Am. Chem. Soc.* **2017,** *139* (12), 4390-4398.

11. Kumar, D.; Pal, S.; Krishnamurty, S., N_2 Activation on Al Metal Clusters: Catalyzing role of BN-Doped Graphene Support. *Phys. Chem. Chem. Phys.* **2016,** *18* (40), 27721-27727.

12. Ludwig, T.; Singh, A. R.; Nørskov, J. K., Subsurface Nitrogen Dissociation Kinetics in Lithium Metal from Metadynamics. *J. Phys. Chem. C* **2020,** *124* (48), 26368-26378.

13. Chan, J. R.; Lambie, S. G.; Trodahl, H. J.; Lefebvre, D.; Le Ster, M.; Shaib, A.; Ullstad, F.; Brown, S. A.; Ruck, B. J.; Garden, A. L.; Natali, F., Facile Dissociation of Molecular Nitrogen Using Lanthanide Surfaces: Towards Ambient Temperature Ammonia Synthesis. *Physical Review Materials* **2020,** *4* (11), 115003.

14. Roy, D.; Navarro-Vazquez, A.; Schleyer, P. v. R., Modeling Dinitrogen Activation by Lithium: A Mechanistic Investigation of the Cleavage of N_2 by Stepwise Insertion into Small Lithium Clusters. *J. Am. Chem. Soc.* **2009,** *131* (36), 13045-13053.

15. Martirez, J. M. P.; Carter, E. A., Prediction of a Low-Temperature N_2 Dissociation Catalyst Exploiting Near-IR–To–Visible Light Nanoplasmonics. *Sci. Adv.* **2017,** *3* (12), eaao4710.

16. Vu, M.-H.; Sakar, M.; Hassanzadeh-Tabrizi, S. A.; Do, T.-O., Photo(electro)catalytic Nitrogen Fixation: Problems and Possibilities. *Adv. Mater. Interfaces* **2019,** *6* (12), 1900091.

17. Martirez, J. M. P.; Carter, E. A., Thermodynamic Constraints in Using AuM (M = Fe, Co, Ni, and Mo) Alloys as N_2 Dissociation Catalysts: Functionalizing a Plasmon-Active Metal. *ACS Nano* **2016,** *10* (2), 2940-2949.

18. Hull, O. A.; Lingerfelt, D. B.; Li, X.; Aikens, C. M., Electronic Structure and Nonadiabatic Dynamics of Atomic Silver Nanowire–N_2 Systems. *J. Phys. Chem. C* **2020,** *124* (38), 20834-20845.

19. Gargiulo, J.; Berté, R.; Li, Y.; Maier, S. A.; Cortés, E., From Optical to Chemical Hot Spots in Plasmonics. *Acc. Chem. Res.* **2019,** *52* (9), 2525-2535.

20. Pandeya, P.; Aikens, C. M., Theoretical Analysis of Optical Absorption Spectra of Parallel Nanowire Dimers and Dolmen Trimers. *J. Phys. Chem. C* **2020,** *124* (24), 13495-13507.

21. Rohrdanz, M. A.; Martins, K. M.; Herbert, J. M., A Long-Range-Corrected Density Functional that Performs well for Both Ground-State Properties and Time-Dependent Density Functional Theory Excitation Energies, Including Charge-Transfer Excited States. *J. Chem. Phys.* **2009,** *130* (5), 054112.

22. Hay, P. J.; Wadt, W. R., Ab Initio Effective Core Potentials for Molecular Calculations. Potentials for K to Au Including the Outermost Core Orbitals. *J. Chem. Phys.* **1985,** *82* (1), 299-310.

23. Wadt, W. R.; Hay, P. J., Ab Initio Effective Core Potentials for Molecular Calculations. Potentials for Main Group Elements Na to Bi. *J. Chem. Phys.* **1985,** *82* (1), 284-298.

24. Hay, P. J.; Wadt, W. R., Ab Initio Effective Core Potentials for Molecular Calculations. Potentials for the Transition Metal Atoms Sc to Hg. *J. Chem. Phys.* **1985,** *82* (1), 270-283.

25. Casida, M. E., Time-Dependent Density Functional Response Theory for Molecules. In *Recent Advances in Density Functional Methods*, WORLD SCIENTIFIC: 1995; Vol. Volume 1, pp 155-192.

26. Goings, J. J.; Lestrange, P. J.; Li, X., Real-Time Time-Dependent Electronic Structure Theory. *Wiley Interdiscip. Rev. Comput. Mol. Sci.* **2018,** *8* (1), e1341.

27. Yabana, K.; Nakatsukasa, T.; Iwata, J. I.; Bertsch, G. F., Real-Time, Real-Space Implementation of the Linear Response Time-Dependent Density-Functional Theory. *Phys. Status Solidi B* **2006,** *243* (5), 1121-1138.

28. Yabana, K.; Bertsch, G. F., Time-Dependent Local-Density Approximation in Real Time. *Phys. Rev. B* **1996,** *54* (7), 4484-4487.

29. Ding, F.; Goings, J. J.; Liu, H.; Lingerfelt, D. B.; Li, X., Ab Initio Two-Component Ehrenfest Dynamics. *J. Chem. Phys.* **2015,** *143* (11), 114105.

30. Wang, F.; Yam, C. Y.; Hu, L.; Chen, G., Time-Dependent Density Functional Theory Based Ehrenfest Dynamics. *J. Chem. Phys.* **2011,** *135* (4), 044126.

31. Li, X.; Tully, J. C.; Schlegel, H. B.; Frisch, M. J., Ab Initio Ehrenfest Dynamics. *J. Chem. Phys.* **2005,** *123* (8), 084106.

32. Frisch, M.; Trucks, G.; Schlegel, H.; Scuseria, G.; Robb, M.; Cheeseman, J.; Scalmani, G.; Barone, V.; Mennucci, B.; Petersson, G., Gaussian 09 (Gaussian, Inc., Wallingford, CT). *Revision D* **2009,** *1*.

33. Momma, K.; Izumi, F., VESTA 3 for Three-Dimensional Visualization of Crystal, Volumetric and Morphology Data. *J. Appl. Crystallogr.* **2011,** *44* (6), 1272-1276.

34. Jmol: an Open-source Java Viewer for Chemical Structures in 3D. http://jmol.sourceforge.net/ (accessed June).

35. Guidez, E. B.; Aikens, C. M., Theoretical Analysis of the Optical Excitation Spectra of Silver and Gold Nanowires. *Nanoscale* **2012,** *4* (14), 4190-4198.

36. Alkan, F.; Aikens, C. M., Understanding Plasmon Coupling in Nanoparticle Dimers Using Molecular Orbitals and Configuration Interaction. *Phys. Chem. Chem. Phys.* **2019,** *21* (41), 23065-23075.

Chapter 7 - Real-time Electron Dynamics Study of Plasmon-mediated Photocatalysis on an Icosahedral Al_{13}^{-1} Nanocluster

Reproduced with permission from:

Pandeya, P.; Aikens, C. M., *J. Phys. Chem. A* ***2021,*** *125 (22),* 4847-4860.

7.1 Abstract

Nitrogen bond dissociation is one of the important steps in the Haber Bosch process, where N_2 is catalytically converted to NH_3; however, the dissociation of the nitrogen triple bond is difficult to achieve. In this study, we investigate the possibility of nitrogen activation using plasmonic excitation of an icosahedral aluminum nanocluster. Real-time time dependent density functional theory is employed to study the electron dynamics of the Al_{13}^{-1} and $[Al_{13}N_2]^{-1}$ systems. Step and trapezoidal electric fields with field strengths of 0.001 au and 0.01 au and different polarization directions are applied to the systems and the electron dynamics are analyzed. Because the occupation of nitrogen antibonding orbitals could potentially activate the N-N bond, we investigated the single-particle electronic transitions corresponding to an excitation from an occupied (O) to virtual (V) molecular orbitals (P_{OV}) of $[Al_{13}N_2]^{-1}$. We found that N_2 antibonding orbitals are more likely to become populated with stronger fields and also by using off-resonance fields.

7.2 Introduction

When light irradiates a metal surface, localized surface plasmons can arise. These surface plasmons are resonantly excited oscillations of free electrons at the metal surface. These surface plasmon resonances have found various applications, e.g. in surface-enhanced spectroscopy,[1] nano-imaging,[2] biochemical sensing,[3] and photovoltaic applications.[4] Plasmonic properties of noble metals like gold and silver nanoparticles are fascinating and have been heavily studied by many research groups.[5-19] However, their industrial applications can be limited due to their scarcity and high cost. In comparison, aluminum is a common base metal which is ten thousand times cheaper than precious metals and possesses highly promising plasmonic properties.[20-21] Aluminum has found many uses due to its low density and ability to resist corrosion due to surface passivation.[22] The oxidation layer in Al terminates after 2–3 layers, thus forming a protective layer and preserving the metal.[20] This property has made Al an ideal material to use in the aerospace, transportation, and building industries.[22] Furthermore, the optical tunability of Al is beyond that of gold and silver.[21] The empty d bands in Al enable the plasmon to lie far into the ultraviolet region.[23] Because the d-band of Al lies above its Fermi energy, its plasmon resonance extends beyond the visible region into the far ultraviolet region.[24] Although many applications utilize visible plasmon resonances, an advantage of plasmons in the UV region is that their high photon energy matches the electronic transition energy of many organic molecules and solids.[25] In spite of these characteristics of Al, there have been very few theoretical studies on the optical and plasmonic properties of Al nanoclusters.[20, 26-29] Thus, it is important to study the plasmonic properties of aluminum nanoclusters.

Aluminum nanoclusters are currently of interest in plasmonic photocatalysis. In plasmonic photocatalysis, incident radiation (such as solar energy) interacts with the plasmonic properties of

nanoparticles to enable their use as a catalyst for different purposes (e.g. to tackle problems related to environmental pollution and global warming).[30] For example, Gómez et al. designed an Al/TiO_2 photocatalyst system for degradation of methylene blue, which is an organic pollutant.[31] They showed that the Al/TiO_2 system exhibits higher photocatalytic activity than bare TiO_2. Aluminum plasmon-enhanced photocatalysts have also been used in a water splitting reaction to generate H_2, which produces a renewable and clean fuel.[32] Similarly, Halas et al. reported the use of Al nanostructures in plasmon-enabled H_2 dissociation in photocatalyst systems.[33-34] Other research groups have also studied the potential application of small Al nanoclusters to break the molecular hydrogen (H_2) bond.[33, 35-38] Although no previous work has examined plasmon-induced dissociation on aluminum nanoparticles, several theoretical studies of plasmonic photocatalysis on gold and silver clusters have been undertaken.[39-44]

In our work, we are specifically interested in breaking the bond in the N_2 molecule. One of the most important applications involving N_2 dissociation is the Haber-Bosch process, where N_2 is catalytically converted to NH_3. Because N_2 has a large bond dissociation energy (224.5 kcal/mol), a highly negative electron affinity (-1.8 eV), and a huge HOMO-LUMO gap (22.9 eV), it requires high temperature and pressure to activate the N_2 bond, and thus N_2 dissociation is the rate determining step of the procedure.[45] Plasmonic photocatalysis can provide an energy-efficient alternative to the Haber-Bosch process if the plasmonic properties of nanoparticles can be used under ambient temperature and pressure to break the N_2 bond. Although Al has highly promising plasmonic properties, there have been very few studies for the reaction and activation of N_2 bond with Al nanoclusters, and the studies that exist focus on ground state dissociation processes.[46-48] Romanowski et al. found that the dissociative adsorption of N_2 on the solid and liquid aluminum surfaces has an activation barrier of 3.2 eV and 3.0 eV respectively, and is exothermic.[47] Cao et

al. studied the chemisorption of N_2 into the $Al_{44}^{+/-}$ cluster where they saw that the N_2 molecule dissociates accompanied by a change of the Al cluster to a liquid state.[46] Pal et al. conducted a first-principles investigation and found that the interaction of nitrogen with Al_n (n = 2–5, 13, 30, and 100) clusters is sensitive to the shape and the orientation of the cluster.[49] In a theoretical work by Kumar et al., the authors observed the activation of N_2 with an Al_n (n = 4-8) cluster supported on a BN-doped graphene sheet.[50]

Because one of the potential ways to activate the N_2 bond is to push electrons into the valence orbitals of the nitrogen molecule,[50] in this paper we examine whether the antibonding orbital of N_2 can become occupied with "hot" or excited electrons from the Al nanocluster. Our study employs real-time time dependent density functional theory (RT-TDDFT).[51-52] RT-TDDFT calculations have been used to examine the electron dynamics occurring in plasmonic systems such as silver and gold nanoparticles and to determine how electron occupancies of orbitals change over time.[53-61] RT-TDDFT can also be used to compute absorption spectra,[62-64] frequency-dependent properties like polarizabilities,[65] magnetic circular dichroism spectra,[66] hyperpolarizabilities,[67] coherence,[53] molecular conductance[68-69] and charge transfer dynamics.[58, 70-71]

7.3 Computational details

A development version of the Gaussian package[72] is used for all calculations with the LC-ωPBE[73] functional and 6-31G(d) basis set. The LC-ωPBE functional is useful for accurately describing charge transfer excitations,[44, 73-74] such as those from the Al_{13}^{-1} cluster to the N_2 molecule. The closed shell icosahedral Al_{13}^{-1} cluster was optimized with no imaginary frequencies (coordinates given in the Supporting Information, Table D-1); the largest Abelian group of the

molecule is the C_{2h} group, which was used in the calculations. Multiple configurations of the N_2 molecule binding to the Al_{13}^{-1} cluster were optimized to form $[Al_{13}N_2]^{-1}$ with no symmetry constraints, and vibrational frequencies were checked to ensure that there are no imaginary frequencies. After optimization, the molecule was translated so that the center of mass of the molecule lies at the origin. The coordinates of the optimized structure and the translated molecule (after aligning the origin at the center of mass) are given in Supporting Information (Table D-2 and Table D-3). This structure is used for all subsequent calculations. The N_2 molecule lies nearly but not exactly in the xy-plane in these coordinates. The optimized $[Al_{13}N_2]^{-1}$ cluster is shown in Figure 7-1.

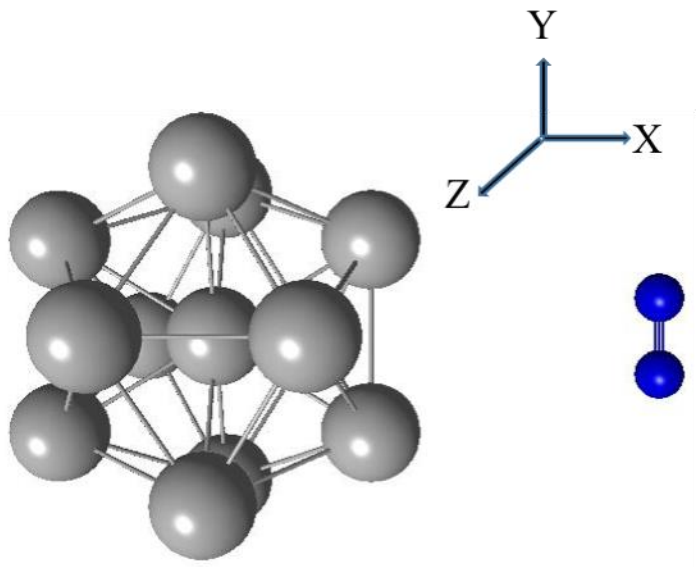

Figure 7-1 Optimized geometry of the $[Al_{13}N_2]^{-1}$ system.

We have used time dependent density functional theory (TDDFT) methods for this study. We employ both linear response TDDFT (LR-TDDFT) and real-time TDDFT (RT-TDDFT) because they are complementary techniques with different advantages. In the limit of a small perturbation that does not shift the electron density significantly from its ground stationary state,

an absorption spectrum obtained from RT-TDDFT agrees with LR-TDDFT. However, we cannot study the interaction of a strong field with the LR method. A LR-TDDFT absorption spectrum is obtained by solving an eigenvalue problem derived from retaining the first order response of the density to a perturbation.[75] LR-TDDFT iteratively solves for the eigenvalues and corresponding transitions, and thus it is useful to study the spectra of smaller systems. RT-TDDFT is helpful as it solves the time-dependent Schrödinger equation for quantum systems and simulates the response to any combination of perturbations, whether they are electromagnetic fields, complex environments, or thermal baths.[76-78] In our study, LR-TDDFT calculations are performed for optimized Al_{13}^{-1} and $[Al_{13}N_2]^{-1}$. The first 1200 excited states are obtained for the LR-TDDFT calculation of the Al_{13}^{-1} system while the lowest 1300 states are computed for $[Al_{13}N_2]^{-1}$. The spectra are plotted with a Gaussian smoothing with a FWHM of 0.2 eV. The absorption spectra are also obtained using RT-TDDFT calculations with a step field perturbation of 0.001 au along the z-direction for Al_{13}^{-1} while perturbation along all three directions (x, y and z) are taken for $[Al_{13}N_2]^{-1}$ because of its symmetry. We have used a simulation time of 240 fs with an integration step size of 0.0012 fs to generate the absorption spectra. In the RT-TDDFT framework, the electronic density matrix is propagated according to the TDDFT equation:[53, 79]

$$i\frac{dP(t)}{dt} = [K(t), P(t)]$$

where *P* and *K* are the density and Kohn-Sham matrices in an orthonormal basis. The density matrix is propagated using a unitary time evolution operator $U(t_n)$:

$$P(t_{n+1}) = U(t_n).P(t_{n-1}).U^{\dagger}(t_n)$$

The time varying density matrix is transformed into canonical molecular orbitals using $P_{OV}(t) = C_0^{\dagger}.P(t).C_0$ at each time step. The variation of off-diagonal molecular orbital density

matrix elements (P_{OV}) over time helps to analyze the amount of single-particle electronic transitions corresponding to an excitation from an occupied (O) to virtual (V) molecular orbital.

The orbital occupation numbers $n_k(t)$ are determined by projecting the time-dependent density matrix $P(t)$ onto the initial orbitals:

$$n_k(t) = C_k^{\dagger}(0)P(t)C_k(0)$$

where $C_k(0)$ is the k^{th} eigenvector of the initial Kohn-Sham matrix and n_k is the occupation of k^{th} molecular orbital.[80] The time-dependent dipole moment, $\mu(t)$, is calculated at each time step as:[53]

$$\mu(t) = Tr[DP(t)]$$

where D is the dipole matrix in the orthonormal basis. To obtain the optical absorption spectra, we take the Fourier transform (FT) of the time-dependent electric dipole moment parallel to the polarization of the electric field perturbation.

RT-TDDFT calculations are performed in this work with both step electric fields and continuous wave electric fields with a trapezoidal envelope (hereafter simply referred to as a "trapezoid field"). Spectral properties are calculated using the step field while the possible dissociation of N_2 triggered by excitation of different electronic states is studied using the trapezoid electric field. A step field is a field that is applied for a short time (t) in a certain direction as:[53]

$$E(t) = E_0 \text{ for } t < 0$$

$$E(t) = 0 \text{ for } t > 0$$

To apply the step field, we prepare the initial electron density by a self-consistent field calculation in the presence of a static electric field (E_0) in a given direction. Then, we turn off the field and propagate the electronic system using the RT-TDDFT method. To use the trapezoid field, a linearly-polarized electric field oscillating with a frequency that matches with a given excited state energy is applied for a certain duration ($t > 0$). In our calculations, we have applied the

trapezoid field for 20 fs. The field is gradually increased to its maximum intensity over the first 1 fs, stays there for 18 fs, and gradually gets turned off between 19 and 20 fs as shown in Figure 7-2a. The FT of the applied electric field is shown in Figure 7-2b. In our calculations, we have applied two different field strengths, 0.001 au (corresponding to a field of 3.51×10^{13} W/cm^2) and 0.01 au (strong field with 3.51×10^{14} W/cm^2), to study the effect of field strength in N_2 activation. We have used a simulation time of 240 fs with an integration step size of 0.0012 fs. We have used the trapezoid field with frequencies corresponding to 7 eV (that corresponds to the plasmon peak of both systems), 6 eV (that corresponds to the charge transfer peak of $[Al_{13}N_2]^{-1}$), and 8 eV (off resonant field). It should be noted that these applied field energies may fall above the vertical ionization energy of the clusters.[81-83]

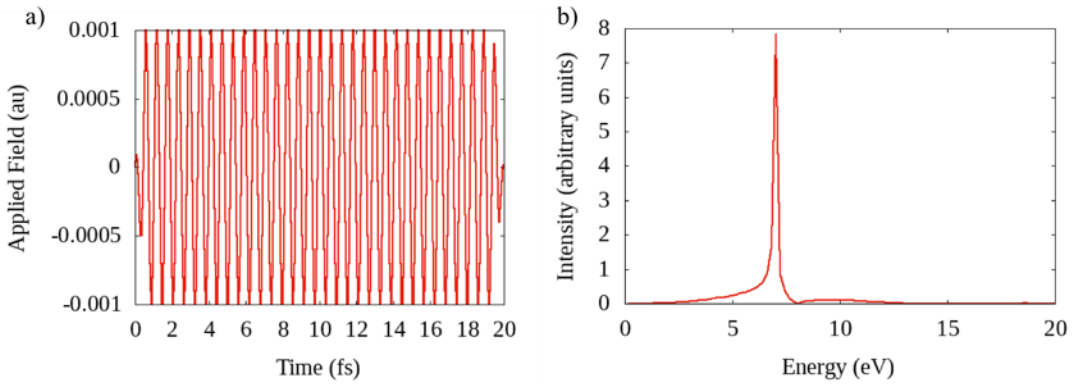

Figure 7-2 a) Trapezoid field of 0.001 au field strength oscillating with a frequency corresponding to 7.0 eV applied for 20 fs and b) FT of the applied electric field in part a.

7.4 Results and discussions

7.4.1 Geometric and electronic structure

The $[Al_{13}N_2]^{-1}$ system has C_1 symmetry because the geometry is optimized without symmetry constraints. As shown in the optimized structure (Figure 7-1), N_2 is essentially parallel

to the y-axis and the intermolecular axis between N_2 and Al_{13}^{-1} is the x-axis. The distance between both N atoms to the nearest Al atom is 4.233 Å.

Figures 3a and 3b show the spectra of Al_{13}^{-1} and $[Al_{13}N_2]^{-1}$ respectively that are obtained from LR-TDDFT and RT-TDDFT methods. The spectrum obtained with LR-TDDFT matches the spectrum obtained with RT-TDDFT for each of the systems. Both systems possess a strong plasmon peak at ~7.0 eV. The inclusion of the N_2 molecule into the Al_{13}^{-1} system yields a very small extra feature in the absorption spectrum, which is a peak at approximately 6 eV. This small peak at 6 eV has an oscillator strength of 0.09 a.u. for $[Al_{13}N_2]^{-1}$ (Table D-5), whereas the oscillator strength of the peak at 6 eV is zero for Al_{13}^{-1}. This extra feature is referred to as a charge transfer peak in the text because transitions from aluminum-based orbitals to nitrogen antibonding orbitals have significant contributions to this peak (Table D-5).

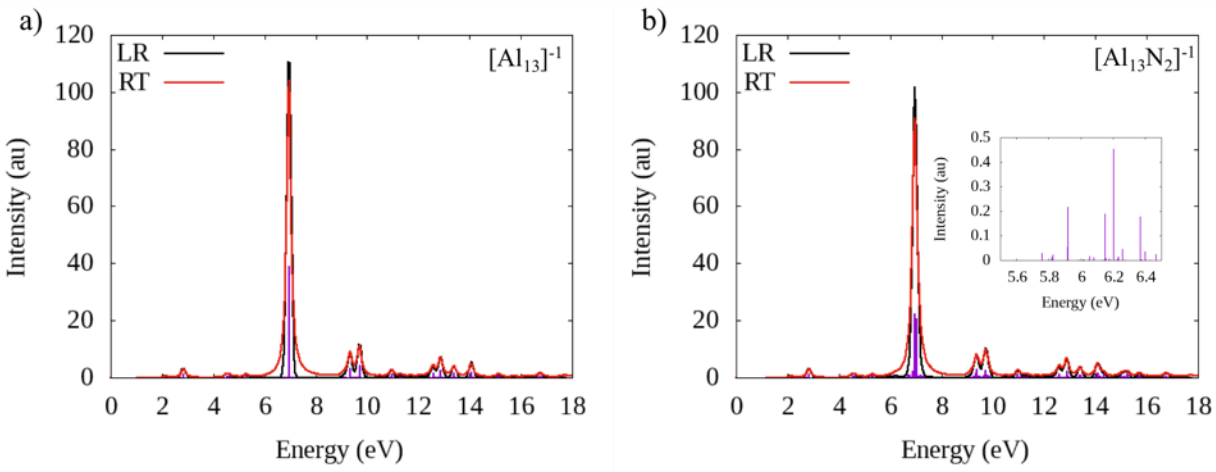

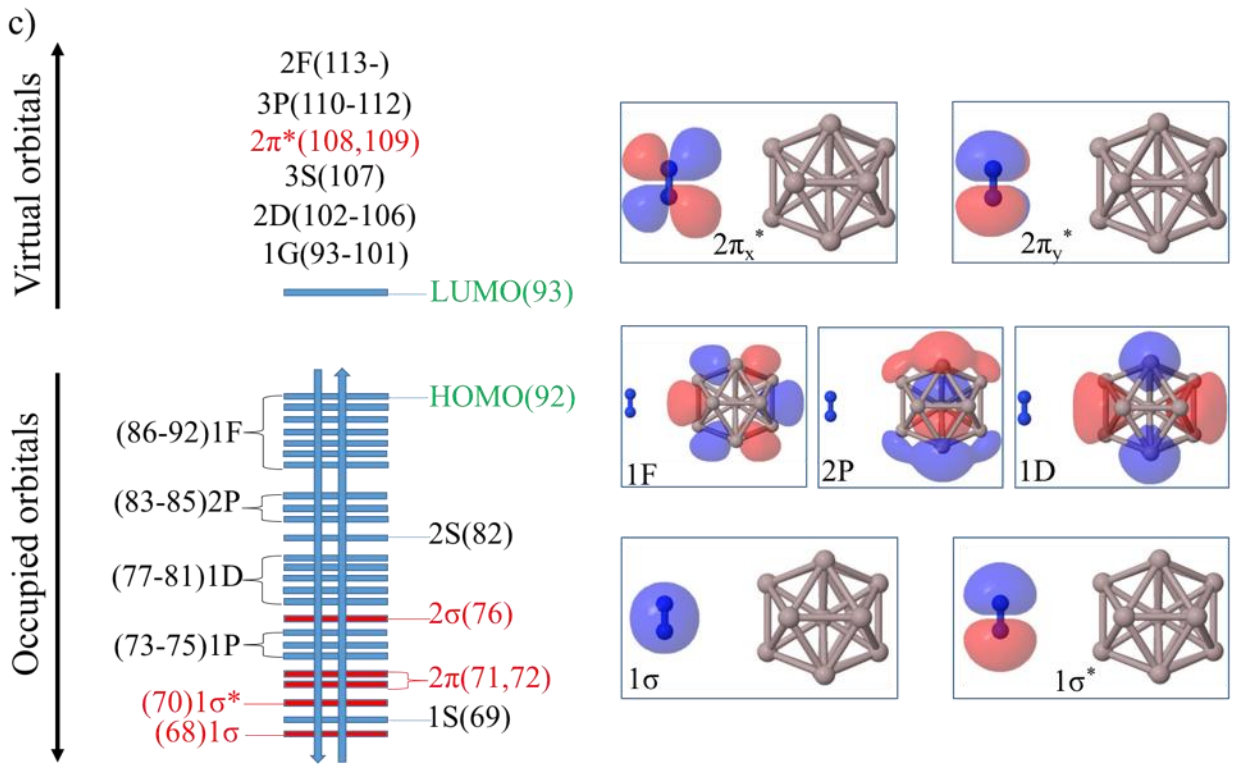

Figure 7-3 a) Absorption spectrum of $[Al_{13}]^{-1}$ and b) Absorption spectrum of $[Al_{13}N_2]^{-1}$ obtained from both LR-TDDFT and RT-TDDFT with a step field of 0.001 au along the z-direction. Purple sticks in both a) and b) show the unbroadened stick spectra obtained from LR-TDDFT; their heights are proportional to their oscillator strengths. The black curve represents the spectrum with Gaussian broadening of 0.2 eV FWHM to account for experimental broadening. The inset in b) shows the spectrum of $[Al_{13}N_2]^{-1}$ near 6 eV. c) Molecular orbital diagram of $[Al_{13}N_2]^{-1}$ system (left). The molecular orbitals localized on the nitrogen molecule are shown as red lines and orbitals arising primarily from aluminum are shown as blue lines. Selected molecular orbitals of $[Al_{13}N_2]^{-1}$, including some localized on the Al_{13} cluster (superatomic orbitals[84-85]) and some around the nitrogen molecule, are shown on the right. Al_{13}^{-1} superatom orbitals are labeled with capital letters such as 1S, 1P, and 1D where the S, P and D superatom orbitals have the same nodal symmetry as the corresponding atomic orbitals. The nitrogen molecular orbitals are labeled as σ and π.

The most significant transitions responsible for the plasmon peak (7.0 eV) in both systems and the 6.0 eV peak in $[Al_{13}N_2]^{-1}$, which is the extra feature after the inclusion of the nitrogen molecule, are given in Table D-4, Table D-5 and Table D-6. These transitions show that collective excitations (superpositions of single particle transitions) having comparatively similar weights are responsible for the emergence of these peaks. The molecular orbital diagram of $[Al_{13}N_2]^{-1}$ is shown

in Figure 7-3c. This figure shows the arrangement of superatomic Al_{13}^{-1} based orbitals together with the molecular nitrogen orbitals (shown in red). These superatomic orbitals include orbitals arising from the five valence electrons ($2s^2 2p^3$) of nitrogen, three valence electrons ($3s^2 3p^1$) of aluminum and an extra electron. In Figure 7-3c, we also observe the five occupied molecular orbitals and two virtual antibonding orbitals from the nitrogen molecule (shown in red). In this project, we are especially interested in the occupation of these antibonding orbitals as this could activate the dinitrogen bond.

7.4.2 Application of step field

7.4.2.1 Al_{13}^{-1}

On application of the step field polarized in the x-, y-, and z- directions, the system shows a dipole response to the field. The electrons of the system respond to the applied electric field; as a result, a dipole moment is induced in the direction of the applied field. The dipole moment induced in the x-, y-, and z-directions due to the application of a 0.001 au field in the z- direction is shown below in Figure 7-4. This figure shows that the dipole moment is primarily induced in the direction of the applied field (z) whereas it is negligible in the x and y directions. Figure D-1 shows the x-, y-, and z-components of the induced dipole moments upon applying a 0.001 au step field along the x-direction. It also shows a strong induced dipole moment in the direction of applied field and insignificant inducement in other directions. An applied field in the y-direction will also induce a significant dipole moment in the y-direction only. The magnitude of the total induced dipole moment remains the same irrespective of the direction of the given field (Figure 7-4 and Figure D-1). We also see that the dipole moment variation is constant throughout the simulation time in the direction of the applied field.

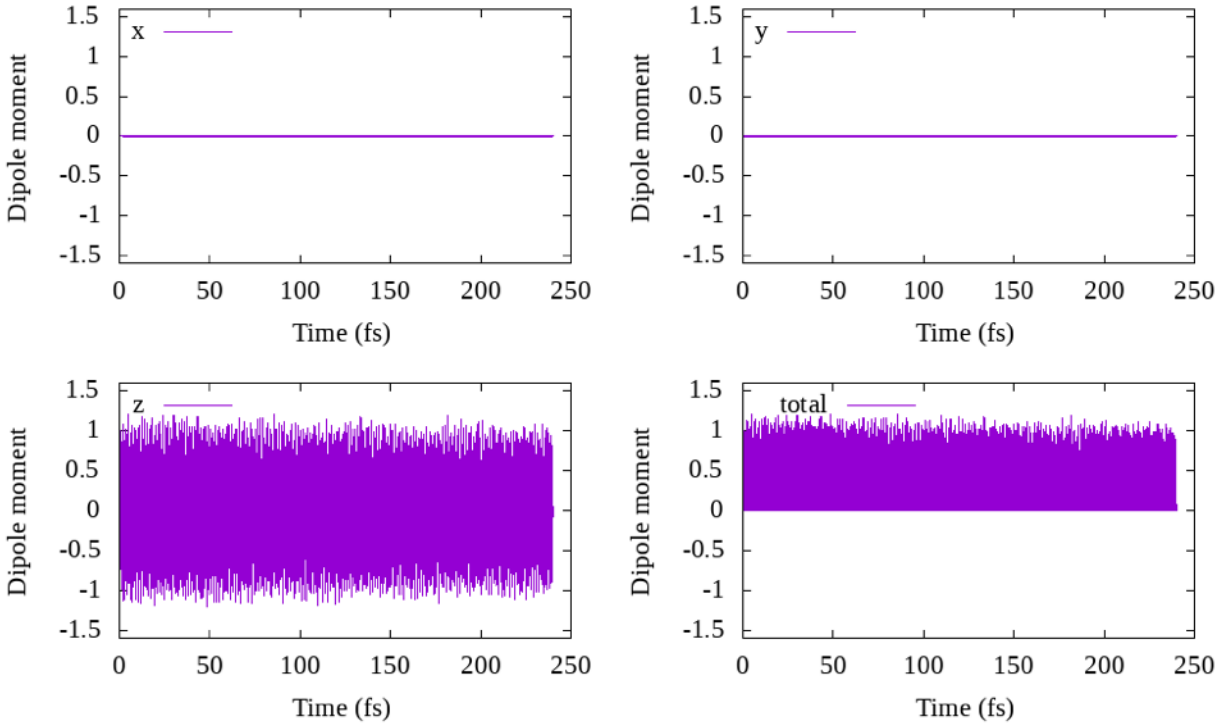

Figure 7-4 Dipole moment (Debye) induced in the Al_{13}^{-1} system on applying a 0.001 au step field along the z-direction.

We also studied the variation of off-diagonal density matrix elements (P_{OV}) over time, which provide an indication of the amount of single-particle electronic transitions corresponding to an excitation from an occupied (O) to virtual (V) molecular orbital. Analysis of the FTs of the P_{OV} elements indicates to which excited states these transitions contribute. On application of the field along z- and x-directions, most of the transitions yield peaks at 2 eV, 2.5 eV, and 7 eV. The variation of P_{OV} with time for the transitions that contribute to these peaks along with the corresponding FTs of P_{OV} elements is shown in Figure D-2 for the step field applied in the z-direction. A few transitions also give peaks at 14 eV, 10 eV, 5 eV, and 4 eV (not shown). This demonstrates that a RT-TDDFT calculation with a step field leads to the excitation of multiple states at different energies. When the field is applied in the z-direction (Figure D-2), the highest intensity FT peaks occur at an energy of ~2–2.5 eV, which mainly corresponds to 1F→2D, and

2P→2D transitions; the importance of the ~2–2.5 eV peaks will be discussed more later in the text. The FTs obtained at 7 eV are slightly smaller than the ones obtained at ~2–2.5 eV and correspond mainly to 1F→3D, 2P→1G, and 1F→1G transitions. Due to symmetry, the excitation in the x- and z-direction is essentially the same. Moreover, the orbital contributions to the 7 eV peaks obtained from RT-TDDFT match with the orbital contributions to the peak obtained with LR-TDDFT (Table D-6).

7.4.2.2 $[Al_{13}N_2]^{-1}$

As in the case of the Al_{13}^{-1} system (Figure 7-4), the dipole moment for $[Al_{13}N_2]^{-1}$ is highest in the direction of the applied field and negligible in other directions (Figure 7-5). When the field is applied in the z-direction, the magnitude of the z-component of the induced dipole moment is essentially the same in both Al_{13}^{-1} and $[Al_{13}N_2]^{-1}$ systems (Figure 7-4 and 7-5). Because the N_2 molecule in $[Al_{13}N_2]^{-1}$ is present along the x-axis (Figure 7-1), the z-component of the induced dipole moment is minimally affected by the addition of this adsorbate. Interestingly, even the application of an x-polarized field does not cause a significant effect on the x-component of the induced dipole moment for the $[Al_{13}N_2]^{-1}$ system (Figure D-3) compared to that of the Al_{13}^{-1} system (Figure D-1); the x-component of the dipole moment varies negligibly around its static value of -2.32 Debye. However, the decay pattern of the dipole moment changes after the inclusion of nitrogen. In Al_{13}^{-1}, the dipole moment is constant up to 240 fs, irrespective of the direction of the applied field (Figures 7-4 and D-1). In contrast, for the $[Al_{13}N_2]^{-1}$ system, the dipole moment changes during the simulation time (Figures 5 and S3). For example, when a z-polarized field is applied to $[Al_{13}N_2]^{-1}$, the z-component of the dipole decreases until 100 fs and then gains magnitude from 100 fs to 240 fs (Figure 7-5). This change in the dipole moment can be explained

by an analysis of orbital occupation numbers for MOs 84 and 109 (Figure D-5) because the 84→109 transition has the highest intensity FT peak (Figure D-6). The occupation of orbital 84 decreases at ~100 fs while the occupation number of orbital 109 increases at ~100 fs (Figure D-5), which may have led to the decrease in the total dipole moment magnitude. When an x-polarized field is applied to $[Al_{13}N_2]^{-1}$ (Figure D-3), more oscillations are observed in the overall envelope of the x-component of the dipole moment. Overall, the dipole moment decreases in its magnitude throughout the simulation time of 240 fs. Because $[Al_{13}N_2]^{-1}$ has distinct x, y, and z axes in contrast to Al_{13}^{-1}, we observe different trends in the dipole moments upon application of laser fields with different polarizations.

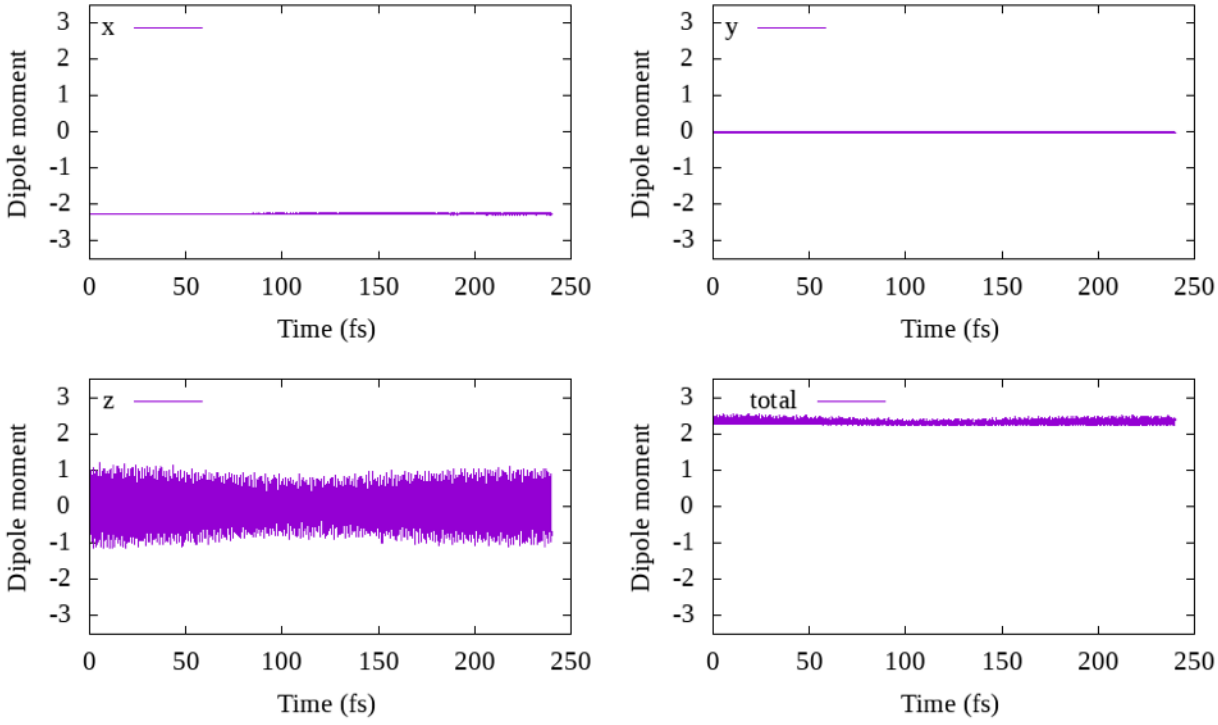

Figure 7-5 Dipole moment (Debye) induced in the $[Al_{13}N_2]^{-1}$ system on applying 0.001 au step field along the z-direction.

On application of electric fields in the z- and x-directions to $[Al_{13}N_2]^{-1}$, most of the transitions give FT peaks at 2 eV, 2.5 eV, and 7 eV, similar to the Al_{13}^{-1} system. A few transitions

also give peaks at 6 eV and 4.5 eV for the $[Al_{13}N_2]^{-1}$ system. Again, the 6 eV peak is a new charge-transfer feature in $[Al_{13}N_2]^{-1}$ compared to the Al_{13}^{-1} system. The transitions that give the highest intensity FT peaks at different energies along with their P_{OV} for the corresponding transitions for a step electric field of 0.001 au applied in the z-direction for the $[Al_{13}N_2]^{-1}$ system are shown in Figure D-6.

7.4.3 Application of trapezoid field

7.4.3.1 Al_{13}^{-1}

Application of fields that are resonant with specific absorptions of a cluster are useful in order to understand how electrons that are excited with these resonant fields subsequently evolve. We applied an electric field strength of 0.001 au and a frequency corresponding to 7 eV (resonant with the plasmon frequency) to the Al_{13}^{-1} system using a trapezoidal envelope for a window of 20 fs and observed the system evolve in time up to 240 fs. Application of a z-polarized trapezoidal field induces the highest dipole moment in the z-direction, while the dipole moment components in other directions are negligible (Figure 7-6), which is similar to the case of the step field (Figure 7-4). Although both the trapezoidal and step fields are z-polarized fields with strengths of 0.001 au, the z-component of the dipole moment becomes much stronger with a trapezoidal field (Figure 7-6) than with step field (Figure 7-4); this occurs because the electric field is applied for a longer time (for 20 fs) when using a trapezoid field whereas the field is only given initially and then turned off when using step field. We observe that the z-component of the dipole decreases after the given field is turned off at 20 fs. Similar to the z-polarized field, only the x-component of the dipole component is significant when the x-polarized field is applied to the system (Figure D-7).

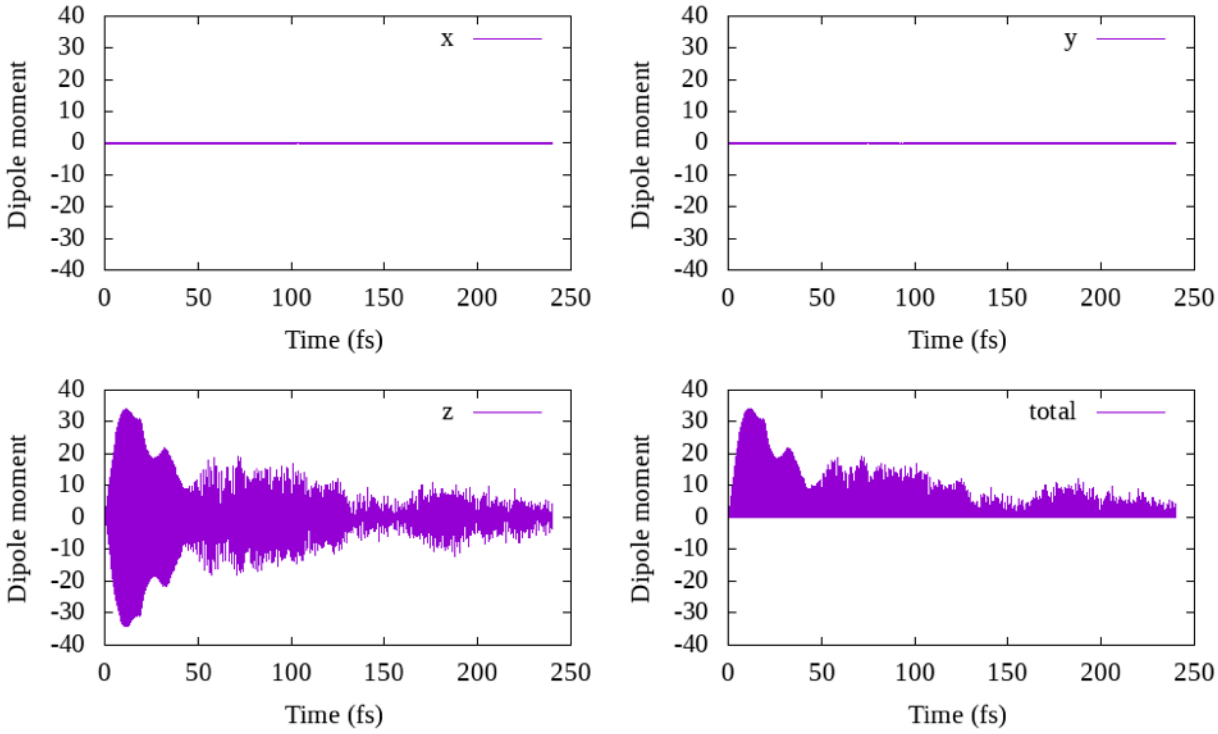

Figure 7-6 Variation of x-, y-, and z-components of the dipole moment (Debye) of the Al_{13}^{-1} arising from the application of a 7 eV trapezoid field with a field strength of 0.001 au along the z-direction.

Application of this z-polarized field gives the highest intensity FT peaks from 2–3 eV (Figure D-8). Although we are applying the frequency corresponding to 7 eV, we do not get highest intensity FT peaks at 7 eV; FT peaks at 7 eV are of less intensity than the FT peaks obtained at 2-3 eV (Figure D-8). It is also observed that most of the transitions that give the peak at 7 eV also give the peaks at 2 eV, 3 eV, 5 eV and 10 eV (Figure D-8). Similar to the z-polarized field, the x-polarized field also gives the highest intensity FT peaks at ~2–3 eV.

7.4.3.2 $[Al_{13}N_2]^{-1}$

(a) Trapezoid field of 7 eV polarized in z-direction:

The $[Al_{13}N_2]^{-1}$ system has C_1 symmetry and hence has nonzero static as well as dynamic polarizability for diagonal and off-diagonal elements. Due to this nonzero off-diagonal polarizability, a small dipole moment can be induced in directions other than the direction of the applied field (Figure 7-7). To confirm this, we prepared the $[Al_{13}N_2]^{-1}$ system with C_{2v} symmetry and calculated its dynamic and static polarizability. The off-diagonal polarizabilities for $[Al_{13}N_2]^{-1}$ system with C_{2v} symmetry were found to be zero (Table D-7) and the induced dipole moment in other directions was also zero (Figure D-9). As the three linear functions of C_{2v} point group belong to different irreducible representations, there is no coupling between them to give a nonzero off-diagonal polarizability and hence no dipole moment is induced in directions other than the direction of applied field. However, because the clusters would not be perfectly symmetrical in nature due to vibrational motion, studying the cluster with C_1 symmetry is advantageous to learn about properties that are likely to be observed.

With the z-polarized field, x- and y-components of the induced dipole moment are significantly smaller than the z-component of the induced dipole moment (Figure 7-7). The dipole moment increases in the x- and y-directions only after the field is turned off at 20 fs. While the field is on, the magnitude of the dipole moment is negligible in other directions compared to the dipole moment in the direction of the applied field.

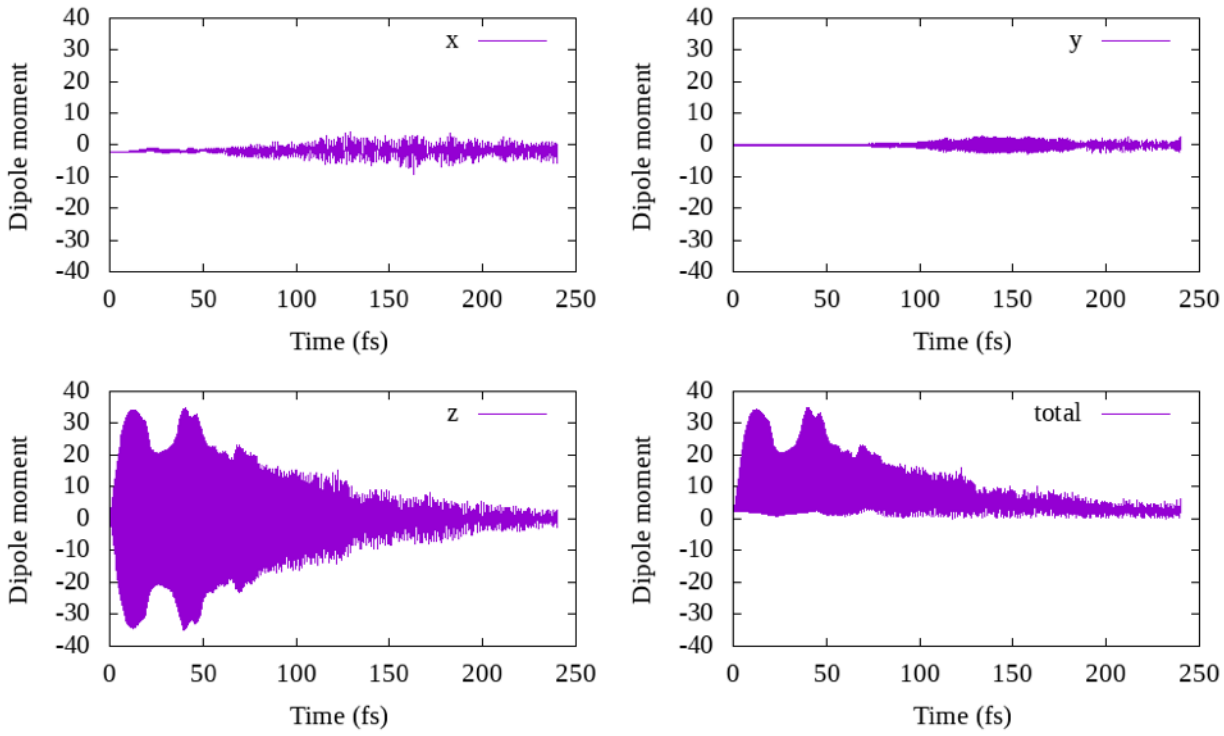

Figure 7-7 Variation of x-, y-, and z-components of the dipole moment (Debye) of the $[Al_{13}N_2]^-$ [1] arising from the application of a 7 eV trapezoid field with a field strength of 0.001 au along the z-direction.

The transitions between the aluminum superatomic orbitals give the highest intensity FT peaks (transitions to orbitals based primarily on N_2 do not give FT peaks with high intensity). The maximum intensity FT peaks lie at energies of 2–3 eV and also at 7 eV (Figure D-10). Also, we notice the appearance of two main kinds of transitions: one where the oscillation of the P_{OV} starts right away, and another where it starts at a later time (Figure 7-8). The transitions that immediately induce the oscillation yield FT peaks at 7 eV and decay at a later time (Figure 7-8 a,b), whereas the transitions that start sometime after the field is switched off at 20 fs give FT peaks at ~2–3 eV and gain intensity over the course of simulation (Figure 7-8 c,d). This suggests that the 7 eV plasmon peak of the system decays to the peaks at energies of 2–3 eV. These two types of transitions along with their FT peaks are given in Figure D-10. In Figure D-10, P_{OV} elements for

92→94 and 85→94 are different compared to other transitions. P_{OV} elements for these transitions start right away and do not decay after 20 fs. They give FT peaks at both 7 eV and 2–3 eV. LR-TDDFT also shows that the 92→94 transition is a primary contributor to the peak at 7 eV that has an oscillator strength of 4.7 (Table D-4). Transitions 92→94 and 85→94 also contribute to the peak at 2.8 eV that has an oscillator strength of 0.2.

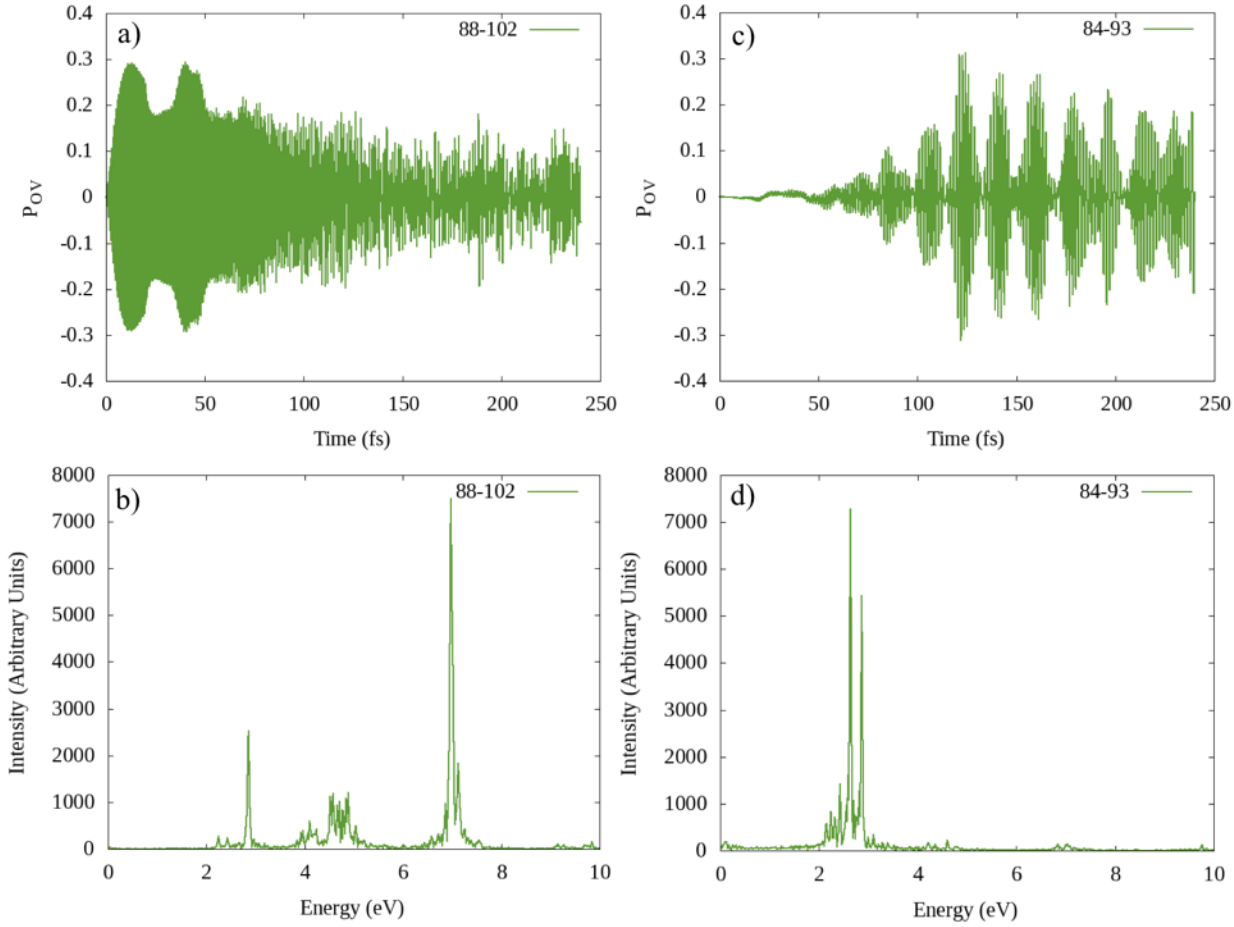

Figure 7-8 Variation of P_{OV} with time (a) and the FT peaks (b) for a characteristic transition that contributes to the major peaks at 7 eV (88→102). Variation of P_{OV} with time (c) and the FT peaks (d) for a transition that contributes the major peaks at 2 - 3 eV (84→93). These are obtained from the application of a 0.001 au trapezoidal laser field with frequency corresponding to 7 eV along the z-direction in the $[Al_{13}N_2]^{-1}$ system.

On applying this field, we also observe transitions into the antibonding orbitals of nitrogen (orbitals 108 and 109), which may lead to activation of the dinitrogen bond. The P_{OV} and the FT peaks of these transitions are shown in Figure 7-9. The FT peaks of most of these transitions are obtained at 7 eV. The P_{OV} of some of these transitions start right away while other P_{OV} elements begin to grow sometime after the field is switched off at 20 fs. For example, P_{OV} for 90→109 begins right away while 89→109 begins after 100 fs. The antibonding molecular orbital (MO) 108 is oriented in the x-direction while the antibonding MO 109 is oriented in the y-direction (Figure 7-3). Also, from Figure 7-9, the P_{OV} values suggest that electrons can begin to occupy either MO 108 or MO 109 right away. For example, the transition from occupied MO 89 to MO 108 ($2\pi_x$) starts right away whereas the oscillation starts after 100 fs when the transition occurs from MO 89 to MO 109 ($2\pi_y$). However, when we examine the transition out of MO 84, the oscillation starts right away during the transition to MO 109 ($2\pi_y$) and starts later when the transition is to MO 108 ($2\pi_x$). The oscillations that start right away are polarized in the z-direction, whereas the oscillations that begin at a later time are polarized in the x-direction. This suggests that the polarization direction of the excitation is a potentially important factor in activating the N_2 bond.

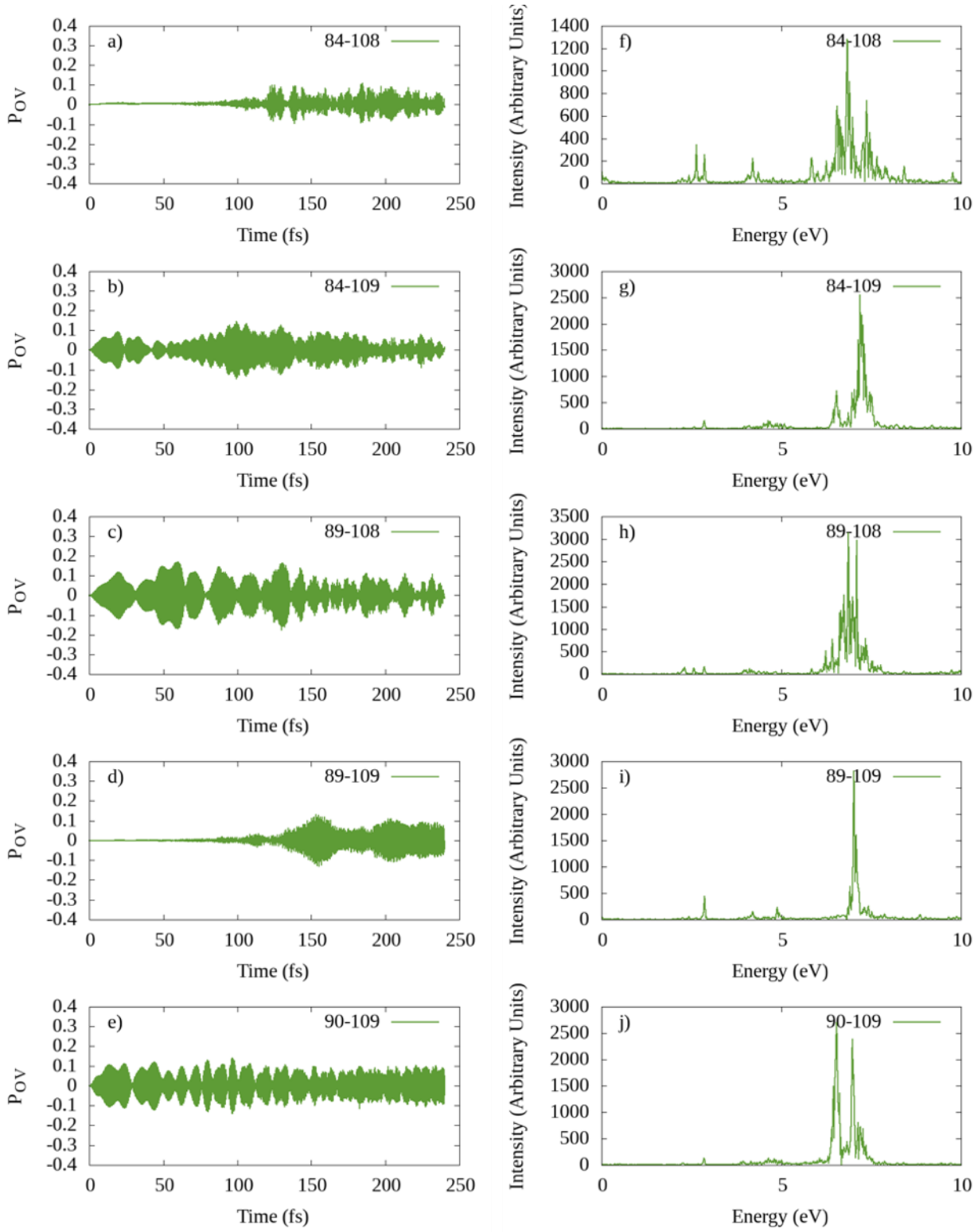

Figure 7-9 P_{OV} variation with time for the transitions to nitrogen antibonding orbitals, and the FT peaks for the corresponding transitions. These are obtained from the application of a 0.001 au trapezoidal laser field with frequency corresponding to 7 eV along the z-direction in the $[Al_{13}N_2]^{-1}$ system.

Interference patterns observed in the P_{OV} dynamics for the transitions in Figure 7-9, (e.g. 90→109, 89→108) during the first 20 fs are caused due to the interaction of the incident electric field (7 eV) with the resonances that are present for the $[Al_{13}N_2]^{-1}$ system. For example, for the 90→109 transition, an interference occurs between the incident field at 7 eV and the peaks of the system at 6.5 eV (Figure 7-9).

We also observe two-photon absorption peaks, which are observed in the FT as peaks at 14 eV, when an electric field of 7 eV is applied to the $[Al_{13}N_2]^{-1}$ system. Transitions out of lower-lying orbitals such as 69→97 give these two-photon absorption peaks. The P_{OV} dynamics and their FT peaks for some of the transitions that yield two-photon absorption peaks are shown in Figure D-11. Two photon absorption has been identified as a plasmon decay mechanism in a previous study on tetrahedral Ag_8 system.[79]

We also investigated the electron dynamics with a higher field strength of 0.01 au. Similar to the applied field with a field strength of 0.001 au, a z-polarized electric field with a 0.01 au field strength produces a high dipole moment in the z-direction compared to other directions while the field is on (Figure D-12). Increasing the field strength by a factor of ten almost doubles the dipole moment magnitude; the maximum value of the dipole moment is ~35 Debye when a 0.001 field is applied (Figure 7-7) compared to the maximum value of ~70 Debye when applying a 0.01 au field (Figure D-12). The dipole moment magnitude does not decrease until ~50 fs after application of the 0.001 au field (Figure 7-7) whereas it decreases drastically after 20 fs upon application of the 0.01 au field (Figure D-12).

Many FT peaks with small intensities along with a few intense peaks are obtained at different energies after application of the 0.01 au field (Figure D-13). With the 0.01 au field, the FT peaks have lower intensity (max intensity of ~5000 as shown in Figure D-13) compared to the

FT peak intensity obtained with the 0.001 au field (max intensity of ~8000, as shown in Figure 7-8). Most of the highest intensity FT peaks are obtained at ~10 eV while some are also obtained at ~ 7 eV and ~14 eV (Figure D-13). With the higher field strength, the highest intensity FT peaks are the charge transfer peaks, which arise from a transition between aluminum-based orbitals and the nitrogen based MOs (MO 108 and MO 109).

Although the FT peak intensity has decreased, the P_{OV} values can be larger with the higher field strength. The highest P_{OV} value is 0.6 in this case (Figure D-13(b)) whereas it is approximately 0.4 after application of the 0.001 au field. Even though the magnitude of P_{OV} oscillation is higher with the 0.01 au field, the intensity of the FT peaks is low which could be due to the drastic reduction of the P_{OV} elements observed after 20 fs. Two types of P_{OV} dynamics are mainly obtained: (a) P_{OV} starts right away with high amplitude and decreases drastically after the field is turned off at 20 fs (e.g. 84→102, Figure D-13(b)), and (b) P_{OV} starts after the field is turned off at 20 fs (e.g. 72→109, Figure D-13(b)). P_{OV} of type (a) yields the 7 eV FT peaks while the FT of P_{OV} of type (b) gives the 10 eV peak (Figure 7-13(a)). In this strong field case, the plasmon peak at 7 eV appears to transform into a 10 eV peak at a later time. Two-photon absorption peaks are also obtained in this case (e.g. 70→109, Figure D-13(b)).

(b) Trapezoid field of 6 eV applied along z-direction:

In this section, we describe the results obtained upon application of a 6 eV electric field, which is resonant with the newly formed charge transfer peak in the $[Al_{13}N_2]^{-1}$ system. The magnitude of the induced dipole moment is smaller when a frequency corresponding to 6 eV is given (Figure 7-10) compared to the magnitude of the induced dipole moment when a frequency corresponding to 7 eV is applied (Figure 7-7), which is due to the weak oscillator strength of the

6 eV excitation observed in the LR-TDDFT calculations. The x- and y-components of the induced dipole moment are negligible on applying a 6 eV field (Figure D-14) whereas they are noticeable when the field of 7 eV is applied (Figure 7-7). An interference pattern in the dipole moment oscillations is observed during the first 20 fs (Figure 7-10). The FT of the dipole moment up to 20 fs shows that the observed pattern is due to interference between the applied field (6 eV) and the plasmon peak (7 eV) of the system (Figure D-15). After the 6 eV field is turned off, the system oscillates at its plasmon frequency (7 eV) only (Figure D-15). The dipole moment decays slowly after 20 fs (Figure 7-10) compared to the decay pattern obtained after application of the 7 eV field (Figure 7-7).

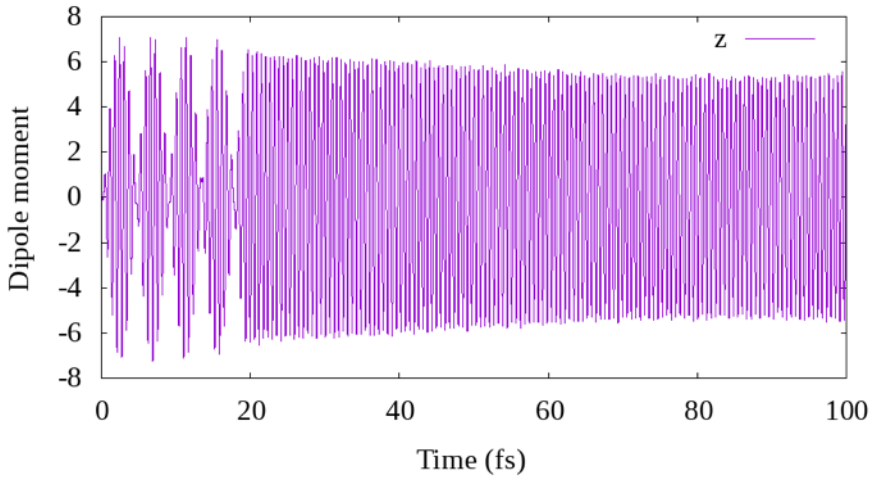

Figure 7-10 Variation of the z-component of the dipole moment (Debye) of $[Al_{13}N_2]^{-1}$ upon application of a 6 eV trapezoid field with a field strength of 0.001 au along the z-direction.

We examined the transitions that show the highest P_{OV} and possess intense FT peaks. Among these transitions, most give FT peaks at 7 eV, while very few yield FT peaks at 5 eV and 14 eV. We do not observe any peaks at ~2–3 eV, unlike those that were observed upon the application of a 7 eV field. Two major patterns of P_{OV} dynamics observed upon application of the

6 eV field are shown in Figure 7-11; the transitions shown are also the transitions that give the highest intensity FT peaks. We observe an interference pattern in both kinds of transitions. An enlarged version of the P_{OV} dynamics in Figure 7-11 is presented in Figure D-16. Although transition 84→109 gives the highest intensity FT peak with the RT-TDDFT method (Figure 7-11), we do not observe any transitions to MO 109 that correspond to the 6 eV peak from LR-TDDFT (Table D-5). Instead, transition 84→108 is obtained with LR-TDDFT and has the highest oscillator strength. Another major transition from RT-TDDFT, 88→102, is also not present in the LR-TDDFT data (Table D-5).

For the 88→102 transition, the interference lasts until the applied electric field is turned off at 20 fs. The difference between two cycles is ~4 fs (Figure D-16). 4 fs corresponds to 1 eV, which is equivalent to the energy difference between the 7 eV plasmon peak and the 6 eV applied field. So, for the 88→102 transition, the interference seen up to 20 fs is the interference between the applied field at 6 eV and the plasmon peak of the system (7 eV). After the electric field is turned off at 20 fs, there is no interference and the oscillation only occurs at the plasmon frequency corresponding to 7 eV. This information about the interference can also be obtained from the FT peaks of this transition (Figure D-17). In Figure D-17, the 7 eV peak is visible at all times; the 6 eV peak is no longer seen after 20 fs. The FT of this transition after 20 fs is obtained by taking the FT of the P_{OV} dynamics after 20 fs.

Transition 84→109 has nonzero P_{OV} that lasts throughout the whole simulation time (Figure 7-11a) and gives FT peaks at 7 eV and 6 eV (Figure 7-11b). FT peaks obtained by taking the P_{OV} elements from 21–130 fs and from 130–240 fs show that the 6 eV and 7 eV peak remains throughout the duration of the simulation (Figure D-18). Because 84→109 gives the highest intensity FT peak and MO 109 is a nitrogen antibonding orbital, this indicates that there is a large

probability for occupation of this nitrogen antibonding orbital when an electric field with an energy of 6 eV is applied to this system.

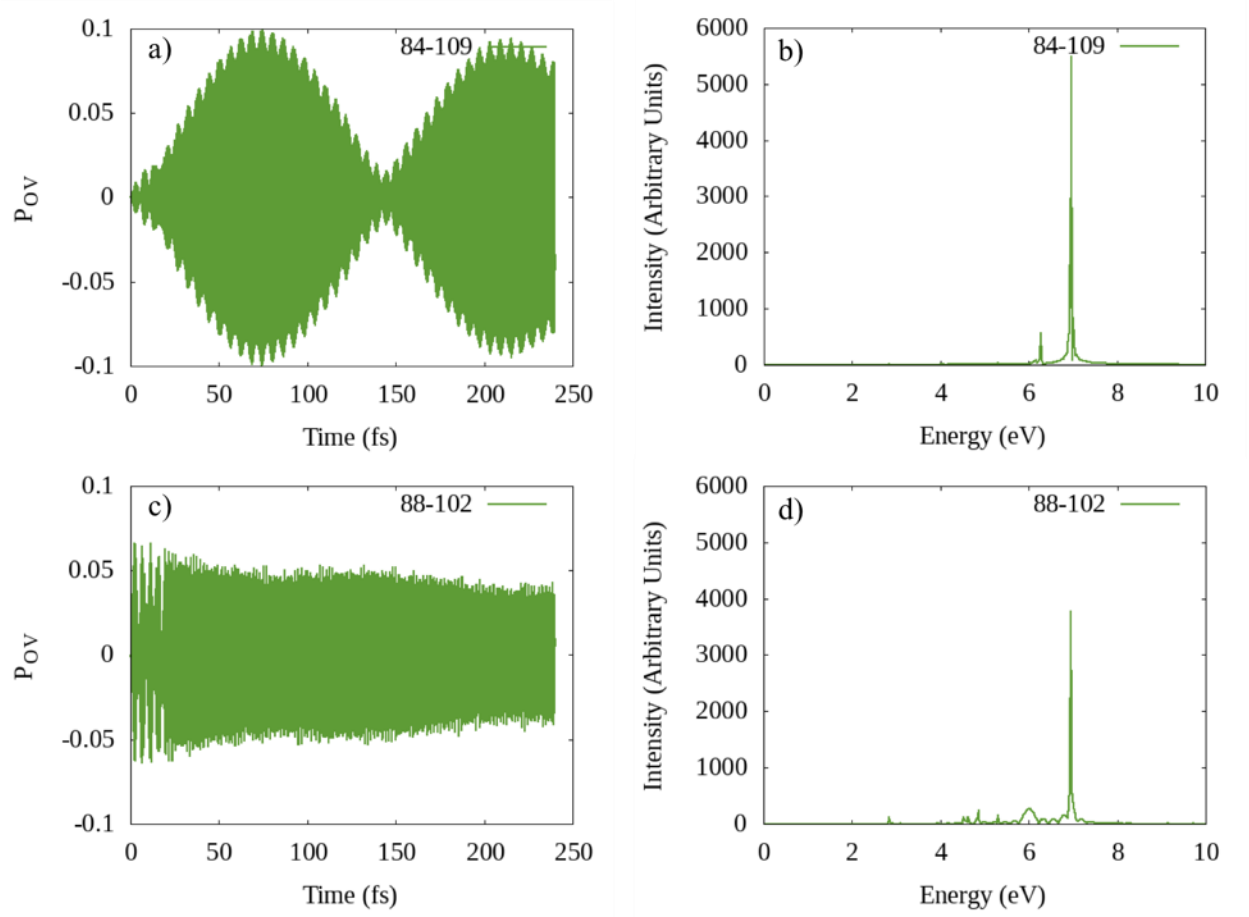

Figure 7-11 P_{OV} variation with time (a, c) and FT peaks (b, d) for the transitions that give the highest intensity FT peaks due to the application of a 0.001 au trapezoidal laser field with a frequency corresponding to 6 eV along the z-direction in the $[Al_{13}N_2]^{-1}$ system. The pattern of the oscillation in (c) also represents the pattern for the majority of the oscillations found in this case.

We also analyzed the dynamics with a higher field strength of 0.01 au. Similar to the above discussed cases, the largest dipole moment is induced in the direction of the applied field and is negligible in other directions. In addition, the dipole moment magnitude decreases suddenly after the applied field is switched off (Figure D-19) whereas it decreases slowly when the 0.001 au field is applied (Figure 7-10). The abrupt decrease of the dipole moment after 20 fs is similar to the

decrease we observed on applying a 0.01 au field with a frequency corresponding to the energy of 7 eV. Increasing the field strength ten times (from 0.001 au to 0.01 au) increases the dipole moment by approximately ten times; from ~7 Debye (Figure 7-10) to ~60 Debye (Figure D-19). So, an approximately linear relationship is observed between the dipole moment and the applied field strength for this system.

Unlike the 7 eV field with a field strength of 0.01 au, in which many FT peaks with small intensities spread over large energy range were observed (Figure D-13), these small peaks are not observed in Figure D-20 for the 6 eV field with a field strength of 0.01 au. The 88→102 transition (Figure D-20), which gives one of the highest intensity FT peaks when the 0.001 au field was applied, gives the highest intensity FT peak in this case as well. The highest P_{OV} values increase from 0.06 to 0.4 upon increasing the field strength from 0.001 au to 0.01 au. Similarly, the highest intensity of the FT peak increases from 6000 to 10,000 upon increasing the field strength from 0.001 au to 0.01 au.

(c) Trapezoid field of 8 eV applied along z-direction:

We have also applied an electric field with a frequency corresponding to 8 eV, which is off-resonance with both the plasmon peak (7 eV) and charge transfer peaks. The nearest charge transfer peaks to 8 eV occur at 7.3 eV and 9 eV. Application of a frequency corresponding to 8 eV in the z-direction induces a high z-component in the dipole moment while the x- and y-components of the induced dipole moment are negligible (Figure D-21). An interference pattern is observed during the first 20 fs. This is due to the interference between the applied field of frequency corresponding to 8 eV and the plasmon peak energy of 7 eV. The magnitude of the induced z-component of the dipole moment obtained via excitation by a field with a frequency corresponding

to 8 eV is higher than that obtained with 6 eV. With the electric field corresponding to 8 eV, the z-component of the dipole abruptly decreases at 20 fs (Figure D-21).

The highest intensity FT peaks from P_{OV} elements in this case are at 7 eV and 8 eV (Figure D-22). We do not obtain any high intensity peaks in an energy range of 2–3 eV, in contrast to the application of the 7 eV electric field. Some FT peaks are also obtained at ~6 eV and at ~10 eV. A charge transfer transition 84(2P)→109(2π*) gives the highest intensity FT peak at 7 eV. This transition also gives the highest intensity peak FT peak at 7 eV when applying an electric field with a frequency corresponding to 6 eV (Figure 7-11). The intensity of the 84→109 transition is higher with the 6 eV applied field (Figure D-18) than with the 8 eV field (Figure D-22) because the 6 eV field is resonant with the charge transfer absorption energy. The P_{OV} dynamics of the 90(1F)→109(2π*) transition shows an interference pattern throughout the simulation time. The interference observed for this transition after 20 fs is between the plasmon peak and the 6 eV charge transfer peak (Figure D-22(b)). On applying this 8 eV field, most of the transitions have P_{OV} oscillations similar to that of transitions 89(1F)→105(2D) and 88(1F)→102(2D), although they do not give the highest intensity FT peaks. They give the FT peaks at 7 eV. The interference observed until 20 fs in these transitions occurs between the applied field and the plasmon frequency. After the electric field is turned off at 20 fs, the electrons oscillate mainly at the 7 eV plasmon frequency of the system (Figure D-22(b)). We observe an interference pattern throughout the simulation time for the transitions that give FT peaks at 8 eV (Figure D-22(c)).

(d) Trapezoid field of 0.001 au and 7 eV applied along x-direction:

Finally, we examine how the system responds to the field when the electric field is polarized in the x-direction, where N_2 lies along the x-axis. Similar to the previously discussed

cases, the field applied in the x-direction gives the highest dipole moment in the x-direction whereas the induced dipole moment is negligible in other directions (Figure 7-12). The magnitude of P_{OV} is higher when the field is given along the x-direction (maximum value 0.6) compared to its magnitude when the field is given along the z-direction (maximum value 0.4), which is likely due to the presence of the molecular nitrogen in the direction of the applied field. The highest intensity for the FT peaks is found to be 8000 in both cases. Similar to the application of the electric field along the z-direction, the maximum intensity FT peaks lie at energies of 2–3 eV and also at 7 eV, suggesting that the frequency of the excitation at 7 eV rather than its direction is responsible for causing the 2-3 eV peaks. Transitions to the nitrogen molecule antibonding orbital have similar dynamics as observed with the z-polarized incident light, where P_{OV} elements have significant values either before 20 fs or after the electric field is switched off at 20 fs. Similar to the case of the application of the field along the z-direction, the 7 eV peak (for which P_{OV} starts right away) decays to the 2–3 eV peak (for which P_{OV} starts at a later time after the applied field is switched off at 20 fs). Two-photon absorption peaks are also observed at 14 eV with a high FT intensity of 8000 for some of the transitions. Low lying orbitals (i.e. MOs 69, 70, 73, 74 and 75) give the two photon absorption peaks with high intensity (Figure D-23).

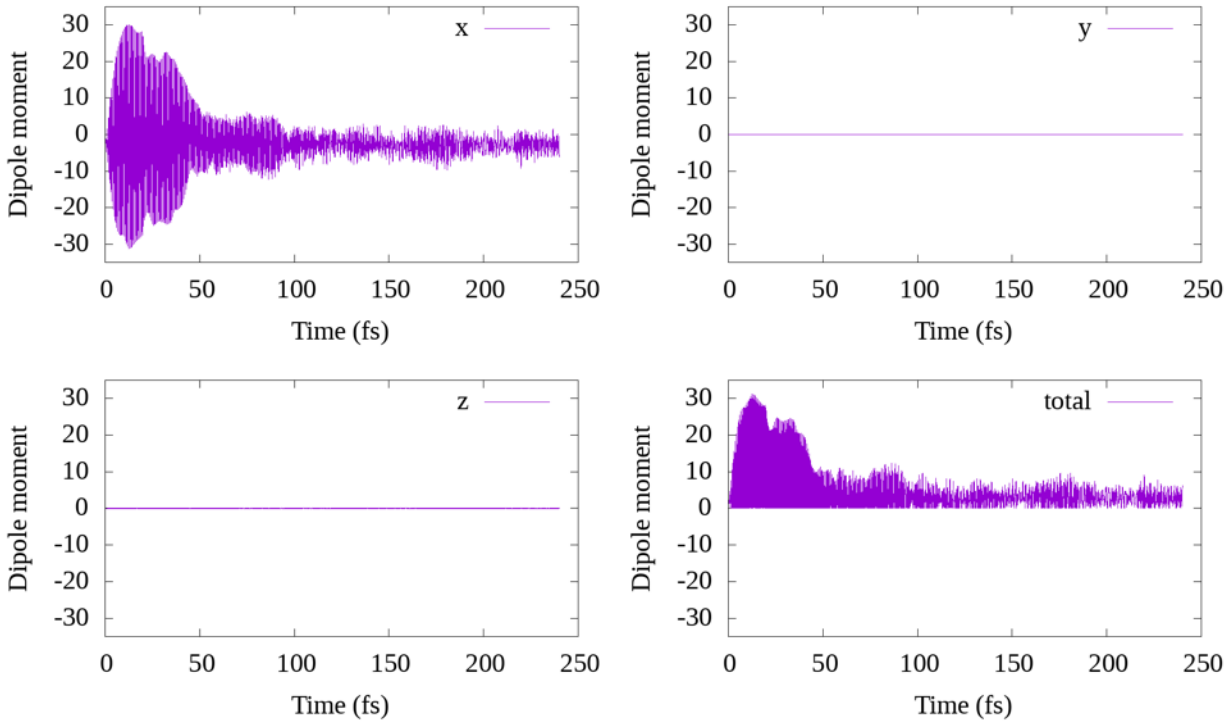

Figure 7-12 Variation of x-, y-, and z-components of the dipole moment (Debye) of $[Al_{13}N_2]^{-1}$ arising from the application of a 7 eV trapezoid field with a field strength of 0.001 au along the x-direction.

7.5 Conclusions

In this study, the excited states and electron dynamics in the Al_{13}^{-1} and $[Al_{13}N_2]^{-1}$ systems have been investigated in order to examine the potential for nitrogen activation on aluminum clusters and nanoparticles. Absorption spectra obtained with the LR-TDDFT method match with spectra obtained with the RT-TDDFT method. The LR-TDDFT spectrum of $[Al_{13}N_2]^{-1}$ shows the appearance of a charge transfer peak at 6 eV that was absent in the spectrum of Al_{13}^{-1}. The dipole moment variation is constant throughout the simulation time on applying a field from any direction to Al_{13}^{-1} whereas it is not constant after adding N_2 to the system. Upon application of laser fields with different polarizations, different trends in the dipole moment are observed for the $[Al_{13}N_2]^{-1}$ system during the simulation time. Because the N_2 is present on the x-axis, the magnitude of the

z-component of the induced dipole moment is not affected by adding N_2 to Al_{13}^{-1}. Even on applying an x-polarized field step field, no significant effect is observed in the magnitudes of the x-components of the induced dipole moment for the $[Al_{13}N_2]^{-1}$ system compared to of Al_{13}^{-1}.

We used both step and trapezoid electric fields for our study. The response of the system's electron density to both fields is similar in the aspect of the induced dipole moment direction; the field applied from a given direction induces the highest dipole moment in the direction of the applied field while the induced dipole moment in other directions is negligible. However, the application of a trapezoid field causes much higher oscillation in the dipole moment, likely due in part to the duration of the application of the field, especially if the field is resonant with an excitation of the system (7 eV). Moreover, the trapezoid field is more targeted to a specific excitation, whereas the step field excites all excitations at once, which means that the intensity of excitation is spread across numerous excitations.

Because of the potential for nitrogen activation via occupation of nitrogen antibonding orbitals, we have mainly studied the real-time density evolution into the MOs of the $[Al_{13}N_2]^{-1}$ system. Transitions to the nitrogen antibonding orbital are observed with almost all the field strengths and applied frequencies. Transitions to the antibonding orbital are more pronounced when the stronger field (0.01 au) is used, and also when the applied electric field is not resonant with the plasmon peak of the system. When a non-resonant field is applied to the system, we observe interference between the non-resonant applied electric field with the plasmon peak of the system while the field is on. For some P_{OV} elements, the interference does not die off even if the applied field is turned off, where the plasmon peak couples with other peaks in the system. Two-photon absorption is observed with all of the field strengths and with the electric fields applied

from any direction studied in this work. Due to the presence of N_2 along the x-axis, P_{OV} values obtained with a x-polarized field are higher than those obtained with a z-polarized field.

Upon applying both step and trapezoid fields, the highest intensity FT peaks are mainly obtained at ~2–2.5 eV and at 7 eV. The 7 eV peak obtained with the 0.001 au z-polarized field corresponding to the frequency of 7 eV decays to the peaks around 2–3 eV. But, with the stronger 0.01 au field, the 7 eV peak instead decays to the peak at ~10 eV. This demonstrates that the plasmonic peak can decay to higher or lower energy peaks depending on the applied field intensity. For fields aligned both along z- and x-directions, FT peaks are observed at 2-3 eV when the applied field corresponding to 7 eV. Thus, the appearance of the 2–3 eV peaks depends on the frequency of the applied field rather than the direction of the applied field. With the 0.01 au field, the FT peaks have lower intensity compared to the FT peak intensity obtained with the 0.001 au field. This could be due to the drastic reduction of P_{OV} values and dipole moment values at 20 fs upon applying the 0.01 au field. The dipole moment and hence the P_{OV} values decrease abruptly also on turning off the non-resonant applied field. Transitions out of lower-lying orbitals such as 69→97 give two-photon absorption peaks (as shown by FT peaks at 14 eV) when an electric field of 7 eV is applied to the $[Al_{13}N_2]^{-1}$ system.

7.6 Acknowledgements

This material is based on work supported by the Department of Energy under grant DE-SC0012273. The computing for this project was performed on the Beocat Research Cluster at Kansas State University, which is funded in part by NSF grants CHE-1726332, CNS-1006860, EPS-1006860, and EPS-0919443. The authors are grateful to Gowri Udayangani Kuda-

Singappulige for the help she provided during this project. The authors thank Prof. Xiaosong Li for the RT-TDDFT code.

7.7 References

1. Willets, K. A.; Van Duyne, R. P., Localized Surface Plasmon Resonance Spectroscopy and Sensing. *Annu. Rev. Phys. Chem.* **2007,** *58* (1), 267-297.

2. Kawata, S.; Inouye, Y.; Verma, P., Plasmonics for Near-Field Nano-Imaging and Superlensing. *Nat. Photonics* **2009,** *3* (7), 388-394.

3. Anker, J. N.; Hall, W. P.; Lyandres, O.; Shah, N. C.; Zhao, J.; Van Duyne, R. P., Biosensing with Plasmonic Nanosensors. In *Nanoscience and Technology*, Co-Published with Macmillan Publishers Ltd, UK: 2009; pp 308-319.

4. Atwater, H. A.; Polman, A., Plasmonics for Improved Photovoltaic Devices. In *Materials for Sustainable Energy*, Co-Published with Macmillan Publishers Ltd, UK: 2010; pp 1-11.

5. Loiseau, A.; Asila, V.; Boitel-Aullen, G.; Lam, M.; Salmain, M.; Boujday, S., Silver-Based Plasmonic Nanoparticles for and Their Use in Biosensing. *Biosensors* **2019,** *9* (2).

6. Ou, J.; Zhou, Z.; Chen, Z.; Tan, H., Optical Diagnostic Based on Functionalized Gold Nanoparticles. *Int. J. Mol. Sci.* **2019,** *20* (18).

7. Lee, S.; Sun, Y.; Cao, Y.; Kang, S. H., Plasmonic Nanostructure-Based Bioimaging and Detection Techniques at the Single-Cell Level. *Trends Analyt Chem* **2019,** *117*, 58-68.

8. Bigdeli, A.; Ghasemi, F.; Golmohammadi, H.; Abbasi-Moayed, S.; Nejad, M. A. F.; Fahimi-Kashani, N.; Jafarinejad, S.; Shahrajabian, M.; Hormozi-Nezhad, M. R., Nanoparticle-Based Optical Sensor Arrays. *Nanoscale* **2017,** *9* (43), 16546-16563.

9. Ginzburg, P., Cavity Quantum Electrodynamics in Application to Plasmonics and Metamaterials. *Rev. Phys.* **2016,** *1*, 120-139.

10. Liu, J.; He, H.; Xiao, D.; Yin, S.; Ji, W.; Jiang, S.; Luo, D.; Wang, B.; Liu, Y., Recent Advances of Plasmonic Nanoparticles and their Applications. *Materials (Basel)* **2018,** *11* (10), 1833.

11. Christensen, T.; Yan, W.; Jauho, A.-P.; Soljačić, M.; Mortensen, N. A., Quantum Corrections in Nanoplasmonics: Shape, Scale, and Material. *Phys. Rev. Lett.* **2017,** *118* (15), 157402.

12. Odom, T. W.; Schatz, G. C., Introduction to Plasmonics. *Chem. Rev.* **2011,** *111* (6), 3667-3668.

13. Amendola, V.; Pilot, R.; Frasconi, M.; Maragò, O. M.; Iatì, M. A., Surface Plasmon Resonance in Gold Nanoparticles: a Review. *J. Phys.: Condens. Matter* **2017,** *29* (20), 203002.

14. Yan, W.; Mortensen, N. A.; Wubs, M., Green's Function Surface-Integral Method for Nonlocal Response of Plasmonic Nanowires in Arbitrary Dielectric Environments. *Phys. Rev. B* **2013,** *88* (15), 155414.

15. Townsend, E.; Bryant, G. W., Plasmonic Properties of Metallic Nanoparticles: The Effects of Size Quantization. *Nano Lett.* **2012,** *12* (1), 429-434.

16. Artuso, R. D.; Bryant, G. W., Quantum Dot--Quantum Dot Interactions Mediated by a Metal Nanoparticle: Towards a Fully Quantum Model. *Phys. Rev. B* **2013,** *87* (12), 125423.

17. Jiang, N.; Zhuo, X.; Wang, J., Active Plasmonics: Principles, Structures, and Applications. *Chem. Rev.* **2018,** *118* (6), 3054-3099.

18. Jain, P. K.; Huang, X.; El-Sayed, I. H.; El-Sayed, M. A., Review of Some Interesting Surface Plasmon Resonance-enhanced Properties of Noble Metal Nanoparticles and Their Applications to Biosystems. *Plasmonics* **2007,** *2* (3), 107-118.

19. Yu, H.; Peng, Y.; Yang, Y.; Li, Z.-Y., Plasmon-Enhanced Light–Matter Interactions and Applications. *Npj Comput. Mater.* **2019,** *5* (1), 45.

20. Knight, M. W.; King, N. S.; Liu, L.; Everitt, H. O.; Nordlander, P.; Halas, N. J., Aluminum for Plasmonics. *ACS Nano* **2014,** *8* (1), 834-840.

21. Maidecchi, G.; Gonella, G.; Proietti Zaccaria, R.; Moroni, R.; Anghinolfi, L.; Giglia, A.; Nannarone, S.; Mattera, L.; Dai, H.-L.; Canepa, M.; Bisio, F., Deep Ultraviolet Plasmon Resonance in Aluminum Nanoparticle Arrays. *ACS Nano* **2013,** *7* (7), 5834-5841.

22. Chen, J.; Luo, Z.; Yao, J., Theoretical Study of Tetrahydrofuran-Stabilized Al_{13} Superatom Cluster. *J. Phys. Chem. A* **2016,** *120* (22), 3950-3957.

23. Mokkath, J. H.; Schwingenschlögl, U., Optical Properties of Al Nanostructures from Time Dependent Density Functional Theory. *J. Chem. Phys.* **2016,** *144* (13), 134305.

24. Knight, M. W.; Liu, L.; Wang, Y.; Brown, L.; Mukherjee, S.; King, N. S.; Everitt, H. O.; Nordlander, P.; Halas, N. J., Aluminum Plasmonic Nanoantennas. *Nano Lett.* **2012,** *12* (11), 6000-6004.

25. Taguchi, A.; Saito, Y.; Watanabe, K.; Yijian, S.; Kawata, S., Tailoring Plasmon Resonances in the Deep-Ultraviolet by Size-Tunable Fabrication of Aluminum Nanostructures. *Appl. Phys. Lett.* **2012,** *101* (8), 081110.

26. Zhang, P.; Jin, W.; Liang, W., Size-Dependent Optical Properties of Aluminum Nanoparticles: From Classical to Quantum Description. *J. Phys. Chem. C* **2018,** *122* (19), 10545-10551.

27. McMahon, B. W.; Yu, J.; Boatz, J. A.; Anderson, S. L., Rapid Aluminum Nanoparticle Production by Milling in NH_3 and CH_3NH_2 Atmospheres: An Experimental and Theoretical Study. *ACS Appl. Mater. Interfaces* **2015,** *7* (29), 16101-16116.

28. Medasani, B.; Vasiliev, I., Computational Study of the Surface Properties of Aluminum Nanoparticles. *Surface Science* **2009,** *603* (13), 2042-2046.

29. Pathak, N. K.; Parthasarathi; Kumar, P. S.; Sharma, R. P., Tuning of the Surface Plasmon Resonance of Aluminum Nanoshell Near-Infrared Regimes. *Phys. Chem. Chem. Phys.* **2019,** *21* (18), 9441-9449.

30. Chen, Y.; Xin, X.; Zhang, N.; Xu, Y.-J., Aluminum-Based Plasmonic Photocatalysis. *Part. Part. Syst. Char.* **2017,** *34* (8), 1600357.

31. Piot, A.; Earl, S. K.; Ng, C.; Dligatch, S.; Roberts, A.; Davis, T. J.; Gómez, D. E., Collective Excitation of Plasmonic Hot-Spots for Enhanced Hot Charge Carrier Transfer in Metal/Semiconductor Contacts. *Nanoscale* **2015,** *7* (18), 8294-8298.

32. Ramadurgam, S.; Lin, T.-G.; Yang, C., Aluminum Plasmonics for Enhanced Visible Light Absorption and High Efficiency Water Splitting in Core–Multishell Nanowire Photoelectrodes with Ultrathin Hematite Shells. *Nano Lett.* **2014,** *14* (8), 4517-4522.

33. Zhou, L.; Zhang, C.; McClain, M. J.; Manjavacas, A.; Krauter, C. M.; Tian, S.; Berg, F.; Everitt, H. O.; Carter, E. A.; Nordlander, P.; Halas, N. J., Aluminum Nanocrystals as a Plasmonic Photocatalyst for Hydrogen Dissociation. *Nano Lett.* **2016,** *16* (2), 1478-1484.

34. Zhang, C.; Zhao, H.; Zhou, L.; Schlather, A. E.; Dong, L.; McClain, M. J.; Swearer, D. F.; Nordlander, P.; Halas, N. J., Al–Pd Nanodisk Heterodimers as Antenna–Reactor Photocatalysts. *Nano Lett.* **2016,** *16* (10), 6677-6682.

35. Moc, J., Hydrogenation of Aluminium Hexamer: Ab Initio Molecular Orbital Theory and Density Functional Theory Study. *Chem. Phys. Lett.* **2008,** *466* (4), 116-121.

36. Pino, I.; Kroes, G. J.; van Hemert, M. C., Hydrogen Dissociation on Small Aluminum Clusters. *J. Chem. Phys.* **2010,** *133* (18), 184304.

37. Udagawa, T.; Suzuki, K.; Tachikawa, M., A Multicomponent QM Study of H_2 Dissociation on Small Aluminum Cluster. *Procedia Comput. Sci.* **2017,** *108*, 2275-2281.

38. Henry, D. J.; Yarovsky, I., Dissociative Adsorption of Hydrogen Molecule on Aluminum Clusters: Effect of Charge and Doping. *J. Phys. Chem. A* **2009,** *113* (11), 2565-2571.

39. Yan, L.; Ding, Z.; Song, P.; Wang, F.; Meng, S., Plasmon-Induced Dynamics of H_2 Splitting on a Silver Atomic Chain. *Appl. Phys. Lett.* **2015,** *107* (8), 083102.

40. Wu, Q.; Zhou, L.; Schatz, G. C.; Zhang, Y.; Guo, H., Mechanistic Insights into Photocatalyzed H_2 Dissociation on Au Clusters. *J. Am. Chem. Soc.* **2020,** *142* (30), 13090-13101.

41. Yan, L.; Xu, J.; Wang, F.; Meng, S., Plasmon-Induced Ultrafast Hydrogen Production in Liquid Water. *J. Phys. Chem. Lett.* **2018,** *9* (1), 63-69.

42. Zhang, Y.; Nelson, T.; Tretiak, S.; Guo, H.; Schatz, G. C., Plasmonic Hot-Carrier-Mediated Tunable Photochemical Reactions. *ACS Nano* **2018,** *12* (8), 8415-8422.

43. Yan, L.; Wang, F.; Meng, S., Quantum Mode Selectivity of Plasmon-Induced Water Splitting on Gold Nanoparticles. *ACS Nano* **2016,** *10* (5), 5452-5458.

44. Hull, O. A.; Lingerfelt, D. B.; Li, X.; Aikens, C. M., Electronic Structure and Nonadiabatic Dynamics of Atomic Silver Nanowire–N_2 Systems. *J. Phys. Chem. C* **2020,** *124* (38), 20834-20845.

45. Shaver, M. P.; Fryzuk, M. D., Activation of Molecular Nitrogen: Coordination, Cleavage and Functionalization of N_2 Mediated By Metal Complexes. *Adv. Synth. Catal.* **2003,** *345* (9-10), 1061-1076.

46. Cao, B.; Starace, A. K.; Judd, O. H.; Bhattacharyya, I.; Jarrold, M. F.; López, J. M.; Aguado, A., Activation of Dinitrogen by Solid and Liquid Aluminum Nanoclusters: A Combined Experimental and Theoretical Study. *J. Am. Chem. Soc.* **2010,** *132* (37), 12906-12918.

47. Romanowski, Z.; Krukowski, S.; Grzegory, I.; Porowski, S., Surface Reaction of Nitrogen with Liquid Group III Metals. *J. Chem. Phys.* **2001,** *114* (14), 6353-6363.

48. Cao, B.; Starace, A. K.; Judd, O. H.; Jarrold, M. F., Melting Dramatically Enhances the Reactivity of Aluminum Nanoclusters. *J. Am. Chem. Soc.* **2009,** *131* (7), 2446-2447.

49. Kulkarni, B. S.; Krishnamurty, S.; Pal, S., Size- and Shape-Sensitive Reactivity Behavior of Al_n (n = 2–5, 13, 30, and 100) Clusters Toward the N_2 Molecule: A First-Principles Investigation. *J. Phys. Chem. C* **2011,** *115* (30), 14615-14623.

50. Kumar, D.; Pal, S.; Krishnamurty, S., N_2 Activation on Al Metal Clusters: Catalyzing role of BN-Doped Graphene Support. *Phys. Chem. Chem. Phys.* **2016,** *18* (40), 27721-27727.

51. Yabana, K.; Bertsch, G. F., Time-DependentLocal-Density Approximation in Real Time. *Phys. Rev. B* **1996,** *54* (7), 4484-4487.

52. Yabana, K.; Nakatsukasa, T.; Iwata, J. I.; Bertsch, G. F., Real-Time, Real-Space Implementation of the Linear Response Time-Dependent Density-Functional Theory. *Phys. Status Solidi B* **2006,** *243* (5), 1121-1138.

53. Ding, F.; Guidez, E. B.; Aikens, C. M.; Li, X., Quantum Coherent Plasmon in Silver Nanowires: A Real-time TDDFT Study. *J. Chem. Phys.* **2014,** *140* (24), 244705.

54. Lian, C.; Hu, S.-Q.; Guan, M.-X.; Meng, S., Momentum-Resolved TDDFT Algorithm in Atomic Basis for Real Time Tracking of Electronic Excitation. *J. Chem. Phys.* **2018,** *149* (15), 154104.

55. Yan, J.; Gao, S., Plasmon Resonances in Linear Atomic Chains: Free-electron Behavior and Anisotropic Screening of d Electrons. *Phys. Rev. B* **2008,** *78* (23), 235413-235422.

56. Yan, J.; Yuan, Z.; Gao, S., End and Central Plasmon Resonances in Linear Atomic Chains. *Phys. Rev. Lett.* **2007,** *98* (21), 216602.

57. Uchida, K.; Watanabe, K., Plasmon Excitation and Electron Emission of a Carbon Nanotube Under a Linearly Polarized Laser: A Real-Time First-Principles Study. *Phys. Rev. B* **2017,** *96* (12), 125419.

58. Peng, B.; Lingerfelt, D. B.; Ding, F.; Aikens, C. M.; Li, X., Real-Time TDDFT Studies of Exciton Decay and Transfer in Silver Nanowire Arrays. *J. Phys. Chem. C* **2015,** *119* (11), 6421-6427.

59. Senanayake, R. D.; Lingerfelt, D. B.; Kuda-Singappulige, G. U.; Li, X.; Aikens, C. M., Real-Time TDDFT Investigation of Optical Absorption in Gold Nanowires. *J. Phys. Chem. C* **2019,** *123* (23), 14734-14745.

60. Gao, B.; Ruud, K.; Luo, Y., Plasmon Resonances in Linear Noble-Metal Chains. *J. Chem. Phys.* **2012,** *137* (19), 194307.

61. Kasper, J. M.; Lestrange, P. J.; Stetina, T. F.; Li, X., Modeling $L_{2,3}$-Edge X-ray Absorption Spectroscopy with Real-Time Exact Two-Component Relativistic Time-Dependent Density Functional Theory. *J. Chem. Theory Comput.* **2018,** *14* (4), 1998-2006.

62. Tussupbayev, S.; Govind, N.; Lopata, K.; Cramer, C. J., Comparison of Real-Time and Linear-Response Time-Dependent Density Functional Theories for Molecular Chromophores Ranging from Sparse to High Densities of States. *J. Chem. Theory Comput.* **2015,** *11* (3), 1102-1109.

63. Repisky, M.; Konecny, L.; Kadek, M.; Komorovsky, S.; Malkin, O. L.; Malkin, V. G.; Ruud, K., Excitation Energies from Real-Time Propagation of the Four-Component Dirac–Kohn–Sham Equation. *J. Chem. Theory Comput.* **2015,** *11* (3), 980-991.

64. Bruner, A.; LaMaster, D.; Lopata, K., Accelerated Broadband Spectra Using Transition Dipole Decomposition and Padé Approximants. *J. Chem. Theory Comput.* **2016,** *12* (8), 3741-3750.

65. Marques, M. A. L.; Castro, A.; Rubio, A., Assessment of Exchange-Correlation Functionals for the Calculation of Dynamical Properties of Small Clusters in Time-Dependent Density Functional Theory. *J. Chem. Phys.* **2001,** *115* (7), 3006-3014.

66. Lee, K. M.; Yabana, K.; Bertsch, G. F., Magnetic Circular Dichroism in Real-Time TIme-Dependent Density Functional Theory. *J. Chem. Phys.* **2011,** *134* (14), 144106.

67. Ding, F.; Van Kuiken, B. E.; Eichinger, B. E.; Li, X., An Efficient Method for Calculating Dynamical Hyperpolarizabilities Using Real-Time Time-Dependent Density Functional Theory. *J. Chem. Phys.* **2013,** *138* (6), 064104.

68. Cheng, C.-L.; Evans, J. S.; Van Voorhis, T., Simulating Molecular Conductance Using Real-Time Density Functional Theory. *Phys. Rev. B* **2006,** *74* (15), 155112.

69. Qian, X.; Li, J.; Lin, X.; Yip, S., Time-Dependent Density Functional Theory with Ultrasoft Pseudopotentials: Real-time Electron Propagation Across a Molecular Junction. *Phys. Rev. B* **2006,** *73* (3), 035408.

70. Petrone, A.; Lingerfelt, D. B.; Rega, N.; Li, X., From Charge-Transfer to a Charge-Separated State: a Perspective from the Real-Time TDDFT Excitonic Dynamics. *Phys. Chem. Chem. Phys.* **2014,** *16* (44), 24457-24465.

71. Chapman, C. T.; Liang, W.; Li, X., Solvent Effects on Intramolecular Charge Transfer Dynamics in a Fullerene Derivative. *J. Phys. Chem. A* **2013,** *117* (13), 2687-2691.

72. Frisch, M.; Trucks, G.; Schlegel, H.; Scuseria, G.; Robb, M.; Cheeseman, J.; Scalmani, G.; Barone, V.; Mennucci, B.; Petersson, G., Gaussian 09 (Gaussian, Inc., Wallingford, CT). *Revision D* **2009,** *1*.

73. Tawada, Y.; Tsuneda, T.; Yanagisawa, S.; Yanai, T.; Hirao, K., A Long-Range-Corrected Time-Dependent Density Functional Theory. *J. Chem. Phys.* **2004,** *120* (18), 8425-8433.

74. Hirao, K.; Chan, B.; Song, J.-W.; Bae, H.-S., Charge-Transfer Excitation Energies Expressed as Orbital Energies of Kohn–Sham Density Functional Theory with Long-Range Corrected Functionals. *J. Phys. Chem. A* **2020,** *124* (39), 8079-8087.

75. Provorse, M. R.; Isborn, C. M., Electron Dynamics with Real-Time Time-Dependent Density Functional Theory. *Int. J. Quantum Chem.* **2016,** *116* (10), 739-749.

76. Goings, J. J.; Lestrange, P. J.; Li, X., Real-Time Time-Dependent Electronic Structure Theory. *Wiley Interdiscip. Rev. Comput. Mol. Sci.* **2018,** *8* (1), e1341.

77. Chapman, C. T.; Liang, W.; Li, X., Open-System Electronic Dynamics and Thermalized Electronic Structure. *J. Chem. Phys.* **2011,** *134* (2), 024118.

78. Morzan, U. N.; Ramírez, F. F.; Oviedo, M. B.; Sánchez, C. G.; Scherlis, D. A.; Lebrero, M. C. G., Electron Dynamics in Complex Environments with Real-Time Time Dependent Density Functional Theory in a QM-MM Framework. *J. Chem. Phys.* **2014,** *140* (16), 164105.

79. Kuda-Singappulige, G. U.; Lingerfelt, D. B.; Li, X.; Aikens, C. M., Ultrafast Nonlinear Plasmon Decay Processes in Silver Nanoclusters. *J. Phys. Chem. C* **2020,** *124* (37), 20477-20487.

80. Li, X.; Smith, S. M.; Markevitch, A. N.; Romanov, D. A.; Levis, R. J.; Schlegel, H. B., A Time-Dependent Hartree–Fock Approach for Studying the Electronic Optical Response of Molecules in Intense Fields. *Phys. Chem. Chem. Phys.* **2005,** *7* (2), 233-239.

81. Casanova, D.; Matxain, J. M.; Ugalde, J. M., Plasmonic Resonances in the Al_{13}^- Cluster: Quantification and Origin of Exciton Collectivity. *J. Phys. Chem. C* **2016,** *120* (23), 12742-12750.

82. Schriver, K. E.; Persson, J. L.; Honea, E. C.; Whetten, R. L., Electronic Shell Structure of Group-IIIA Metal Atomic Clusters. *Phys. Rev. Lett.* **1990,** *64* (21), 2539-2542.

83. Smith, Q. A.; Gordon, M. S., Electron Affinity of Al_{13}: A Correlated Electronic Structure Study. *J. Phys. Chem. A* **2011,** *115* (5), 899-903.

84. Khanna, S. N.; Jena, P., Atomic Clusters: Building Blocks for a Class of Solids. *Phys. Rev. B* **1995,** *51* (19), 13705-13716.

85. Walter, M.; Akola, J.; Lopez-Acevedo, O.; Jadzinsky, P. D.; Calero, G.; Ackerson, C. J.; Whetten, R. L.; Grönbeck, H.; Häkkinen, H., A Unified View of Ligand-protected Gold Clusters as Superatom Complexes. *Proc. Natl. Acad. Sci. U.S.A.* **2008,** *105* (27), 9157.

Chapter 8 - Conclusions

Electrons that are excited to excited states cannot remain there for a long time and they need to dissipate their energy in some way. There are various mechanisms/pathways through which the electrons lose their energy and go back to the ground state. If the electrons relax through the radiative pathway, they emit light in a process called fluorescence or phosphorescence. If the electrons relax through the nonradiative pathways, they lose their energy in the form of heat and light is not emitted. Luminescent systems can find application in the field of sensing whereas non-luminescent systems can be used in purposes like photo-thermal therapy. So, it is important to understand the electron relaxation mechanism as well as the lifetimes of excited electrons to choose a right candidate for the right application. In this dissertation, we have studied the radiative and nonradiative relaxation of excited electrons in various thiolate protected nanoclusters.

We studied the effect of silver doping on the nonradiative relaxation dynamics of excited electrons in $[Au_{25-n}Ag_n(SH)_{18}]^{-1}$ (n = 1, 12, 25) using the fewest switches surface hopping approach. Electron relaxation from the first excited state (HOMO → LUMO) is found to have the longest decay time compared to the relaxation time from higher excited states in all of the studied clusters. This behavior is similar to that observed for the un-doped system. Because there is large gap between the orbitals that corresponds to the first excited state (HOMO-LUMO gap), the excited state population takes a long time to relax from one state to another. But, the orbitals that correspond to the higher excited states are closer to each other (compared to the HOMO-LUMO gap) in the studied systems. Because the orbitals are closer, the excited state population can immediately relax to the nearby orbitals which causes the faster relaxation of excited state population. So, the nonradiative decay of excited states was found to depend on the compactness of the excited states/orbitals. Because the orbitals are closer in $[Au_{13}Ag_{12}(SH)_{18}]^{-1}$ than in other

nanoclusters, we observed the fastest decay of excited electrons in this cluster. The decay times of the S_1 state are 18.0 ps, 6.5 ps, and 18.0 ps respectively for $[Au_{24}Ag(SH)_{18}]^{-1}$, $[Au_{13}Ag_{12}(SH)_{18}]^{-1}$, and $[Ag_{25}(SH)_{18}]^{-1}$. Among the higher excited states, S_7 (HOMO → LUMO+2) has the longest decay times because of the large gap between LUMO+1 and LUMO+2 orbitals. In all systems, the ground state growth times (times for the population in excited state to relax to the ground state) are found to be significantly longer than the decay times due to the population relaxation into intermediate states. Due to having the slowest decay of excited state electrons to the ground state, $[Au_{13}Ag_{12}(SH)_{18}]^{-1}$ is found to be the best candidate for a solar cell sensitizer among the studied clusters.

We also investigated the radiative and nonradiative relaxation of excited electrons in $Au_{20}(SCH_3)_{16}$. For the nonradiative relaxation, similar to the doped $[Au_{25}(SH)_{18}]^{-1}$ systems, the electron relaxation time from the first excited state (HOMO → LUMO) is the longest (17.0 ps) which is again due to the large HOMO-LUMO gap. S_2 (HOMO → LUMO+1), S_4 (HOMO → LUMO+3), S_8 (HOMO-1 → LUMO), and S_9 (HOMO-1 → LUMO+1) are the other states from which electronic population relaxes slower, with decay times of 11.1 ps, 3.2 ps, 2.5 ps, and 3.3 ps respectively. Since there is a large gap between LUMO, LUMO+1, LUMO+2 and LUMO+3 orbitals, population relaxation to neighboring states takes a longer time. Population from other higher excited states relaxes faster (with decay times of 0.2 – 2 ps). We observed the gradual nonradiative relaxation of excited electrons from excited states to the ground state (stepwise electron relaxation) through the manifold of hole states. Luminescence is observed from S_1, S_2, and S_6 states. The S_1 state shows dual luminescence at 0.41 eV and 0.68 eV while S_2 and S_6 emission are observed at 0.91 eV and 1.50 eV respectively. The S_6 luminescence at 1.50 eV matches with the experimentally observed luminescence at 1.51 eV without considering the

underestimation from the use of GGA functionals. S_2 emission at 1.21 eV obtained upon adding the underestimation of 0.3 eV obtained in our calculations is also reasonably close to the experimental emission. The cluster structure becomes the most distorted in the first excited state with luminescence at 0.41 eV. The distortion is mainly observed on the ring and trimeric staple motif of the cluster. The cluster structure does not distort significantly in the other S_1, S_2, and S_6 states.

Cylindrical nanoparticles (e.g. nanowires) have two main peaks in their absorption spectra: longitudinal and transverse. The longitudinal peak appears due to the plasmon oscillation along the long axis of nanowire and the transverse peak appears due to the plasmon oscillation along the short axis of the nanowire. Herein, we have analyzed the optical absorption spectra of Ag_4, Ag_6 and Ag_{10} nanowire dimers (parallel) and trimers (dolmen) at an interparticle separation of 0.4-2.0 nm. We have observed that an extra peak appears between the longitudinal and transverse peak when the interparticle separation is 0.6 nm and less. The extra peak shows charge transfer character where there is tunneling of electron density from one nanowire to another. We also observed that the electron tunneling is more significant for the parallel monomers compared to the tunneling of the perpendicular monomer.

Plasmon mediated photocatalytic dissociation of dinitrogen is gaining significant attention because it may provide an energy efficient alternative to the Haber Bosch process. From the previous study from our group,[1] dinitrogen dissociation is found to be possible upon excitation of the longitudinal excitation of nanowire monomers on using 0.05 au electric field. In this dissertation, we have also observed that the optical properties of nanowire assemblies are different than those of the monomer because a charge transfer excitation appears at small interparticle separations. In order to find the effect of the interparticle distance and hence the charge transfer

excitation on the requirement of the electric field intensity for nitrogen dissociation, we studied the plasmon-mediated dinitrogen dissociation upon activation of plasmon resonances for silver nanowire dimers using real-time TDDFT. We constructed parallel, end-to-end and hotspot (dinitrogen in the hotspot of two monomers) orientations of Ag_4 nanowires at interparticle separations of 1 nm, 0.75 nm and 0.5 nm. We observed that the dissociation is more likely upon excitation of plasmon resonances of the nanowires at smaller interparticle separations. A higher possibility of dissociation is observed on using the end-to-end oriented nanowire dimer than with other dimer orientations.

Finally, we investigated the plasmon-mediated dinitrogen dissociation upon activation of plasmon resonances of an icosahedral Al_{13}^{-1} nanocluster. The Al_{13}^{-1} nanocluster is a stable cluster that is found experimentally.[2] Aluminum nanoparticles are getting significant attention due to their plasmon resonance in UV region which is important for photocatalysis and for the detection of the molecules that absorb UV light. Using real-time time dependent density functional methods, the electron density was propagated. Then we examined the occupation of virtual orbitals in the system since the occupation of nitrogen antibonding orbitals can lead to dinitrogen dissociation. We found that the probability of occupation of the nitrogen antibonding orbitals is higher on using off-resonance electric fields than resonant fields. And as expected, the occupation is higher with stronger electric field intensity of 0.01 au than on using weaker electric field intensity of 0.001 au.

For future work, we can study the nonradiative electron relaxation dynamics on neutral and positively charged silver-doped $[Au_{25}(SR)_{18}]$ systems. In this work, we have studied the electron relaxation mechanism only in negatively charged system. Experimental studies show that the relaxation mechanism depends on the charge state of the $[Au_{25}(SR)_{18}]$ cluster.[3-4] So, it would be interesting to investigate the electron relaxation mechanism and the decay time constants in the

neutral and positively charged clusters as well. Moreover, different group transition metals are found to occupy different positions in $[Au_{25}(SR)_{18}]^{-1}$.[5-6] Group X dopants are found to prefer the central location whereas the group XI-XIII dopants prefer the surface of the core and the ligand shell location. So, we can also investigate the effect of doping of other elements (other than silver) on the electron relaxation dynamics. Investigation of electron relaxation dynamics for systems with Group X dopants that occupy the central position might be especially interesting because this might cause a larger change in the electronic structure than when the dopants are in the ligand shell.

In chapter 7 of this dissertation, we have used RT-TDDFT electron dynamics methods to excite the plasmon resonances of Al_{13}^{-1} and examine the possible dissociation of dinitrogen due to the occupation of nitrogen antibonding orbitals. For the future work, we can use the RT-TDDFT with Ehrenfest method to observe the N-N bond length throughout the simulation time. Because Ehrenfest is an electron-nuclear dynamics method where the atoms are also moved, we can observe how the bond length changes. Moreover, because the silver nanoparticles are known to have narrow and intense plasmonic peaks in visible region, nitrogen dissociation can also be investigated on excitation of plasmon resonance for the Ag_{13}^{-1} cluster. Unlike aluminum nanoparticles which absorb in the UV region, silver nanoparticles have absorption in visible region and hence would be important for photocatalysis using the solar radiation. In chapter 6, we have used the Ehrenfest method to investigate the possibility of nitrogen dissociation upon excitation of plasmon resonances of silver nanowire dimers. The dissociation probability can be compared in the future with the probabilities calculated using the FSSH method. We can obtain the electronic population of different states and how the population relaxes within the states using FSSH method. This will be helpful to understand the mechanism of electron relaxation and nitrogen dissociation.

8.1 References

1. Hull, O. A.; Lingerfelt, D. B.; Li, X.; Aikens, C. M., Electronic Structure and Nonadiabatic Dynamics of Atomic Silver Nanowire–N_2 Systems. *J. Phys. Chem. C* **2020,** *124* (38), 20834-20845.

2. Leuchtner, R. E.; Harms, A. C.; Castleman, A. W., Aluminum Cluster Reactions. *J. Chem. Phys.* **1991,** *94* (2), 1093-1101.

3. Qian, H.; Sfeir, M. Y.; Jin, R., Ultrafast Relaxation Dynamics of $[Au_{25}(SR)_{18}]^{q}$ Nanoclusters: Effects of Charge State. *J. Phys. Chem. C* **2010,** *114* (47), 19935-19940.

4. Green, T. D.; Knappenberger, K. L., Relaxation Dynamics of $Au_{25}L_{18}$ Nanoclusters Studied by Femtosecond Time-resolved Near Infrared Transient Absorption Spectroscopy. *Nanoscale* **2012,** *4* (14), 4111-4118.

5. Alkan, F.; Pandeya, P.; Aikens, C. M., Understanding the Effect of Doping on Energetics and Electronic Structure for Au_{25}, Ag_{25}, and Au_{38} Clusters. *J. Phys. Chem. C* **2019,** *123* (14), 9516-9527.

6. Fei, W.; Antonello, S.; Dainese, T.; Dolmella, A.; Lahtinen, M.; Rissanen, K.; Venzo, A.; Maran, F., Metal Doping of $Au_{25}(SR)_{18}^{-}$ Clusters: Insights and Hindsights. *J. Am. Chem. Soc.* **2019,** *141* (40), 16033-16045.

Appendix A - Supporting Information for "Nonradiative Relaxation Dynamics in the $[Au_{25-n}Ag_n(SH)_{18}]^{-1}$ (n = 1, 12, 25) Thiolate-protected Nanoclusters"

Energy Correction

A 0.55 eV energy correction is considered for $Au_{24}Ag$ in this work because the theoretical and experimental[1] peak positions are similar for this system and Au_{25}. Because there is no over/underestimation in the peak position of $Au_{13}Ag_{12}$ compared to experiment,[1] no energy correction is initially used for $Au_{13}Ag_{12}$. The gap in Ag_{25} is ~0.33 eV smaller than the optical gap of ~1.48 eV (~840 nm) found from the experimental optical absorption spectrum reported by Bakr and co-workers.[2] Therefore, it is important to consider a correction to the excited states to compensate for the underestimation in the calculated DFT optical band gap compared to the experiment. In our current work, energy corrections of 0.55 eV and 0.33 eV are employed in our calculations on $Au_{24}Ag$ and Ag_{25}, respectively. Our previous relaxation dynamics calculations on Au_{25} showed that the inclusion of the correction lengthens the ground state growth times but has minor effects on the overall excited state lifetimes,[3] and we expect similar effects for the systems studied in this work.

We performed two different calculation sets, one considering the uncorrected energy gaps (main text) and another including the energy correction on the S_1-S_6 excited states for $Au_{24}Ag$ and Ag_{25} as mentioned above. The population dynamics for $Au_{24}Ag$ and Ag_{25} performed with the energy corrections are shown in Figures S1 and S2; they display similar relaxation patterns to those shown without the energy corrections in Figures 4 and 6 for $Au_{24}Ag$ and Ag_{25} respectively. The corresponding ground state recovery times (Table A-1) and excited state population decay times (Table A-2) are determined. Compared to the ground state recovery times in Table 3-5, there is a

significant increase in the ground state growth times with the addition of the correction although the growth time patterns are retained. The excited state population decays are not significantly changed compared to those in Table 3-6.

Furthermore, for $Au_{24}Ag$ (Table A-9) and for Ag_{25} (Table A-10), decay time constants calculated in the presence of higher excited states without an energy correction are similar to the time constants calculated considering the correction. In the Au_{25} cluster, the first excitation peak was underestimated by around 0.55 eV with the PBE level of theory compared to the experimental first peak and the second peak had a smaller underestimation. Therefore, the 0.55 eV correction was only added to the S_1-S_6 states and not for the higher excited states. As in the case of $[Au_{25}(SR)_{18}]^{-1}$, the first absorption peak of $Au_{24}Ag$ is underestimated by 0.55 eV but the underestimation is much smaller for the second peak. Thus, a 0.55 eV energy correction is used for the S_1 to S_6 states of $Au_{24}Ag$ and no correction is used for higher excited states. No energy correction is used for $Au_{13}Ag_{12}$ as the theoretical peak obtained by using the PBE level of theory matches with the experimental peak by Negishi et al.[1] In Ag_{25}, the underestimation of the gap (~0.33 eV) is less than that in Au_{25} (0.55 eV). In order to have the Ag_{25} relaxation calculations be consistent with Au_{25}, the 0.33 eV correction was only added to the S_1-S_6 states in Ag_{25}.

Moreover, we then compared the decay times of excited states using both 0.33 eV and 0.55 eV energy correction for all of the studied systems (Tables A-11 and A-14). The comparison shows that decay times do not change significantly when including different values for the energy correction. States S_1 and S_7 have the highest decay times, while higher excited states have comparatively lower decay times, both with and without energy corrections.

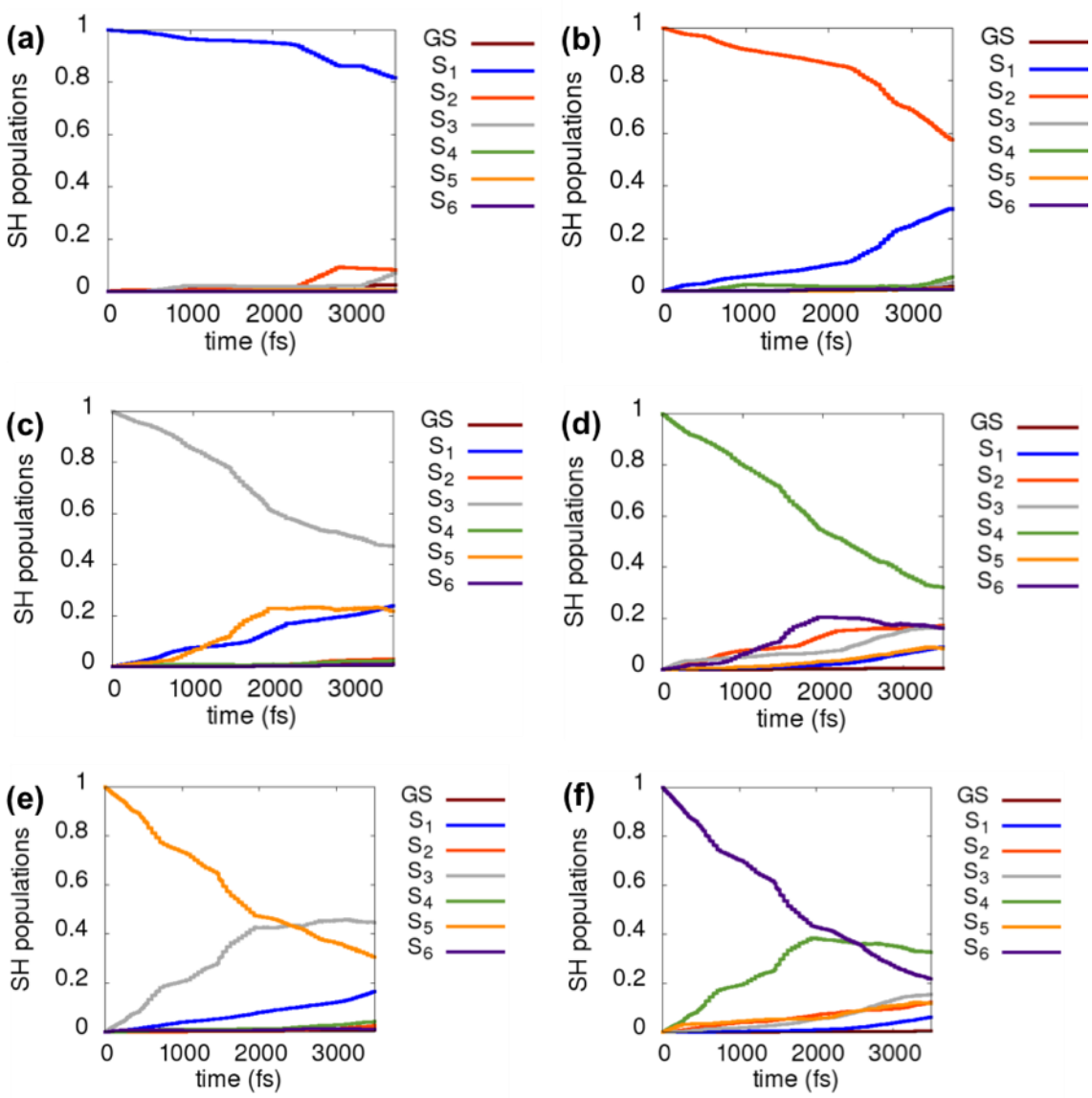

Figure A-1 Evolution of the populations of S_1, S_2, S_3, S_4, S_5, S_6 states for $[Au_{24}Ag(SH)_{18}]^{-1}$ with 0.55 eV energy correction.

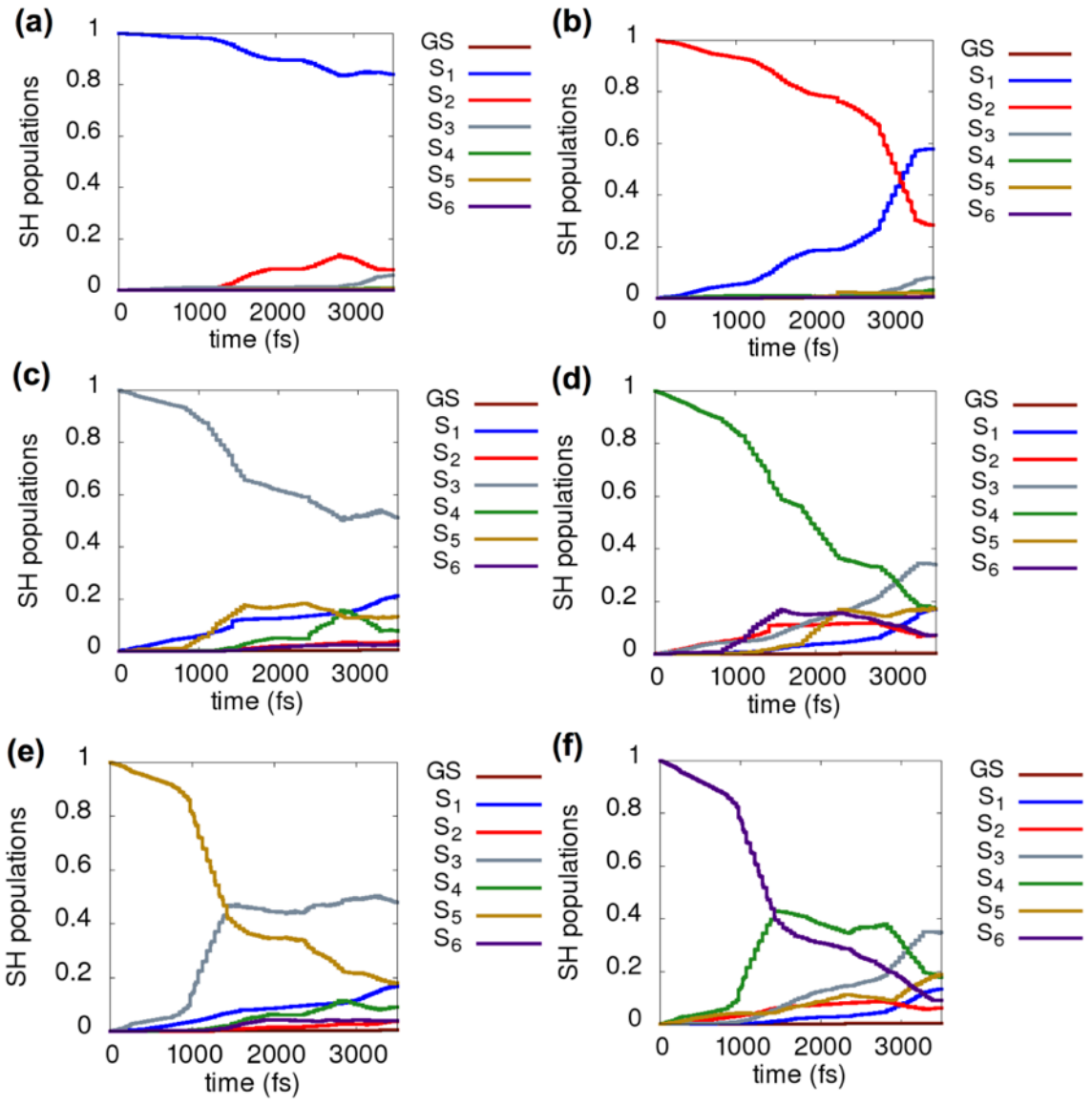

Figure A-2 Evolution of the populations of S_1, S_2, S_3, S_4, S_5, S_6 states for $[Ag_{25}(SH)_{18}]^{-1}$ with 0.33 eV energy correction.

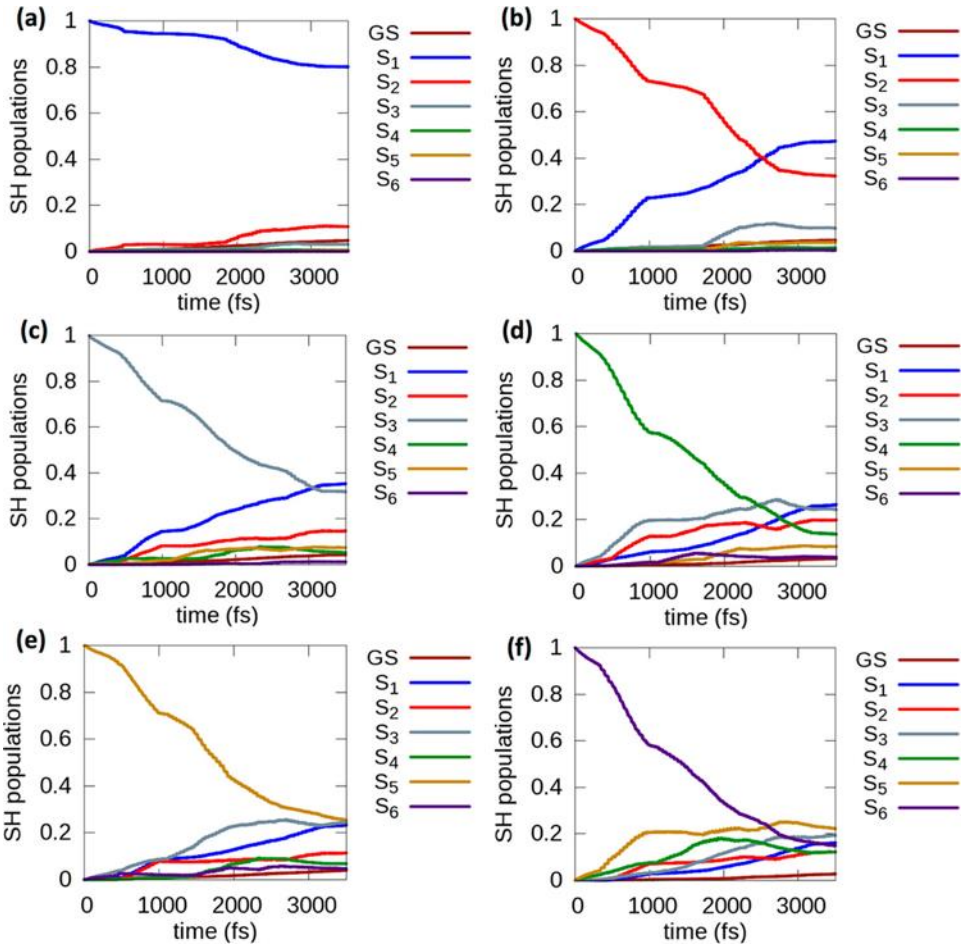

Figure A-3 Evolution of the populations of S_1, S_2, S_3, S_4, S_5, S_6 states for $[Au_{25}(SH)_{18}]^{-1}$ without energy correction. Reproduced with permission from J. Phys. Chem. C 121, 10653 (2016). Copyright 2016 American Chemical Society.

Table A-1 Ground state population increase lifetimes after excitation to first six excited states that contribute to the first peak in the optical absorption spectrum of the studied clusters. $[Au_{25}(SH)_{18}]^{-1}$ numbers reproduced with permission from J. Phys. Chem. C 121, 10653 (2016). Copyright 2016 American Chemical Society.

Excited State	GS growth time (ps) with energy corrections		
	$[Au_{25}(SH)_{18}]^{-1}$ (Ref. 3)	$[Au_{24}Ag(SH)_{18}]^{-1}$	$[Ag_{25}(SH)_{18}]^{-1}$
S_1	313	140	447
S_2	365	273	659
S_3	441	354	751
S_4	690	684	1926
S_5	750	544	890
S_6	1429	1037	1405

Table A-2 Decay times of excited state population of the six excited states contributing to the first peak in the optical absorption spectrum of the studied clusters. $[Au_{25}(SH)_{18}]^{-1}$ numbers reproduced with permission from J. Phys. Chem. C 121, 10653 (2016). Copyright 2016 American Chemical Society.

Excited State	Decay time (ps) with energy corrections		
	$[Au_{25}(SH)_{18}]^{-1}$ (Ref. 3)	$[Au_{24}Ag(SH)_{18}]^{-1}$	$[Ag_{25}(SH)_{18}]^{-1}$
S_1	18.0	25.9	20.0
S_2	3.3	10.2	6.0
S_3	3.1	4.8	4.7
S_4	1.9	3.5	2.8
S_5	2.6	3.0	2.2
S_6	1.9	2.5	2.0

Table A-3 The most probable transitions with highest oscillator strengths and their weights that contribute to the peak around 2.5 eV for $[Au_{24}Ag(SH)_{18}]^{-1}$.

Excited state	Energy (eV)	Oscillator strength	Weight	Most weighted transitions
26	2.37	0.0116	0.4983	HOMO→ LUMO+6
			0.1557	HOMO-8→ LUMO+1
			0.0447	HOMO-2→ LUMO+4
			0.0442	HOMO-1→ LUMO+3
			0.0366	HOMO-1→ LUMO+5
			0.0290	HOMO-9→ LUMO
			0.0269	HOMO→ LUMO+4
			0.0198	HOMO-7→ LUMO
			0.0193	HOMO-6→ LUMO+1
			0.0178	HOMO-9→ LUMO+1
			0.0160	HOMO-1→ LUMO+2
			0.0152	HOMO-8→ LUMO
27	2.38	0.0227	0.2898	HOMO→ LUMO+6
			0.1248	HOMO-9→ LUMO
			0.1194	HOMO-1→ LUMO+3
			0.0923	HOMO-1→ LUMO+5
			0.0620	HOMO-6→ LUMO+1
			0.0601	HOMO→ LUMO+4
			0.0395	HOMO-8→ LUMO
			0.0363	HOMO-7→ LUMO
			0.0316	HOMO-1→ LUMO+2
			0.0225	HOMO-2→ LUMO+2
29	2.41	0.0145	0.3725	HOMO→ LUMO+7
			0.2181	HOMO-2→ LUMO+4
			0.0744	HOMO-2→ LUMO+5
			0.0571	HOMO-9→ LUMO
			0.0374	HOMO-1→ LUMO+4

			0.0352	HOMO-8→ LUMO
			0.0233	HOMO-1→ LUMO+5
			0.0210	HOMO-2→ LUMO+2
			0.0190	HOMO-2→ LUMO+3
			0.0122	HOMO-7→ LUMO
			0.0107	HOMO-5→ LUMO
30	2.42	0.0256	0.2398	HOMO-1→ LUMO+1
			0.1658	HOMO→ LUMO+7
			0.0883	HOMO-2→ LUMO+5
			0.0637	HOMO-2→ LUMO+3
			0.0434	HOMO-2→ LUMO+2
			0.0172	HOMO-1→ LUMO+3
			0.0133	HOMO→ LUMO+2
31	2.43	0.0220	0.2783	HOMO-2→ LUMO+4
			0.2289	HOMO-9→ LUMO+1
			0.0973	HOMO-9→ LUMO+1
			0.0369	HOMO-1→ LUMO+3
			0.0337	HOMO-1→ LUMO+4
			0.0296	HOMO→ LUMO+2

Table A-4 The most probable transitions with highest oscillator strengths and their weights that contribute to the peak around 2.5 eV for $[Au_{13}Ag_{12}(SH)_{18}]^{-1}$.

Excited state	Energy (eV)	Oscillator strength	Weight	Most weighted transitions
12	2.32	0.007512	0.7674	HOMO-2 → LUMO+4
			0.0398	HOMO→ LUMO+5
			0.0390	HOMO-2→ LUMO+2
			0.0380	HOMO-2 → LUMO+3
			0.0264	HOMO → LUMO+4
			0.0223	HOMO → LUMO+3
			0.0166	HOMO-1 → LUMO+4
13	2.36	0.006827	0.4516	HOMO → LUMO+5
			0.2314	HOMO-1 → LUMO+4
			0.0954	HOMO-2 → LUMO+4
			0.0821	HOMO-2 → LUMO+2
			0.0345	HOMO-1 → LUMO+2
			0.0316	HOMO-1 → LUMO+5
			0.0183	HOMO → LUMO+4
			0.0151	HOMO → LUMO+3
14	2.39	0.01975	0.3765	HOMO-1 → LUMO+5
			0.1724	HOMO-2 → LUMO+2
			0.1346	HOMO → LUMO+4
			0.1070	HOMO → LUMO+5
			0.0716	HOMO-1 → LUMO+4

			0.0503	HOMO-2 → LUMO+3
			0.0349	HOMO-2 → LUMO+5
			0.0158	HOMO-1 → LUMO+2
15	2.44	0.04721	0.3400	HOMO-2 → LUMO+5
			0.3186	HOMO-2 → LUMO+3
			0.0838	HOMO-1 → LUMO+2
			0.0664	HOMO-2 → LUMO+4
			0.0555	HOMO-1 → LUMO+5
			0.0325	HOMO → LUMO+3
			0.0225	HOMO-2 → LUMO+2
			0.0131	HOMO → LUMO+5
16	2.50	0.1404	0.3797	HOMO-1 → LUMO+4
			0.2735	HOMO → LUMO+5
			0.0928	HOMO → LUMO+3
			0.0330	HOMO → LUMO+4
			0.0268	HOMO-1 → LUMO+5
			0.0248	HOMO-2 → LUMO+3
			0.0162	HOMO-2 → LUMO+1
			0.0160	HOMO-2 → LUMO
17	2.50	0.1037	0.2758	HOMO-1 → LUMO+5
			0.2424	HOMO-2 → LUMO+5
			0.1103	HOMO-2 → LUMO+2
			0.0836	HOMO-2 → LUMO+3
			0.0736	HOMO → LUMO+4
			0.0478	HOMO → LUMO+5
			0.0371	HOMO → LUMO+3
			0.0197	HOMO-2 → LUMO+4
18	2.54	0.1157	0.3637	HOMO-2 → LUMO+5
			0.1923	HOMO-1 → LUMO+5
			0.1082	HOMO-2 → LUMO+3
			0.0878	HOMO-1 → LUMO+2
			0.0600	HOMO-2 → LUMO+2
			0.0577	HOMO → LUMO+4
			0.0159	HOMO → LUMO+5

Table A-5 The most probable transitions with highest oscillator strengths and their weights that contribute to the peak around 2.5 eV for $[Ag_{25}(SH)_{18}]^{-1}$.

Excited state	Energy (eV)	Oscillator strength	Weight	Most weighted transitions
13	2.23	0.0153	0.5862	HOMO-3 → LUMO
			0.1145	HOMO-5 → LUMO
			0.1005	HOMO-2 → LUMO+4
			0.0824	HOMO-1 → LUMO+3
			0.0259	HOMO-2 → LUMO+2

			0.0163	HOMO-1 → LUMO+5
			0.0117	HOMO → LUMO+4
14	2.24	0.0328	0.2139	HOMO-4 → LUMO
			0.1076	HOMO-1 → LUMO+3
			0.0845	HOMO-4 → LUMO+1
			0.0831	HOMO-2 → LUMO+2
			0.0825	HOMO-2 → LUMO+4
			0.0572	HOMO → LUMO+3
			0.0492	HOMO-5 → LUMO
			0.0462	HOMO → LUMO+2
			0.0408	HOMO-3 → LUMO+1
			0.0393	HOMO-2 → LUMO+3
			0.0325	HOMO → LUMO+4
			0.0304	HOMO-1 → LUMO+5
			0.0258	HOMO → LUMO+5
15	2.25	0.0585	0.2997	HOMO → LUMO+4
			0.1651	HOMO-4 → LUMO
			0.1113	HOMO-1 → LUMO+2
			0.0487	HOMO-6 → LUMO+1
			0.0472	HOMO-2 → LUMO+4
			0.0462	HOMO-1 → LUMO+3
			0.0415	HOMO-2 → LUMO+5
			0.0387	HOMO-6 → LUMO
			0.0339	HOMO → LUMO+5
16	2.26	0.0361	0.2067	HOMO-2 → LUMO+4
			0.186	HOMO-3 → LUMO
			0.1672	HOMO-4 → LUMO
			0.1036	HOMO-5 → LUMO
			0.0709	HOMO → LUMO+5
			0.0613	HOMO-2 → LUMO+5
			0.0535	HOMO → LUMO+3
			0.0379	HOMO-2 → LUMO+3
17	2.27	0.0294	0.3133	HOMO-4 → LUMO
			0.1222	HOMO-3 → LUMO
			0.1084	HOMO-6 → LUMO
			0.0786	HOMO-5 → LUMO
			0.0774	HOMO-1 → LUMO+3
			0.0585	HOMO-2 → LUMO+2
			0.0458	HOMO → LUMO+4
			0.035	HOMO-1 → LUMO+5
18	2.29	0.0289	0.5026	HOMO-5 → LUMO

			0.1204	HOMO-1 → LUMO+3
			0.0572	HOMO-1 → LUMO+5
			0.0492	HOMO-2 → LUMO+2
			0.0461	HOMO-3 → LUMO+1
			0.0454	HOMO → LUMO+5

Table A-6 Transitions considered for higher excited states for $[Au_{24}Ag(SH)_{18}]^{-1}$.

Excited State	Transition	Excited State	Transition
S_1	HOMO → LUMO	S_{41}	HOMO-5→ LUMO
S_2	HOMO → LUMO+1	S_{42}	HOMO-5→ LUMO+1
S_3	HOMO-1 → LUMO	S_{43}	HOMO-5→ LUMO+2
S_4	HOMO-1 → LUMO+1	S_{44}	HOMO-5→ LUMO+3
S_5	HOMO-2 → LUMO	S_{45}	HOMO-5→ LUMO+4
S_6	HOMO-2 → LUMO+1	S_{46}	HOMO-5→ LUMO+5
S_7	HOMO→ LUMO+2	S_{47}	HOMO-5→ LUMO+6
S_8	HOMO→ LUMO+3	S_{48}	HOMO-5→ LUMO+7
S_9	HOMO→ LUMO+4	S_{49}	HOMO-6→ LUMO
S_{10}	HOMO→ LUMO+5	S_{50}	HOMO-6→ LUMO+1
S_{11}	HOMO→ LUMO+6	S_{51}	HOMO-6→ LUMO+2
S_{12}	HOMO→ LUMO+7	S_{52}	HOMO-6→ LUMO+3
S_{13}	HOMO-1→ LUMO+2	S_{53}	HOMO-6→ LUMO+4
S_{14}	HOMO-1→ LUMO+3	S_{54}	HOMO-6→ LUMO+5
S_{15}	HOMO-1→ LUMO+4	S_{55}	HOMO-6→ LUMO+6
S_{16}	HOMO-1→ LUMO+5	S_{56}	HOMO-6→ LUMO+7
S_{17}	HOMO-1→ LUMO+6	S_{57}	HOMO-7→ LUMO
S_{18}	HOMO-1→ LUMO+7	S_{58}	HOMO-7→ LUMO+1
S_{19}	HOMO-2→ LUMO+2	S_{59}	HOMO-7→ LUMO+2
S_{20}	HOMO-2→ LUMO+3	S_{60}	HOMO-7→ LUMO+3
S_{21}	HOMO-2→ LUMO+4	S_{61}	HOMO-7→ LUMO+4
S_{22}	HOMO-2→ LUMO+5	S_{62}	HOMO-7→ LUMO+5
S_{23}	HOMO-2→ LUMO+6	S_{63}	HOMO-7→ LUMO+6
S_{24}	HOMO-2→ LUMO+7	S_{64}	HOMO-7→ LUMO+7
S_{25}	HOMO-3→ LUMO	S_{65}	HOMO-8→ LUMO
S_{26}	HOMO-3→ LUMO+1	S_{66}	HOMO-8→ LUMO+1
S_{27}	HOMO-3→ LUMO+2	S_{67}	HOMO-8→ LUMO+2
S_{28}	HOMO-3→ LUMO+3	S_{68}	HOMO-8→ LUMO+3
S_{29}	HOMO-3→ LUMO+4	S_{69}	HOMO-8→ LUMO+4
S_{30}	HOMO-3→ LUMO+5	S_{70}	HOMO-8→ LUMO+5
S_{31}	HOMO-3→ LUMO+6	S_{71}	HOMO-8→ LUMO+6
S_{32}	HOMO-3→ LUMO+7	S_{72}	HOMO-8→ LUMO+7
S_{33}	HOMO-4→ LUMO	S_{73}	HOMO-9→ LUMO
S_{34}	HOMO-4→ LUMO+1	S_{74}	HOMO-9→ LUMO+1
S_{35}	HOMO-4→ LUMO+2	S_{75}	HOMO-9→ LUMO+2

S_{36}	HOMO-4→ LUMO+3	**S_{76}**	HOMO-9→ LUMO+3
S_{37}	HOMO-4→ LUMO+4	**S_{77}**	HOMO-9→ LUMO+4
S_{38}	HOMO-4→ LUMO+5	**S_{78}**	HOMO-9→ LUMO+5
S_{39}	HOMO-4→ LUMO+6	**S_{79}**	HOMO-9→ LUMO+6
S_{40}	HOMO-4→ LUMO+7	**S_{80}**	HOMO-9→ LUMO+7

Table A-7 Transitions considered for higher excited states for $[Au_{13}Ag_{12}(SH)_{18}]^{-1}$.

Excited State	Transition	Excited State	Transition
S_1	HOMO → LUMO	**S_{10}**	HOMO → LUMO+5
S_2	HOMO → LUMO+1	**S_{11}**	HOMO-1→ LUMO+2
S_3	HOMO-1 → LUMO	**S_{12}**	HOMO-1→ LUMO+3
S_4	HOMO-1 → LUMO+1	**S_{13}**	HOMO-1→ LUMO+4
S_5	HOMO-2 → LUMO	**S_{14}**	HOMO-1→ LUMO+5
S_6	HOMO-2 → LUMO+1	**S_{15}**	HOMO-2→ LUMO+2
S_7	HOMO → LUMO+2	**S_{16}**	HOMO-2→ LUMO+3
S_8	HOMO → LUMO+3	**S_{17}**	HOMO-2→ LUMO+4
S_9	HOMO → LUMO+4	**S_{18}**	HOMO-2→ LUMO+5

Table A-8 Transitions considered for higher excited states for $[Ag_{25}(SH)_{18}]^{-1}$.

Excited state	Transition	Excited state	Transition
S_1	HOMO → LUMO	**S_{22}**	HOMO-4 → LUMO+1
S_2	HOMO → LUMO+1	**S_{23}**	HOMO-4 → LUMO+2
S_3	HOMO-1 → LUMO	**S_{24}**	HOMO → 4-LUMO+3
S_4	HOMO-1 → LUMO+1	**S_{25}**	HOMO-4 → LUMO+4
S_5	HOMO-2 → LUMO	**S_{26}**	HOMO-5 → LUMO
S_6	HOMO-2 → LUMO+1	**S_{27}**	HOMO-5 → LUMO+1
S_7	HOMO →LUMO+2	**S_{28}**	HOMO-5 → LUMO+2
S_8	HOMO → LUMO+3	**S_{29}**	HOMO-5 → LUMO+3
S_9	HOMO → LUMO+4	**S_{30}**	HOMO-5 → LUMO+4
S_{10}	HOMO-1 → LUMO+2	**S_{31}**	HOMO-6 → LUMO
S_{11}	HOMO-1 → LUMO+3	**S_{32}**	HOMO-6 → LUMO+1
S_{12}	HOMO-1 → LUMO+4	**S_{33}**	HOMO-6 → LUMO+2
S_{13}	HOMO-2 → LUMO+2	**S_{34}**	HOMO-6 → LUMO+3
S_{14}	HOMO-2 → LUMO+3	**S_{35}**	HOMO-6 → LUMO+4
S_{15}	HOMO-2 → LUMO+4	**S_{36}**	HOMO → LUMO+5
S_{16}	HOMO-3 → LUMO	**S_{37}**	HOMO-1 → LUMO+5
S_{17}	HOMO-3 → LUMO+1	**S_{38}**	HOMO-2 → LUMO+5
S_{18}	HOMO-3 → LUMO+2	**S_{39}**	HOMO-3 → LUMO+5
S_{19}	HOMO-3 → LUMO+3	**S_{40}**	HOMO-4 → LUMO+5
S_{20}	HOMO-3 → LUMO+4	**S_{41}**	HOMO-5 → LUMO+5

S_{21}	HOMO-4 → LUMO	**S_{42}**	HOMO-6 → LUMO+5

Table A-9 The decay time constants obtained for $[Au_{24}Ag(SH)_{18}]^{-1}$ nanoclusters for the higher excited states including the S_1-S_6 states. The decay time constants are given when no correction is added and when the 0.55 eV correction added to the S_1-S_6 states. The decay time constants obtained for the $[Au_{25}(SH)_{18}]^{-1}$ nanocluster (Ref. 3) are also shown here. Time constants are calculated only for the states as obtained for $[Au_{25}(SH)_{18}]^{-1}$. $[Au_{25}(SH)_{18}]^{-1}$ numbers reproduced with permission from J. Phys. Chem. C 121, 10653 (2016). Copyright 2016 American Chemical Society.

Excited state	Decay time (ps) without the correction to the first six states (Au_{24})	Decay time (ps) with the 0.55 eV correction to the first six states (Au_{24})	Decay time (ps) with the 0.55 eV correction to the first six states (Au_{25}) (Ref. 3)
S_1	19.2	25.9	15.0
S_2	8.9	8.1	3.3
S_3	5.1	4.6	2.9
S_4	3.7	3.2	1.7
S_5	2.9	2.1	1.8
S_6	2.5	1.7	1.4
S_7	12.3	15.5	9.9
S_8	3.7	3.8	2.7
S_9	1.7	1.6	1.5
S_{10}-Au_{25} = S_{13}-Au_{24}	4.6	4.8	3.3
S_{11}-Au_{25} = S_{14}-Au_{24}	2.6	2.5	1.6
S_{12}-Au_{25} = S_{15}-Au_{24}	1.5	1.4	1.2
S_{13}-Au_{25} = S_{19}-Au_{24}	2.3	2.4	2.3
S_{14}-Au_{25} = S_{20}-Au_{24}	1.8	1.7	1.5
S_{15}-Au_{25} = S_{21}-Au_{24}	0.9	0.9	1.2
S_{16}-Au_{25} = S_{25}-Au_{24}	3.7	3.7	2.9
S_{17}-Au_{25} = S_{26}-Au_{24}	2.8	2.8	1.7
S_{18}-Au_{25} = S_{27}-Au_{24}	2.8	2.8	2.7
S_{19}-Au_{25} = S_{28}-Au_{24}	1.8	1.8	1.4
S_{20}-Au_{25} = S_{29}-Au_{24}	1.1	1.1	1.0
S_{21}-Au_{25} = S_{33}-Au_{24}	2.6	2.3	1.8
S_{22}-Au_{25} = S_{34}-Au_{24}	2.1	1.9	1.2
S_{23}-Au_{25} = S_{35}-Au_{24}	2.1	2.1	1.7
S_{24}-Au_{25} = S_{36}-Au_{24}	1.6	1.5	1.1
S_{25}-Au_{25} = S_{37}-Au_{24}	1.0	0.9	0.9
S_{26}-Au_{25} = S_{41}-Au_{24}	1.4	1.3	1.5
S_{27}-Au_{25} = S_{42}-Au_{24}	1.3	1.2	1.0
S_{28}-Au_{25} = S_{43}-Au_{24}	1.4	1.4	1.3
S_{29}-Au_{25} = S_{44}-Au_{24}	1.1	1.1	0.9

S_{30}-Au_{25} = S_{45}-Au_{24}	0.8	0.8	0.7
S_{31}-Au_{25} = S_{49}-Au_{24}	1.2	1.1	1.3
S_{32}-Au_{25} = S_{50}-Au_{24}	1.1	1.0	1.0
S_{33}-Au_{25} = S_{51}-Au_{24}	1.2	1.1	1.2
S_{34}-Au_{25} = S_{52}-Au_{24}	0.9	0.9	0.9
S_{35}-Au_{25} = S_{53}-Au_{24}	0.6	0.6	0.8

Table A-10 The The decay time constants obtained for $[Ag_{25}(SH)_{18}]^{-1}$ nanoclusters for the higher excited states including the S_1-S_6 states. The decay time constants are given when no correction is added and when the 0.33 eV correction added to the S_1-S_6 states. The decay time constants obtained for the $[Au_{25}(SH)_{18}]^{-1}$ nanocluster (Ref. 3) are also shown here. $[Au_{25}(SH)_{18}]^{-1}$ numbers reproduced with permission from J. Phys. Chem. C 121, 10653 (2016). Copyright 2016 American Chemical Society.

Excited state	Decay time (ps) without the correction to the first six states (Ag_{25})	Decay time (ps) with the 0.33 eV correction to the first six states (Ag_{25})	Decay time (ps) with the 0.55 eV correction to the first six state (Au_{25}) (Ref. 3)
S_1	17.0	18.0	15.0
S_2	6.2	6.2	3.3
S_3	4.6	4.9	2.9
S_4	2.8	3.0	1.7
S_5	2.3	2.3	1.8
S_6	2.0	2.0	1.4
S_7	11	11	9.9
S_8	2.9	2.8	2.7
S_9	2.9	2.9	1.5
S_{10}	5.2	5.4	3.3
S_{11}	2.1	2.1	1.6
S_{12}	1.8	1.8	1.2
S_{13}	2.1	2.1	2.3
S_{14}	1.3	1.3	1.5
S_{15}	1.4	1.4	1.2
S_{16}	2.5	2.3	2.9
S_{17}	1.9	1.8	1.7
S_{18}	2.4	2.4	2.7
S_{19}	1.6	1.5	1.4
S_{20}	1.4	1.4	1.0
S_{21}	1.5	1.4	1.8
S_{22}	1.3	1.2	1.2
S_{23}	1.4	1.4	1.7

S_{24}	1.0	1.0	1.1
S_{25}	1.0	1.0	0.9
S_{26}	1.0	0.9	1.5
S_{27}	0.9	0.9	1.0
S_{28}	1.0	1.0	1.3
S_{29}	0.7	0.7	0.9
S_{30}	0.8	0.8	0.7
S_{31}	1.1	1.1	1.3
S_{32}	1.0	1.0	1.0
S_{33}	1.0	1.0	1.2
S_{34}	0.8	0.8	0.9
S_{35}	0.8	0.8	0.8
S_{36}	2.5	2.6	N/A
S_{37}	1.9	1.9	N/A
S_{38}	1.4	1.4	N/A
S_{39}	1.3	1.3	N/A
S_{40}	0.9	0.9	N/A
S_{41}	0.7	0.7	N/A
S_{42}	0.8	0.8	N/A

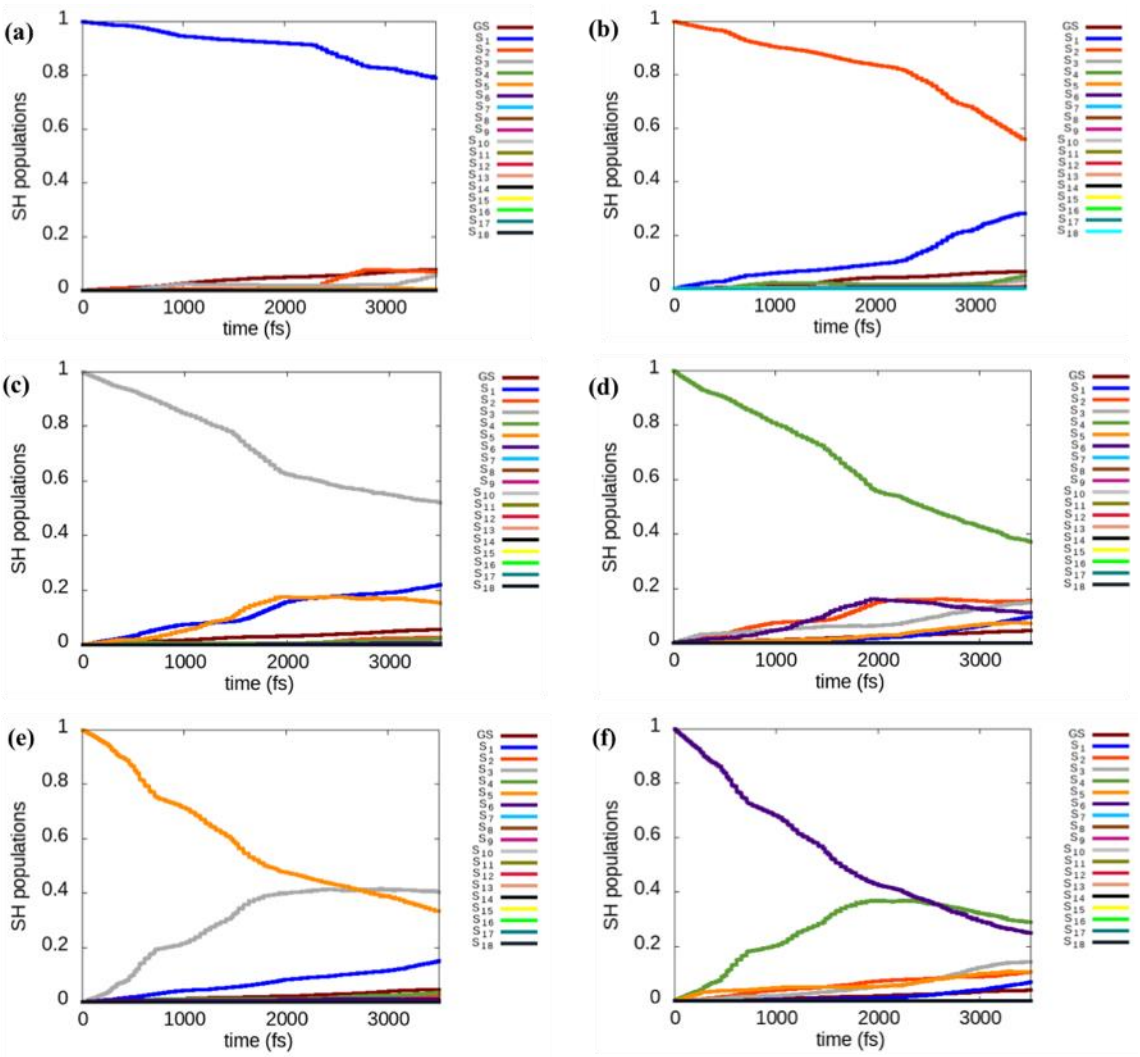

Figure A-4 Population relaxations of S_1, S_2, S_3, S_4, S_5, S_6 states in $[Au_{24}Ag(SH)_{18}]^{-1}$ in the presence of higher energy states. Parts (a) to (f) represent S_1-S_6 respectively.

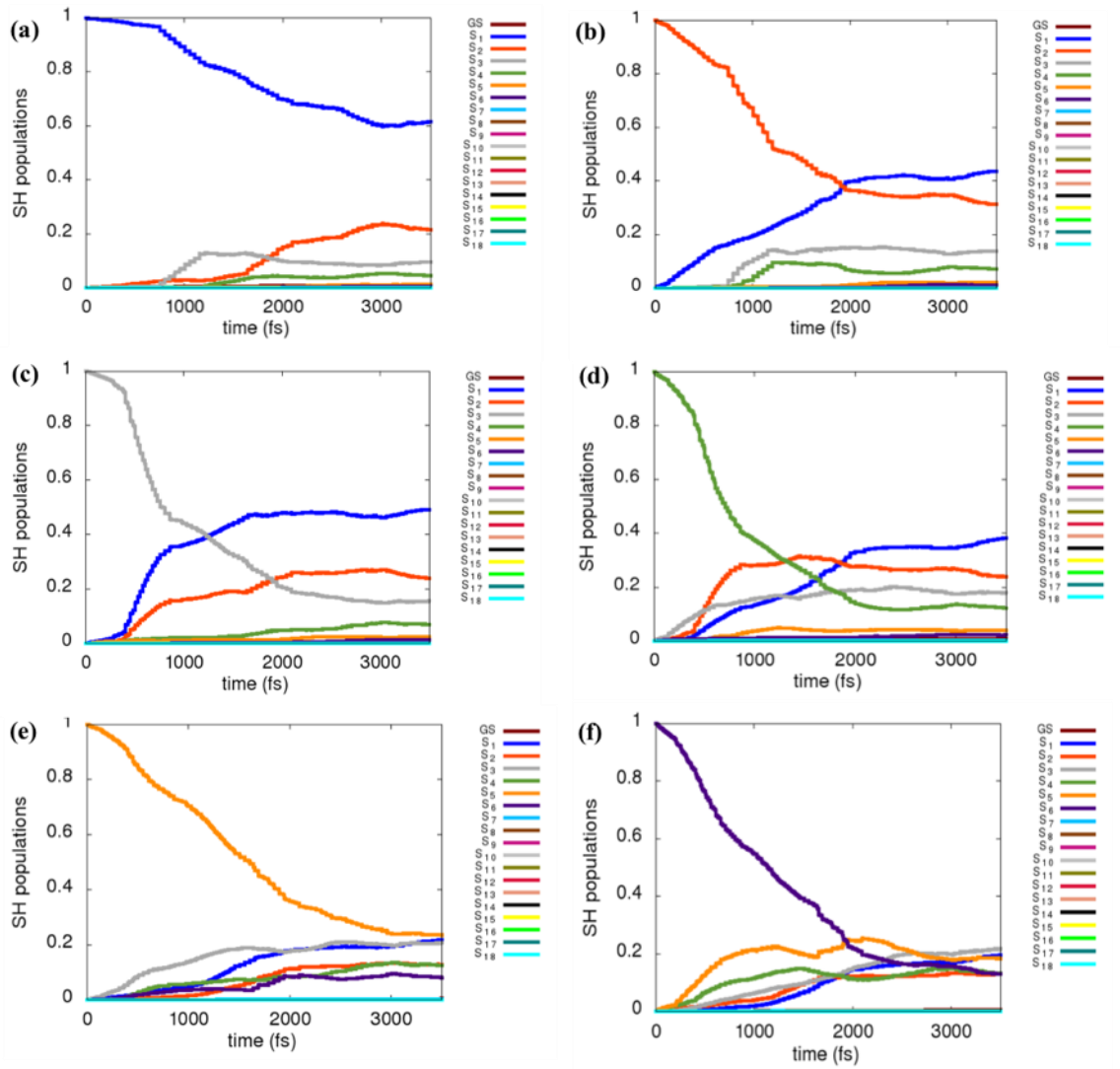

Figure A-5 Population relaxations of S_1, S_2, S_3, S_4, S_5, S_6 states in $[Au_{13}Ag_{12}(SH)_{18}]^{-1}$ in the presence of higher energy states. Parts (a) to (f) represent S_1-S_6 respectively.

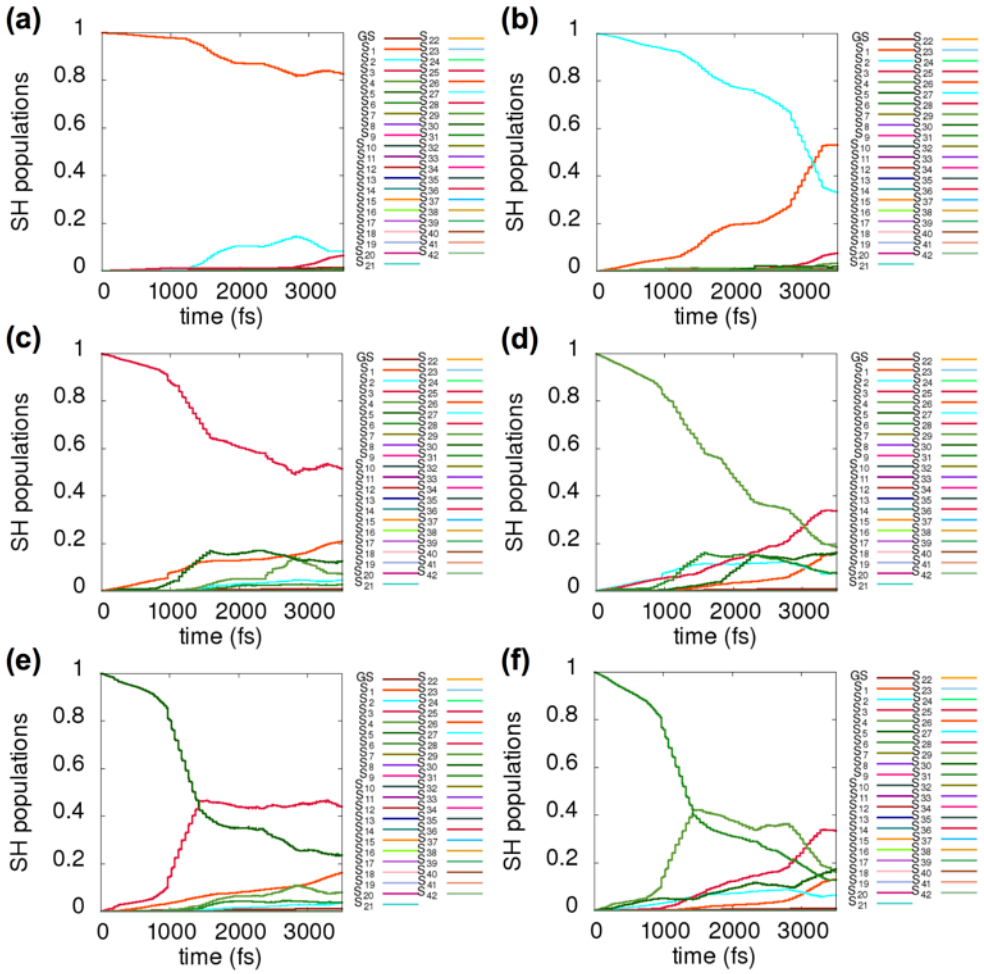

Figure A-6 Population relaxations of S_1, S_2, S_3, S_4, S_5, S_6 states with the energy correction in the presence of higher energy states for $[Ag_{25}(SH)_{18}]^{-1}$. Parts (a) to (f) represent S_1-S_6 respectively.

Table A-11 Decay times of first six excited states including 0.33 eV and 0.55 eV energy correction for three studied clusters.

Excited State	Decay time (ps) with energy corrections					
	$[[Au_{13}Ag_{12}(SH)_{18}]^{-1}$		$[Au_{24}Ag(SH)_{18}]^{-1}$		$[Ag_{25}(SH)_{18}]^{-1}$	
	0.33 eV	0.55 eV	0. 0.33 eV	0.55 eV	0. 0.33 eV	0.55 eV
S_1	6.8	6.9	23.1	25.9	20.0	21.4
S_2	2.3	2.3	9.6	10.2	6.0	7.0
S_3	1.5	1.5	4.5	4.8	4.7	4.9
S_4	1.1	1.1	3.4	3.5	2.8	3.0
S_5	2.0	2.0	3.0	3.0	2.2	2.4
S_6	1.6	1.6	2.5	2.5	2.0	2.0

Table A-12 Decay times (ps) of excited states in the presence of all excited states for $[Ag_{25}(SH)_{18}]^{-1}$ including energy corrections.

Excited state	Without correction	With 0.33 eV correction to the first six states	With 0.55 eV correction to the first six states
S_1	17.0	18.0	16.4
S_2	6.2	6.2	6.3
S_3	4.6	4.9	5.5
S_4	2.8	3.0	3.4
S_5	2.3	2.3	1.9
S_6	2.0	2.0	1.6
S_7	11	11	13.7
S_8	2.9	2.8	3.0
S_9	2.9	2.9	3.0
S_{10}	5.2	5.4	5.7
S_{11}	2.1	2.1	2.2
S_{12}	1.8	1.8	1.8
S_{13}	2.1	2.1	2.2
S_{14}	1.3	1.3	1.4
S_{15}	1.4	1.4	1.4
S_{16}	2.5	2.3	2.6
S_{17}	1.9	1.8	2.0
S_{18}	2.4	2.4	2.5
S_{19}	1.6	1.5	1.6
S_{20}	1.4	1.4	1.5
S_{21}	1.5	1.4	1.4
S_{22}	1.3	1.2	1.2
S_{23}	1.4	1.4	1.4
S_{24}	1.0	1.0	1.0
S_{25}	1.0	1.0	1.0
S_{26}	1.0	0.9	0.9
S_{27}	0.9	0.9	0.9
S_{28}	1.0	1.0	1.0
S_{29}	0.7	0.7	0.8
S_{30}	0.8	0.8	0.8
S_{31}	1.1	1.1	1.0
S_{32}	1.0	1.0	1.0
S_{33}	1.0	1.0	1.1
S_{34}	0.8	0.8	0.8
S_{35}	0.8	0.8	0.8
S_{36}	2.5	2.6	2.6

S_{37}	1.9	1.9	1.9
S_{38}	1.4	1.4	1.4
S_{39}	1.3	1.3	1.3
S_{40}	0.9	0.9	0.9
S_{41}	0.7	0.7	0.7
S_{42}	0.8	0.8	0.8

Table A-13 Decay times (ps) of excited states in the presence of all excited states for $[Au_{13}Ag_{12}(SH)_{18}]^{-1}$ including energy corrections.

Excited state	Without correction	With 0.33 eV correction to the first six states	With 0.55 eV correction to the first six states
S_1	6.6	5.8	3.8
S_2	2.4	2.1	1.8
S_3	1.5	1.4	1.3
S_4	1.2	1.1	1.0
S_5	2.3	1.7	1.6
S_6	1.6	1.4	1.3
S_7	5.6	9.9	17.3
S_8	1.8	2.0	2.1
S_9	1.3	1.3	1.3
S_{10}-Au_{25} = S_{11}-Au_{13}	1.4	1.6	1.7
S_{11}-Au_{25} = S_{12}-Au_{13}	0.9	0.9	0.9
S_{12}-Au_{25} = S_{13}-Au_{13}	0.8	0.8	0.8
S_{13}-Au_{25} = S_{15}-Au_{13}	1.7	1.9	2.2
S_{14}-Au_{25} = S_{16}-Au_{13}	1.1	1.1	1.1
S_{15}-Au_{25} = S_{17}-Au_{13}	1.0	0.9	0.9

Table A-14 Decay times (ps) of excited states in the presence of all excited states for $[Au_{24}Ag(SH)_{18}]^{-1}$ including energy corrections.

Excited state	Without correction	With 0.33 eV correction to the first six states	With 0.55 eV correction to the first six states
S_1	19.2	24.0	25.9
S_2	8.9	9.6	8.1
S_3	5.1	5.2	4.6
S_4	3.7	3.7	3.2
S_5	2.9	3.0	2.1
S_6	2.5	2.4	1.7
S_7	12.3	13.4	15.5
S_8	3.7	3.6	3.8
S_9	1.7	1.7	1.6
S_{10}-Au_{25} = S_{13}-Au_{24}	4.6	4.5	4.8

S_{11}-Au_{25} = S_{14}-Au_{24}	2.6	2.5	2.5
S_{12}-Au_{25} = S_{15}-Au_{24}	1.5	1.4	1.4
S_{13}-Au_{25} = S_{19}-Au_{24}	2.3	2.4	2.4
S_{14}-Au_{25} = S_{20}-Au_{24}	1.8	1.8	1.7
S_{15}-Au_{25} = S_{21}-Au_{24}	0.9	0.9	0.9
S_{16}-Au_{25} = S_{25}-Au_{24}	3.7	3.2	3.7
S_{17}-Au_{25} = S_{26}-Au_{24}	2.8	2.6	2.8
S_{18}-Au_{25} = S_{27}-Au_{24}	2.8	2.8	2.8
S_{19}-Au_{25} = S_{28}-Au_{24}	1.8	1.8	1.8
S_{20}-Au_{25} = S_{29}-Au_{24}	1.1	1.1	1.1
S_{21}-Au_{25} = S_{33}-Au_{24}	2.6	2.2	2.3
S_{22}-Au_{25} = S_{34}-Au_{24}	2.1	1.9	1.9
S_{23}-Au_{25} = S_{35}-Au_{24}	2.1	2.2	2.1
S_{24}-Au_{25} = S_{36}-Au_{24}	1.6	1.6	1.5
S_{25}-Au_{25} = S_{37}-Au_{24}	1.0	1.0	0.9
S_{26}-Au_{25} = S_{41}-Au_{24}	1.4	1.4	1.3
S_{27}-Au_{25} = S_{42}-Au_{24}	1.3	1.2	1.2
S_{28}-Au_{25} = S_{43}-Au_{24}	1.4	1.4	1.4
S_{29}-Au_{25} = S_{44}-Au_{24}	1.1	1.1	1.1
S_{30}-Au_{25} = S_{45}-Au_{24}	0.8	0.8	0.8
S_{31}-Au_{25} = S_{49}-Au_{24}	1.2	1.1	1.1
S_{32}-Au_{25} = S_{50}-Au_{24}	1.1	1.0	1.0
S_{33}-Au_{25} = S_{51}-Au_{24}	1.2	1.1	1.1
S_{34}-Au_{25} = S_{52}-Au_{24}	0.9	0.9	0.9
S_{35}-Au_{25} = S_{53}-Au_{24}	0.6	0.6	0.6

References

1. Negishi, Y.; Iwai, T.; Ide, M., Continuous Modulation of Electronic Structure of Stable Thiolate-Protected Au_{25} Cluster by Ag Doping. *Chem. Commun.* **2010,** *46* (26), 4713-4715.

2. Joshi, C. P.; Bootharaju, M. S.; Alhilaly, M. J.; Bakr, O. M., $[Ag_{25}(SR)_{18}]^{-}$: The "golden" Silver Nanoparticle. *J. Am. Chem. Soc.* **2015,** *137* (36), 11578-11581.

3. Senanayake, R. D.; Akimov, A. V.; Aikens, C. M., Theoretical Investigation of Electron and Nuclear Dynamics in the $[Au_{25}(SH)_{18}]^{-1}$ Thiolate-Protected Gold Nanocluster. *J. Phys. Chem. C* **2016,** *121* (20), 10653-10662.

Appendix B - Supporting Information for "Theoretical Analysis of Optical Absorption Spectra of Parallel Nanowire Dimers and Dolmen Trimers"

Table B-1 Coordinates of Ag_4, Ag_6 and Ag_{10} monomers

Ag_4:

1.Ag	0.000000	0.000000	-1.373754
2.Ag	0.000000	0.000000	1.373754
3.Ag	0.000000	0.000000	-3.997090
4.Ag	0.000000	0.000000	3.997090

Ag_6:

1.Ag	0.0000000	0.0000000	6.6903889
2.Ag	0.0000000	0.0000000	4.0636955
3.Ag	0.0000000	0.0000000	1.3280370
4.Ag	0.0000000	0.0000000	-1.3280370
5.Ag	0.0000000	0.0000000	-4.0636955
6.Ag	0.0000000	0.0000000	-6.6903889

Ag_{10}:

1.Ag	0.000000	0.000000	1.334961
2.Ag	0.000000	0.000000	-1.334961
3.Ag	0.000000	0.000000	4.049779
4.Ag	0.000000	0.000000	-4.049779
5.Ag	0.000000	0.000000	6.711155
6.Ag	0.000000	0.000000	-6.711155
7.Ag	0.000000	0.000000	9.440900
8.Ag	0.000000	0.000000	-9.440900
9.Ag	0.000000	0.000000	12.067917
10.Ag	0.000000	0.000000	-12.067917

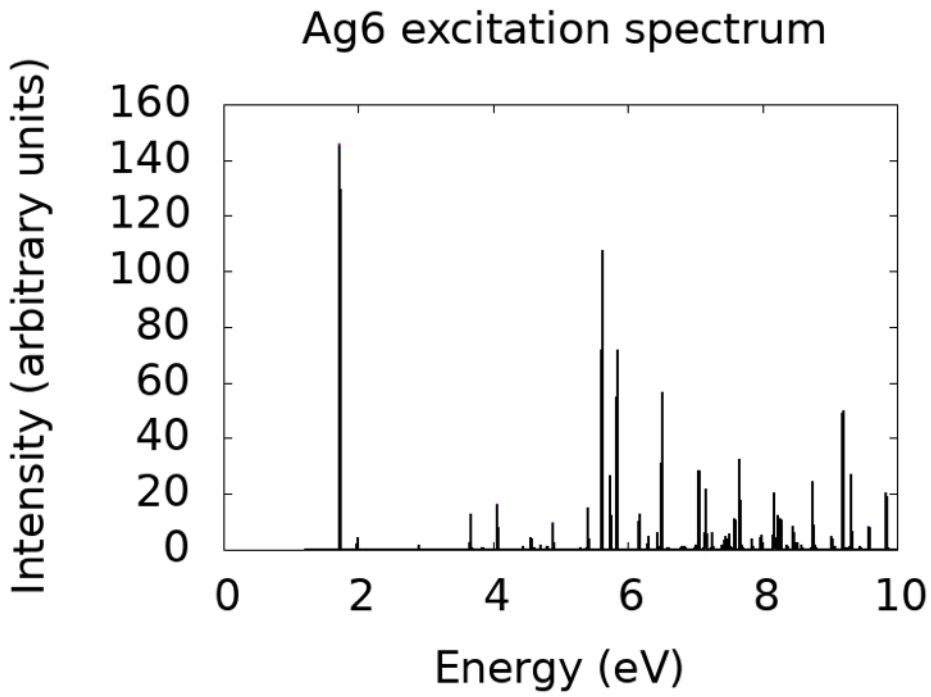

Figure B-1 Absorption spectra of Ag_6 monomer (FWHM = 0.01).

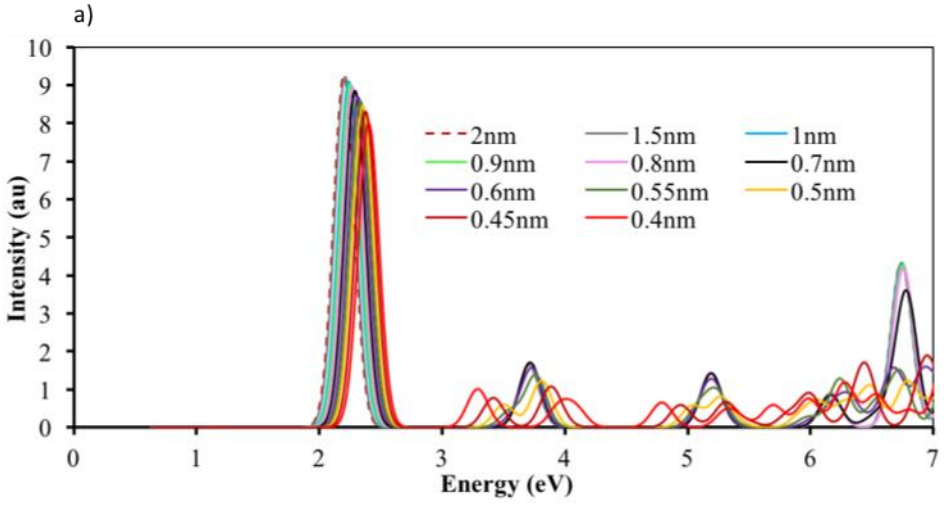

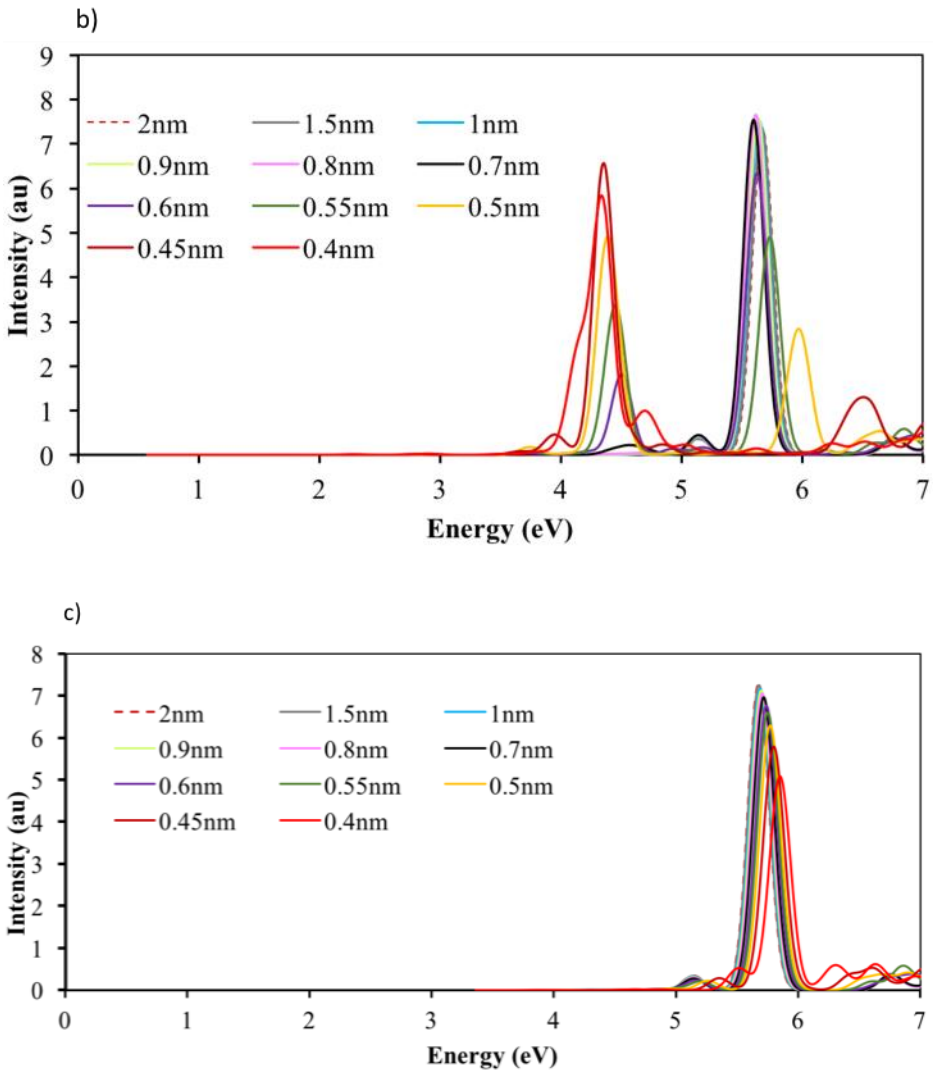

Figure B-2 Absorption spectra for Ag_4 dimer at different inter-particle separations and for different excited state symmetry representations: a) B_{1u} (*z*-polarized), b) B_{2u} (*y*-polarized) and c) B_{3u} (*x*-polarized).

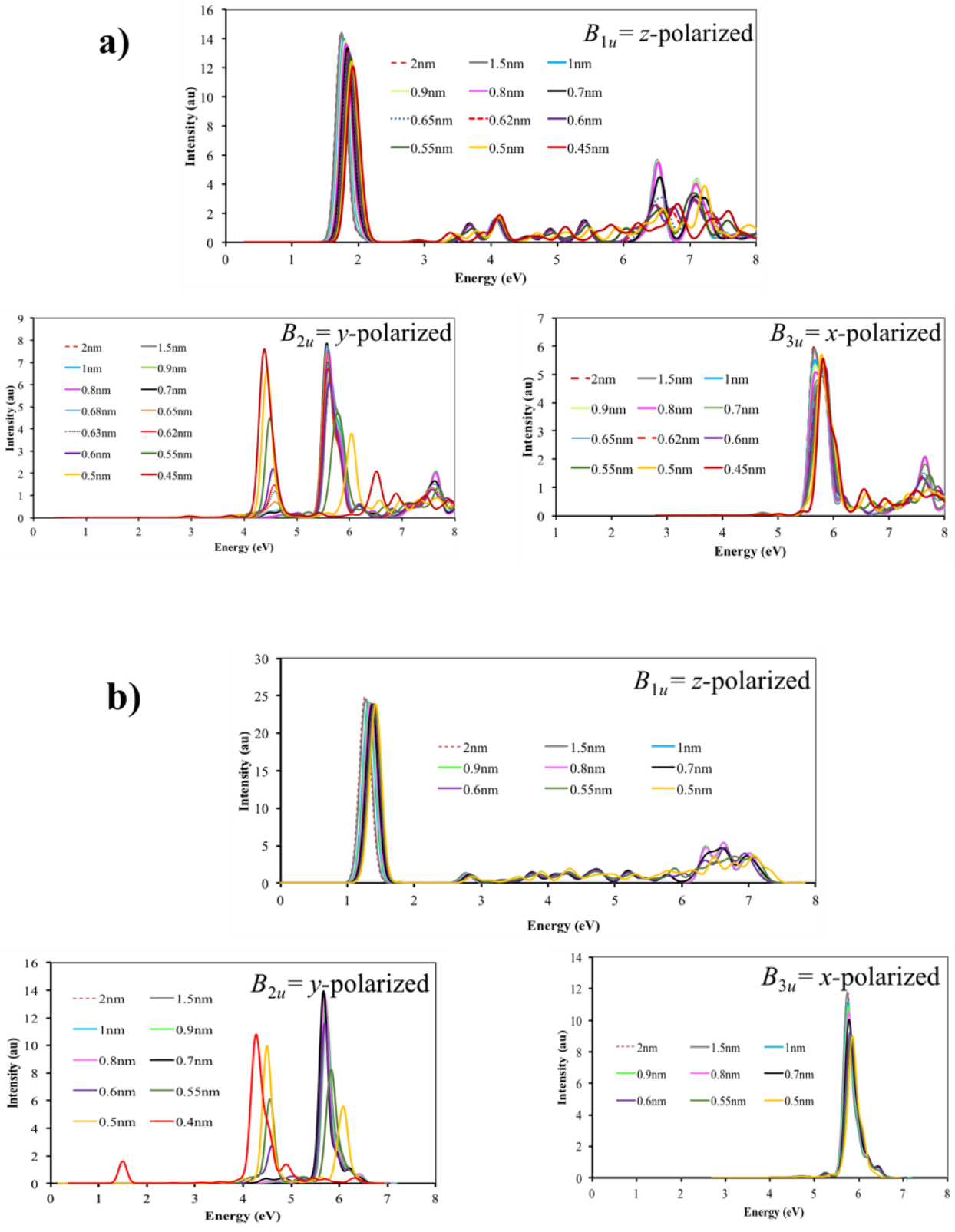

Figure B-3 Absorption spectra at different inter-particle separations and for different excited state symmetry representations of (a) Ag_6 dimer (b) Ag_{10} dimer.

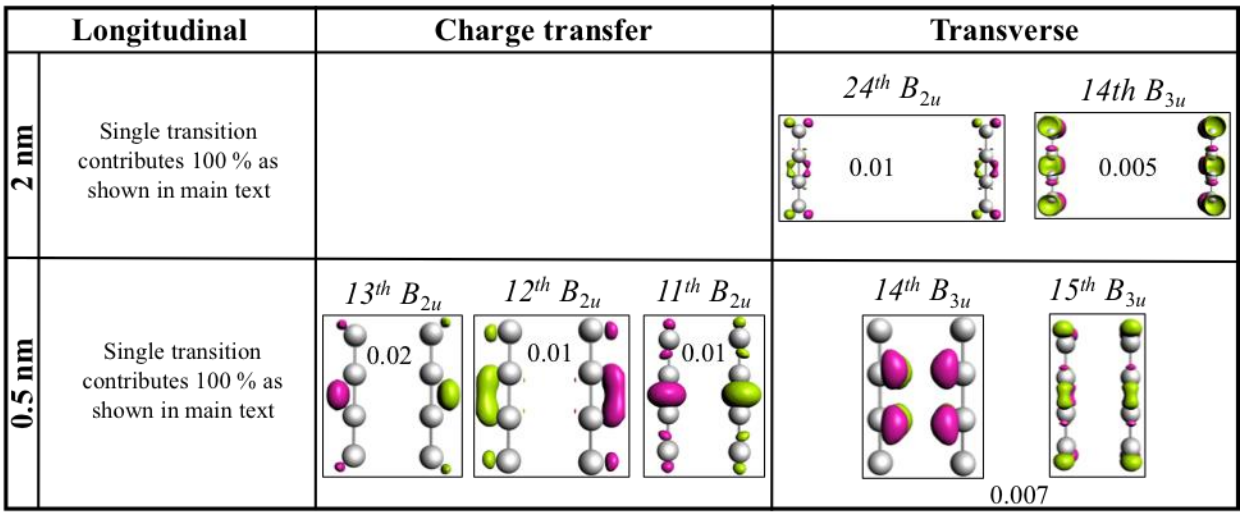

2 nm	State	Energy (eV)	Oscillator strength (a.u.)
Longitudinal	2nd B_{1u}	2.2015	1.9706
Transverse	12th B_{3u}	5.6757	1.5138
	14th B_{3u}	5.7679	0.0607
	22nd B_{2u}	5.6683	1.5331
	24th B_{2u}	5.7676	0.0527
0.5 nm			
Longitudinal	2nd B_{1u}	2.3548	1.8022
Charge transfer	10th B_{2u}	4.3771	0.87270
	13th B_{2u}	4.4706	0.22687
	12th B_{2u}	4.4527	0.03745
	11th B_{2u}	4.4149	0.01117
Transverse	26th B_{2u}	5.9284	0.28505
	27th B_{2u}	6.0051	0.37977
	13th B_{3u}	5.7712	1.3136
	14th B_{3u}	5.8594	0.02784
	15th B_{3u}	5.9054	0.02850

Figure B-4 Transition electron densities of weaker excitations (shown in black in the table) that lie close in energy to the stronger excitations that have been discussed in the main text (shown in red in the table). The table shows the oscillator strength of each excited state.

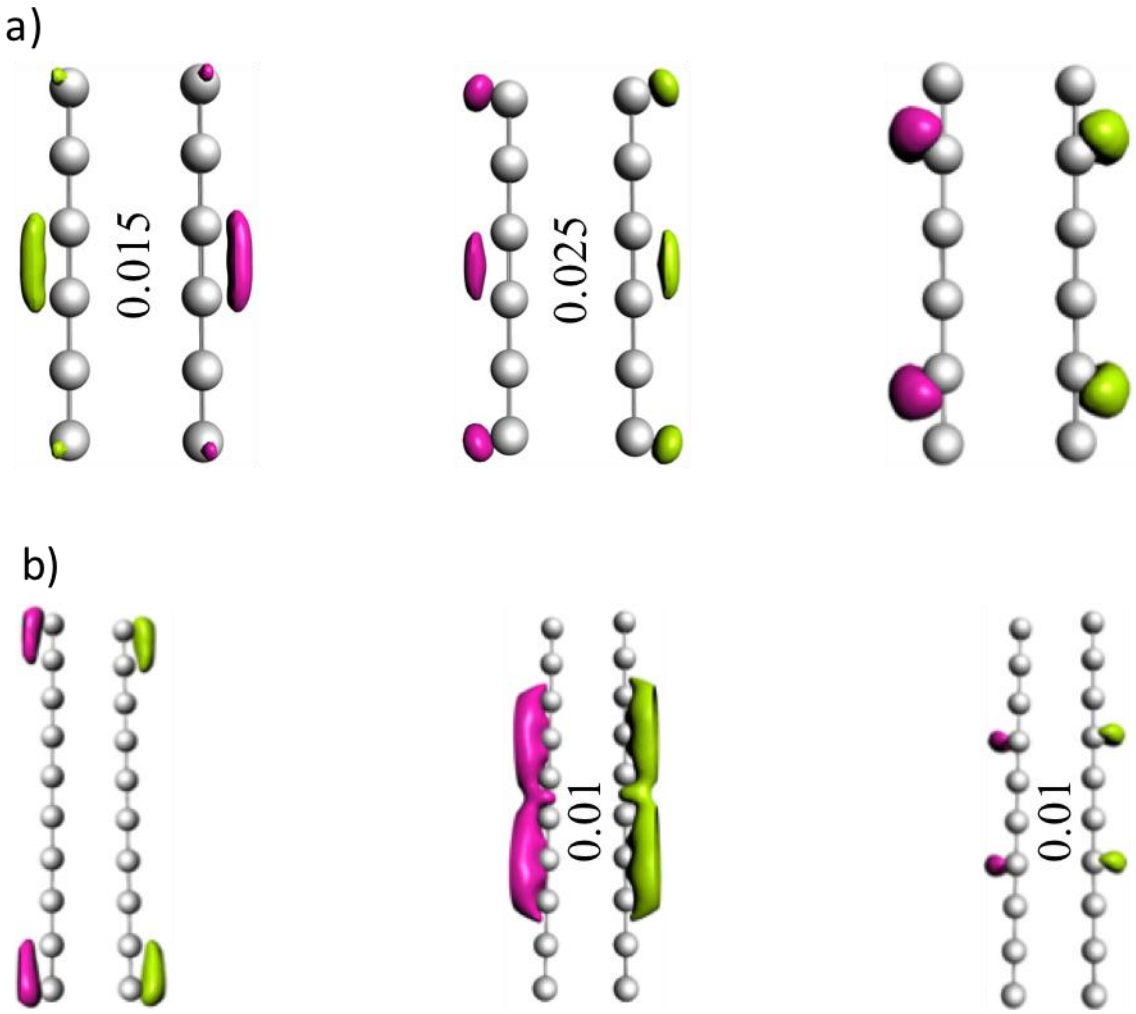

Figure B-5 Transition densities for the charge transfer peak of a) Ag_6 dimer at 0.5 nm separation, and b) Ag_{10} dimer at 0.5 nm separation. Transition densities are drawn with an iso-value of 0.02 unless stated.

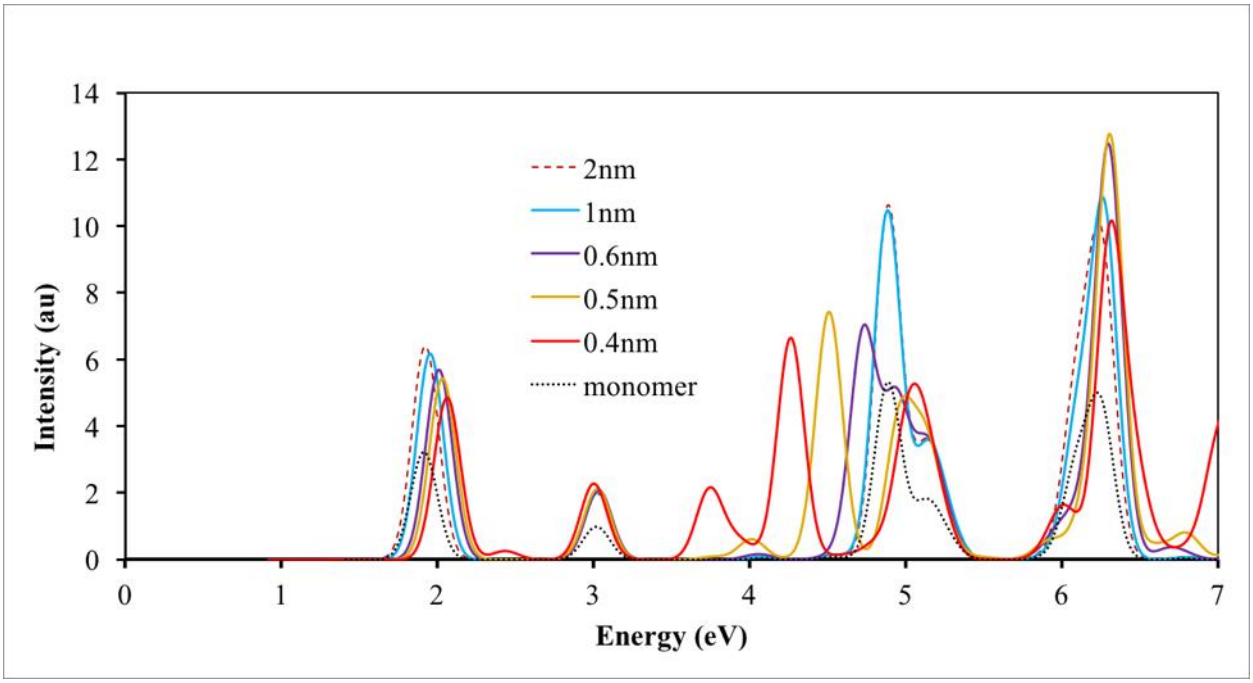
Intensity (au)
Energy (eV)
2nm
1nm
0.6nm
0.5nm
0.4nm
monomer
0
2
4
6
8
10
12
14
0
1
2
3
4
5
6
7

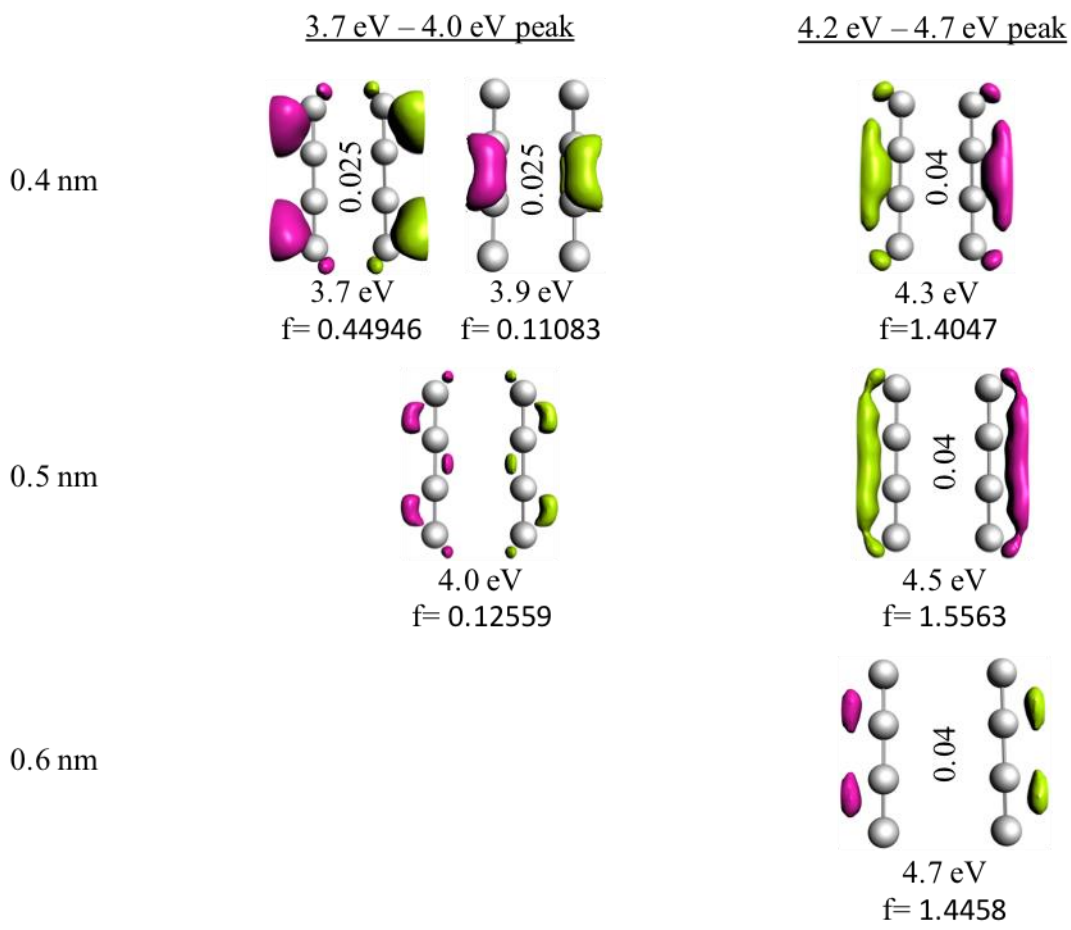

Figure B-6 Spectra obtained with TDHF at different monomer separations; transition density plots for the newly formed charge-transfer peaks.

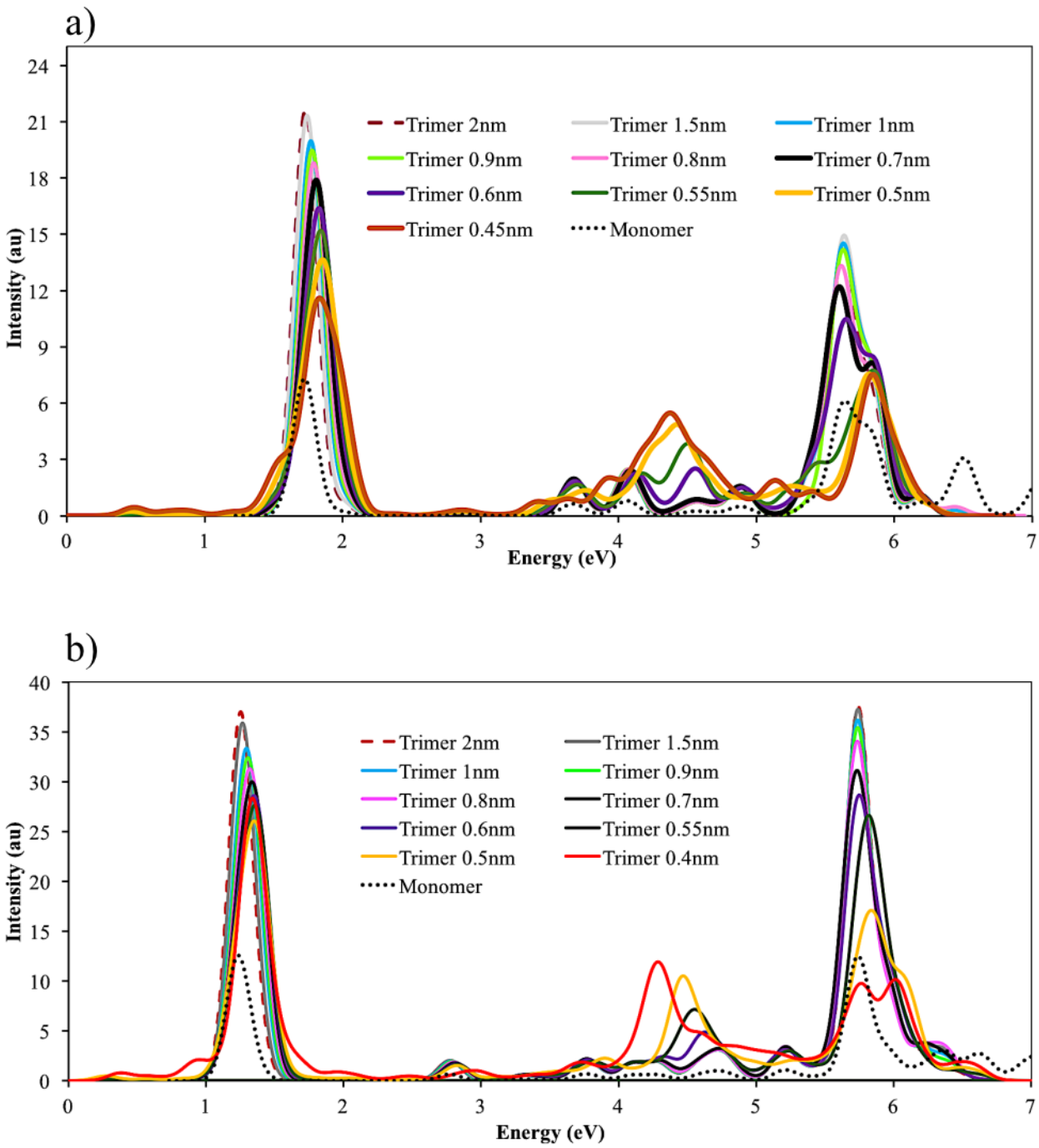

Figure B-7 Absorption spectra of a) Ag_6 and b) Ag_{10} trimers at different inter-particle separation.

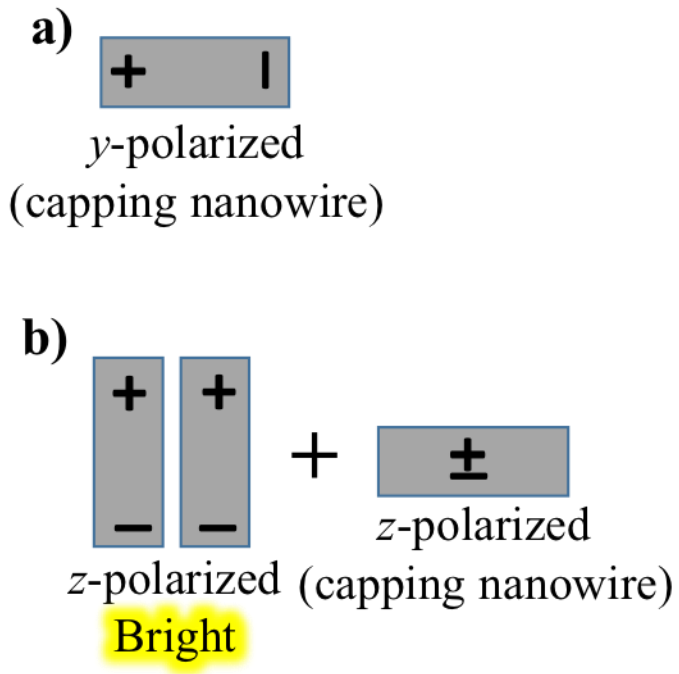

Figure B-8 Plasmon interaction diagram showing different possibilities for the longitudinal peak of the trimer.

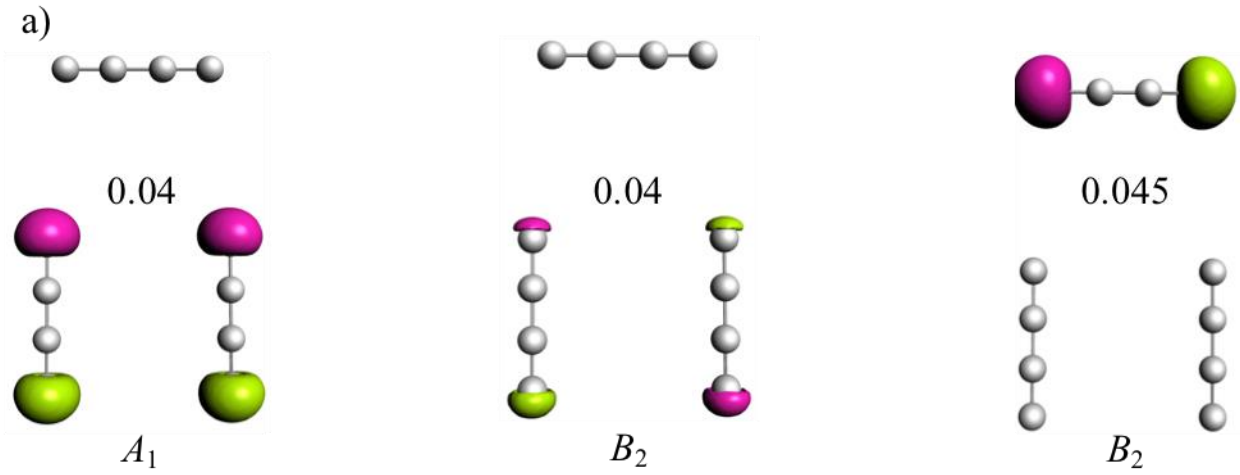

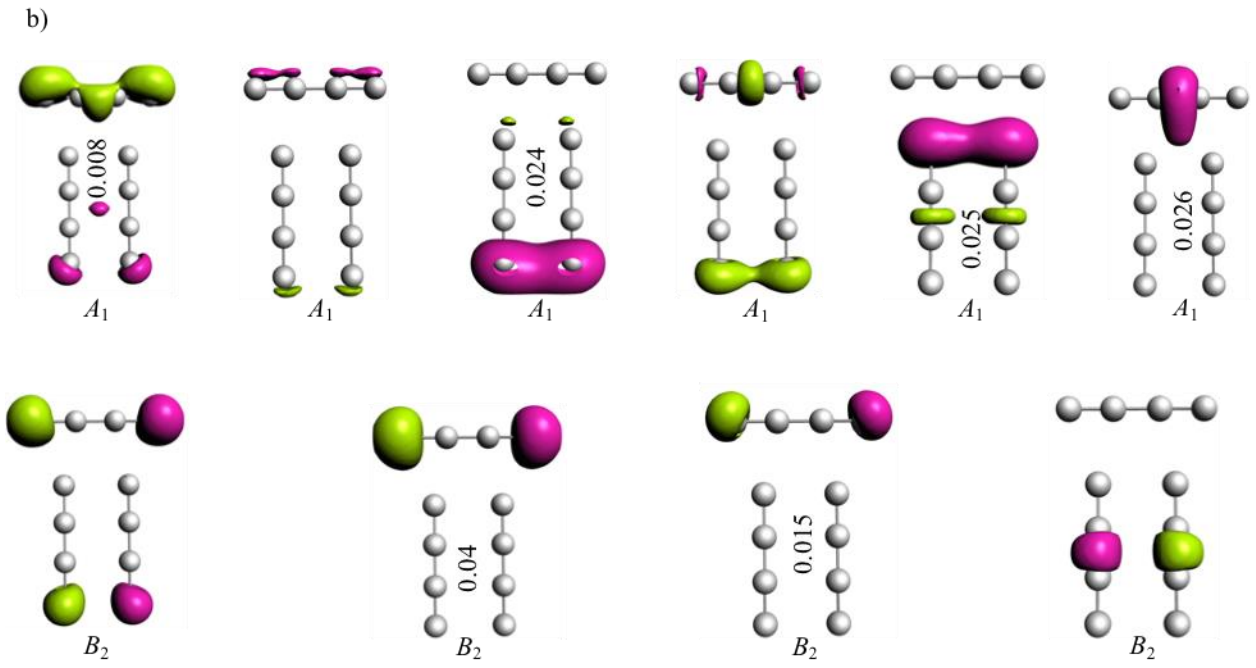

Figure B-9 Transition electron densities for the longitudinal peak of the trimer at a) 1 nm separation, and b) 0.45 nm separation.

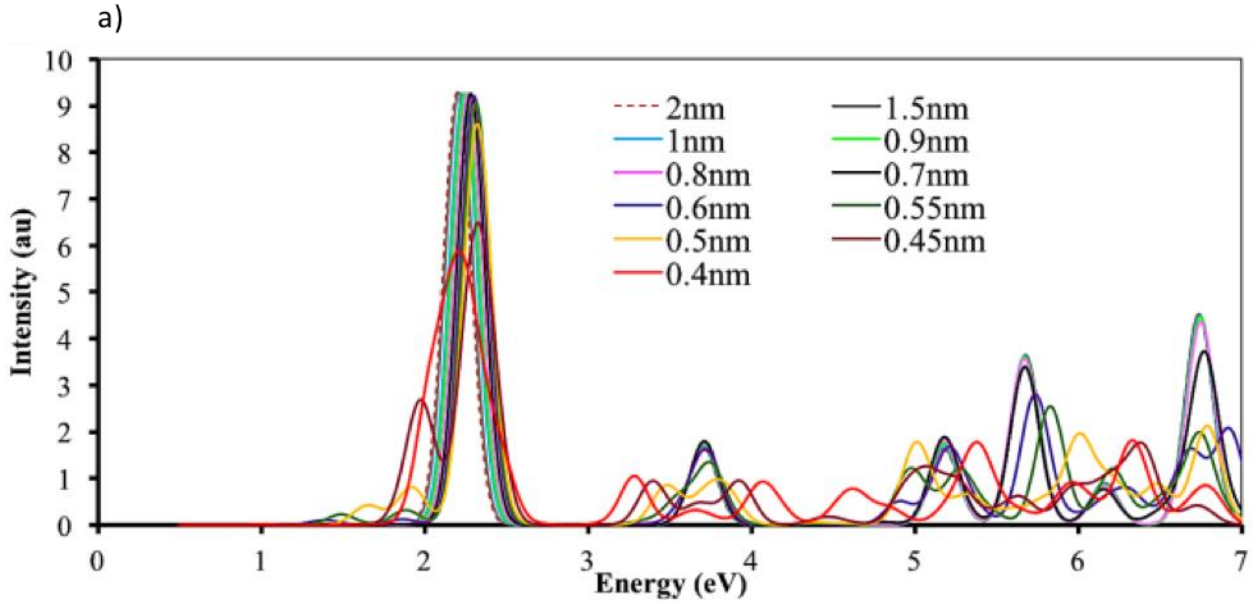

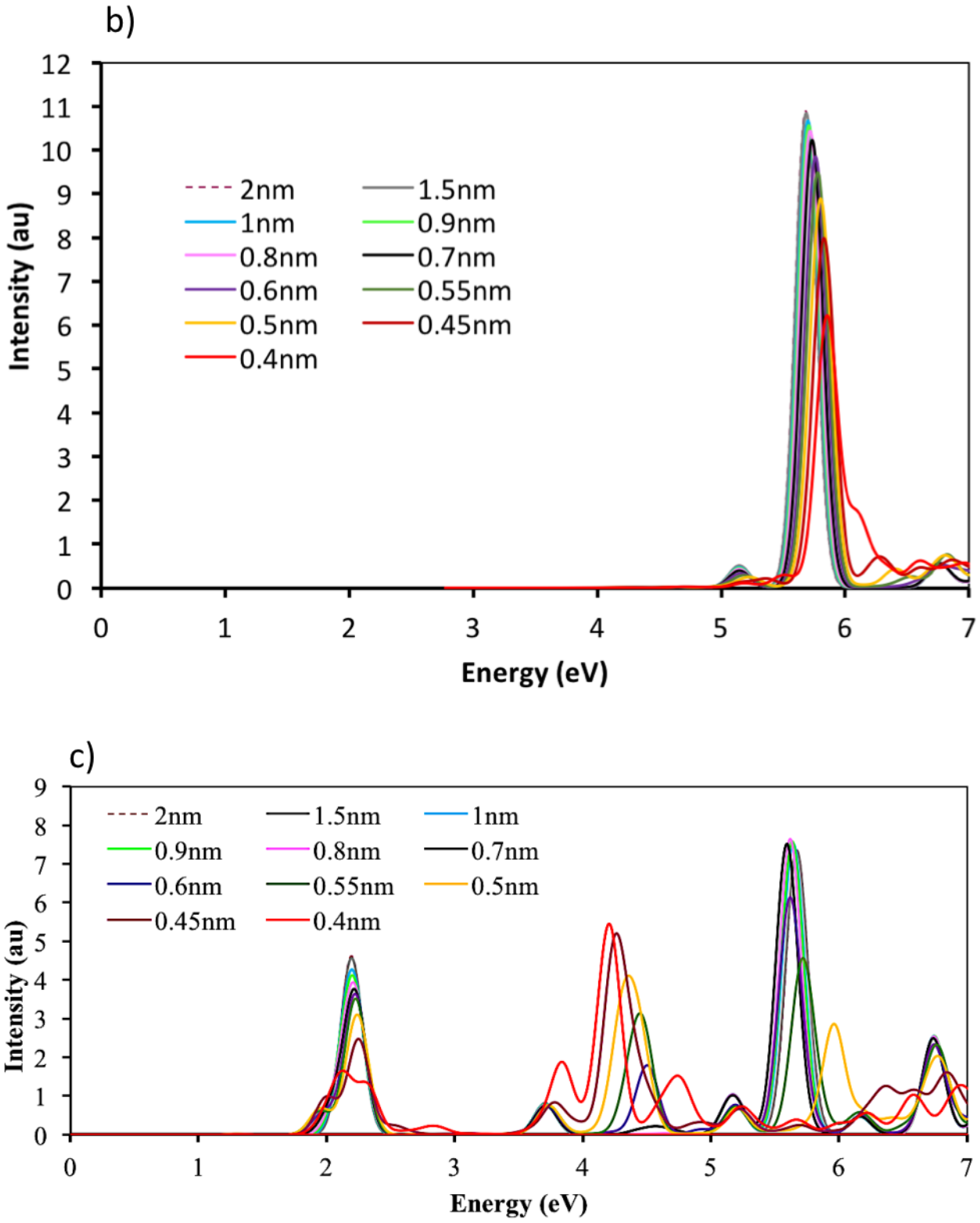

Figure B-10 Absorption spectra for Ag_4 trimer at different inter-particle separations and for different excited state symmetry representations: a) A_1, b) B_1 and c) B_2.

Appendix C - Supporting Information for "RT-TDDFT Examination of Nanowire Arrays for the Plasmonic Enhanced Dissociation of Dinitrogen"

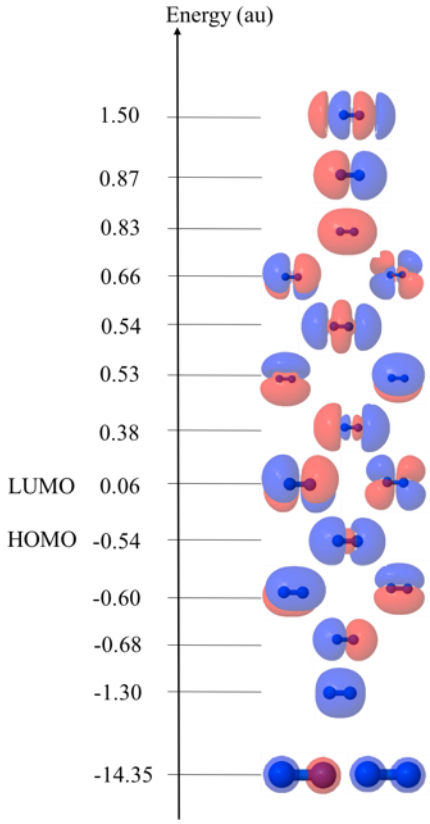

Figure C-1 Molecular orbital diagram of nitrogen molecule. Orbitals are obtained with contour value of 0.02.

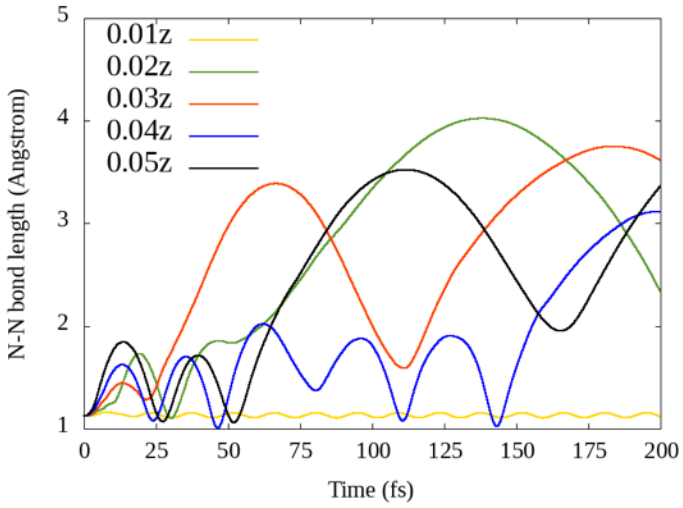

Figure C-2 Variation of N-N bond length in the N_2 molecule on applying a z-polarized field corresponding to a frequency of 18.39 eV with field intensities of 0.01-0.05 au. Initial velocities are set to zero during these calculations.

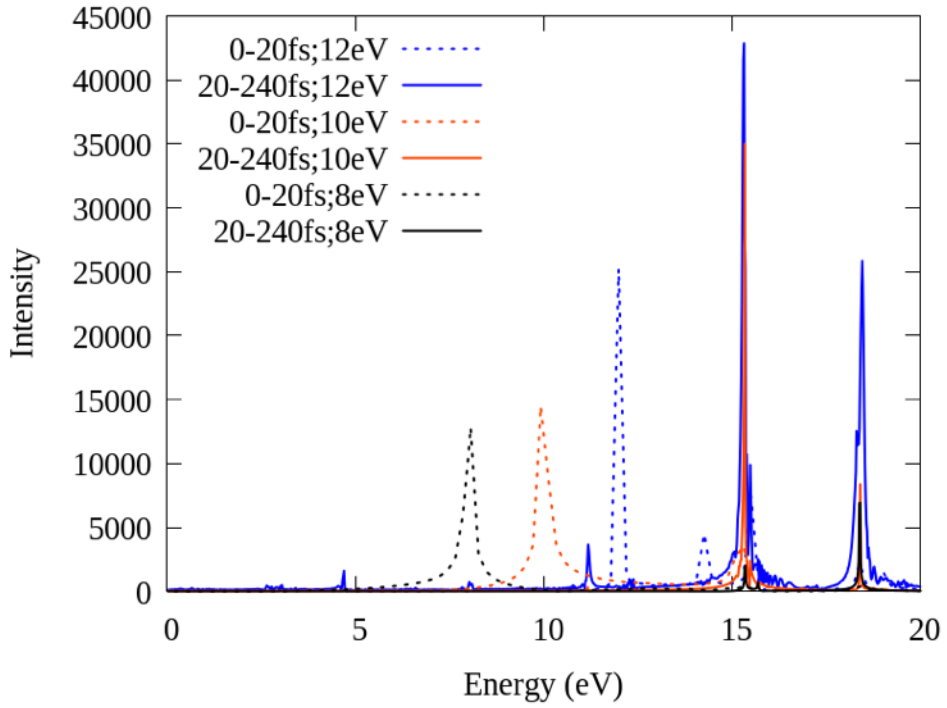

Figure C-3 Fourier transformed peaks of the dipole moment obtained at different time ranges. These are obtained from the calculation using the applied field intensity of 0.04 au at different applied frequencies as shown in the legend.

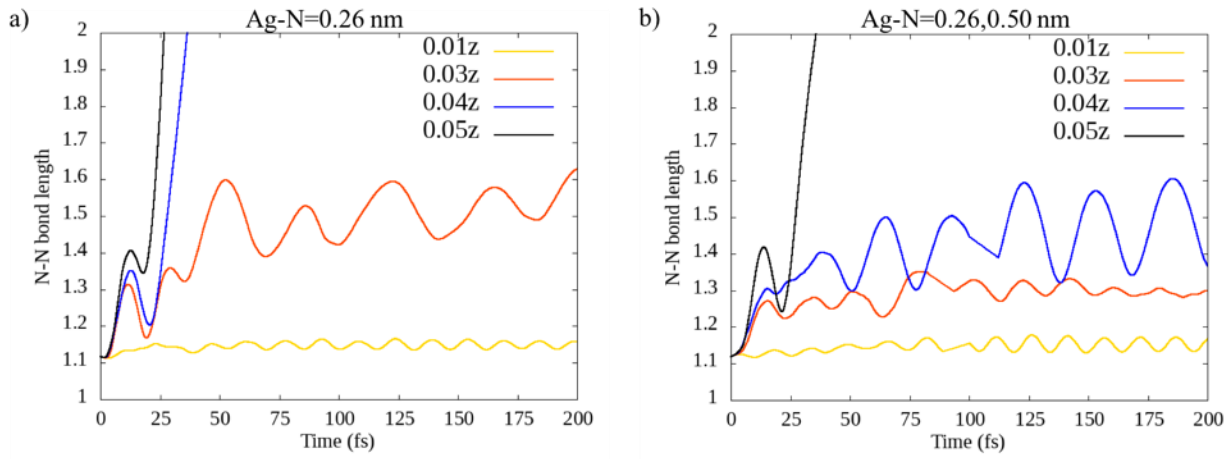

Figure C-4 Variation of N-N bond length with time for hotspot orientation. (a) is obtained for using two different values for 'd': the Ag-N distance is 0.26 nm on one end and 0.50 nm on the other end. (b) is obtained when Ag-N distance is 0.26 nm on both ends, i.e., has the same values of 'd'. This is the optimized hotspot structure. The graphs are obtained using z-polarized fields with field strengths of 0.01 au, 0.03 au, 0.04 au and 0.05 au as shown in the figures. The applied field has a frequency corresponding to 2.36 eV.

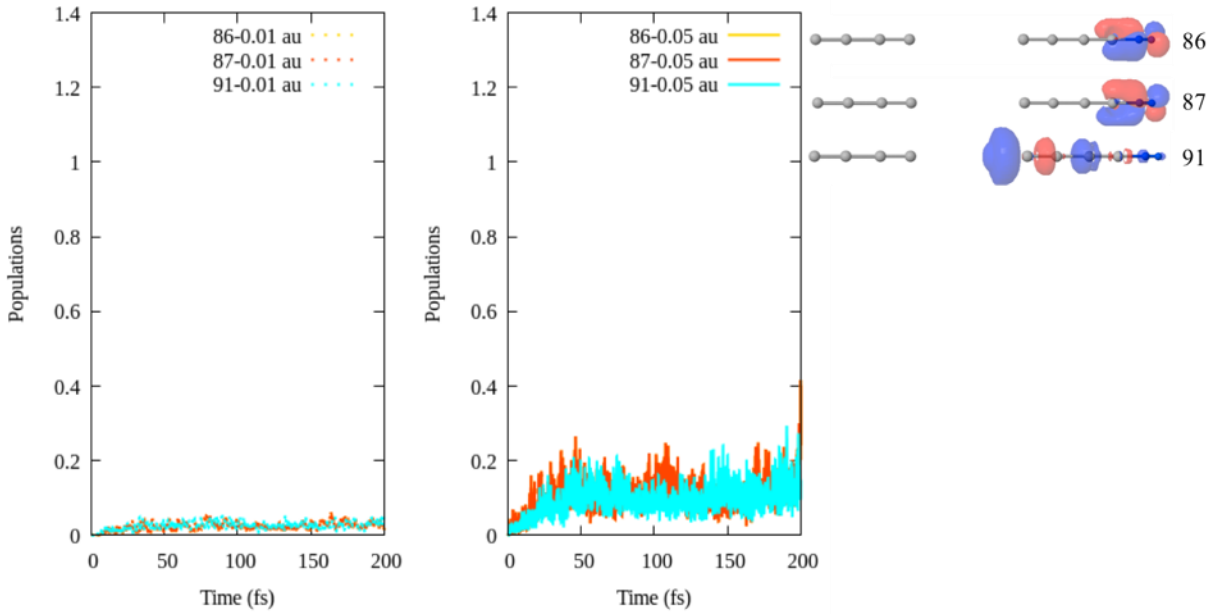

Figure C-5 Variation of electronic populations in virtual molecular orbitals 86, 87, and 91 throughout the simulation time upon applying electric fields with 0.01 au and 0.05 au field intensities. This plot is obtained for the end-to-end dimer with an inter-particle distance of 0.50 nm.

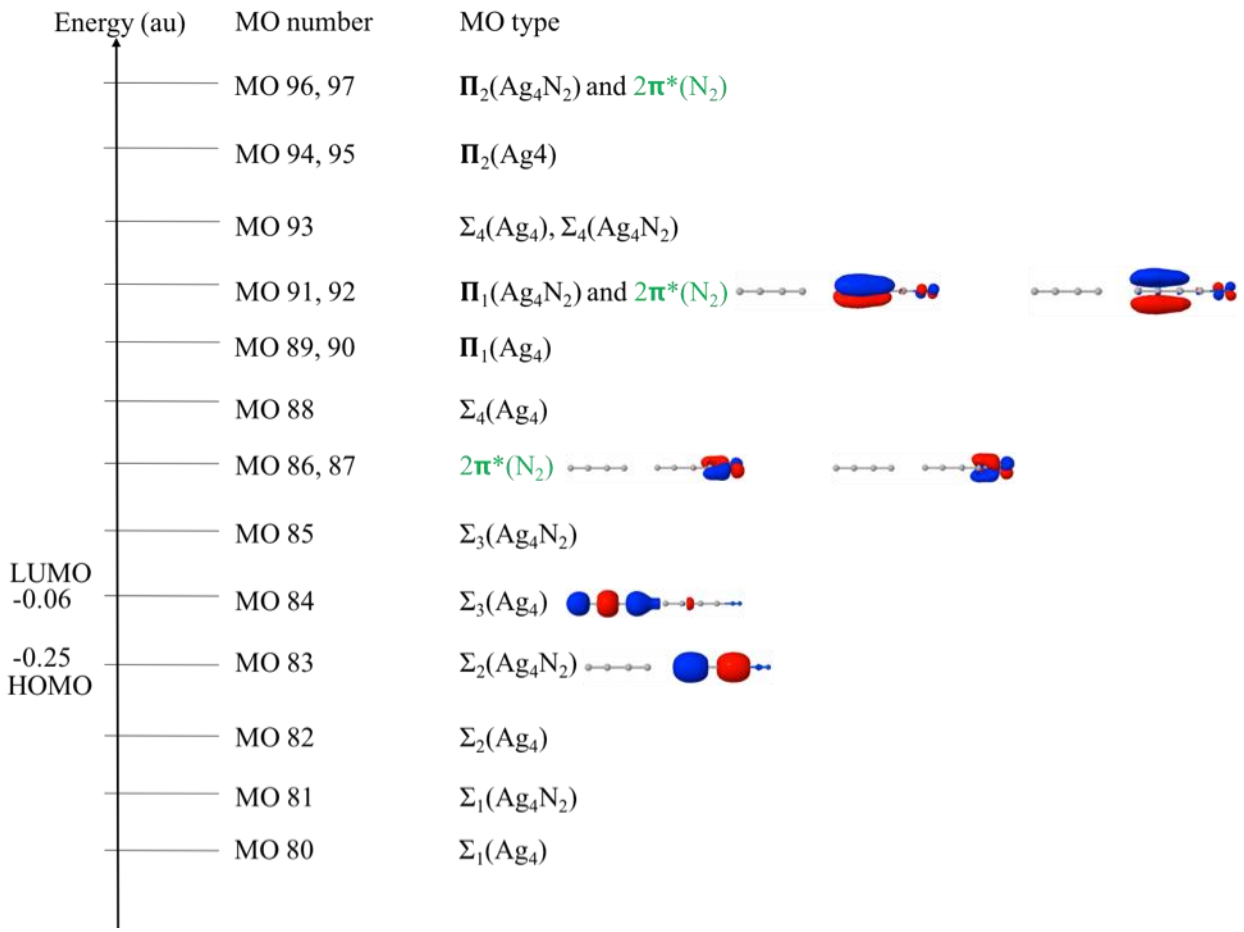

Figure C-6 Molecular orbital diagram of the end-to-end dimer with an inter-particle distance of 0.50 nm. Shape of some of the Ag-wire based sigma orbitals (83, 84), nitrogen antibonding orbitals (86,87), and Ag-wire based pi orbitals (91, 92) are shown. The nitrogen antibonding orbitals are highlighted in green text. The orbitals are obtained with contour value of 0.02.

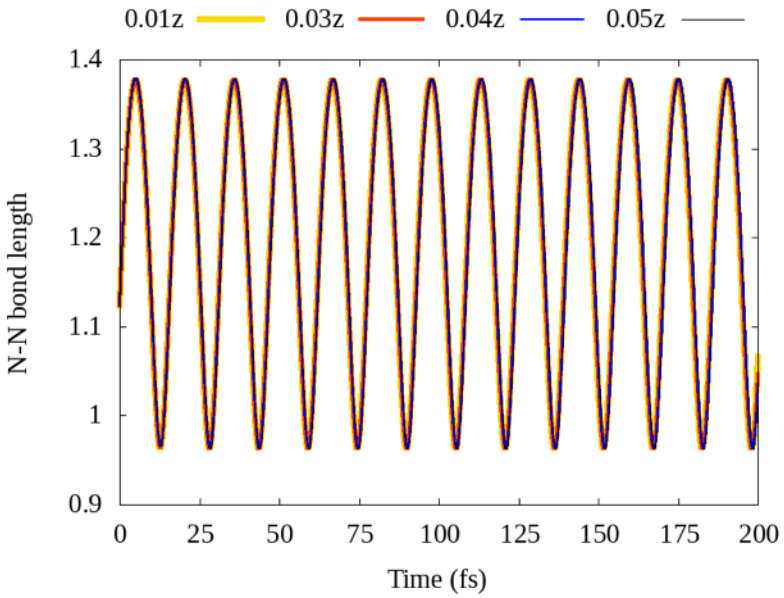

Figure C-7 Variation of N-N bond length with time for the N_2 molecule in the presence of field intensities shown in the legend. The applied field has the frequency corresponding to 2.36 eV.

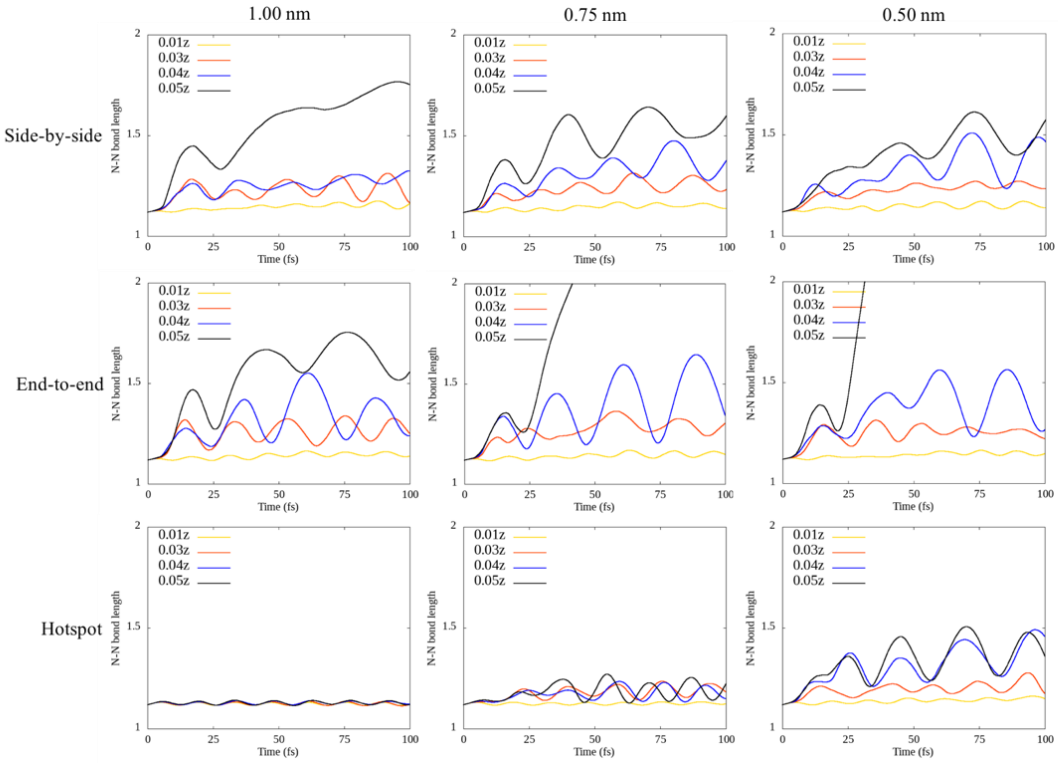

Figure C-8 Variation of the N-N bond length with time for different dimer orientations (row) and at different inter-particle separations (columns). The graphs are obtained using z-

polarized fields with field strengths of 0.01 au, 0.03 au, 0.04 au and 0.05 au as shown in the figures. The applied electric field has a frequency corresponding to the dimer longitudinal peak frequency of each of the systems. For dimers with side-by-side orientation, the longitudinal peak frequencies are 2.38, 2.40, and 2.46 eV for inter-particle separations of 1.00 nm, 0.75 nm and 0.50 nm, respectively. For dimers with end-to-end orientation, longitudinal peak frequencies are 2.25, 2.23, and 2.13 eV for inter-particle separations of 1.00 nm, 0.75 nm and 0.50 nm, respectively. For dimers with the hotspot orientation, longitudinal peak frequencies are 2.26, 2.25, and 2.24 eV for inter-particle separations of 1.00 nm, 0.75 nm and 0.50 nm, respectively.

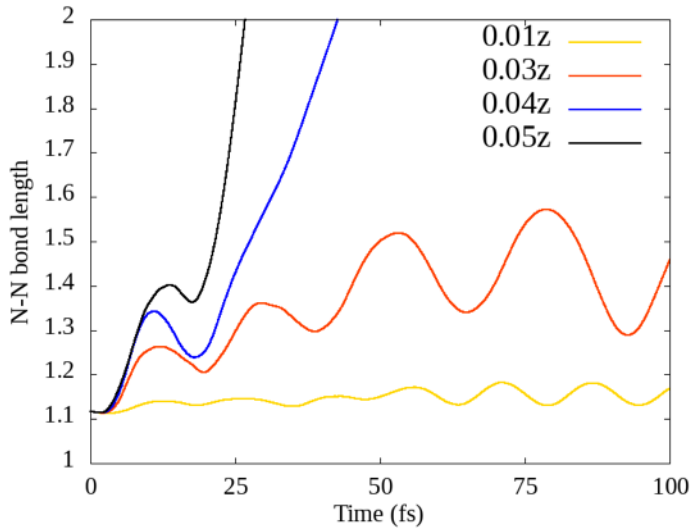

Figure C-9 Variation of N-N bond length with time for the optimized hotspot orientation with the Ag-N distance of 0.26 nm on both ends, i.e., has the same values of 'd'. The applied field has a frequency corresponding to 2.26 eV (i.e., the longitudinal peak energy of the system).

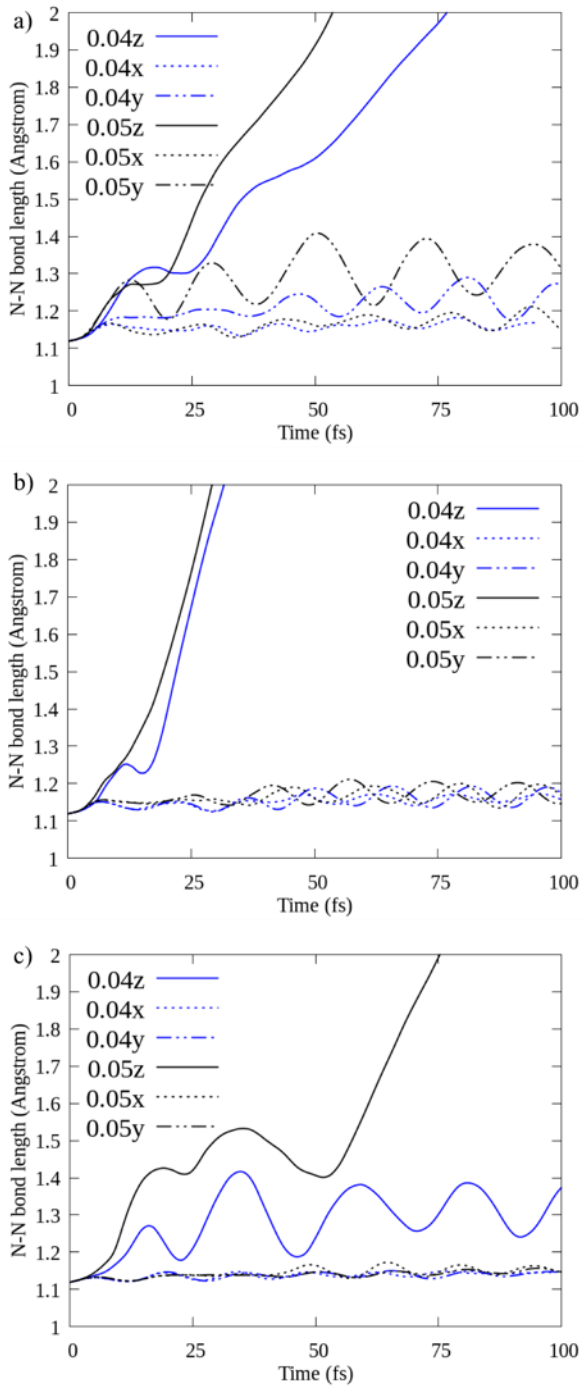

Figure C-10 Variation of N-N bond length over time upon applying x-, y-, and z-polarized electric fields with frequencies of 4.60 eV and applied field strengths of 0.04 and 0.05 au on a) side-by-side dimer with an inter-particle distance of 0.50 nm, b) end-to-end dimer with an inter-particle distance of 0.50 nm, and c) hotspot dimer with Ag-N distances of 0.50 nm.

Table C-1 Optimized Ag_4 coordinates

Ag	0.000000	0.000000	1.432089
Ag	0.000000	0.000000	-1.432089
Ag	0.000000	0.000000	4.012869
Ag	0.000000	0.000000	-4.012869

Table C-2 Optimized Ag_4N_2 coordinates (center of mass of system is not at origin)

Ag	0.000000	0.000000	-0.940170
Ag	0.000000	0.000000	1.916518
Ag	0.000000	0.000000	-3.516021
Ag	0.000000	0.000000	4.497527
N	0.000000	0.000000	-6.013148
N	0.000000	0.000000	-7.132448

Table C-3 Optimized Ag_4N_2 coordinates; monomer (center of mass of system is at origin)

Ag	0.00000000	0.00000000	-0.99553511
Ag	0.00000000	0.00000000	1.86115289
Ag	0.00000000	0.00000000	-3.57138611
Ag	0.00000000	0.00000000	4.44216189
N	0.00000000	0.00000000	-6.06851311
N	0.00000000	0.00000000	-7.18781311

Table C-4 Ag_8N_2 coordinates (Side-by-side, d = 1.00 nm)

Ag	0.00000000	-5.00000000	-0.99553511
Ag	0.00000000	-5.00000000	1.86115289
Ag	0.00000000	-5.00000000	-3.57138611
Ag	0.00000000	-5.00000000	4.44216189
N	0.00000000	-5.00000000	-6.06851311
N	0.00000000	-5.00000000	-7.18781311
Ag	0.00000000	5.00000000	-0.99553511
Ag	0.00000000	5.00000000	1.86115289
Ag	0.00000000	5.00000000	-3.57138611
Ag	0.00000000	5.00000000	4.44216189

Table C-5 Ag_8N_2 coordinates (End-to-end, d = 1.00 nm)

Ag	0.00000000	0.00000000	-9.92813630
Ag	0.00000000	0.00000000	-7.07144830
Ag	0.00000000	0.00000000	-12.50398730
Ag	0.00000000	0.00000000	-4.49043930
N	0.00000000	0.00000000	-15.00111430
N	0.00000000	0.00000000	-16.12041430
Ag	0.00000000	0.00000000	5.50956070

Ag	0.00000000	0.00000000	8.09056970
Ag	0.00000000	0.00000000	10.94725770
Ag	0.00000000	0.00000000	13.52310870

Table C-6 Ag_8N_2 coordinates (Hotspot, d = 1.00 nm)

Ag	0.00000000	0.00000000	13.13674961
Ag	0.00000000	0.00000000	15.99343761
Ag	0.00000000	0.00000000	10.56089861
Ag	0.00000000	0.00000000	18.57444661
N	0.00000000	0.00000000	0.56089861
N	0.00000000	0.00000000	-0.55840139
Ag	0.00000000	0.00000000	-10.55840139
Ag	0.00000000	0.00000000	-13.13941039
Ag	0.00000000	0.00000000	-15.99609839
Ag	0.00000000	0.00000000	-18.57194939

Table C-7 Ag_8N_2 coordinates (Hotspot, d = optimized structure)

Ag	0.000000	0.000000	-5.744458
Ag	0.000000	0.000000	-8.606900
Ag	0.000000	0.000000	-3.167973
Ag	0.000000	0.000000	-11.187565
N	0.000000	0.000000	-0.558786
N	0.000000	0.000000	0.558893
Ag	0.000000	0.000000	3.167968
Ag	0.000000	0.000000	5.744454
Ag	0.000000	0.000000	8.606897
Ag	0.000000	0.000000	11.187562

Table C-8 Transitions that correspond to states 1 - 5 in the absorption spectrum of N_2

Excited State	Energy (eV)	Oscillator strength (au)	Transitions	Weight
1	8.6630	0.0000	$7 \rightarrow 9$ ($2\Sigma \rightarrow 2\mathbf{\Pi}_x^*$)	0.70627
2	8.6630	0.0000	$7 \rightarrow 8$ ($2\Sigma \rightarrow 2\mathbf{\Pi}_y^*$)	0.70627
3	8.8569	0.0000	$5 \rightarrow 8$ ($1\mathbf{\Pi}y \rightarrow 2\mathbf{\Pi}_y^*$) $6 \rightarrow 9$ ($1\mathbf{\Pi}x \rightarrow 2\mathbf{\Pi}_x^*$)	-0.49968 0.49968
4	9.5467	0.0000	$5 \rightarrow 8$ ($1\mathbf{\Pi}y \rightarrow 2\mathbf{\Pi}_y^*$) $6 \rightarrow 9$ ($1\mathbf{\Pi}x \rightarrow 2\mathbf{\Pi}_x^*$)	0.49949 0.49949
5	9.5467	0.0000	$5 \rightarrow 9$ ($1\mathbf{\Pi}y \rightarrow 2\mathbf{\Pi}_x^*$) $6 \rightarrow 8$ ($1\mathbf{\Pi}x \rightarrow 2\mathbf{\Pi}_y^*$)	-0.49949 0.49949

Table C-9 Binding energies of the studied systems. Par, ETE, and HS in first column refer to the side-by-side, end-to-end and hotspot orientation respectively.

Systems	E(N_2) (au)	Emonomer(Ag_4) OR Edimer(Ag_8) (au)	Ecomposite (au)	Reaction Energy (au)	Binding Energy (au)	Binding Energy (kJ/mol)
Ag_4N_2	-109.401	-583.010	-692.422	-0.011	0.011	28.7
Ag_8N_2-Par-1.00 nm	-109.401	-1166.020	-1275.432	-0.011	0.011	28.5
Ag_8N_2-Par-0.75 nm	-109.401	-1166.020	-1275.432	-0.011	0.011	28.4
Ag_8N_2-Par-0.50 nm	-109.401	-1166.020	-1275.432	-0.011	0.011	28.1
Ag_8N_2-ETE-1.00 nm	-109.401	-1166.020	-1275.433	-0.011	0.011	28.9
Ag_8N_2-ETE-0.75 nm	-109.401	-1166.020	-1275.433	-0.011	0.011	29.0
Ag_8N_2-ETE-0.50 nm	-109.401	-1166.019	-1275.432	-0.011	0.011	29.3
Ag_8N_2-HS-1.00 nm	-109.401	-1166.020	-1275.422	0.000	0.000	0.0
Ag_8N_2-HS-0.75 nm	-109.401	-1166.020	-1275.422	0.000	0.000	0.8
Ag_8N_2-HS-0.50 nm	-109.401	-1166.020	-1275.425	-0.004	0.004	9.4
Ag_8N_2-HS-opt	-109.401	-1166.020	-1275.436	-0.015	0.015	38.2

Appendix D - Supporting Information for "Real-time Electron Dynamics Study of Plasmon-mediated Photocatalysis on an Icosahedral Al_{13}^{-1} Nanocluster"

Table D-1 Coordinates for the optimized Al_{13}^{-1} cluster

Al	0.000000	0.000000	0.000000
Al	2.627919	-0.000000	-0.000000
Al	1.174943	2.350519	0.000000
Al	1.174943	0.726350	2.235477
Al	1.174943	-1.901610	1.381600
Al	1.174943	-1.901610	-1.381600
Al	1.174943	0.726350	-2.235477
Al	-1.174943	1.901610	-1.381600
Al	-1.174943	1.901610	1.381600
Al	-1.174943	-0.726350	2.235477
Al	-1.174943	-2.350519	0.000000
Al	-1.174943	-0.726350	-2.235477
Al	-2.627919	0.000000	-0.000000

Table D-2 Coordinates for the optimized $[Al_{13}N_2]^{-1}$ cluster

Al	0.488829	-0.000001	0.000001
Al	-0.901510	0.006595	2.230322
Al	0.492878	2.239647	1.374889
Al	-1.743594	1.386401	-0.003893
Al	-1.743578	-1.386428	0.004321
Al	0.492917	-2.231467	1.388097
Al	1.861571	0.006664	2.240452
Al	2.727053	1.376380	-0.004316
Al	0.492617	2.231469	-1.388092
Al	-0.901939	-0.006614	-2.230056
Al	0.492643	-2.239651	-1.374882
Al	2.727074	-1.376347	0.003877
Al	1.861131	-0.006645	-2.240722
N	-5.892812	0.549900	-0.000276
N	-5.892786	-0.549902	0.000277

Table D-3 Coordinates for the optimized $[Al_{13}N_2]^{-1}$ cluster with origin at center of mass

Al	0.47247928	-0.00000114	0.00000111
Al	-0.91785972	0.00659486	2.23032211
Al	0.47652828	2.23964686	1.37488911
Al	-1.75994372	1.38640086	-0.00389289
Al	-1.75992772	-1.38642814	0.00432111
Al	0.47656728	-2.23146714	1.38809711
Al	1.84522128	0.00666386	2.24045211
Al	2.71070328	1.37637986	-0.00431589
Al	0.47626728	2.23146886	-1.38809189
Al	-0.91828872	-0.00661414	-2.23005589
Al	0.47629328	-2.23965114	-1.37488189
Al	2.71072428	-1.37634714	0.00387711
Al	1.84478128	-0.00664514	-2.24072189
N	-5.90916172	0.54989986	-0.00027589
N	-5.90913572	-0.54990214	0.00027711

Table D-4 Transitions for the $[Al_{13}N_2]^{-1}$ system with the highest oscillator strengths for the 7 eV plasmon peak from the LR-TDDFT calculation

Excited States	Energy (eV)	Oscillator Strength	Weight	Transitions	Orbitals
218	6.9429	1.2839	0.23646	78→96	1D→1G
			0.14799	80→94	1D→1G
			-0.16659	81→95	1D→1G
			0.20255	87→115	1F→2F
			-0.10132	88→114	1F→2F
			-0.10088	88→118	1F→2F
			0.30276	89→113	1F→2F
			0.10196	89→116	1F→2F
			0.12760	90→122	1F→1H
			-0.18630	92→111	1F→3P
			-0.11116	92→117	1F→2F
220	6.9483	1.0050	0.20787	77→94	1D→1G
			-0.17846	78→97	1D→1G
			-0.15903	84→109	2P→2π*
			-0.10356	86→112	1F→3P
			-0.15355	86→114	1F→2F
			0.37828	87→113	1F→2F
			0.11446	90→120	1F→1H
			0.10714	91→112	1F→3P
			-0.13142	92→110	1F→3P
221	6.9487	4.7267	0.10826	77 → 94	1D→1G
			-0.11315	83 →104	2P→2D
			0.13206	84 →102	2P→2D
			0.29849	84 →109	2P→2π*

			0.10118	85 →103	2P→2D
			0.12902	86 →101	1F→1G
			-0.12504	86 →104	1F→2D
			0.12648	87 →100	1F→1G
			0.16748	87 →113	1F→2F
			0.12595	88 →99	1F→1G
			0.14374	88 →102	1F→2D
			-0.12653	89 →98	1F→1G
			0.12356	89 →105	1F→2D
			-0.11294	90 →109	1F→2π*
			0.12354	91 →95	1F→1G
			-0.14139	92 →94	1F→1G
222	6.9565	4.1771	-0.10948	81 →95	1D→1G
			0.13244	83 →102	2P→2D
			0.34741	83 →109	2P→2π*
			0.11350	86 →99	1F→1G
			0.14833	86 →109	1F→2π*
			-0.11593	87 →98	1F→1G
			-0.13466	87 →105	1F→2D
			-0.12069	88 →101	1F→1G
			-0.13534	88 →104	1F→2D
			-0.13809	88 →114	1F→2F
			-0.11819	89 →100	1F→1G
			-0.11703	89 →103	1F→2D
			0.10009	90 →97	1F→1G
			-0.13411	91 →96	1F→1G
223	6.9624	2.3853	0.55974	84 →109	2P→2π*
			-0.10243	88 →102	1F→2D
			-0.12256	90 →109	1F→2π*
224	6.9689	1.9399	0.56900	83 →109	2P→2π*
			0.11488	86 →109	1F→2π*
228	7.0138	1.3099	0.13661	77 →95	1D→1G
			-0.19635	79 →97	1D→1G
			0.37841	83 →113	2P→2F
			0.23795	85 →114	2P→2F
			0.12954	88 →111	1F→3P
			0.14307	88 →115	1F→3P
			-0.12293	92 →112	1F→3P
230	7.0275	4.3596	0.11735	78 →94	1D→1G
			0.18668	79 →97	1D→1G
			-0.15895	81 →93	1D→1G
			0.10796	85 →107	2P→3S
			-0.12519	85 →114	2P→2F
			0.12021	86 →100	1F→1G
			-0.13231	86 →103	1F→2D
			-0.13242	86 →113	1F→2F

			-0.11591	87 →101	1F→1G
			0.12633	87 →106	1F→2D
			0.11222	88 →98	1F→1G
			0.10072	88 →108	1F→2π*
			-0.11439	88 →115	1F→2F
			0.11691	89 →99	1F→1G
			-0.10293	89 →102	1F→2D
			-0.13012	90 →93	1F→1G
			-0.10303	92 →97	1F→1G

Table D-5 Transitions for the $[Al_{13}N_2]^{-1}$ system with the highest oscillator strengths for the 6 eV peak from the LR-TDDFT calculation

Excited States	Transition electric dipole moment (au)			Energy (eV)	Oscillator Strength	Weight	Transitions	Orbitals
	X	Y	Z					
153	-0.0009	0.2775	-0.0001	5.9177	0.0112	0.18933	77 → 93	1D→1G
						-0.31868	82 →93	2S→1G
						0.13338	84 →112	2P→3P
						-0.14818	85 →108	2P→2π*
						0.37852	87 →108	1F→2π*
						0.19265	87 →111	1F→3P
						0.15114	87 →115	1F→2F
						0.25256	92 →108	1F→2π*
154	-0.5634	-0.0005	-0.0000	5.9190	0.0460	-0.40961	82 →97	2S→1G
						0.42582	90 →108	1F→2π*
						0.21123	90 →111	1F→3P
165	-0.5148	-0.0000	-0.0000	6.1502	0.0399	0.16778	82 →97	2S→1G
						0.40635	86 →110	1F→3P
						0.15696	88 →108	1F→2π*
						0.24619	88 →111	1F→3P
						0.24223	90 →108	1F→2π*
						-0.22195	90 →111	1F→3P
						0.17228	92 →112	1F→3P
169	0.7957	-0.0000	-0.0000	6.2042	0.0962	-0.10890	82 →95	2S→1G
						-0.10650	84 →108	2P→2π*
						0.12224	86 →110	1F→3P
						-0.21662	87 →112	1F→3P
						0.13517	88 →108	1F→2π*
						0.36077	88 →111	1F→3P
						-0.27973	90 →108	1F→2π*
						0.18560	90 →111	1F→3P
						-0.28467	92 →112	1F→3P
175	-0.0000	-0.4919	0.0003	6.3686	0.0377	0.14938	77 →93	1D→1G
						0.18436	82 →93	2S→1G
						0.43086	85 →108	2P→2π*

						0.18924 0.14886 0.34927	87 →115 92 →108 92 →111	1F→2F 1F→2π* 1F→3P

Table D-6 Transitions for the $[Al_{13}]^{-1}$ system with the highest oscillator strengths for the 7 eV plasmon peak from the LR-TDDFT calculation

Excited States	Energy (eV)	Oscillator Strength	Weight	Transitions	Orbitals
203	6.9547	8.2360	0.11475	75→103	2P→3P
			-0.13265	76→98	2P→1G
			-0.13324	77→99	2P→1G
			0.10922	78→86	2P→2D
			-0.15428	78→97	2P→1G
			0.16565	79→94	1F→1G
			-0.10405	79→96	1F→1G
			0.16569	80→93	1F→1G
			-0.10057	80→95	1F→1G
			-0.16601	81→91	1F→1G
			0.20463	81→99	1F→1G
			-0.16604	82→92	1F→1G
			0.20424	82→98	1F→1G
			-0.11316	83→88	1F→2D
			-0.11867	83→93	1F→1G
			0.11349	84→87	1F→2D
			-0.11998	84→94	1F→1G
			-0.19316	85→86	1F→2D
			-0.11818	85→97	1F→1G
			0.13818	85→121	1F→3D
204	6.9550	8.2369	0.11468	75→102	2S→3P
			0.13437	76→96	2P→1G
			0.13500	77→95	2P→1G
			-0.13415	78→99	2P→1G
			0.16659	79→92	1F→1G
			0.15819	79→95	1F→1G
			0.16659	80→91	1F→1G
			0.15463	80→96	1F→1G
			0.16627	81→93	1F→1G
			0.17562	81→97	1F→1G
			0.16627	82→94	1F→1G
			0.11123	83→87	1F→2D
			0.11680	83→89	1F→2D
			-0.10745	84→88	1F→2D
			0.11820	84→90	1F→2D
			0.11682	85→89	1F→2D
			-0.11762	85→91	1F→1G

205	6.9550	8.2369	0.11468	75→101	2S→3P
			0.10850	76→88	2P→2D
			-0.13308	76→95	2P→1G
			0.13445	77→96	2P→1G
			-0.13358	78→98	2P→1G
			0.16655	79→91	1F→1G
			-0.15006	79→96	1F→1G
			0.10460	79→99	1F→1G
			-0.16657	80→92	1F→1G
			0.14707	80→95	1F→1G
			-0.11100	80→98	1F→1G
			0.16622	81→94	1F→1G
			-0.16625	82→93	1F→1G
			0.17659	82→97	1F→1G
			-0.11417	83→88	1F→2D
			-0.11330	83→90	1F→2D
			-0.12019	84→87	1F→2D
			0.11088	84→89	1F→2D
			0.11308	85→ 90	1F→2D
			-0.11955	85→92	1F→1G

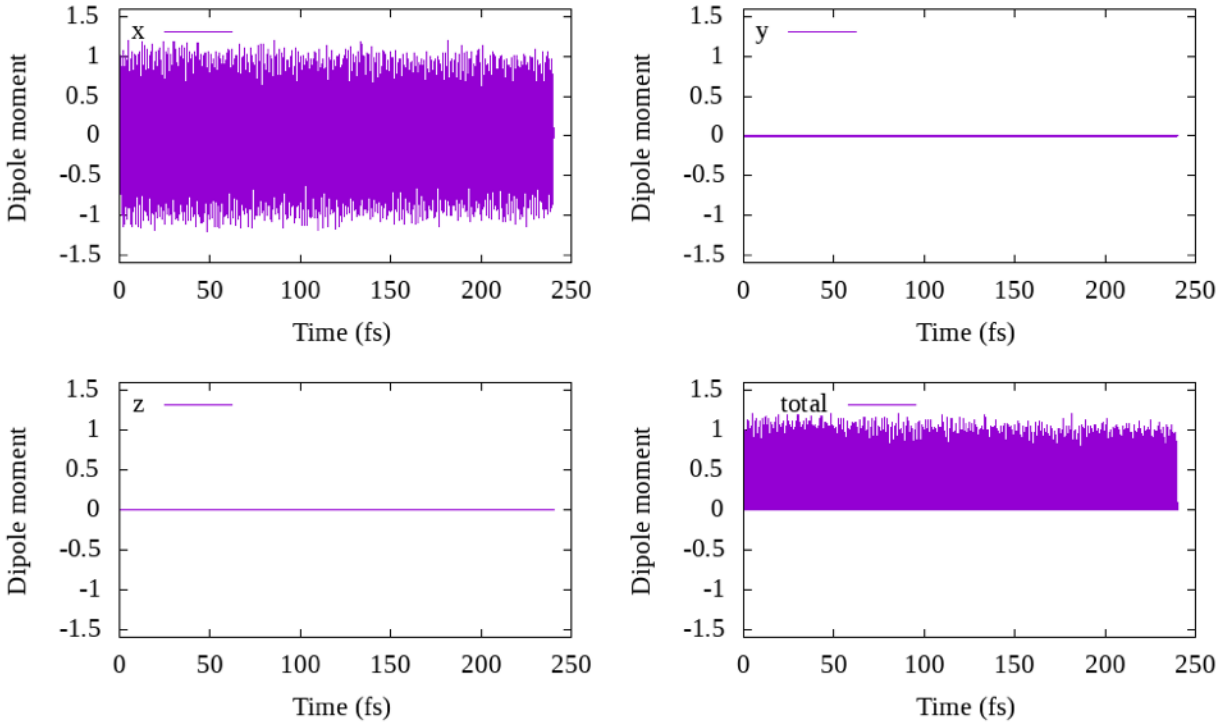

Figure D-1 Dipole moment (Debye) induced in the Al_{13}^{-1} system on applying a 0.001 au step field along the x-direction.

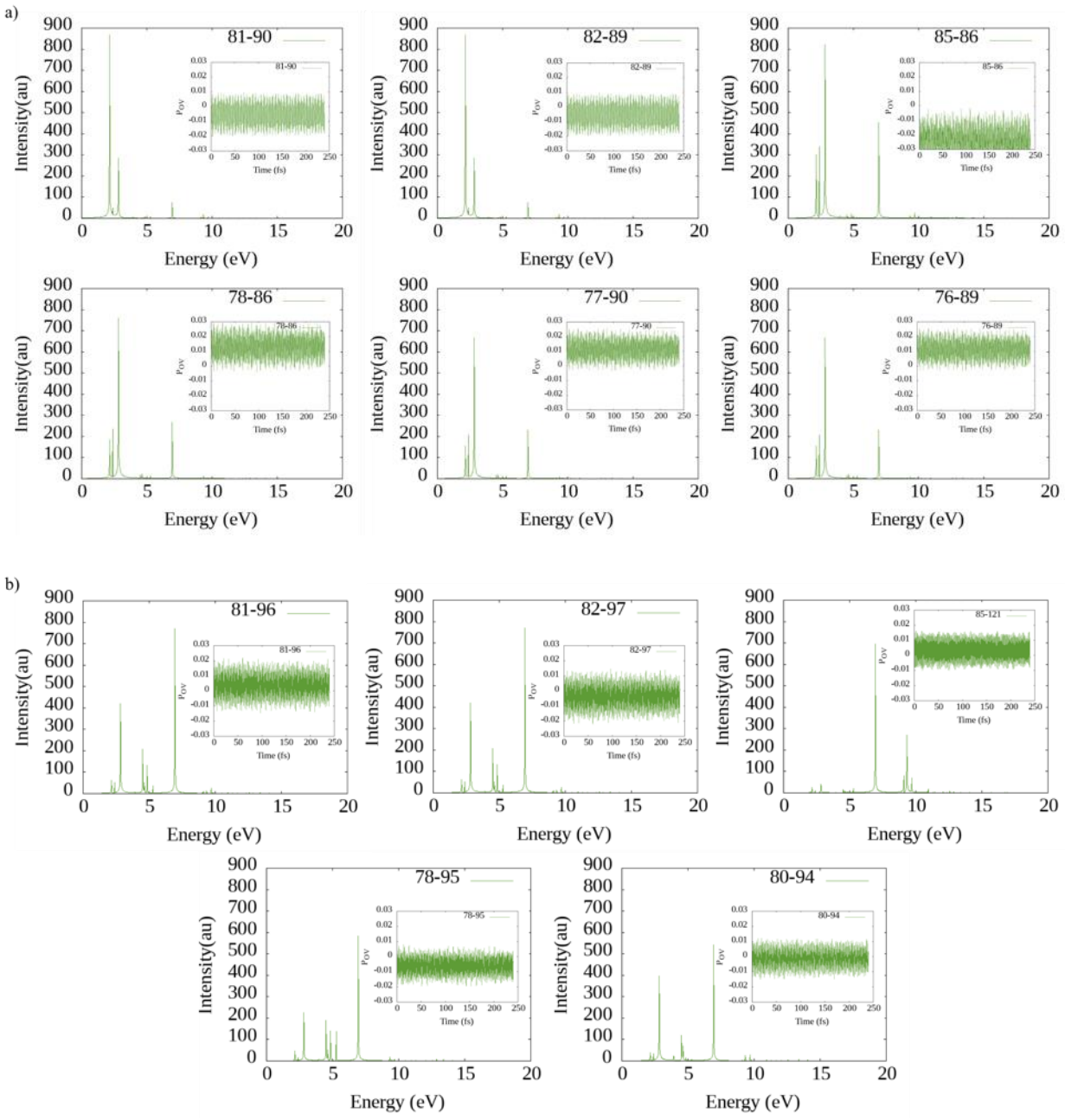

Figure D-2 (a) FT peaks and their corresponding P_{OV} elements for the transitions that correspond to the peaks at 2 - 2.5 eV. (b) FT peaks and their corresponding P_{OV} for the transitions that corresponds to the peak at 7 eV. These are obtained from the application of a step electric field of 0.001 au along the z-direction in the Al_{13}^{-1} system.

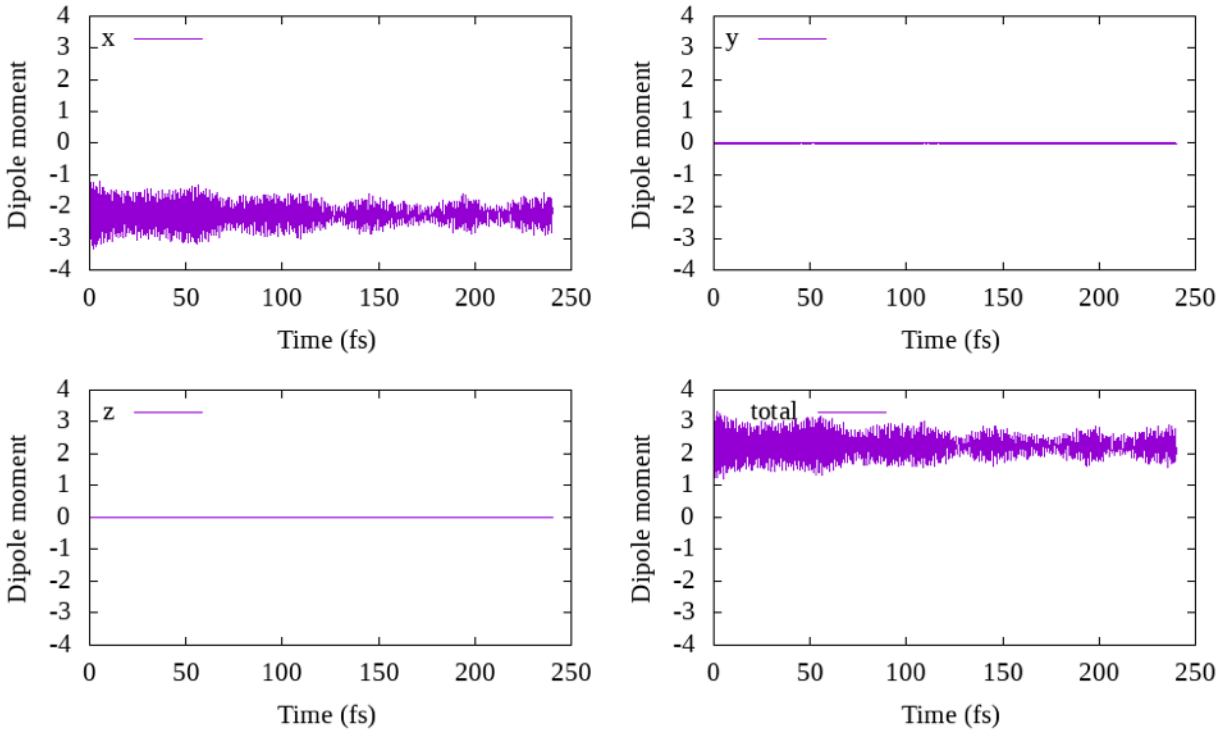

Figure D-3 Dipole moment (Debye) induced in $[Al_{13}N_2]^{-1}$ on applying a 0.001 au step field along the x-direction.

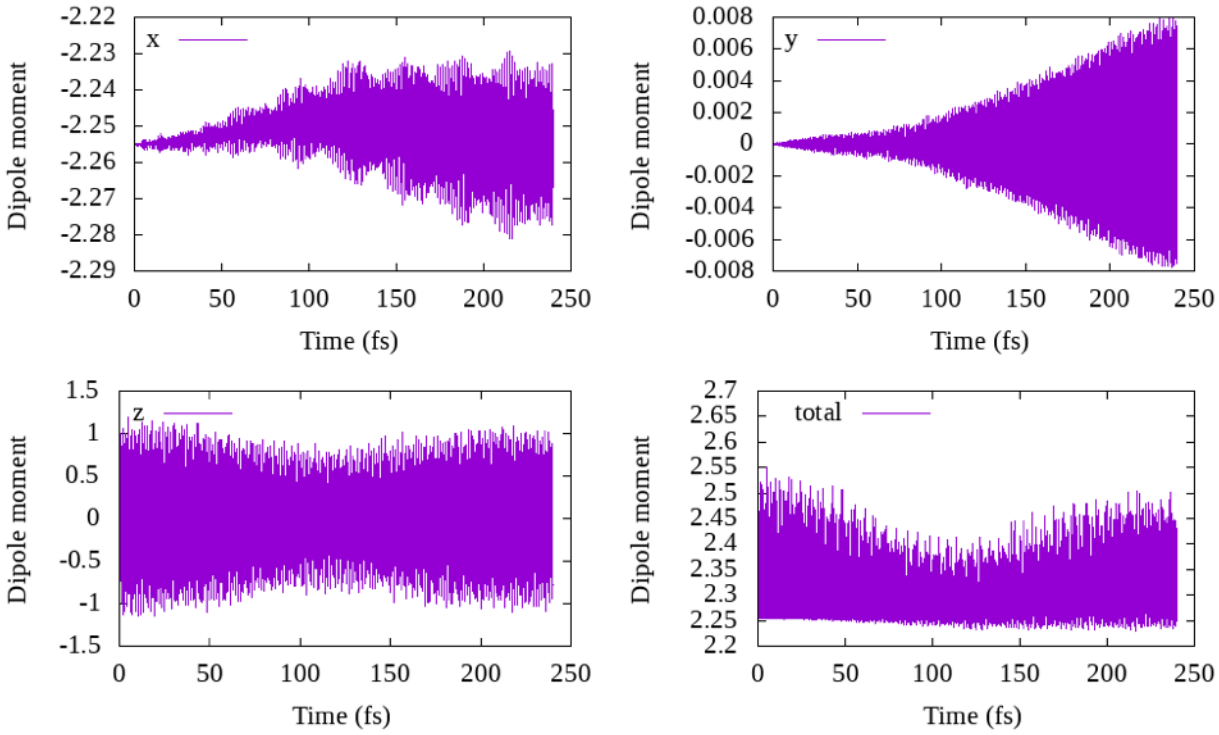

Figure D-4 Dipole moment (Debye) induced from the application of 0.001 au step laser field along the z-direction in $[Al_{13}N_2]^{-1}$.

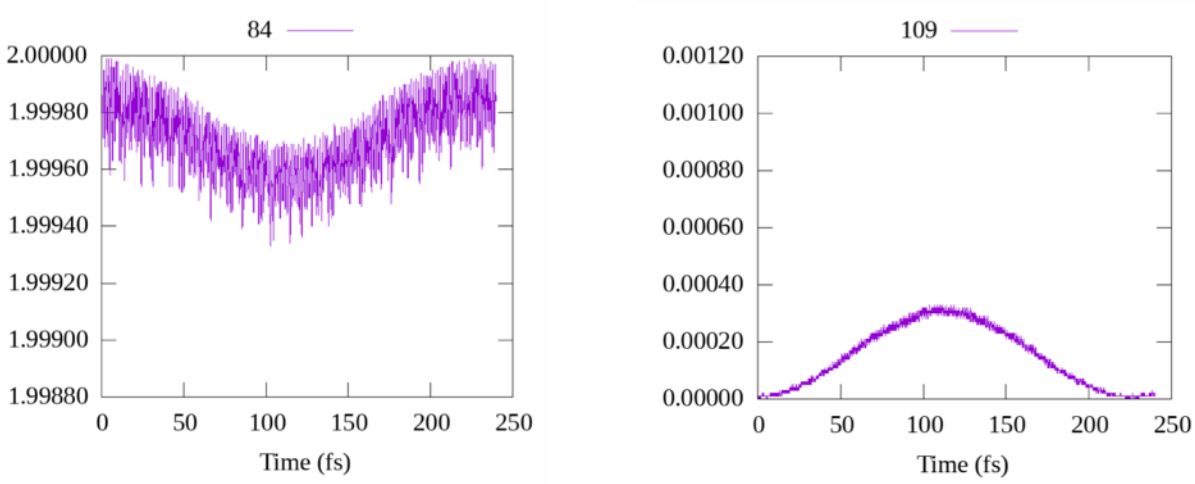

Figure D-5 Orbital occupation numbers in orbital 84 and orbital 109 after the application of 0.001 au step field along the z-direction in $[Al_{13}N_2]^{-1}$.

a)

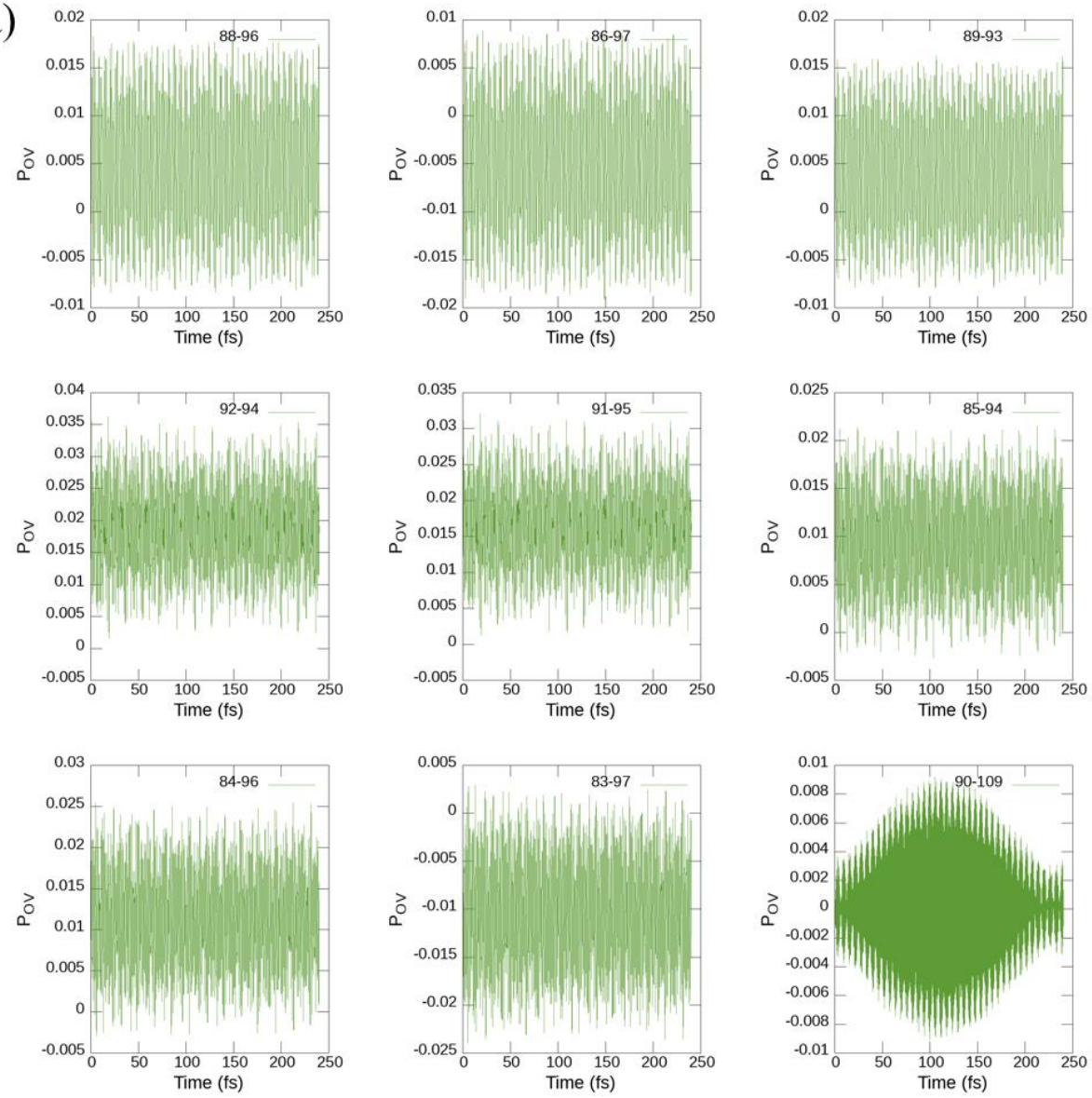

b)

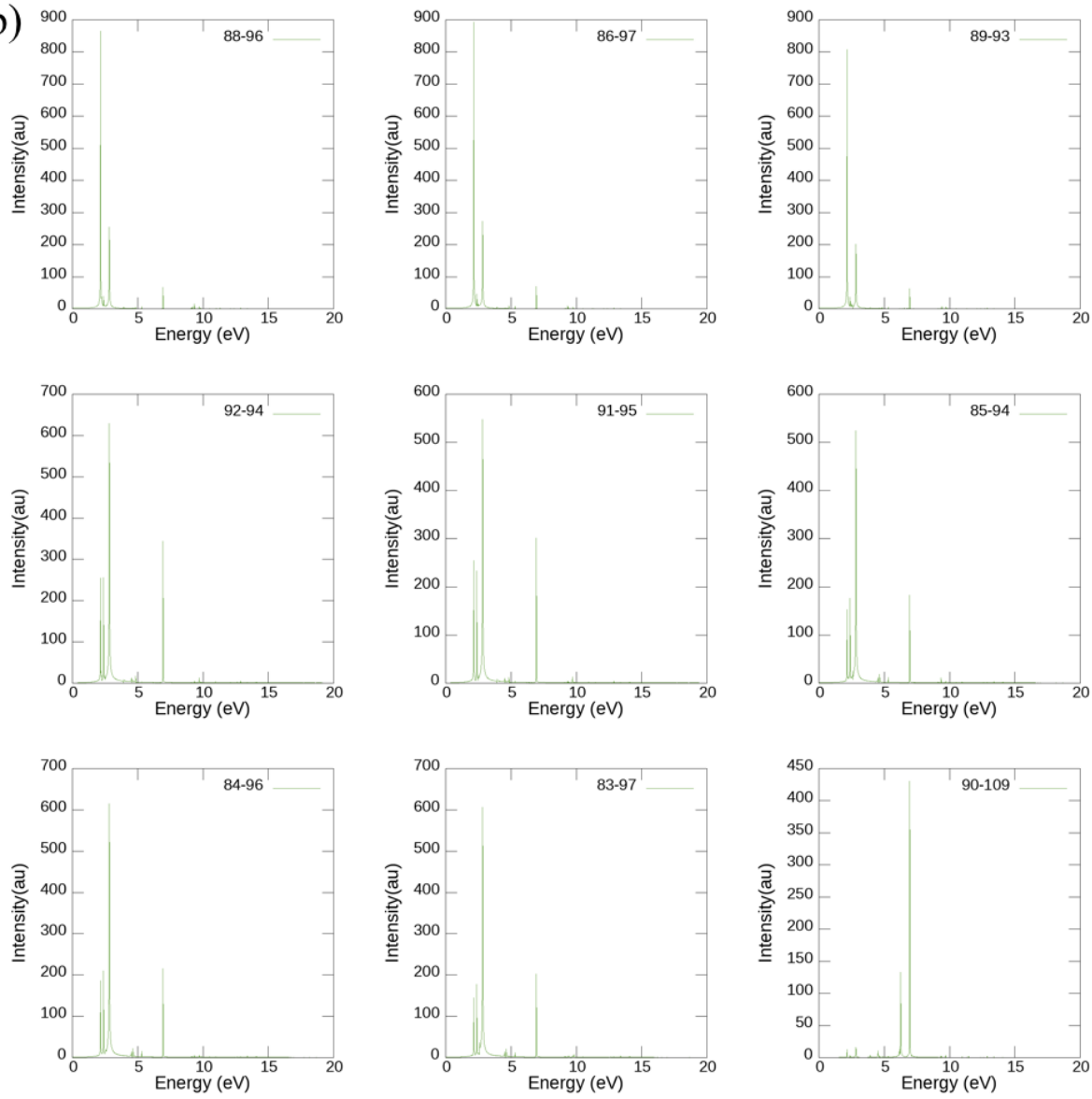
88-96
86-97
89-93
92-94
91-95
85-94
84-96
83-97
90-109
Intensity(au)
Energy (eV)

c)

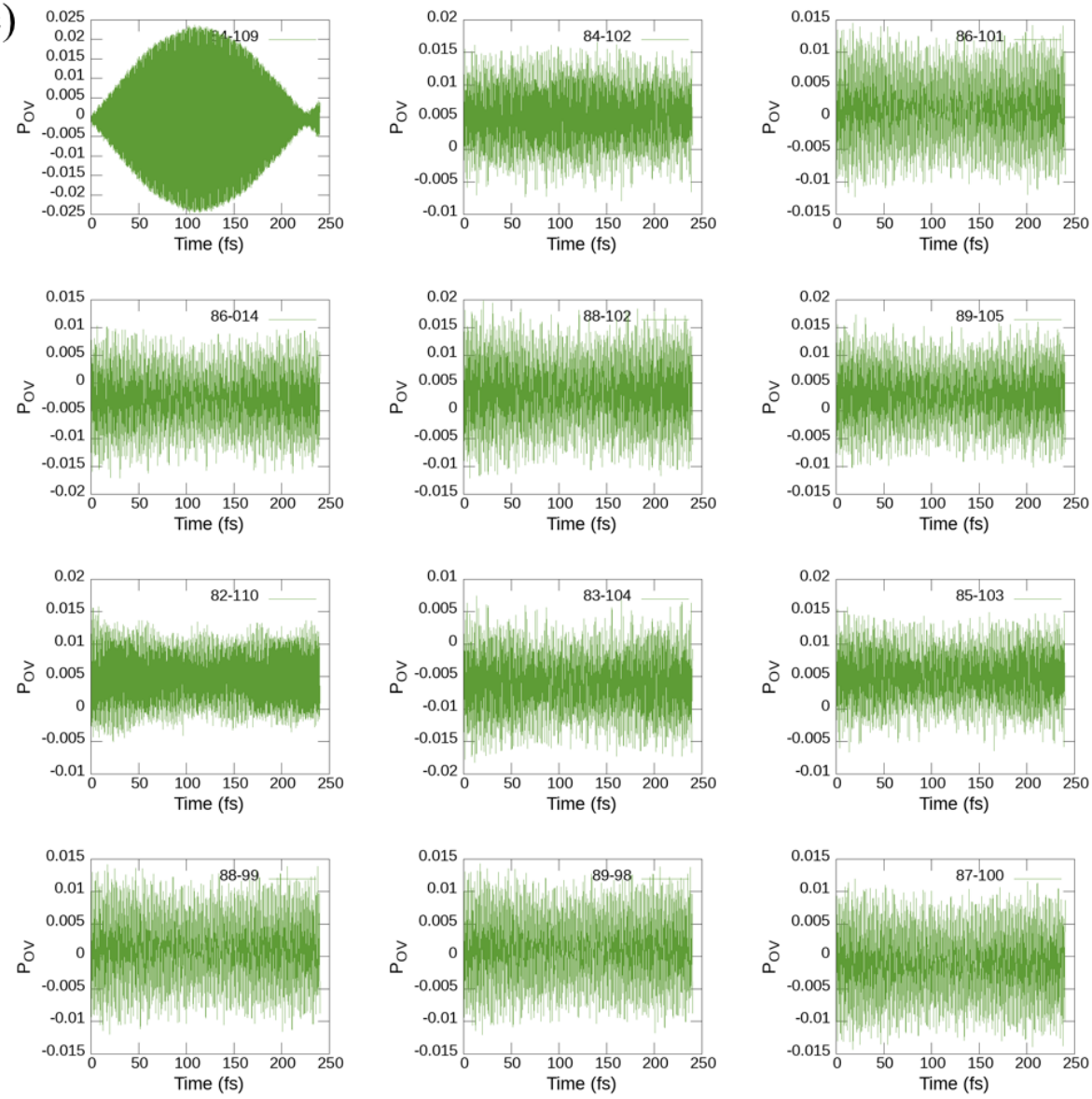
84-109
84-102
86-101
86-014
88-102
89-105
82-110
83-104
85-103
88-99
89-98
87-100
POV
Time (fs)

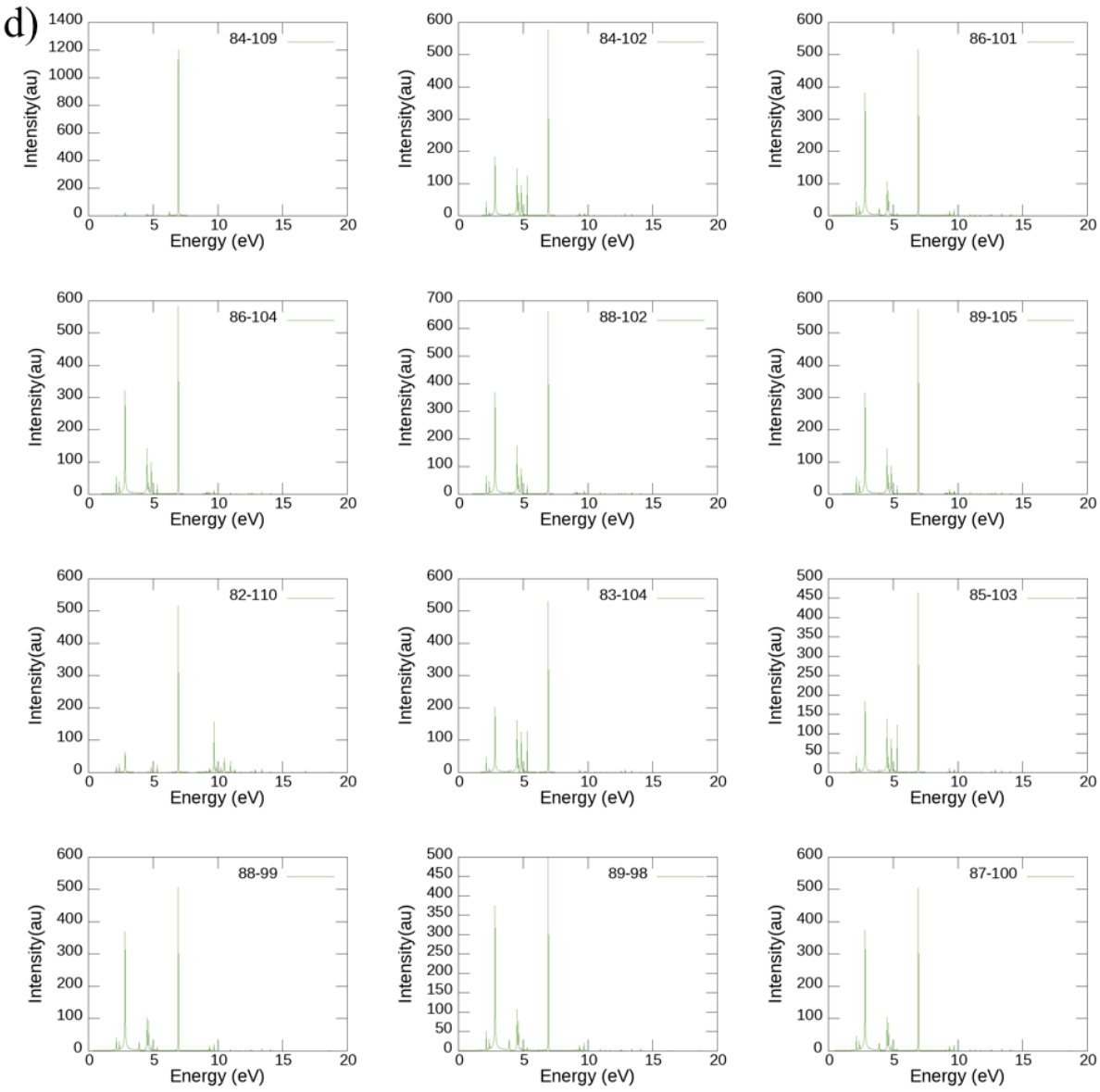

Figure D-6 P_{OV} for different transitions that contribute to the major peaks at 2-2.5 eV and 6 eV (a), and the FT peaks for the corresponding transitions (b). Only the 90 → 109 transition contributes to the FT peak at 6 eV. P_{OV} for different transitions that contribute to the major peaks at 7 eV (c) and the FT peaks for the corresponding transitions (d). These are obtained from the application of a 0.001 au step field along the z-direction in the $[Al_{13}N_2]^{-1}$ system.

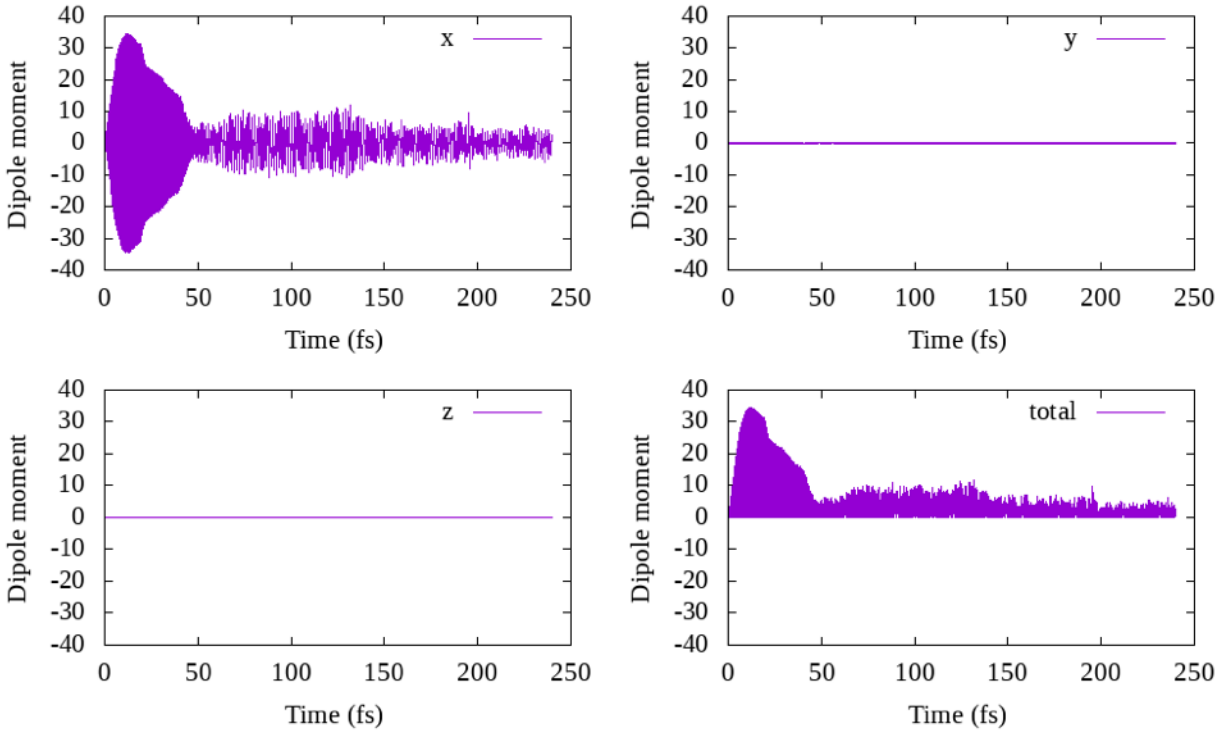

Figure D-7 Variation of different components of the dipole moment (Debye) with time after the application of a 0.001 au trapezoid field with an energy of 7 eV along the x-direction to the Al_{13}^{-1} system.

a)

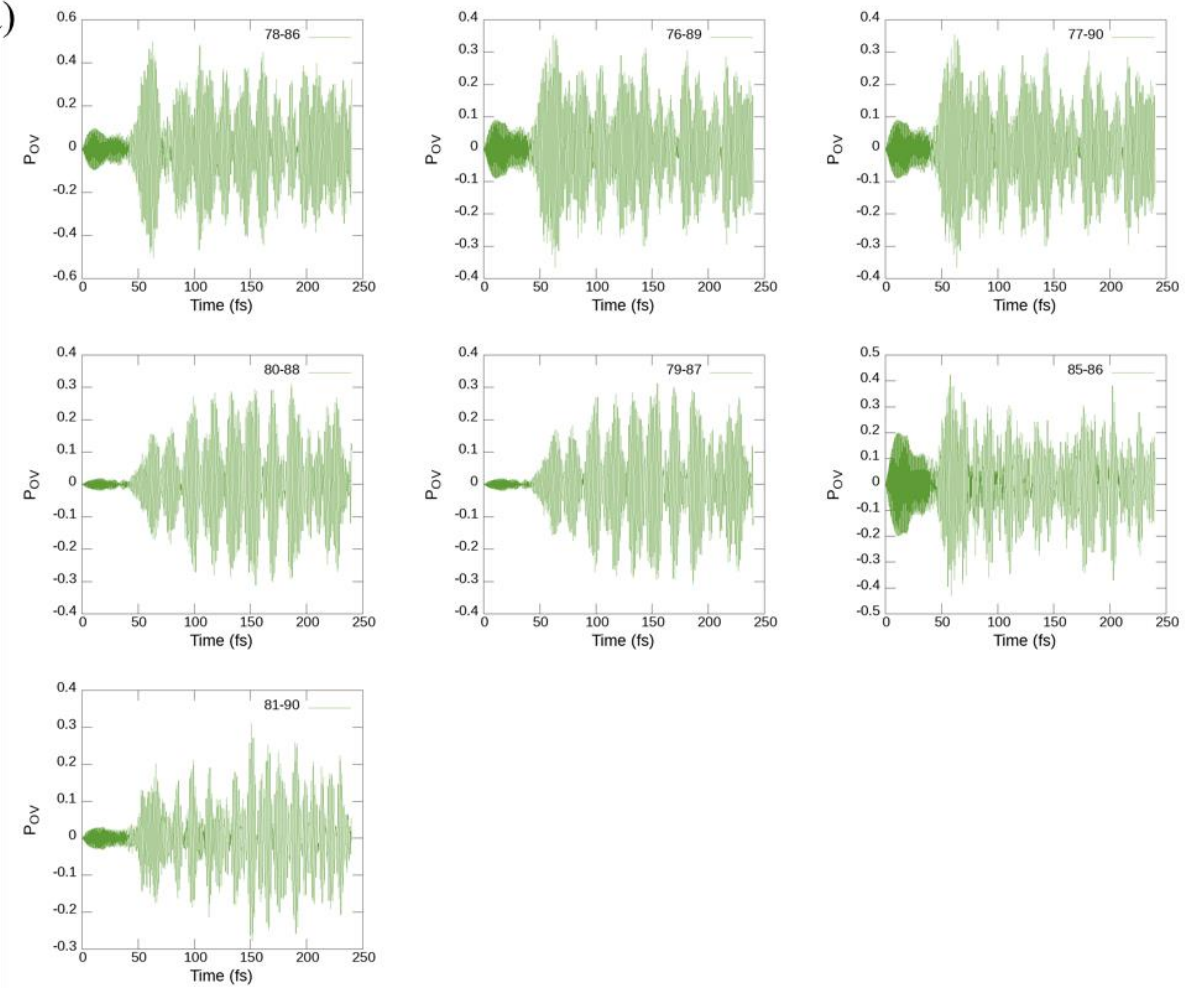

b)

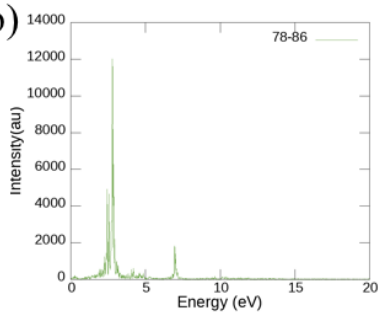
78-86
Intensity(au)
Energy (eV)

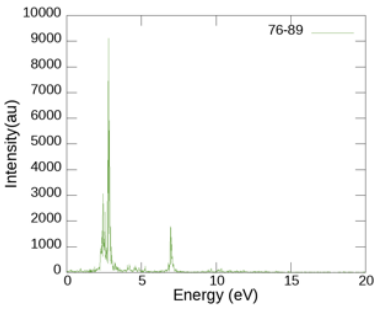
76-89
Intensity(au)
Energy (eV)

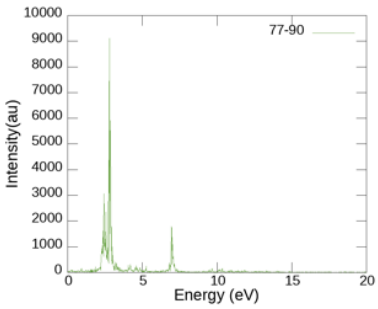
77-90
Intensity(au)
Energy (eV)

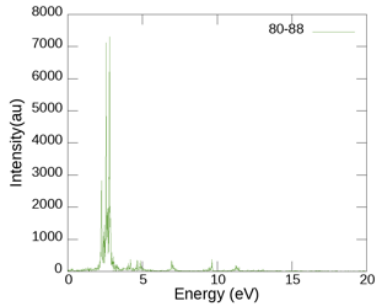
80-88
Intensity(au)
Energy (eV)

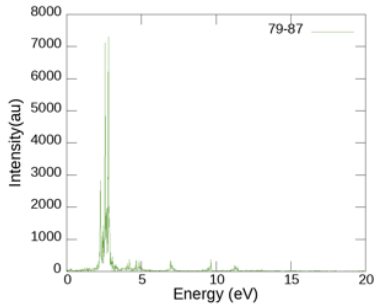
79-87
Intensity(au)
Energy (eV)

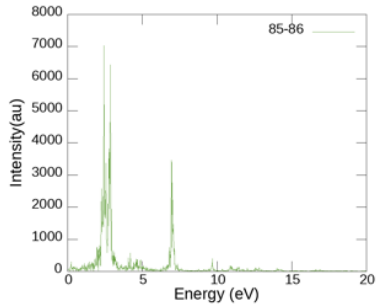
85-86
Intensity(au)
Energy (eV)

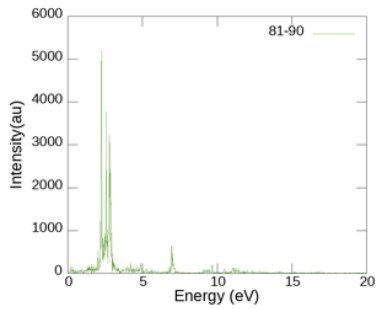
81-90
Intensity(au)
Energy (eV)

c)

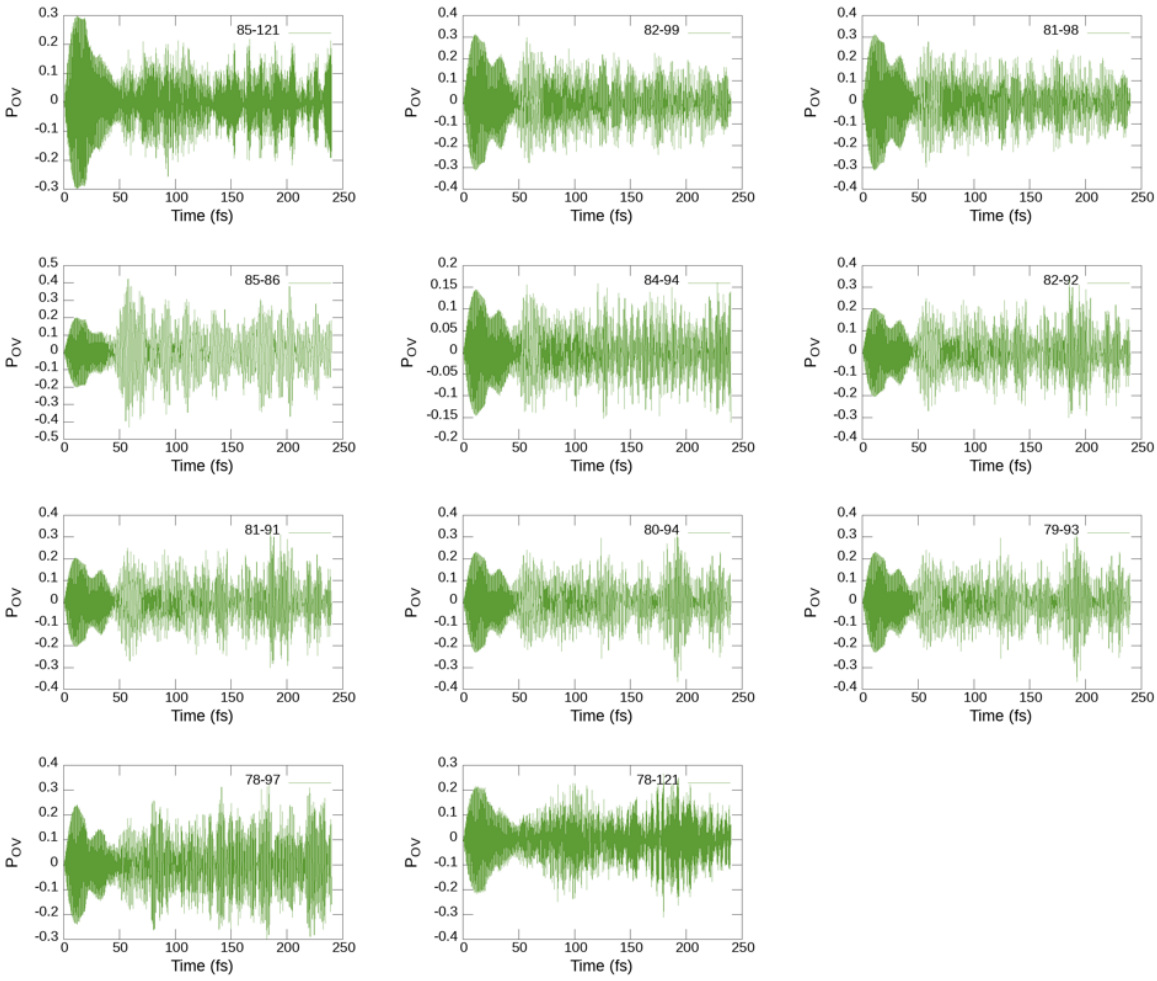
85-121
82-99
81-98
85-86
84-94
82-92
81-91
80-94
79-93
78-97
78-121
POV
Time (fs)

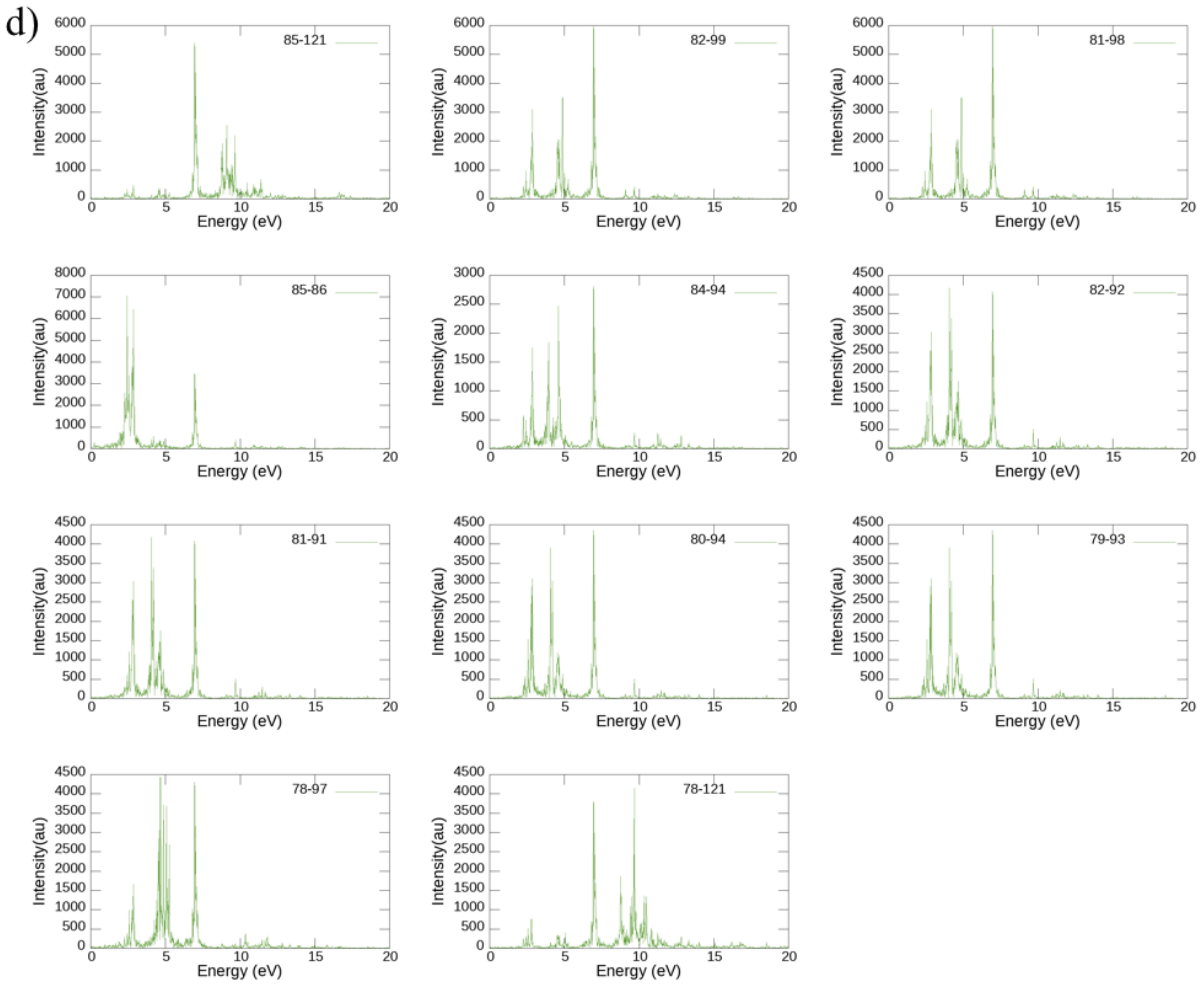

Figure D-8 P_{OV} for different transitions that contribute the major peaks at 2-3 eV (a), and the FT peaks for the corresponding transitions (b). P_{OV} for different transitions that contribute the major peaks at 7 eV (c) and the FT peaks for the corresponding transitions (d). These are obtained from the application of a 0.001 au trapezoid laser field of frequency corresponding to 7 eV along the z-direction in the $[Al_{13}]^{-1}$ system.

Table D-7 Dynamic and static polarizabilities of the $[Al_{13}N_2]^{-1}$ with C_{2v} symmetry.

Frequency corresponding to 0 eV (static polarizability):

558.54	0.0000	0.0000
0.0000	560.89	0.0000
0.0000	0.0000	571.05

Frequency corresponding to 7 eV or 0.257 au (dynamic polarizability):

-31503.7	0.00000	0.00000
0.00000	-11894.6	0.00000
0.00000	0.00000	11444.5

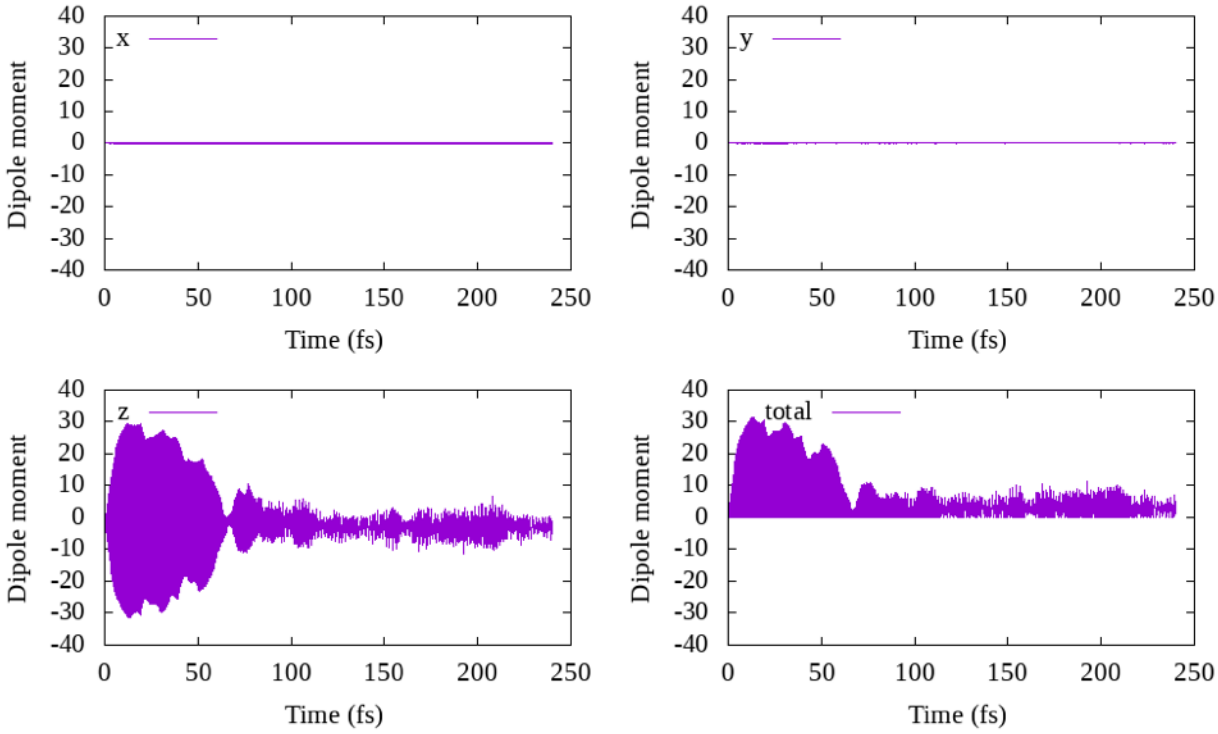

Figure D-9 Variation of different components of the dipole moment (Debye) from the application of a 0.001 au trapezoid electric field along z-direction in $[Al_{13}N_2]^{-1}$ with C_{2v} symmetry.

a)

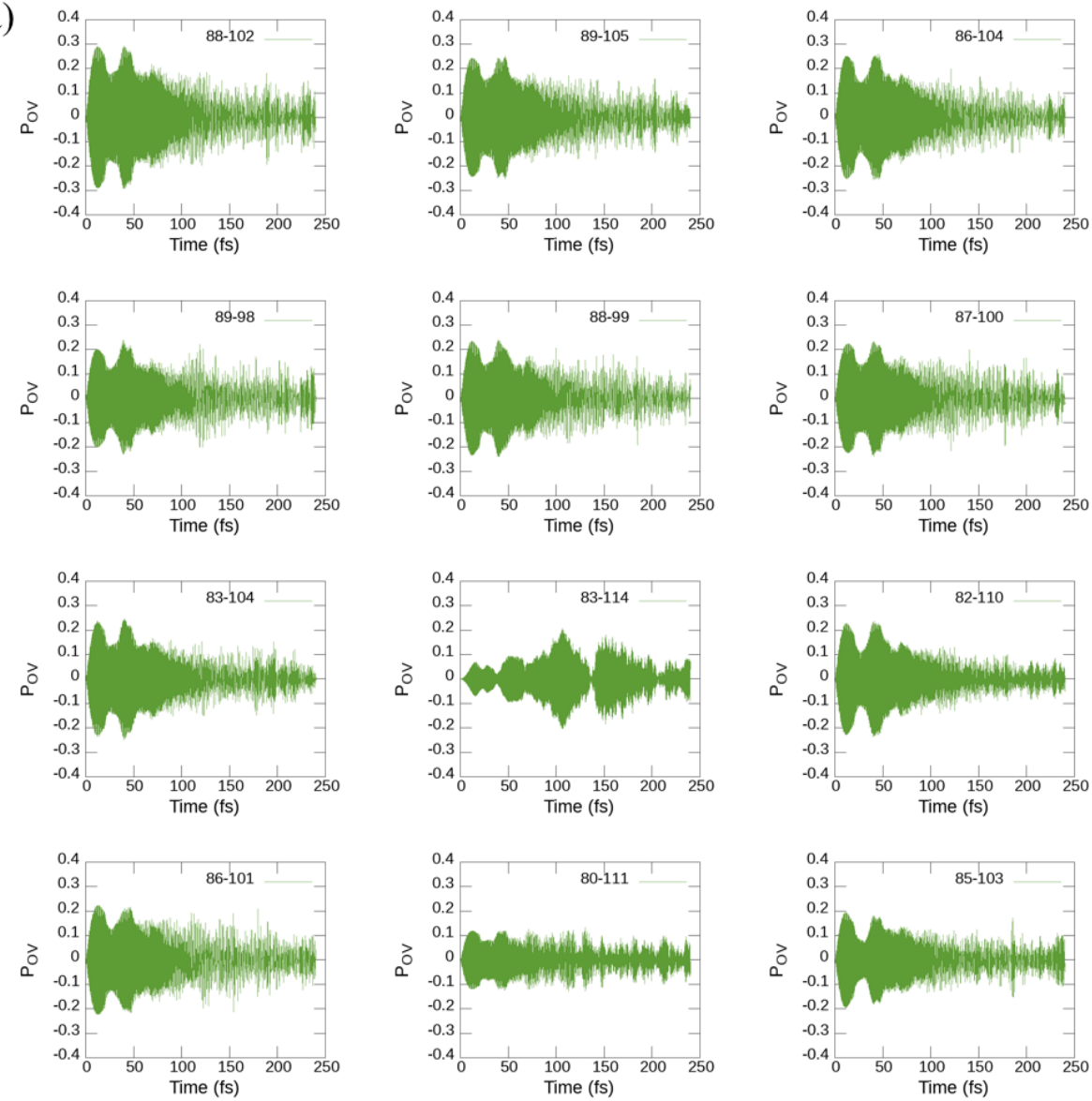
88-102
89-105
86-104
89-98
88-99
87-100
83-104
83-114
82-110
86-101
80-111
85-103
P_OV
Time (fs)

b)

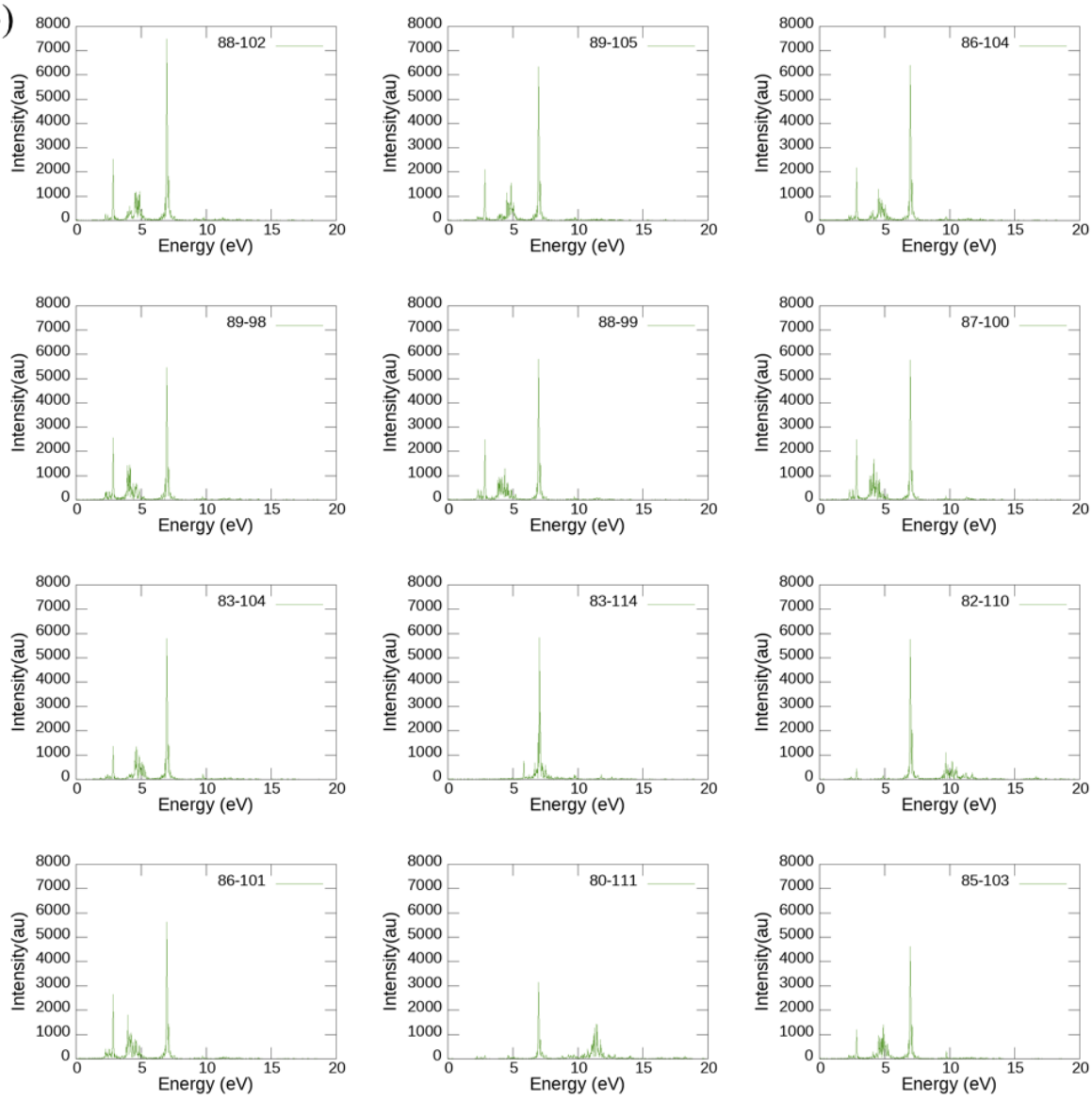
88-102
89-105
86-104
89-98
88-99
87-100
83-104
83-114
82-110
86-101
80-111
85-103
Intensity(au)
Energy (eV)
0
1000
2000
3000
4000
5000
6000
7000
8000
0
5
10
15
20

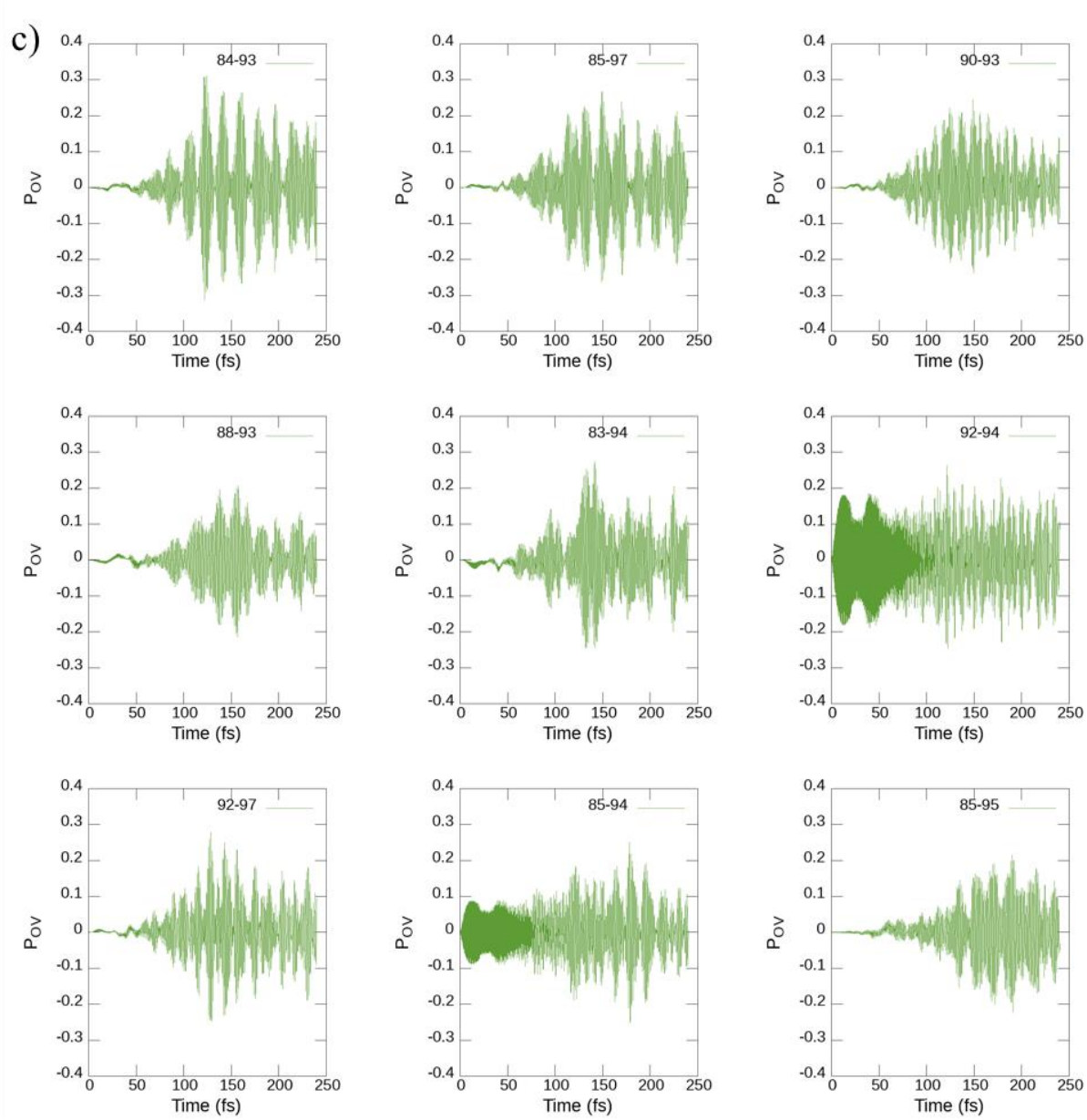
c)
84-93
85-97
90-93
88-93
83-94
92-94
92-97
85-94
85-95
POV
Time (fs)

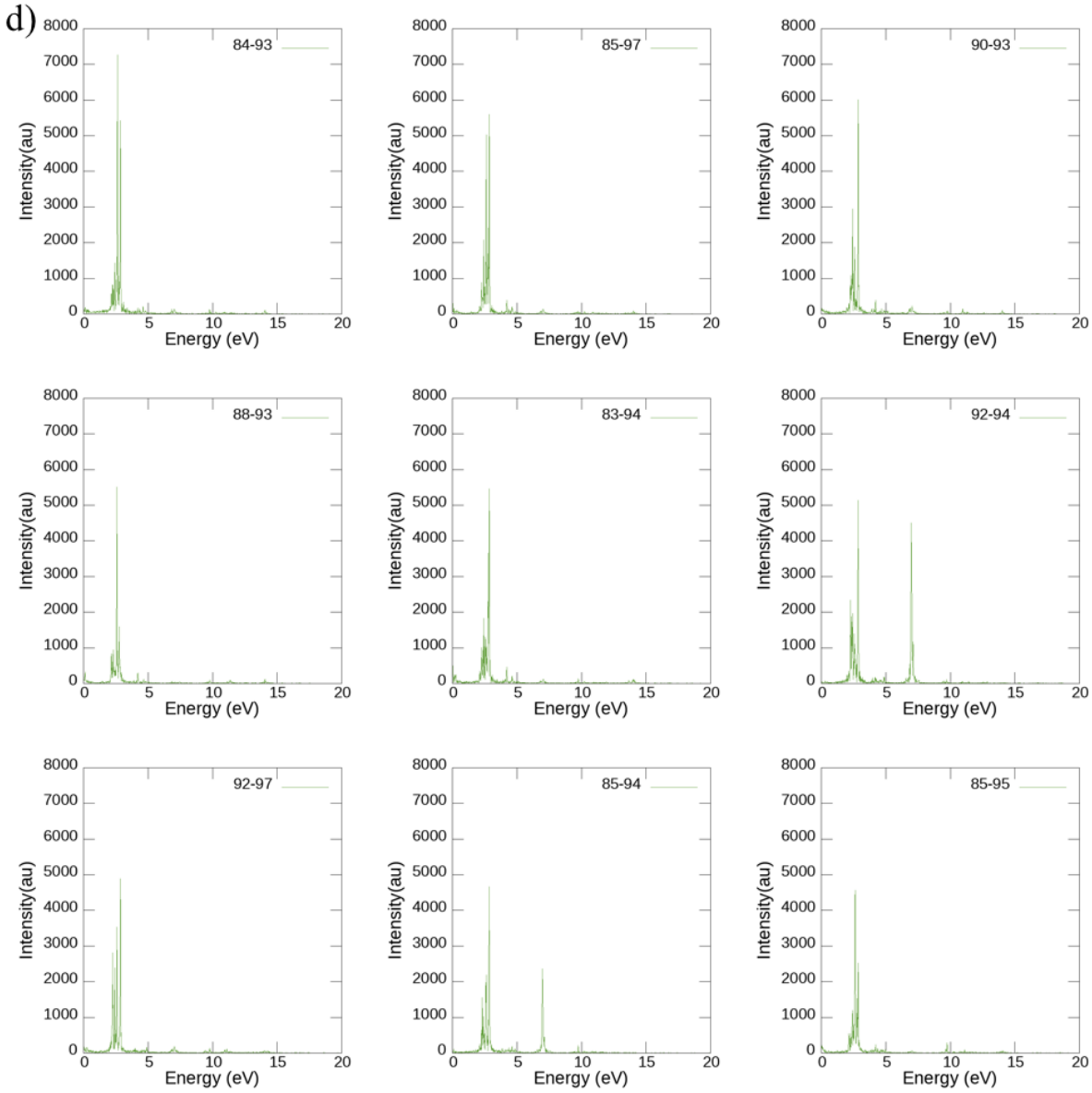

Figure D-10 P_{OV} for different transitions that contribute the major peaks at 7 eV (a), and the FT peaks for the corresponding transitions (b). P_{OV} for different transitions that contribute the major peaks at 2 eV - 3 eV (c) and the FT peaks for the corresponding transitions (d). These are obtained from the application of a 0.001 au trapezoid field with a frequency corresponding to 7 eV along the z-direction in the $[Al_{13}N_2]^{-1}$ system.

a)

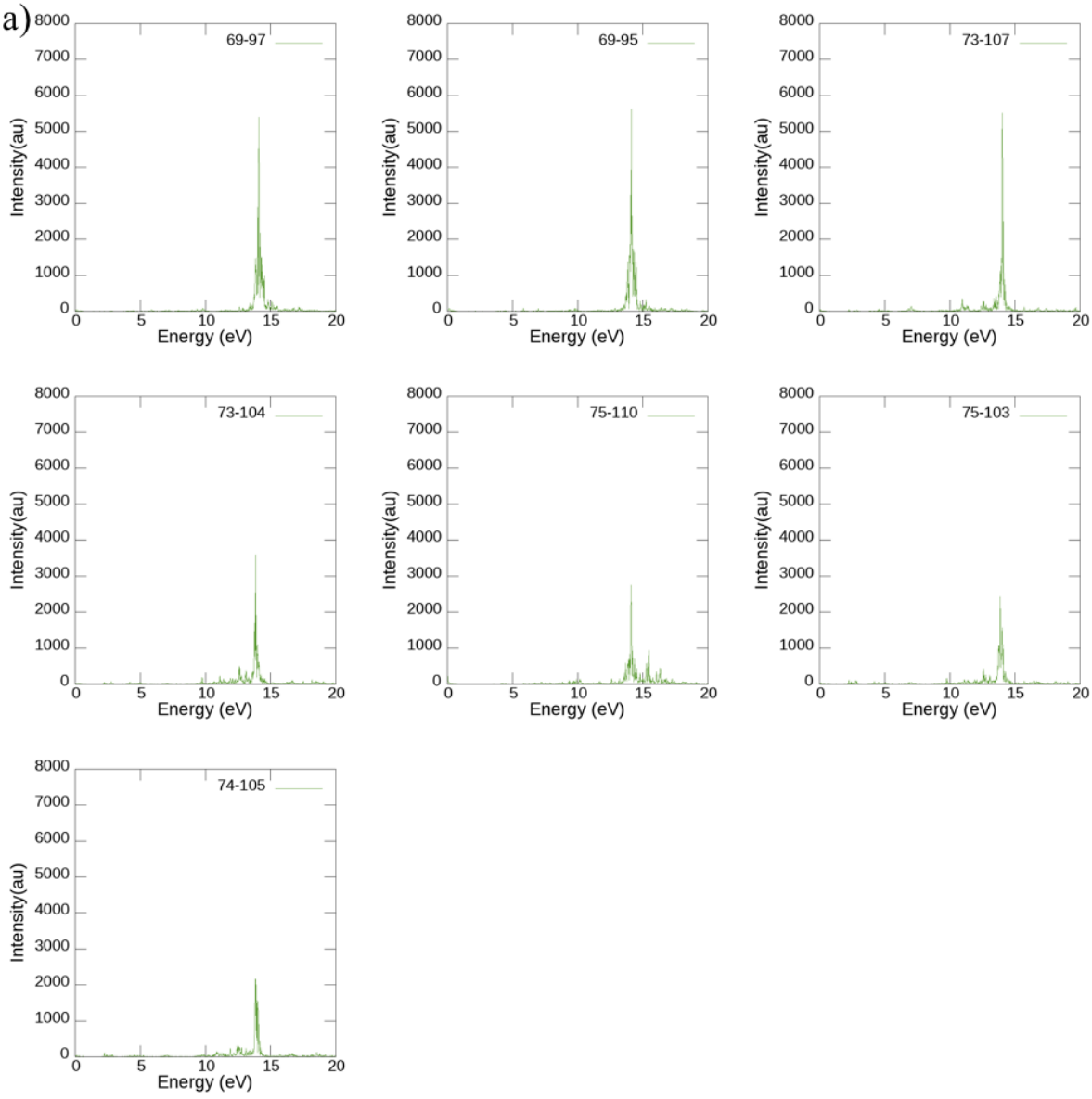
69-97
69-95
73-107
73-104
75-110
75-103
74-105
Intensity(au)
Energy (eV)
0
1000
2000
3000
4000
5000
6000
7000
8000
0
5
10
15
20

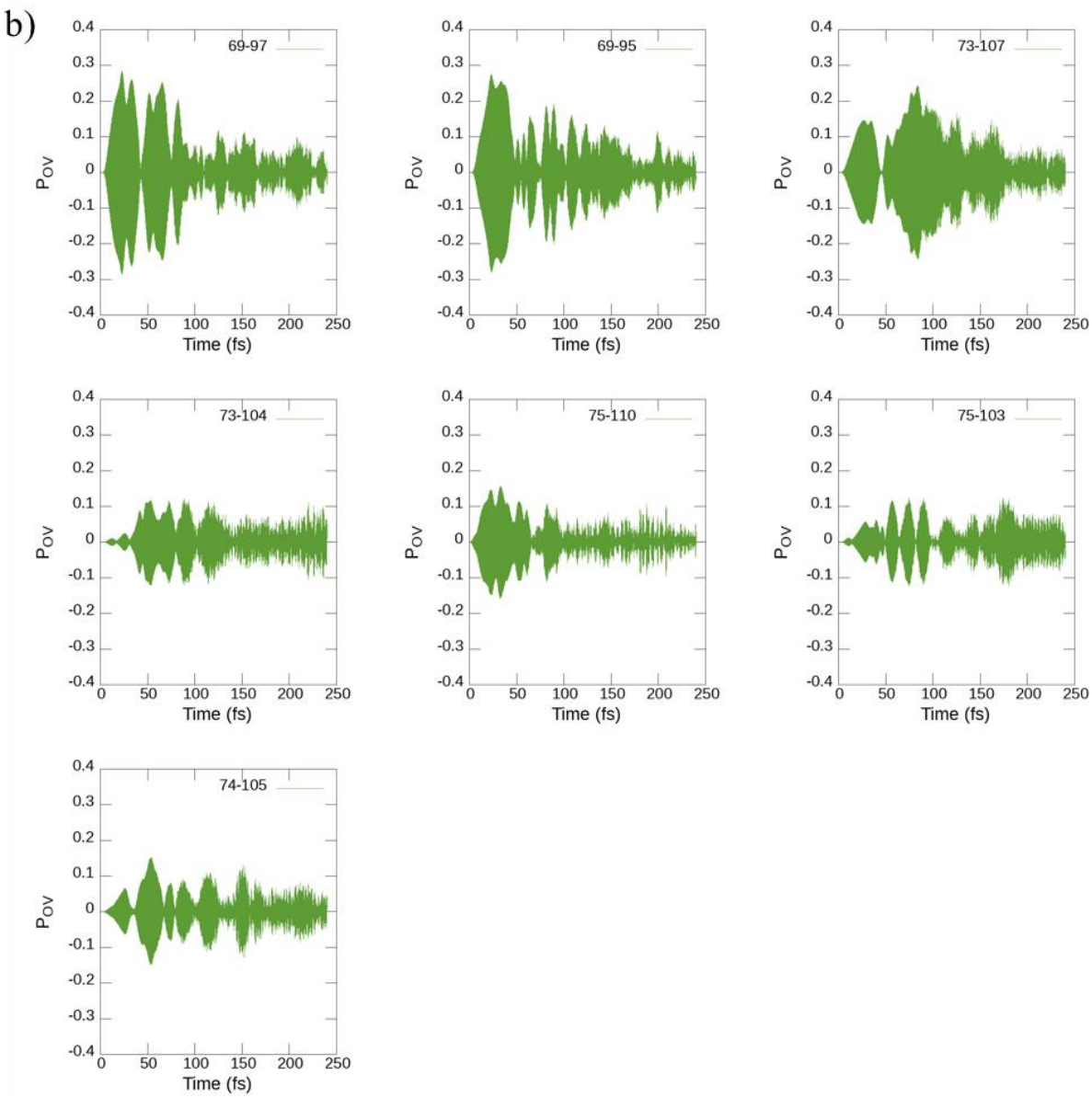

Figure D-11 FT peaks (a) and the P_{OV} (b) for the transitions that give two-photon absorption peaks. These are obtained from the application of a 0.001 au trapezoid field with a frequency corresponding to 7 eV along the z-direction in the $[Al_{13}N_2]^{-1}$ system.

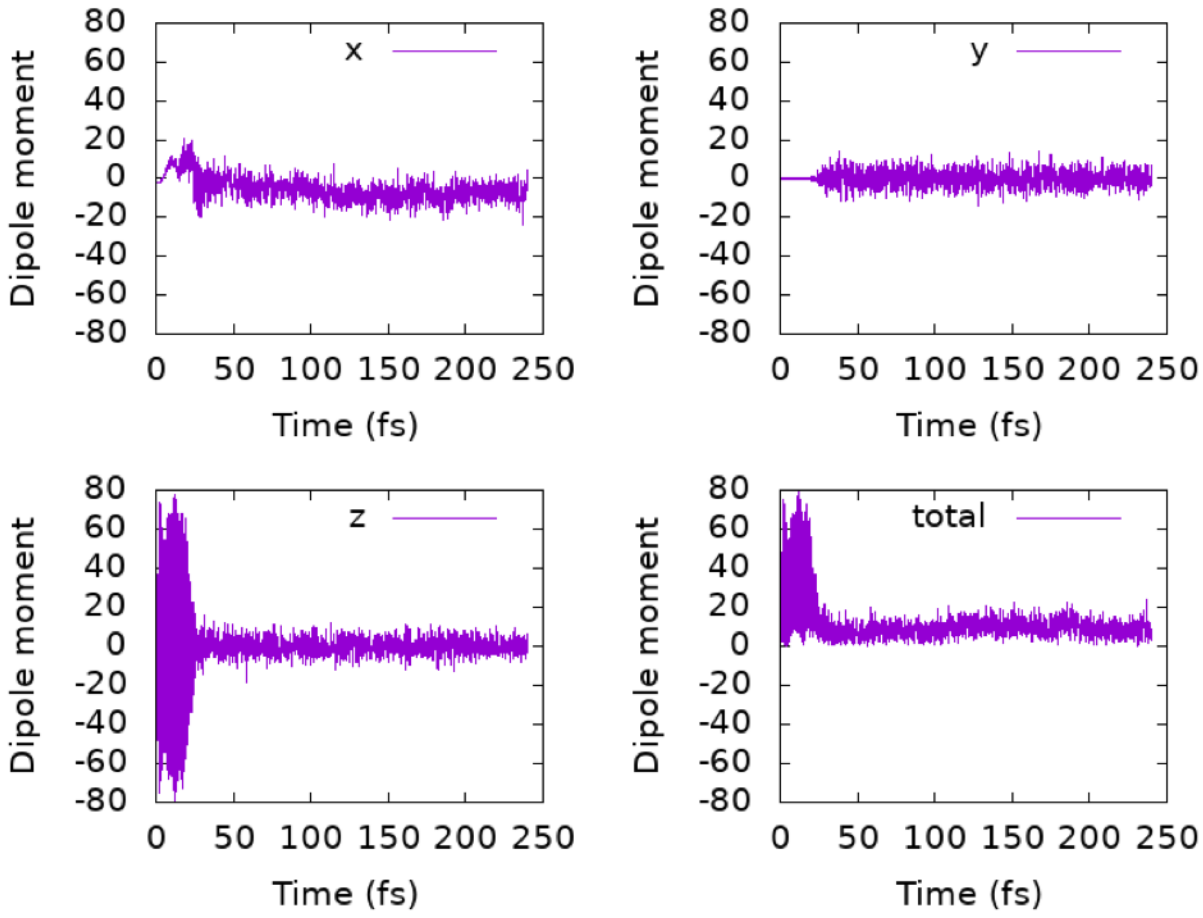

Figure D-12 Variation of different components of the dipole moment (Debye) from the application of the 7 eV trapezoid field of 0.01 au along the z-direction of the $[Al_{13}N_2]^{-1}$ system.

a)

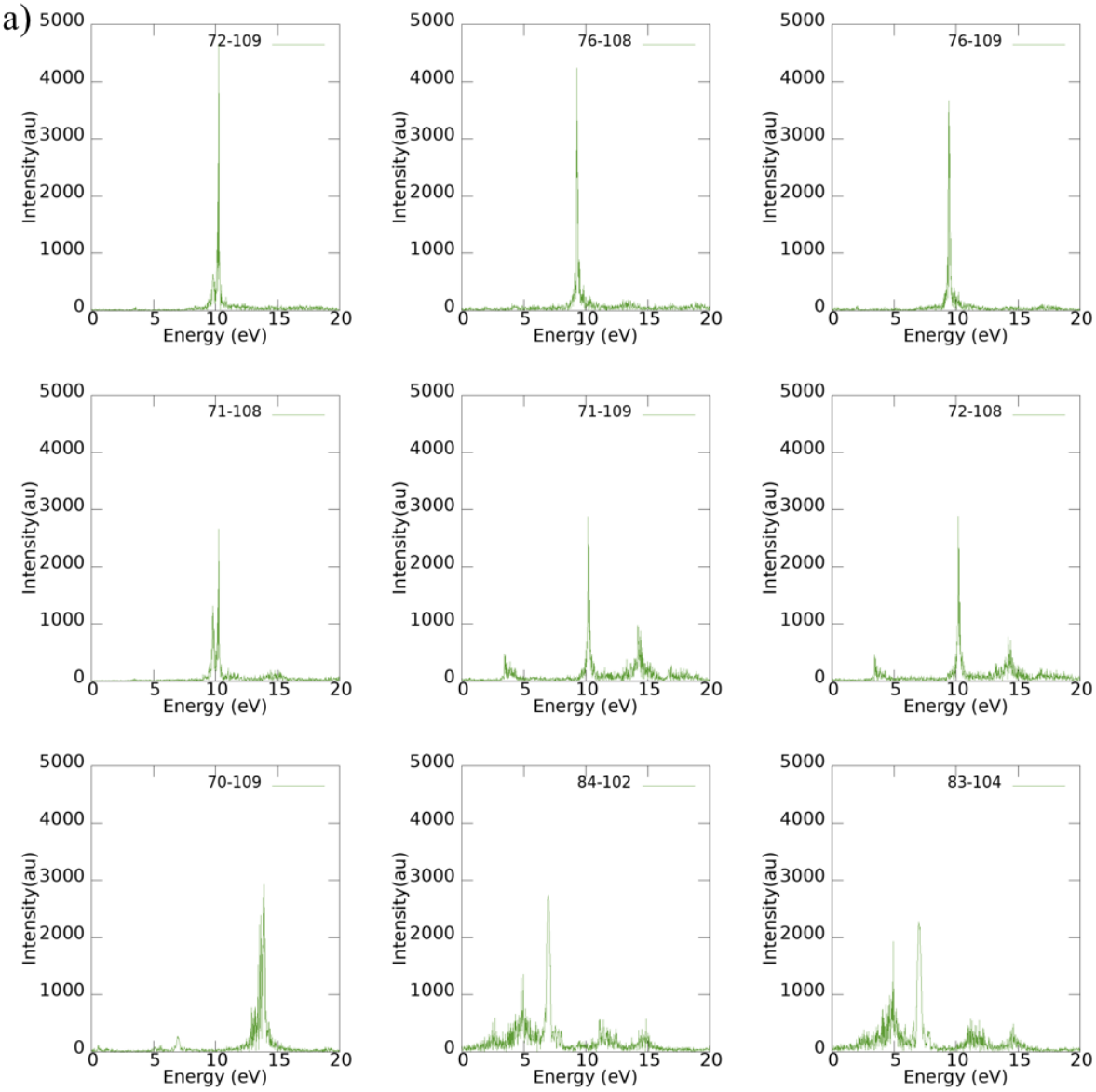
72-109
76-108
76-109
71-108
71-109
72-108
70-109
84-102
83-104
Intensity(au)
Energy (eV)
0
1000
2000
3000
4000
5000
0
5
10
15
20

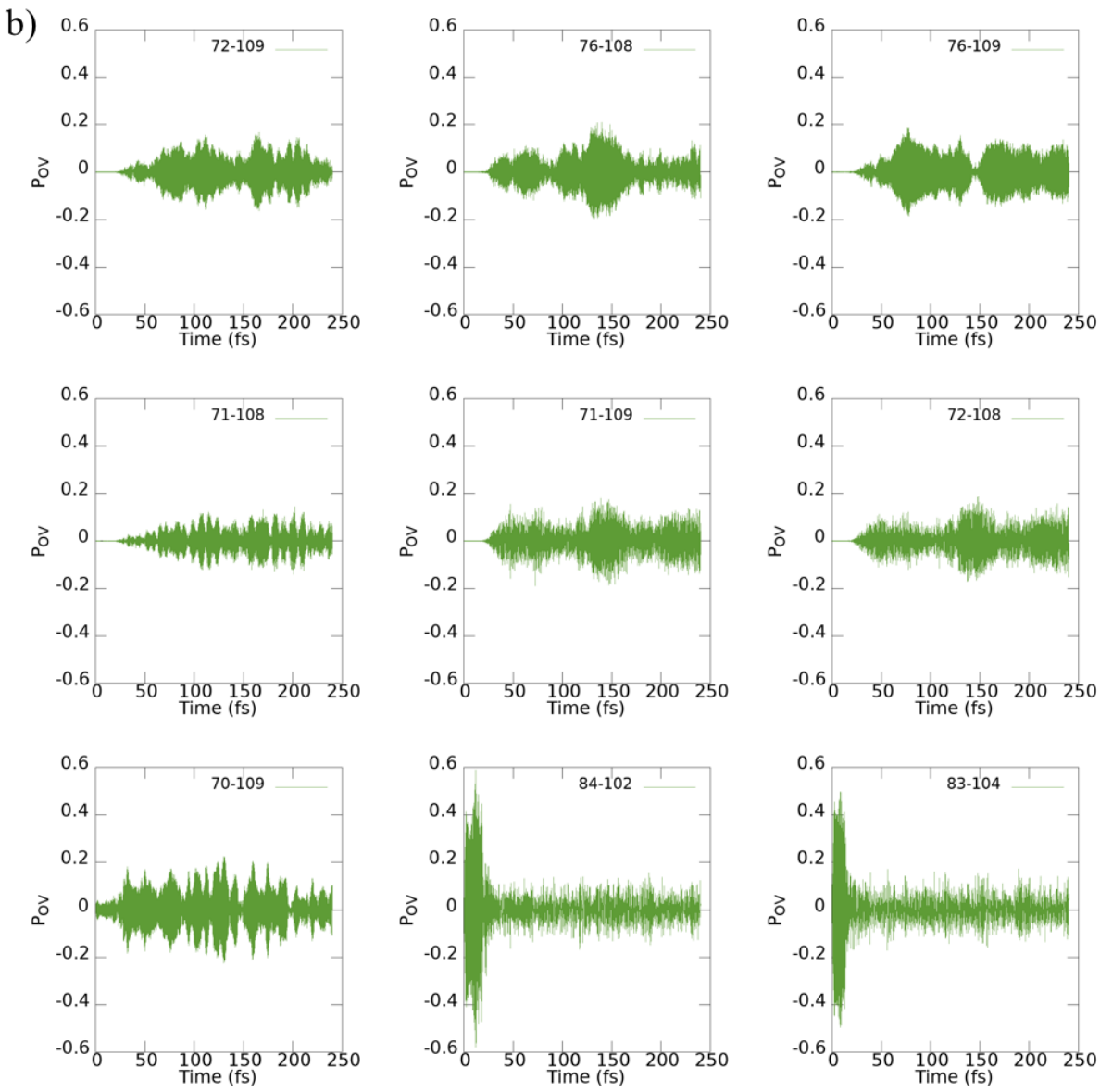

Figure D-13 (a) Highest intensity Fourier transformed peaks and (b) the P_{OV} elements for different single-particle transitions when a 0.01 au trapezoid wave electric field of 7 eV is applied along the z-direction in $[Al_{13}N_2]^{-1}$.

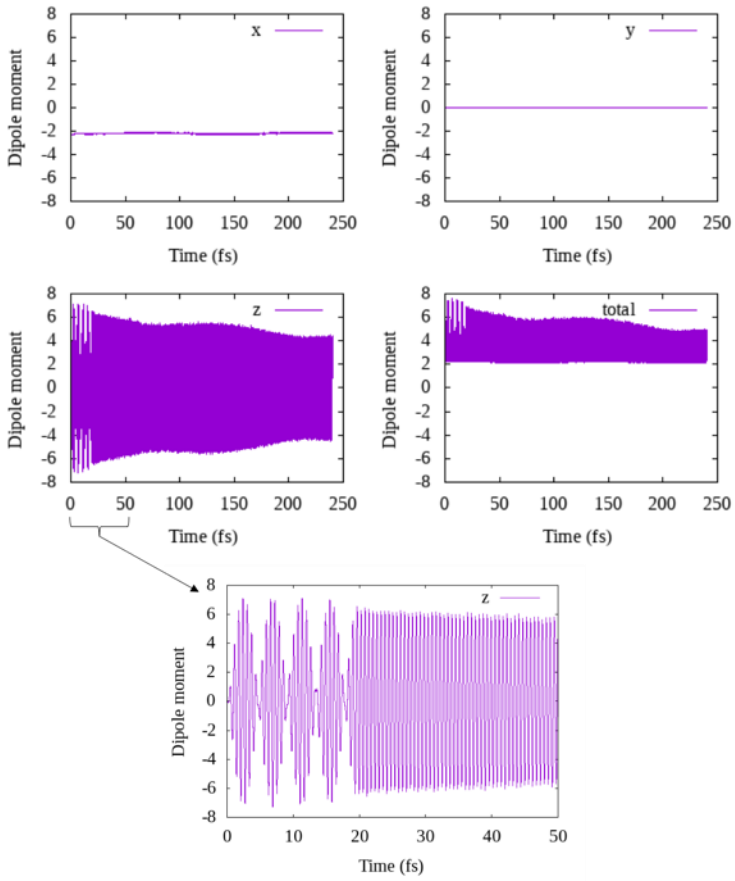

Figure D-14 Variation of different components of the dipole moment (Debye) from the application of a 6 eV trapezoid field with a field strength of 0.001 au applied along the z-direction of the $[Al_{13}N_2]^{-1}$ system.

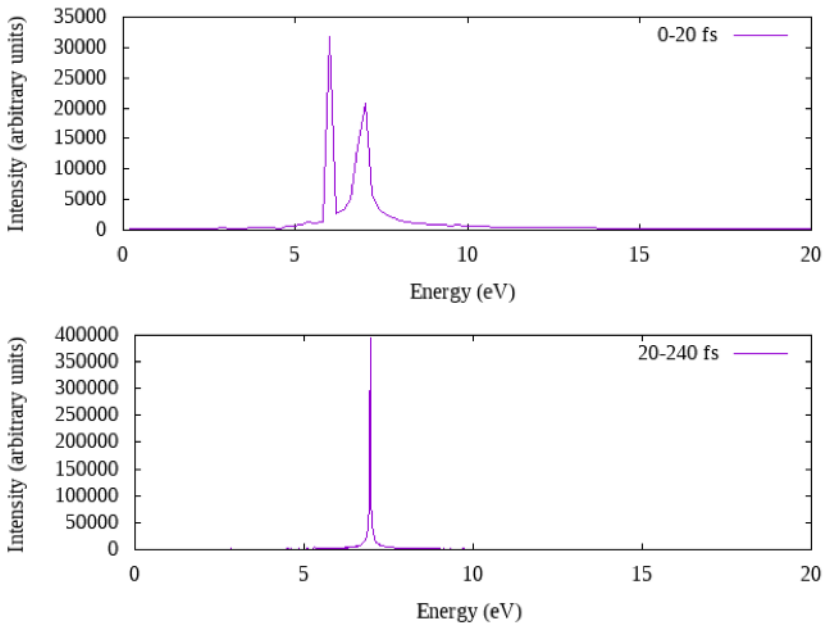

Figure D-15 Fourier transform of the dipole moment (Debye) on application of a 0.001 au z-polarized 6 eV trapezoidal field along the z-direction in the $[Al_{13}N_2]^{-1}$ system.

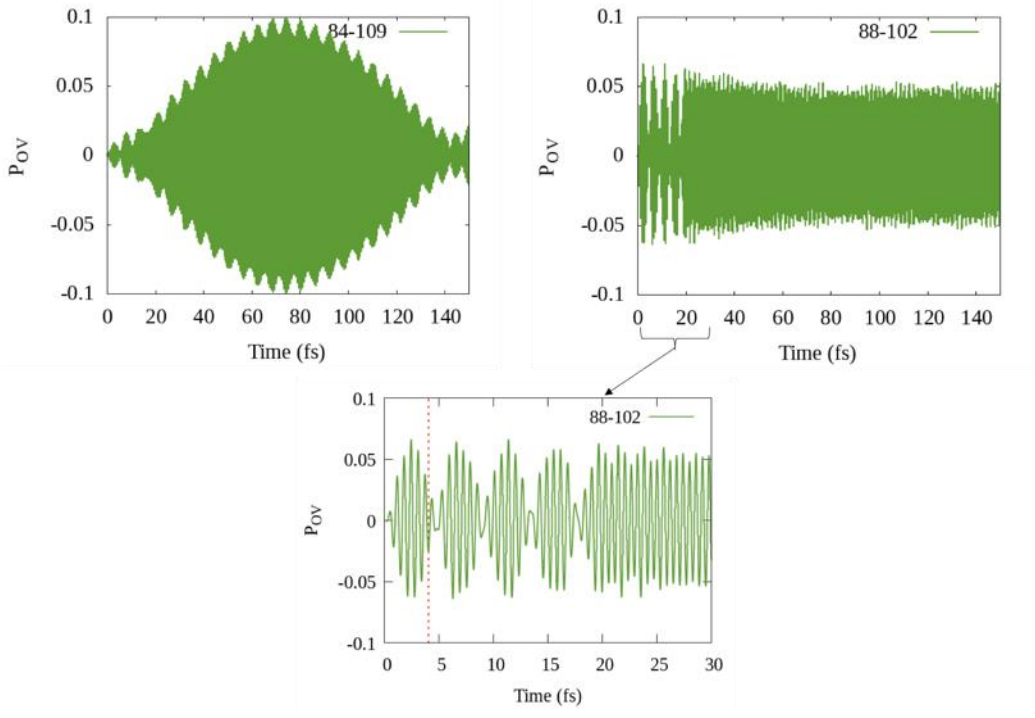

Figure D-16 P_{OV} for the transitions that give the highest intensity FT peaks when a 0.001 au trapezoid field electric field of 6 eV is applied along the z-direction to $[Al_{13}N_2]^{-1}$.

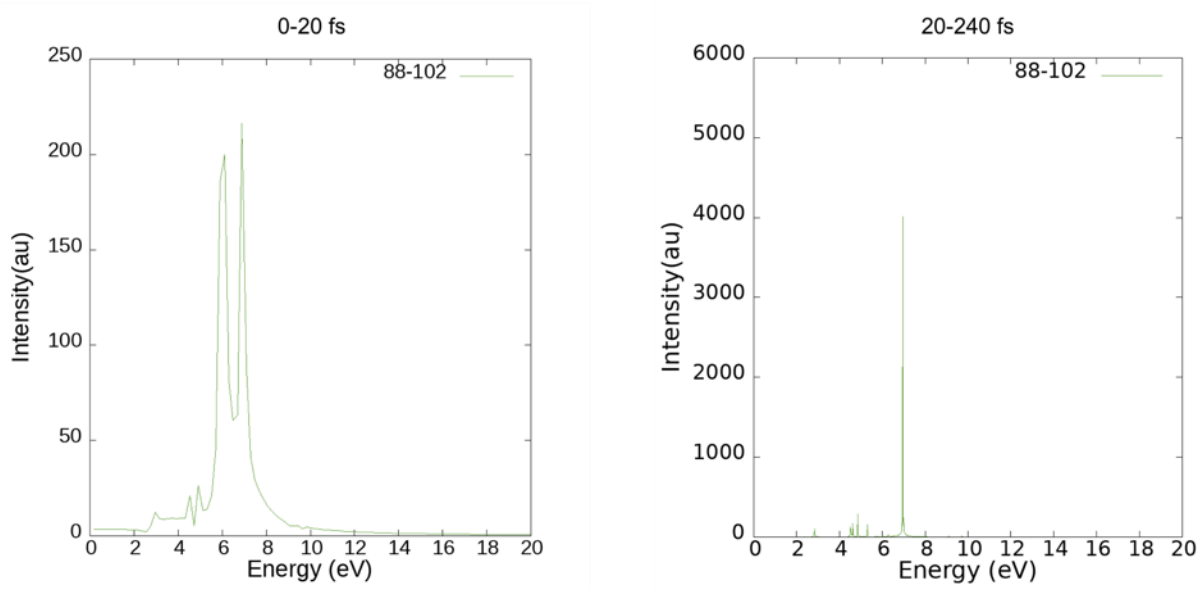

Figure D-17 Fourier transformed peaks for the transition 88→102 during and after the application of the applied laser field. The FT after the application of the field does not show the peak at 6 eV which was present when the Fourier transform was taken during the application of laser field. These FTs are obtained from the application of a 0.001 au trapezoid field with frequency corresponding to 6 eV along the z-direction in $[Al_{13}N_2]^{-1}$.

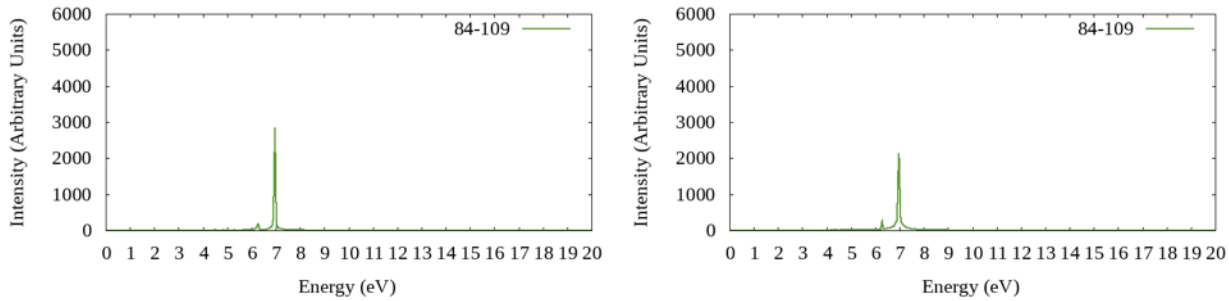

Figure D-18 Fourier transformed peaks for the 84→109 transition from 21-130 fs (left) and from 130-240 fs (right). These are obtained after the application of a 0.001 au trapezoid field with a frequency corresponding to 6 eV along the z-direction in $[Al_{13}N_2]^{-1}$.

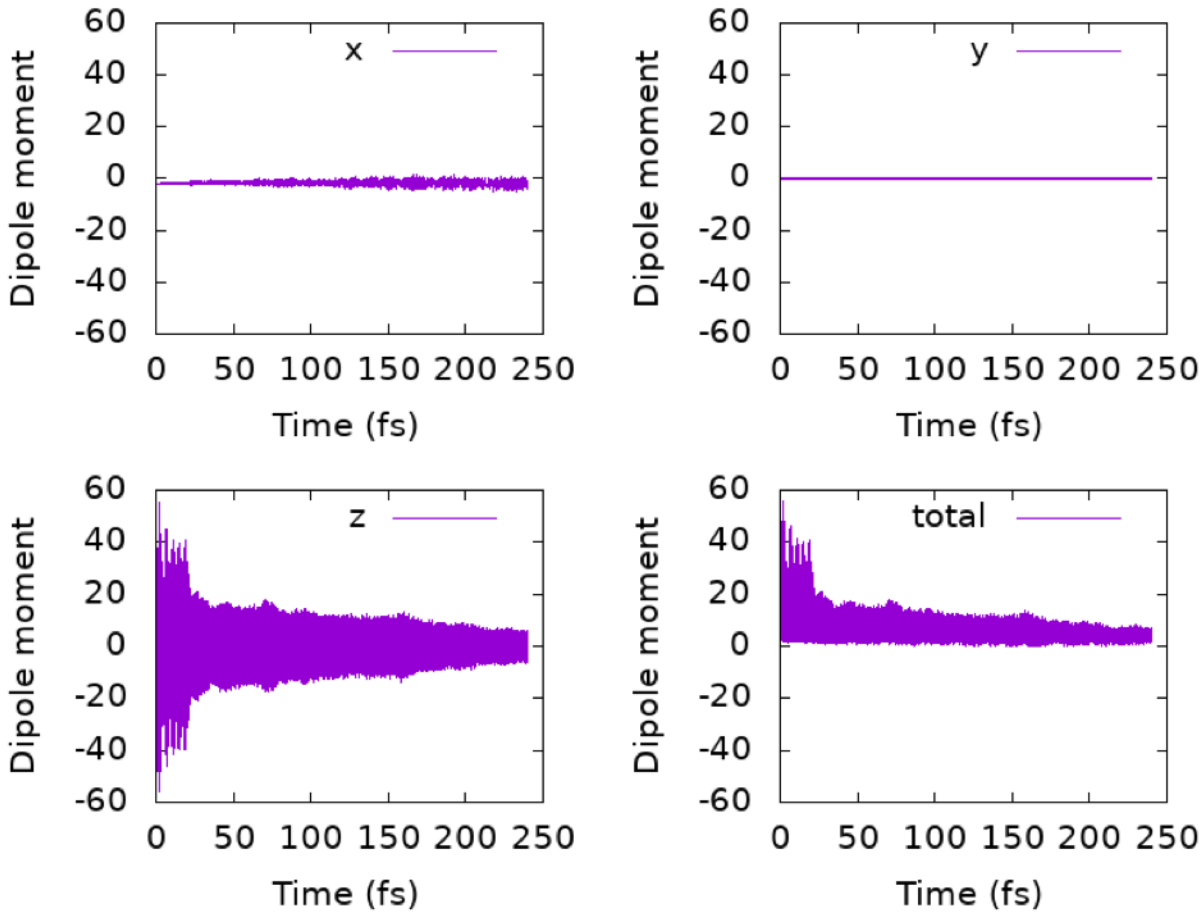

Figure D-19 Variation of different components of the dipole moment (Debye) upon the application of a 6 eV trapezoid field with a field strength of 0.01 au along the z-direction of $[Al_{13}N_2]^{-1}$.

a)

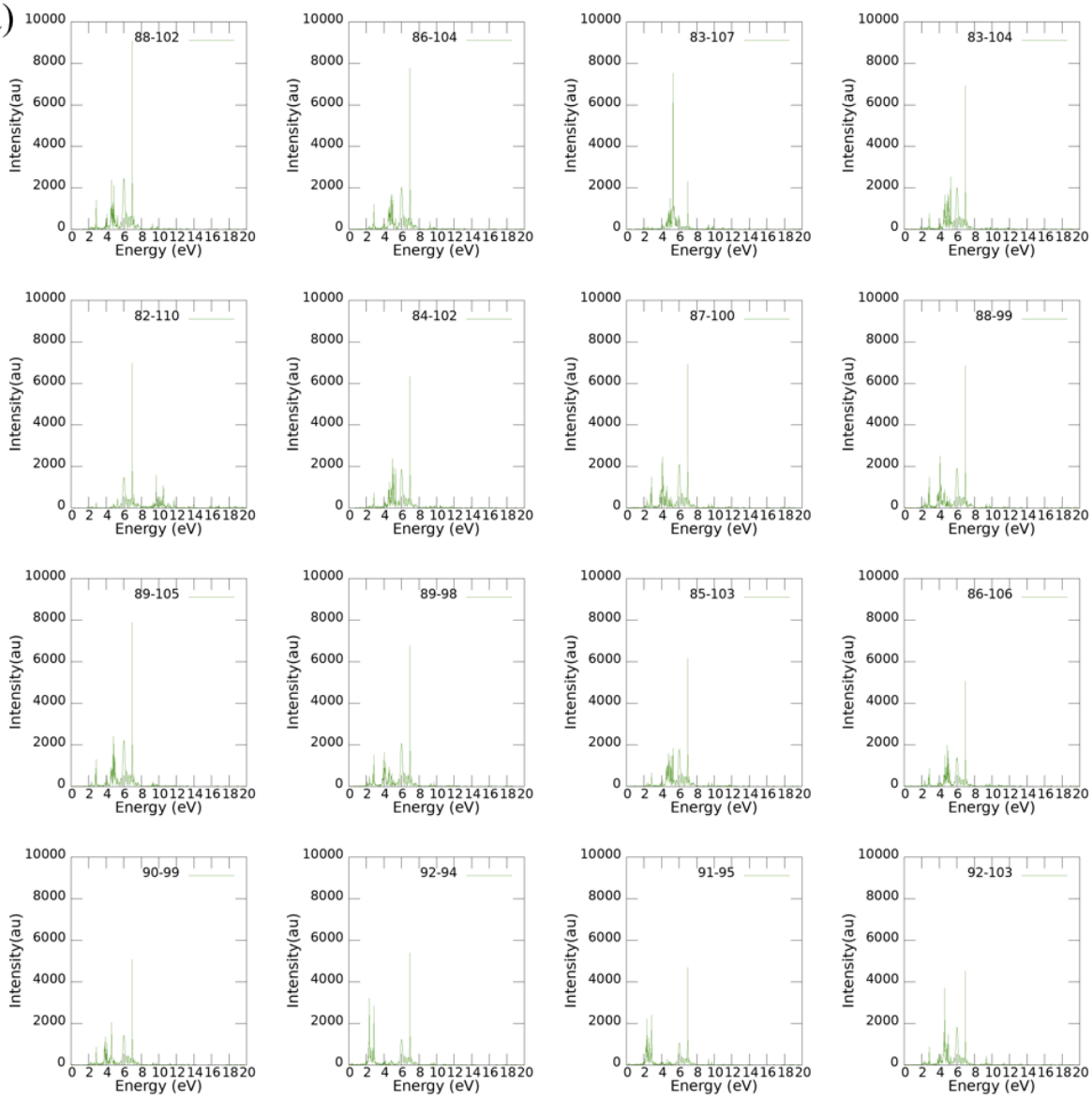
88-102
86-104
83-107
83-104
82-110
84-102
87-100
88-99
89-105
89-98
85-103
86-106
90-99
92-94
91-95
92-103
Intensity(au)
Energy (eV)

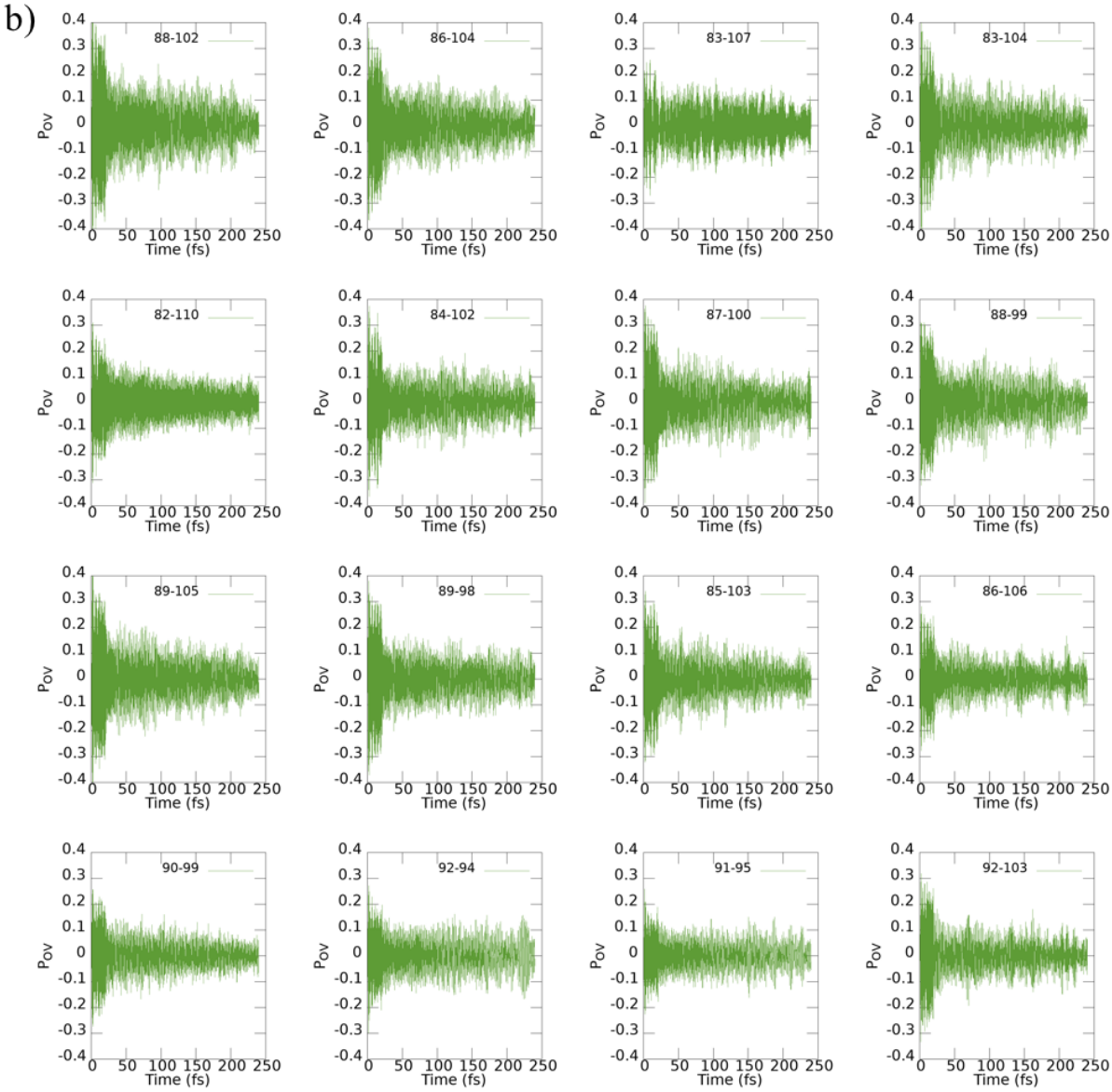

Figure S20 (a) Highest intensity Fourier transformed peaks and (b) P_{OV} elements when a 0.01 au trapezoid electric field with a frequency of 6 eV is applied along the z-direction in $[Al_{13}N_2]^{-1}$.

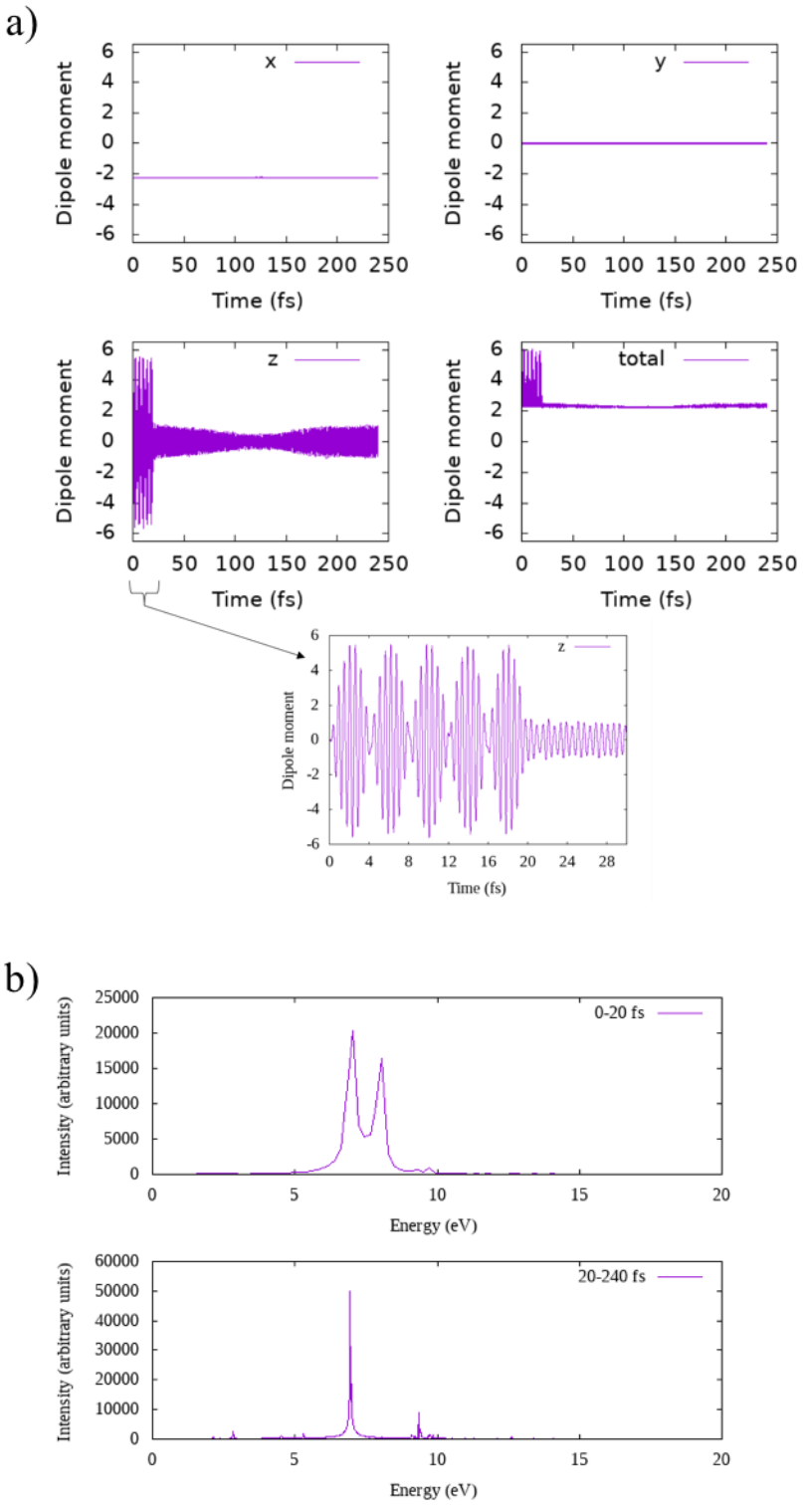

Figure D-21 (a) Variation of different components of the dipole moment (Debye) from the application of a 8 eV trapezoid field with a field strength of 0.001 au along the z-direction of the $[Al_{13}N_2]^{-1}$ system. (b) Fourier transform of the dipole moment (Debye) on application of a 0.001 au z-polarized 8 eV trapezoidal field along the z-direction in the $[Al_{13}N_2]^{-1}$ system

a)

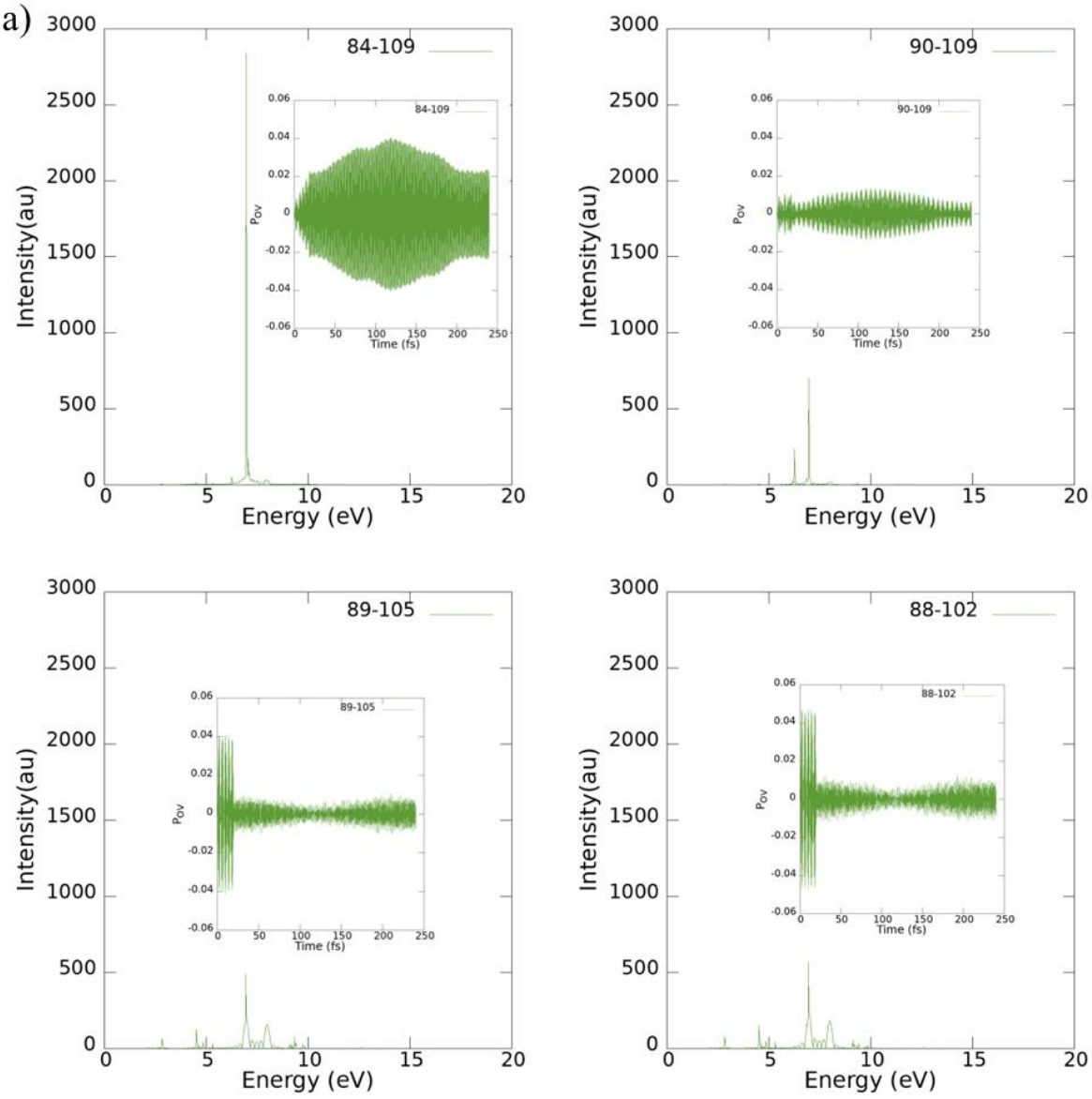

b)

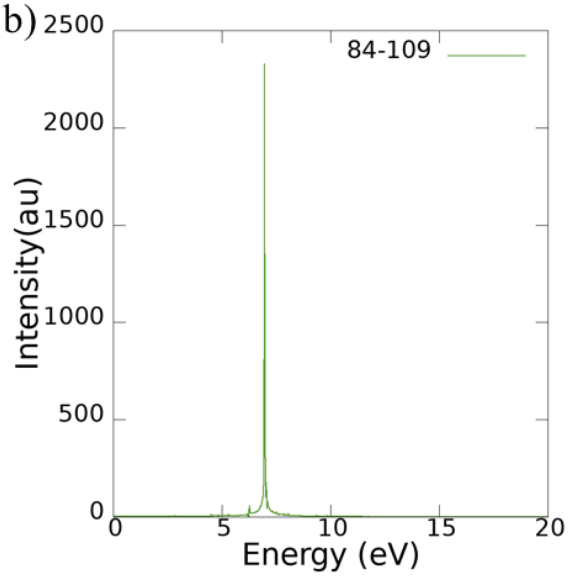
84-109
Intensity(au)
Energy (eV)
0
500
1000
1500
2000
2500
0
5
10
15
20

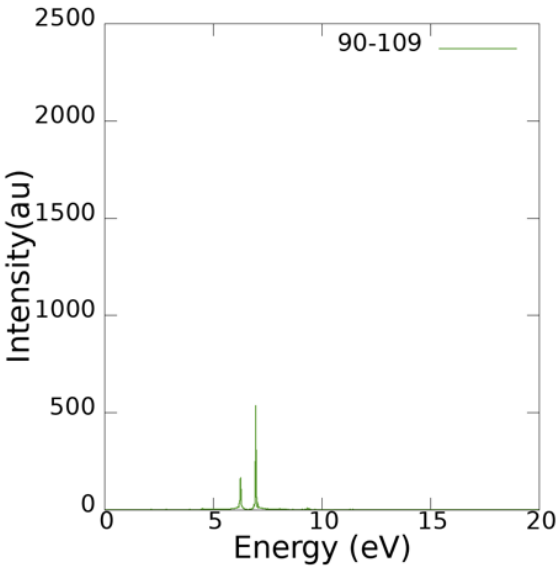
90-109
Intensity(au)
Energy (eV)
0
500
1000
1500
2000
2500
0
5
10
15
20

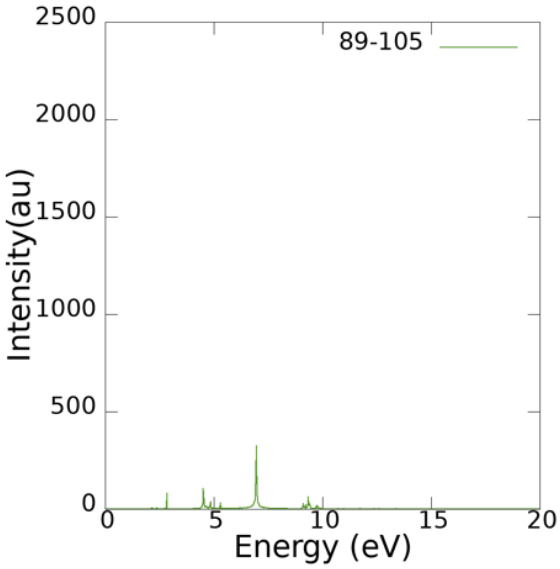
89-105
Intensity(au)
Energy (eV)
0
500
1000
1500
2000
2500
0
5
10
15
20

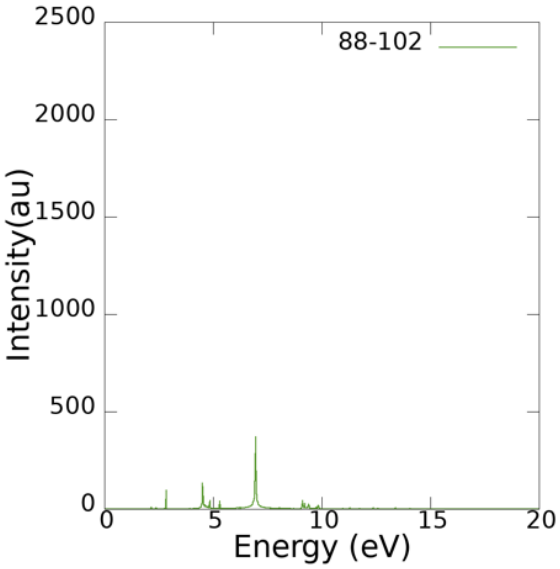
88-102
Intensity(au)
Energy (eV)
0
500
1000
1500
2000
2500
0
5
10
15
20

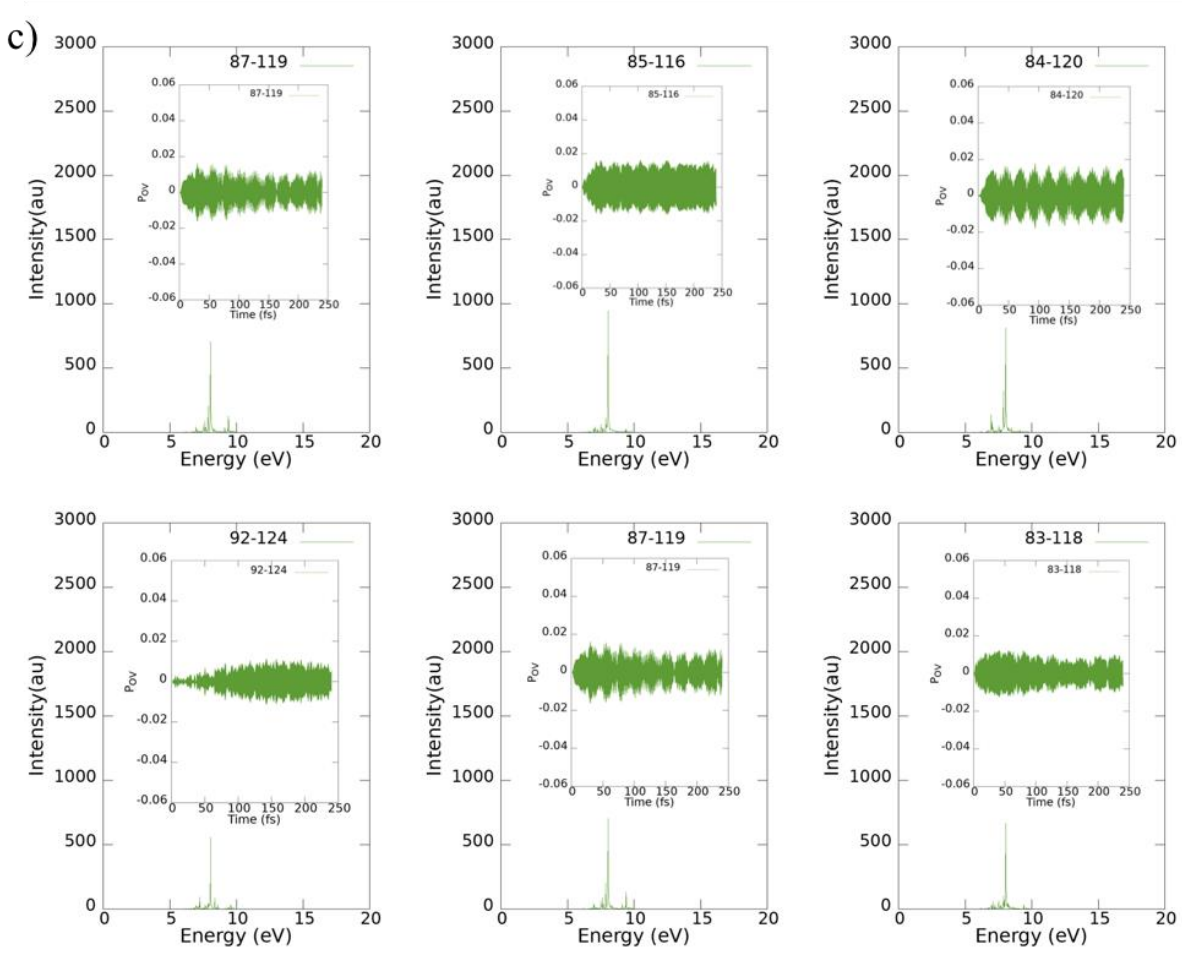

Figure D-22 (a) Transitions that give highest intensity FT peaks at 7 eV and the P_{OV} for the corresponding transitions as insets. The FT are obtained with P_{OV} dynamics from 0-240 fs. (b) FT peaks obtained by only considering P_{OV} dynamics after 20 fs for the transitions that give the 7 eV peak. (c) Transitions that give the highest intensity FT peaks at 8 eV and the P_{OV} for the corresponding transitions as insets. These are obtained from the application of a 0.001 au trapezoid field with a frequency corresponding to 8 eV along the z-direction in $[Al_{13}N_2]^{-1}$.

a)

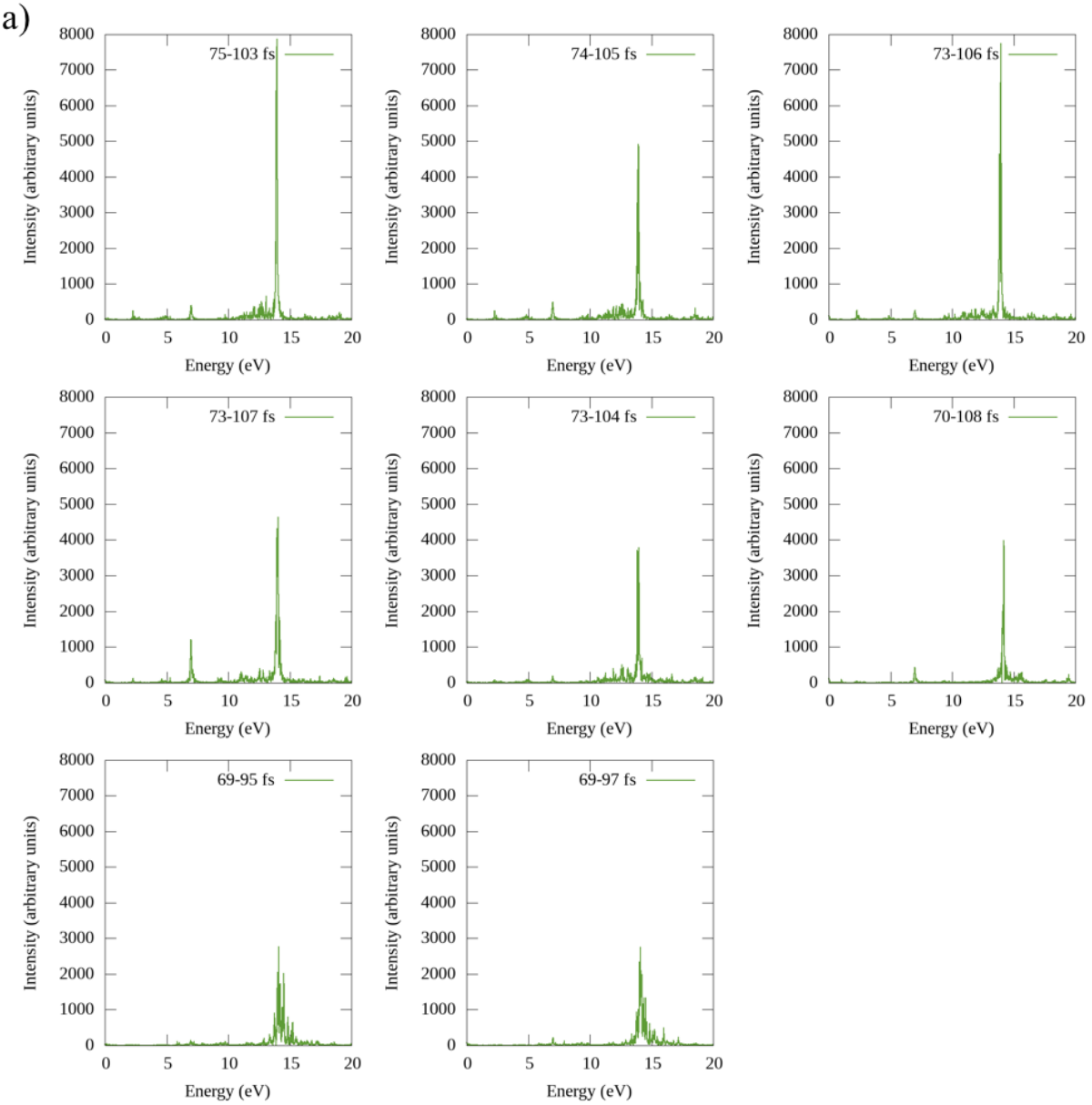
75-103 fs
74-105 fs
73-106 fs
73-107 fs
73-104 fs
70-108 fs
69-95 fs
69-97 fs
Intensity (arbitrary units)
Energy (eV)
0
1000
2000
3000
4000
5000
6000
7000
8000
0
5
10
15
20

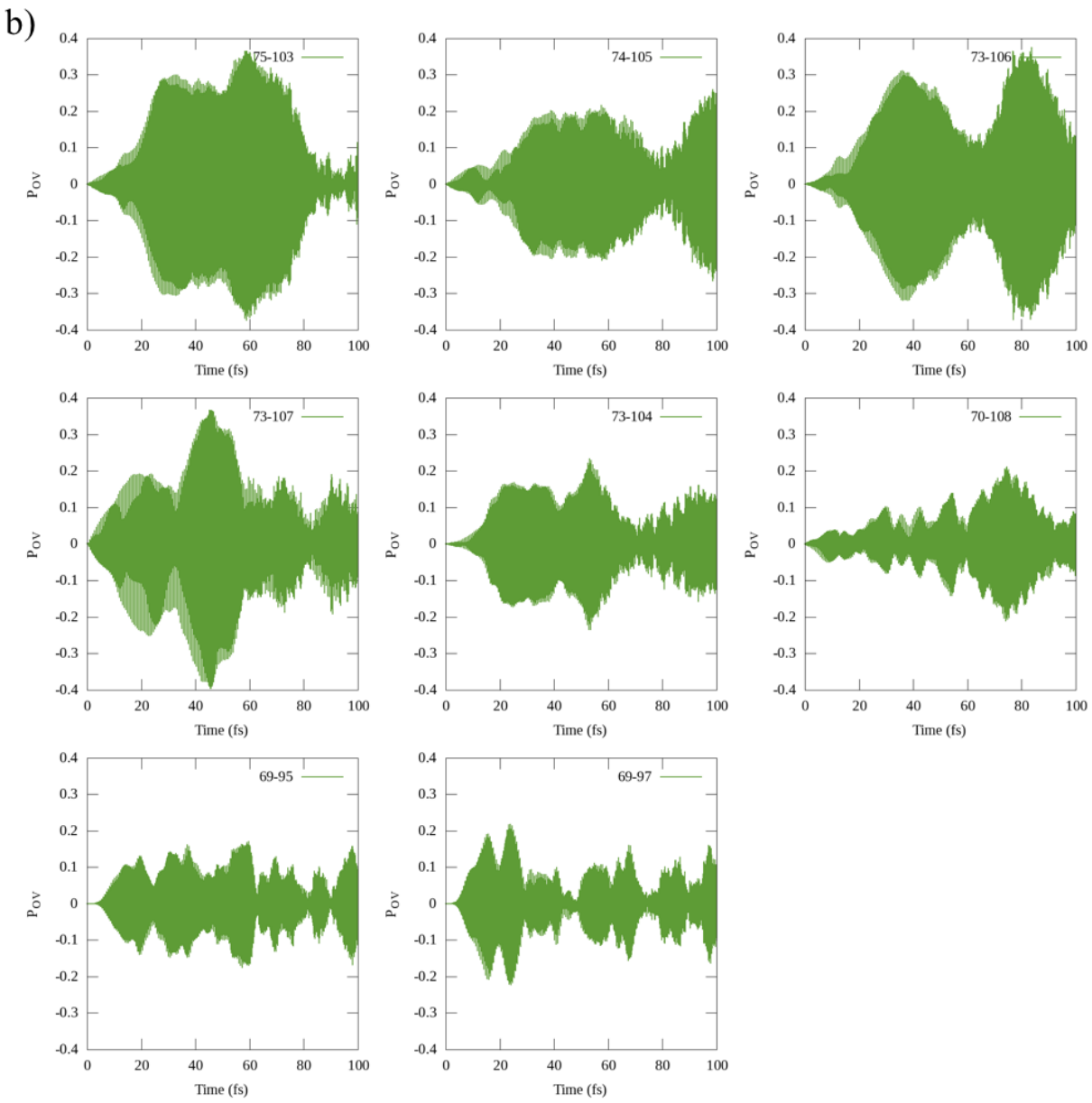

Figure D-23 FT peaks (a) and the P_{OV} (b) for the transitions that give two-photon absorption peaks. These are obtained from the application of a 0.001 au trapezoid field with a frequency corresponding to 7 eV along the x-direction in the $[Al_{13}N_2]^{-1}$ system.